VNIVERSITAT DE VALÈNCIA Facultat de Física

Departament de Física Aplicada i Electromagnetisme

Synthesis and characterization of indium oxide at high pressures

PhD dissertation by

Braulio García Domene

Supervisors

Domingo Martínez García

Francisco Javier Manjón Herrera

Valencia, Spain; April 2018

Don Domingo Martínez García, profesor titular de la Universidad de Valencia y Don Francisco Javier Manjón Herrera, catedrático de la Universidad Politécnica de Valencia

INFORMAN:

Que la presente memoria “Synthesis and characterization of indium oxide at high pressures” se ha realizado bajo su dirección tanto en el departamento de Física Aplicada de la Universidad de Valencia como en el Instituto de Diseño para la Fabricación y Producción Automatizada de la Universidad Politécnica de Valencia por el licenciado en Física Don Braulio García Domene, y que constituye su tesis para optar al grado de Doctor en Física.

Y para que aquí conste, en cumplimiento de la legislación vigente, presenta en la Universidad de Valencia la referida Tesis Doctoral.

Burjassot, a 16 de abril de 2018

Firmado:

Domingo Martínez García

Francisco Javier Manjón Herrera

Nunca dejes de creer en ti.

Contents

Acknowledgements **xi**

Previously published work **xv**

List of abbreviations **xix**

Resumen **xxi**

1. Introduction **1**

2. Theoretical foundations **7**

2.1. X-ray diffraction …… 7

2.1.1. Scattering by electrons, atoms and lattices ….....…….. 8

2.1.2. Geometry of diffraction by a lattice ……..……. 12

2.1.2.1. Laue equations ……...…… 12

2.1.2.2. Bragg's law ……...……. 13

2.1.2.3. Reciprocal lattice and Ewald's sphere ……...…… 14

2.1.3. Powder diffraction pattern ……..…….. 16

2.2. Equations of state ……. 23

2.2.1. Murnaghan equation of state ……. 24

2.2.2. Birch-Murnaghan equation of state ……...…… 25

2.3. Raman spectroscopy ……...……. 26

2.3.1. Fundamentals of non-resonant Raman scattering ……...…….. 26

2.3.2. Resonant versus non-resonant Raman scattering ……..…… 30

2.4 Optical absorption ……..…… 32

2.4.1. Direct and indirect absorption ……..……. 32

3. Experimental methods and techniques and theoretical *ab initio* calculations 37

3.1. Crystal growth technique using a large volume press …….. 37

3.1.1. Paris-Edinburg press ……...…….. 37

3.1.1.1. The anvils ……...…… 41

3.1.1.2. The sample assembly ……...…….. 42

3.1.1.3. Pressure calibration ……..…….. 45

3.1.1.4. Temperature calibration …….…… 50

3.1.2. Multi-anvil press …….…….. 54

3.1.2.1. The sample assembly ……. 55

3.1.2.2. Pressure calibration …… 57

3.1.2.3. Temperature calibration …….…… 58

3.2. High-pressure measurements ……...……. 59

3.2.1. The diamond-anvil cell ……. 59

3.2.2. Pressure calibration …….…….. 61

3.3. Characterization of as-grown materials at ambient and

extreme conditions of pressure and temperature …….…..…….... 63

3.3.1. Scanning electron microscopy …….. 63

3.3.2. Synchrotron radiation sources ……..……. 65

3.3.2.1. Angle-dispersive powder X-ray diffraction

(MSPD beamline at ALBA synchrotron) ……... 65

3.3.3. Raman scattering ……..……. 67

3.3.4. Optical spectroscopy …….…… 70

3.4. Theoretical *ab initio* calculations ……. 71

4. High-pressure lattice dynamical study of bulk and nanocrystalline In_2O_3 73

4.1. Abstract …… 73

4.2. Introduction …….. 73

4.3 Experimental details …….. 75

4.4. *Ab initio* calculations details ……..……. 77

4.5. Results and discussion …….…… 78

4.6. Conclusions …….……. 85

5. *Pbca*-type In_2O_3: The high-pressure post-corundum phase at room temperature 87

5.1. Abstract ……...……. 87

5.2. Introduction …….……. 87

5.3. Experimental section ……..…….. 89

5.4. Results and discussion ……....……. 90

5.5. Conclusions …… 100

Appendix 5.1: Raman studies under pressure of bulk powder c-In_2O_3 with silicone oil and without pressure transmitting medium ……..……. 101

Appendix 5.2: Raman study of the c-In_2O_3 and its high-pressure phases (*Pbcn*, *Pbca* and *R-3c*) ……....…….…… 109

Appendix 5.3: Study of the second upstroke XRD and RS experiment ……...… 115

6. Synthesis and high-pressure study of corundum-type In_2O_3 119

6.1. Abstract …….……. 119

6.2. Introduction ……..…….. 120

6.3. Experimental details ……..……. 121

6.4. Theoretical calculations …….…… 122

6.5. Results and discussion …….…….. 123

6.5.1. Characterization of samples at ambient conditions …… 123

6.5.2. XRD measurements at high pressures ……..…….. 125

6.5.3. RS measurements at high pressures ……..……...…….. 134

6.6. Conclusions ……..…….. 137

6.7. Supplementary material ……..…… 138

Appendix 6.1: "P-T phase diagram" starting from

c-In_2O_3 and rh-In_2O_3 samples ……..…….…….…… 141

Appendix 6.2: Synthesis of metastable corundum-type Cr^{3+}-doped In_2O_3 ……..…. 157

7. Structural and vibrational properties of corundum-type

In_2O_3 nanocrystals under compression **161**

7.1. Abstract ……..…… 161

7.2. Introduction ……..…….. 161

7.3. Methods ……..…… 162

7.3.1. Experimental details ……...……. 162

7.3.2. Theoretical calculations …….. 163

7.4. Results ……..…….. 164

7.4.1. XRD measurements …… 164

7.4.2. Raman scattering ……..…… 169

7.5. Conclusions ……..…….. 173

Appendix 7.1: Theoretical and experimental energy bandgap

of several polymorph of In_2O_3 ……..……..…..……...…… 175

8. Conclusions **181**

Bibliography **185**

Acknowledgements

Me gustaría dedicar unas palabras de agradecimiento a todas las personas que han permitido mi desarrollo, tanto científica como personalmente, a lo largo de esta etapa tan importante de mi vida.

En primer lugar, me gustaría agradecer a los doctores Domingo Martínez García y Francisco Javier Manjón Herrera, mis dos magníficos directores de Tesis, por todas las experiencias que hemos compartido a lo largo de estos años, por todo lo que me han enseñado, por sus consejos, por su ayuda incondicional, dedicación para sacar este trabajo hacia adelante y por su gran compresión en uno de los momentos más difíciles de mi vida.

Sin duda, una de las personas más especiales que he conocido durante la realización de esta tesis doctoral, ha sido el Dr. Juan Ángel Sans Tresserras debido tanto a su implicación en la evolución y desarrollo de mi trabajo como en la amistad que hemos creado. Han sido tantas las experiencias que hemos vivido, los consejos que me ha dado, que debo de agradecerle de corazón todo lo que me ha enseñado durante estos años.

Otro de los pilares fundamentales de estos años ha sido el Dr. Javier Ruiz Fuertes por brindarme siempre su ayuda en todo aquello que he necesitado, por pensar en nuevos experimentos sobre todo en mis estancias de investigación, por sus sabios consejos, por saber motivarme y confiar en mí en los momentos más difíciles. Sin duda, de estos años, me llevo otro gran amigo.

También quiero dar las gracias a todos los miembros tanto del departamento de Física Aplicada y Electromagnetismo de la Universidad de Valencia como a los del Instituto de Diseño para la Fabricación y Producción Automatizada de la Universidad Politécnica de Valencia por todas las vivencias que hemos compartido y sobre todo por hacerme sentir como en casa. En especial, me gustaría agradecer al Dr. Alfredo Segura García Del Río, por ser la persona que me introdujo en el mundo de la investigación y poder aprender de él, al Dr. Oscar Gomis Hilario, al Dr. David Santamaría Pérez al Dr. Errandonea Ponce por su cercanía, amabilidad y disponibilidad para ayudarme a comprender y debatir los datos experimentales.

Me gustaría mostrar mi agradecimiento tanto al Dr. Alfonso Muñoz González y a la Dra. Plácida Rodríguez Hernández por su gran gentileza, su bondad y su extraordinaria rapidez y eficacia a la hora de realizar los cálculos teóricos que hemos necesitado.

Al Dr. Catalin Popescu, tanto por todo lo que nos ha ayudado para sacar hacia adelante los experimentos realizados en el sincrotrón ALBA como por toda la información técnica que me proporcionó acerca del funcionamiento del propio sincrotrón, así como por los buenos momentos vividos (ayudado siempre de su fiel amigo Juan Ángel) tanto en los sincrotrones ALBA como Diamond. Recordáis: ¿Cómo bajé aquella mini colina en Diamond?, o cuando me preguntaron: With what do you want to accompany the chili?, y yo respondí: Chili.

I would like to thank the great reception received by Dr. Yann Le Godec at the Institut de Minéralogie, de Physique des Matériaux et de Cosmochimie (IMPMC) and his implication of both *ex-situ* and *in-situ* high-pressure high-temperature syntheses performed at the IMPMC and Soleil synchrotron, respectively. Specially, its implications in the development of the automatic power control to ensure a stability of the high-pressure high-temperature syntheses using a Paris-Edinburgh press located in the Applied Physics department of the University of Valencia. I thank Mr. Hicham Moutaabbid for helping me both in the laboratory and in the data analysis. Moreover, I would like to thank Dr. Julia Contreras García for making me feel at home and the “bombones team” for all the time that we have shared together.

I would like to express my gratitude to Dr. Leonid Dubrovinsky for accepting me to work with him and his group in the Bayerisches Geoinstitut (BGI), the great reception received and for allowing me the access to all laboratories. I would like to thanks to Dr. Sergey Ovsyannikov, Dr. Alexander Kurnosov and Dr. Natalia Solopova for having patient to teach me and for all the time that they dedicated to me, specially using the multi-anvil press to perform high-pressure high-temperature syntheses. From that research stay, I would like to

thank very warmly my Russian community of friends, especially Dr. Natalia Solopova, Dr. Anna Pakhomova and Mr. Alexander Serovaysky for all the special moments that we spent together.

No puedo olvidarme de mi querido amigo Diego Gómez Hernández, el mejor técnico de la Universidad de Valencia, por muchos motivos. Primero, porque nos ha fabricado numerosas piezas en el taller mecánico y nos ha permitido seguir avanzando en nuestras investigaciones y segundo y más importante, porque han sido muchos los momentos que hemos compartido juntos. Quería darte las gracias por escucharme, aconsejarme y apoyarme en los momentos más difíciles.

También me gustaría agradecer al Dr. Vicente Muñoz SanJosé por las amenas conversaciones que hemos tenido, por los momentos que hemos compartido, por sus consejos, en definitiva, por la amistad que hemos creado durante estos años.

También quiero dar las gracias a la Dra. Chantal Ferrer Roca por darme la oportunidad de colaborador en el desarrollo de cuatro ediciones del concurso de experimentos y demostraciones de Física y Tecnología para estudiantes de enseñanza media.

Sin duda, durante la realización de esta tesis, he podido conocer a mucha gente maravillosa. Comenzaré hablando de la Dra. Gloria Almonacid Caballer, mi amiga y compañera de despacho que me ayudó en todo lo que necesité, me integró en el grupo de estudiantes y compartimos muchos momentos juntos al Dr. Carlos Renero Lecuna en numerosas escuelas de altas presiones y congresos internacionales. ¡Simplemente, inolvidable! Otro grupo de los que marcó una época fue el “Evolution running” compuesto por los mejores atletas de Valencia como son: Juan Ángel (el míster), Diego, Salva, Julio Pellicer, David, Gloria y yo por supuesto. Otro proyecto deportivo donde conocí a muchas personas fue en la creación de un equipo de Fútbol 7, con la magnífica ayuda de los directores técnicos Vicent y Lluís. Me gustaría decir que casi llevamos el nombre de Física Aplicada a lo más alto de la competición. Gracias por todos los momentos que hemos compartido y por ayudarme en la organización de la defensa de mi tesis doctoral. ¡Os debo un karting! Agradezco también a todos los compañeros del departamento que han hecho que la hora del café o la hora de la comida fueran momentos agradables. Entre ellos están, Min, Gloria, Erica, Mauricio, Javi, Mauro, Pere, Mauricio, David, Antonio Carrascosa, Salva, Enrico, Emmanuel, Luis, Vicent, Lluís, Ade, Kumar, Said, Esther, Oleksii, Nathalie, Rosa, Miguel, Martina, Lorena, Antonio Diez,

José Luis, Juan Carlos, Juan Damas y Manuel. Perdonad si me dejo a alguien, pero es que sois muchísimos. ¡Gracias a todos!

Me gustaría agradecer a numerosas personas con las que he compartido gratos momentos durante este último año en las Islas Canarias y que me han motivado para que finalizara de una vez mi etapa como estudiante de doctorado. Me refiero a Sonia, Bati, Cheikh, Adeun, Jorge, Alicia, Cristina Protasio, Ysia, Johanna, Diksha, Manu, Alberto, Juan y Kenny. ¡Sois geniales! Nos vemos pronto.

También me gustaría dar las gracias a tres grandes personas que me están acompañando en mi vida. Concretamente me refiero a Tarek, Alex y Fernando Pinto. Gracias por ayudarme en todo lo que he necesitado, por compartir conmigo numerosos momentos tan especiales, por valorar los pequeños detalles de la vida y por motivarme a alcanzar mis sueños.

Para concluir, me gustaría agradecer de todo corazón a mi familia, especialmente a mis padres, Miguel y Encarna y a mis hermanos Miguel Ángel, Nuria y Patricia por su apoyo incondicional en todas las decisiones que he tomado, por sus consejos, por todos los grandes momentos que hemos compartido y por los que aún nos quedan por compartir. No me gustaría acabar sin citar a los dos bombones de la casa, Elena y Anais. Simplemente, ¡Os quiero!

Previously published work

Thesis work:

- J.A. Sans, R. Vilaplana, D. Errandonea, V.P. Cuenca-Gotor, B. García-Domene, C. Popescu, F.J. Manjón, A. Singhal, S.N. Achary, D. Martínez-García, J. Pellicer-Porres, P. Rodríguez-Hernández and A. Muñoz, "Structural and vibrational properties of corundum-type In_2O_3 nanocrystals under compression", *Nanotechnology* **28**, 205701 (2017).
- B. García-Domene, J.A. Sans, F.J. Manjón, Sergey V. Ovsyannikov, L.S. Dubrovinsky, D. Martínez-García, O. Gomis, D. Errandonea, H. Moutaabbid, Y. Le Godec, H. M. Ortiz, A. Muñoz, P. Rodríguez-Hernández and C. Popescu, "Synthesis and High-Pressure Study of Corundum-Type In_2O_3", *J. Phys. Chem. C* **119**, 29076-29087 (2015).
- B. García-Domene, J.A. Sans, O. Gomis, F.J. Manjón, H.M. Ortiz, D. Errandonea, D. Santamaría-Pérez, D. Martínez-García, R. Vilaplana, A.L.J. Pereira, A. Morales-García, P. Rodríguez-Hernández, A. Muñoz, C. Popescu and A. Segura, "*Pbca*-Type In_2O_3: The High-Pressure Post-Corundum phase at Room Temperature", *J. Phys. Chem. C* **118**, 20545-20552 (2014).
- B. García-Domene, H.M. Ortiz, O. Gomis, J.A. Sans, F.J. Manjón, A. Muñoz, P. Rodríguez-Hernández, S.N. Achary, D. Errandonea, D. Martínez-García, A.H. Romero, A. Singhal and A.K. Tyagi, "High-Pressure Lattice Dynamical Study of Bulk and Nanocrystalline In_2O_3", *J. Appl. Phys.* **112**, 123511 (2012).

Collaborations:

- R. Vilaplana, J.A. Sans, F.J. Manjón, A. Andrada-Chacón, J. Sánchez-Benítez, C. Popescu, O. Gomis, A.L.J. Pereira, B. García-Domene, P. Rodríguez-Hernández, A. Muñoz, D. Daisenberger, O. Oeckler, "Structural and electrical study of the topological insulator $SnBi_2Te_4$ at high pressure", *J. Alloys. Comp.* **685**, 962-970 (2016).
- D. Errandonea, O. Gomis, D. Santamaría-Pérez, B. García-Domene, A. Muñoz, P. Rodríguez-Hernández, S.N. Achary, A.K. Tyagi, and C. Popescu, "Exploring the high-pressure behavior of the three known polymorphs of $BiPO_4$: Discovery of a new polymorph", *J. Appl. Phys.* **117**, 105902 (2015).
- O. Gomis, D. Santamaría-Pérez, J. Ruiz-Fuertes, J.A. Sans, R. Vilaplana, H.M. Ortiz, B. García-Domene, F.J. Manjón, D. Errandonea, P. Rodríguez-Hernández, A. Muñoz and M. Mollar, "High-pressure structural and elastic properties of Tl_2O_3", *J. Appl. Phys.* **116**, 133521 (2014).
- D. Santamaría-Pérez, O. Gomis, J.A. Sans, H.M. Ortiz, Á. Vegas, D. Errandonea, J. Ruiz-Fuertes, D. Martínez-García, B. García-Domene, A.L.J. Pereira, F.J. Manjón, P. Rodríguez-Hernández, A. Muñoz, F. Piccinelli, M. Bettinelli and C. Popescu, "Compressibility Systematics of Calcite-Type Borates: An Experimental and Theoretical Structural Study on ABO_3 (A = Al, Sc, Fe, and In)", *J. Phys. Chem.* C **118**, 4354-4361 (2014).
- A.L.J. Pereira, D. Errandonea, A. Beltrán, L. Gracia, O. Gomis, J.A. Sans, B. García-Domene, A. Miquel-Veyrat, F.J. Manjón, A. Muñoz and C. Popescu, "Structural study of α-Bi_2O_3 under pressure", *J. Phys.: Condens. Matter* **25**, 475402 (2013).
- D. Errandonea, O. Gomis, B. García-Domene, J. Pellicer-Porres, V. Katari, S. N. Achary, A.K. Tyagi and C. Popescu, "New Polymorph of $InVO_4$: A High-Pressure Structure with Six-Coordinated Vanadium", *Inorg. Chem.* **52**, 12790-12798 (2013).
- D. Santamaría-Pérez, A. Morales-García, D. Martínez-García, B. García-Domene, C. Mühle and M. Jansen, "Structural Phase Transitions on AgCuS Stromeyerite Mineral under Compression", *Inorg. Chem.* **52**, 355-361 (2013).

- S.J. Gilliland, J.A. Sans, J.F. Sánchez-Royo, G. Almonacid, B. García-Domene, A. Segura, G. Tobias and E. Canadell, "Role of p-d and s-d interactions in the electronic structure and band gap of $Zn_{1-x}M_xO$ (M = Cr, Mn, Fe, Co, Ni, and Cu): Photoelectron and optical spectroscopy and first-principles band structure calculations", *Phys. Rev. B* **86**, 155203 (2012).
- J. Ibáñez, A. Segura, B. García-Domene, R. Oliva, F.J. Manjón, T. Yamaguchi, Y. Nanishi and L. Artús, "High-pressure optical absorption in InN: Electron density dependence in the wurtzite phase and reevaluation of the indirect band gap of rocksalt InN", *Phys. Rev. B* **86**, 035210 (2012).
- A. Segura, J.F. Sánchez-Royo, B. García-Domene and G. Almonacid, "Current underestimation of the optical gap and Burstein-Moss shift in CdO thin films: A consequence of extended misuse of α^2-versus-hν plots", *Appl. Phys. Lett.* **99**, 151907 (2011).

List of abbreviations

Abbreviation	Definition
BGI	Bayerisches Geoinstitut
BM2	2^{nd} order Birch-Murnaghan
BM3	3^{rd} order Birch-Murnaghan
BZ	Brillouin zone
c-	Cubic bixbyite-type structure
CB	Conduction band
CBM	Conduction band minimum
DAC	Diamond-anvil cell
DFT	Density functional theory
EoS	Equation of state
GGA	Generalized-gradient approximation
h-	Hexagonal
HP	High-pressure
HT	High-temperature
IR	Infrared
KB	Kirkpatrick-Baez
LDA	Local-density approximation
MA	Multi-anvil
MCT	Mercury cadmium telluride
MEW	Methanol-ethanol-water
MSPD	Materials science and powder diffraction
NA	Numerical aperture
NIR	Near-infrared
o1-	Orthorhombic Rh_2O_3−II-type structure
o2-	Orthorhombic α-Gd_2S_3-type structure
o3-	Orthorhombic Rh_2O_3−III-type structure

P	Pressure
PAW	Projector-augmented wave
PBE	Perdew-Burke-Enzerhof
PBEsol	Perdew-Burke-Enzerhof for solids
PE	Paris-Edinburgh
PTM	Pressure-transmitting medium
RF	Resonance fluorescence
rh-	Rhombohedral corundum-type structure
RR	Resonant Raman
RS	Raman scattering
SD	Sintered diamond
SEM	Scanning electron microscopy
SG	Space group
T	Temperature
TCO	Transparent conducting oxide
ToF	Time-of-flight
UV	Ultraviolet
V	Volume
VASP	Vienna *ab initio* simulation package
VB	Valence band
VBM	Valence band maximum
VIS	Visible
XRD	X-ray diffraction
WC	Tungsten carbide
Z	Number of formula units in the unit cell

Resumen

Introducción

La naturaleza es sorprendente pero a la vez limitada. A mi entender, nada tiene más potencial que aplicar el ingenio humano para modificar lo que nos rodea y crear algo completamente nuevo.

La Física de la Materia Condensada es un campo que actualmente está ganando importancia en la Física moderna. En virtud de los éxitos logrados en Física de la Materia Condensada se han producido enormes avances en el campo de la electrónica cuántica, de los semiconductores y de la ciencia de materiales, teniendo como resultado numerosas aplicaciones tecnológicas que han cambiado nuestras vidas drásticamente en los últimos 50 años. Una de las ramas de la Física de la Materia Condensada es el estudio de las propiedades de la materia sometidas a condiciones extremas de presión y temperatura. Este estudio tiene como objetivo comprender las fuerzas que actúan dentro de un sólido, las cuales, rigen sus propiedades estructurales, elásticas, vibracionales, ópticas, eléctricas y magnéticas, permitiendo reproducir los procesos y fenómenos que ocurren tanto dentro de la Tierra como en muchos otros planetas.

Gracias a estos estudios, se puede ayudar a comprender los fenómenos físicos, químicos, geológicos e incluso biológicos que ocurren bajo condiciones de alta presión y temperatura.

Tradicionalmente, los experimentos realizados en los laboratorios eran los mayores responsables de proporcionar la mayoría de la información sobre las propiedades de la materia. Sin embargo, en las últimas décadas, el desarrollo de la ciencia computacional con los métodos teóricos de cálculo a partir de los primeros principios o métodos *ab initio*, en perfecta colaboración con los científicos experimentales, se han convertido en una herramienta indispensable, no solamente para comprender y predecir las propiedades de los materiales, sino para diseñar nuevos materiales, provocando un gran desarrollo en el estudio de las técnicas de HP-HT. Especialmente, los métodos *ab initio* están fundamentados en la teoría cuántica donde solo se tienen en cuenta el tipo de átomos presentes en el material, sus localizaciones aproximadas en el espacio real y sus interacciones.

La estructura cúbica tipo bixbyita está presente en diversos óxidos binarios como el In_2O_3, Sc_2O_3 y Mn_2O_3. De hecho, aparte del In_2O_3, muchos óxidos binarios, como ZnO, SnO_2 y TiO_2 han sido ampliamente estudiados para ser empleados en dispositivos optoelectrónicos debido a sus propiedades especiales como ser un TCO **[1–3]**. El amplio uso de la estructura cúbica tipo bixbyita de In_2O_3 (c-In_2O_3) en procesos industriales abarca desde la fabricación de capas transparentes en celdas solares **[3–5]**, diodos emisores de luz **[6–9]**, ventanas electrocrómicas **[10]**, pantallas de cristal líquido **[11, 12]** y sensores de gas **[13–17]**. Sin embargo, la escasez y el alto coste para obtener indio metálico ha conducido al estudio de nuevos sistemas, como el In_2O_3 dopado con estaño (ITO) y $In_{2-2x}Zn_xSn_xO_3$ ($x \leq 0.4$), también llamado ZITO, con el objetivo de reducir el precio de su proceso de producción **[18–20]**.

Se conocen varios polimorfos de In_2O_3. En condiciones ambiente, el In_2O_3 cristaliza en la estructura cúbica tipo bixbyita (SG *Ia-3*, N.º 206, Z = 16) **[21, 22]**, siendo la fase mejor conocida y la más común en los sesquióxidos de tierras raras. Sin embargo, otros polimorfos menos conocidos del In_2O_3 son la estructura romboédrica tipo corindón (SG *R-3c*, N.º 167, Z = 6), la estructura ortorrómbica tipo Rh_2O_3−II (SG *Pbcn*, N.º 60, Z = 4) y la estructura ortorrómbica tipo α-Gd_2S_3 (SG *Pnma*, N.º 62, Z = 4) **[23–44]** que pueden ser obtenidas a través de la aplicación de presión y temperatura. En la estructura cúbica, romboédrica y Rh_2O_3−II los cationes tienen coordinación 6; sin embargo, la coordinación de los cationes aumenta hasta alcanzar el valor de 7 y 8 para la estructura α-Gd_2S_3.

HT han sido empleadas sistemáticamente en estudios de HP para inducir transiciones de fase retardadas o incluso impedidas en In_2O_3 a temperatura ambiente debido a la presencia de efectos cinéticos **[36, 37, 40, 41, 43, 45]**. En cuanto a los estudios de c-In_2O_3 bajo HP-HT, se

ha observado que el c-In_2O_3 permanece estable hasta 6 GPa y 1450 ºC **[46]**. Además, en la década de 1960 se ha citado que el c-In_2O_3 al someterlo a presiones de 6.5 GPa y temperaturas comprendidas entre 880 y 1300 ºC resulta el crecimiento de la estructura romboédrica tipo corindón en el In_2O_3 (rh-In_2O_3) cuando se recupera el material sintetizado a condiciones ambiente **[23, 25]**. También se ha sintetizado de forma metaestable nanoestructuras y capas delgadas de rh-In_2O_3 en condiciones ambiente **[27, 28, 30–35, 38, 41, 47–50]** y aplicando ondas de choque en el rango de presiones entre 15–25 GPa a c-In_2O_3 **[26]**.

El gran interés para obtener rh-In_2O_3 como fase metaestable en condiciones ambiente es porque se espera que muestre mejores propiedades que c-In_2O_3, como una mejor estabilidad y una mayor conductividad **[21, 51]**. Estas propiedades hacen rh-In_2O_3 especialmente adecuado para el uso en células solares, catálisis y sensores de gas.

Yusa *et al*. observaron en el In_2O_3 a través de medidas de XRD la fase Rh_2O_3−II como la fase posterior a la corindón a 7GPa y 1630 ºC y la fase α-Gd_2S_3 como la fase posterior de la Rh_2O_3−II sobre 40 GPa y 1730 ºC **[36, 37]**.

Uno de los resultados contradictorios que nos ha motivado a realizar un estudio más detallado de c-In_2O_3 a HP y temperatura ambiente fue la propuesta de Liu et al. **[52]** y Qi et al. **[53]**, donde argumentaban a través de diversos estudios de XRD en material en volumen y en nanocristales, respectivamente, que rh-In_2O_3 era la fase de HP de c-In_2O_3. Otro de los motivos que existían era la controversia de obtener la estructura ortorrómbica tipo Rh_2O_3−II del In_2O_3 (o1-In_2O_3) como una fase metaestable en condiciones ambiente mediante tratamientos a HP-HT **[40, 41, 43]**. La obtención del o1-In_2O_3 en condiciones ambiente, abriría una nueva vía para ajustar las propiedades de los materiales **[54]**.

En los últimos años, las propiedades de los nanocristales del In_2O_3 están recibiendo una mayor atención porque sus propiedades son prácticamente desconocidas. Se han realizado importantes esfuerzos de investigación para la preparación exitosa de nanocristales de In_2O_3 de tamaño y forma controlada **[53, 55, 56]**. Además, las propiedades vibracionales de nanoestructuras de In_2O_3 han comenzado a ser investigadas **[57, 58]**.

Objetivos

Los objetivos fundamentales de esta tesis doctoral han sido estudiar la estabilidad en presión y temperatura de diversos polimorfos tanto en material en volumen como en forma

nanocristalina de In_2O_3 y conocer las condiciones óptimas de alta presión y temperatura para sintetizar rh-In_2O_3 y recuperarla de forma metaestable en condiciones ambiente, partiendo de c-In_2O_3.

Metodología

En esta sección se describen los montajes experimentales y las técnicas empleadas para estudiar las propiedades físicas de los materiales estudiados (c-In_2O_3 y rh-In_2O_3) tanto a presión ambiente como a altas presiones.

Durante esta tesis doctoral se han empleado dos prensas de gran volumen para sintetizar nuevas fases del In_2O_3 en condiciones extremas de presión y temperatura. Concretamente se ha empleado la prensa PE (200 toneladas) situada en el departamento de Física Aplicada de la Universidad de Valencia y la prensa MA (Sumitomo 1200 toneladas) situada en el Bayerisches Geoinstitut (BGI) en la ciudad de Bayreuth (Alemania).

Tanto las muestras de partida como las muestras sintetizadas se han caracterizado a través de la microscopía electrónica de barrido, difracción de rayos X y espectroscopía Raman y óptica. Se ha empleado tanto la celda de membrana **[59]** con yunques de diamante como la celda de yunques de diamante tipo ALMAX-Boehler **[60, 61]** para generar altas presiones y poder estudiar las propiedades físicas en función de la presión. La gran diferencia entre ambas celdas es el mecanismo para generar la presión. La celda de membrana no es necesario moverla para incrementar o reducir la presión, por lo que es muy útil para medidas sincrotrón debido al ahorro de tiempo en el procedimiento de centrado y alineamiento de la celda con el haz de rayos X. Sin embargo, la celda de yunques de diamante tipo ALMAX-Boehler, aunque requiere más tiempo de ajuste para incrementar la presión, presenta una mayor apertura angular (hasta $4\theta = 90^{o}$) comparada con la celda de membrana. Esto permite observar un mayor número de reflexiones de Bragg y facilitar la resolución de la estructura de una fase desconocida de un material.

Además, se han realizado colaboraciones con el profesor A. Muñoz y la profesora P. Rodríguez-Hernández para hacer cálculos *ab initio* y poder contrastar la información teórica con los resultados obtenidos experimentalmente. Para realizar los cálculos teóricos, se ha empleado tanto la DFT como la aproximación de pseudopotenciales.

Resultados y conclusiones

Los resultados y las conclusiones más relevantes que se han obtenido al realizar la tesis doctoral, se pueden resumir en las siguientes ideas.

Por una parte, se ha realizado un estudio de espectroscopía Raman bajo presión en el c-In_2O_3, comparando el comportamiento del material en volumen y en forma nanocristalina. Este estudio se hizo empleando una mezcla de MEW en las proporciones 16:3:1 como medio transmisor de presión. Se observa que la estructura c-In_2O_3 es estable hasta 30 GPa en unas condiciones de cuasi hidrostaticidad, tanto para el material en volumen como para la forma nanocristalina como se pueden apreciar en la evolución de los espectros Raman en función de la presión en la **Figura 1**.

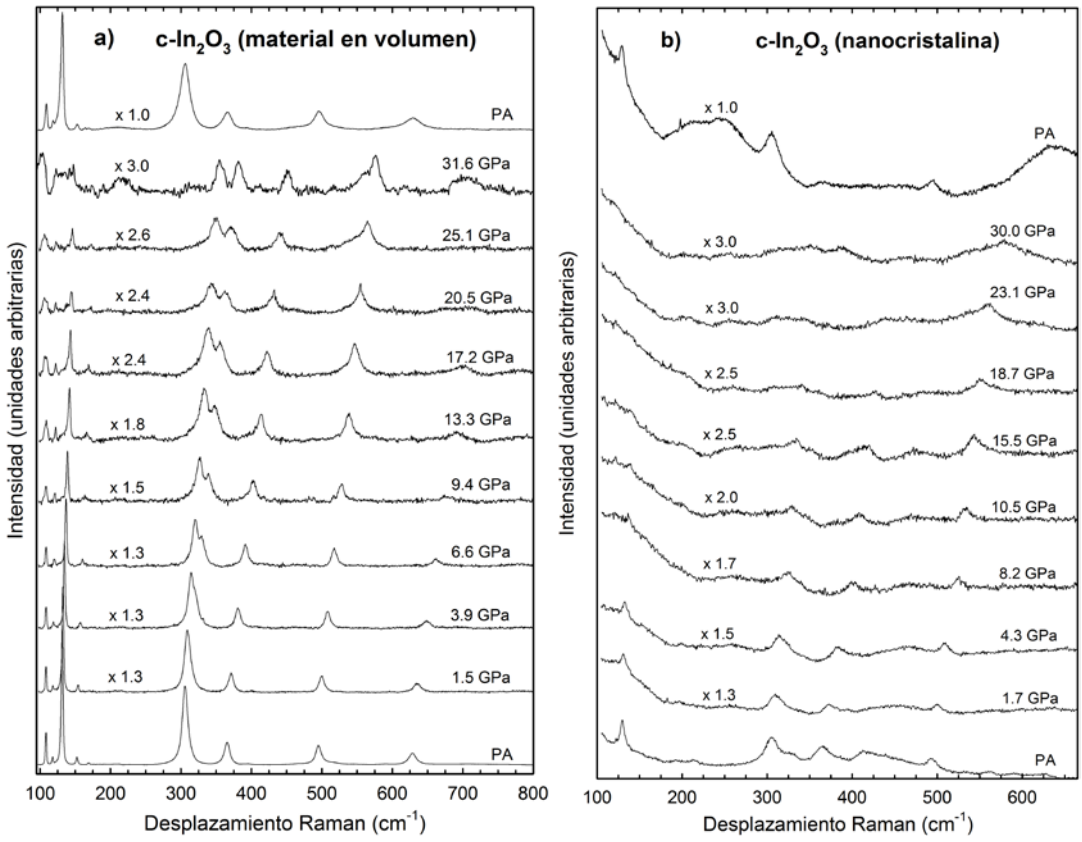

Figura 1: *Diferentes espectros Raman en función de la presión para la fase c-In_2O_3 en material en volumen* ***(a)*** *y forma nanocristalina* ***(b)***.

Gracias a los cálculos *ab initio* ha sido posible asignar la simetría de los 16 (8) modos activos Raman observados en el material en volumen (nanocristales) del c-In_2O_3. Las frecuencias de los modos activos Raman obtenidas en los cálculos difieren en un 5% (subestimación) respecto de las observadas experimentalmente. Por otra parte, los modos siguen una evolución

no lineal bajo presión, tal y como se puede apreciar en la **Figura 2**, en la que se comparan los resultados experimentales y los cálculos teóricos.

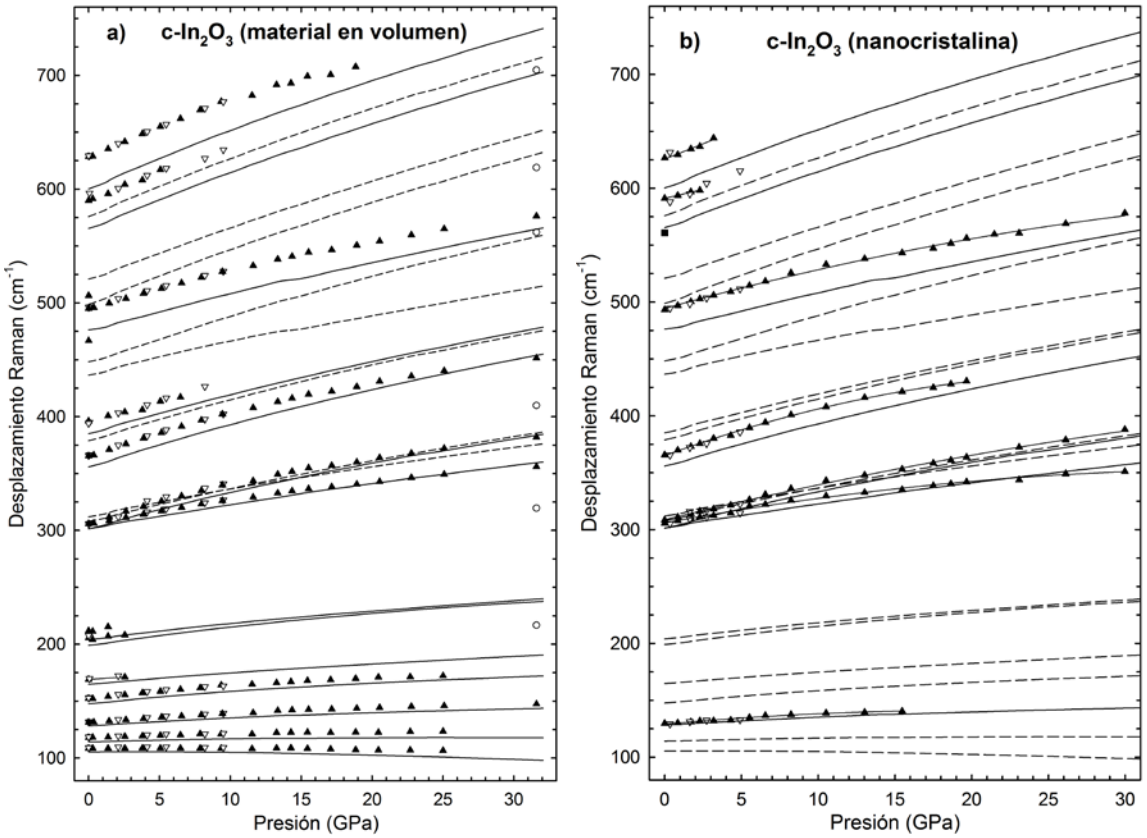

Figura 2: *Dependencia en presión de las frecuencias de los modos activos Raman para el material en volumen* ***(a)*** *y en forma nanocristalina* ***(b)****. Los triángulos rellenos (vacíos) corresponden con las medidas experimentales subiendo (bajando) la presión. Las líneas continuas (discontinuas) representan los datos teóricos para los modos activos Raman observados (no observados) para la fase c-In_2O_3 del material en volumen.*

Se ha descubierto un nuevo polimorfo de In_2O_3 a altas presiones. La **Figura 3** muestra la celda unidad de la estructura del nuevo polimorfo (o3-In_2O_3), el cual cristaliza en la estructura ortorrómbica Rh_2O_3−III con grupo espacial *Pbca* (N.º 61). Para determinar este polimorfo, hemos realizado un estudio estructural y vibracional en función de la presión hasta 50 GPa del material en volumen, partiendo de la fase cúbica, c-In_2O_3, y con la ayuda de los cálculos teóricos *ab initio*.

El **esquema 1** muestra la secuencia de transiciones de fase inducidas bajo presión en el In_2O_3 hasta 50 GPa en condiciones cuasi hidrostáticas. En ambos experimentos, ya sea empleando helio, en el estudio de XRD, o la mezcla de MEW en las proporciones 16:3:1, en el estudio de espectroscopía Raman como medios transmisores de presión, la estructura c-In_2O_3 se

transforma en la estructura o1-In_2O_3 sobre los 35 GPa en el proceso de subida en presión. En el proceso de bajada en presión, la muestra se transforma de o1-In_2O_3 a o3-In_2O_3 entre 40 y 20 GPa (dependiendo del medio transmisor empleado en el experimento) y posteriormente, a 8 GPa transita a rh-In_2O_3, la estructura metaestable recuperada en condiciones ambiente de presión y temperatura.

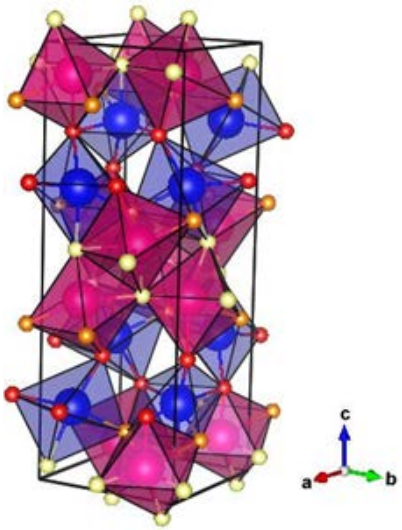

Figura 3: *Nuevo polimorfo de In_2O_3 con estructura ortorrómbica y grupo espacial Pbca (o3-In_2O_3). Los átomos azules y rosas representan los dos átomos de In no equivalentes, mientras que los átomos rojos, naranjas y amarillos representan los átomos no equivalentes de O. Los diferentes poliedros InO_6 se muestran en la imagen.*

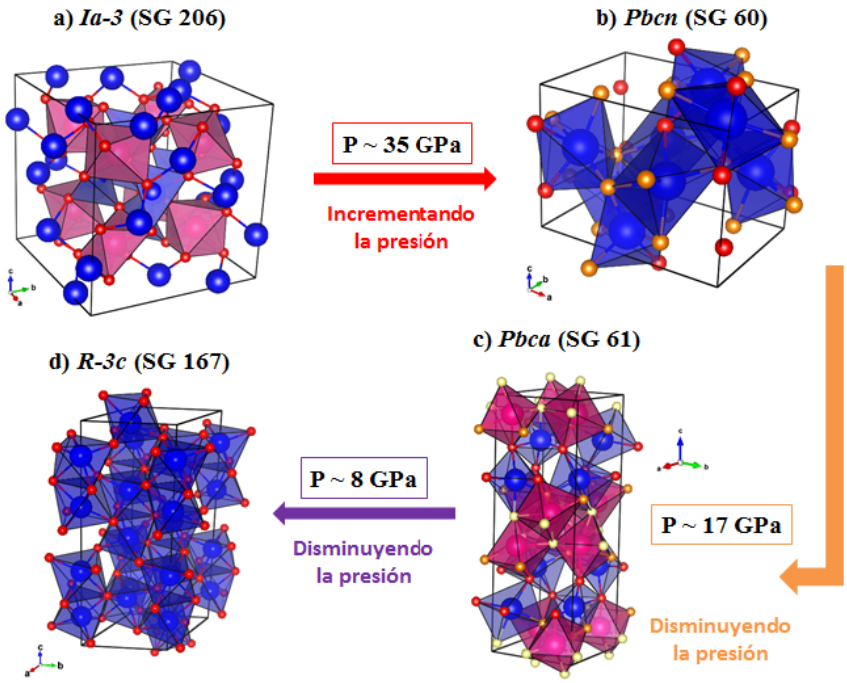

Esquema 1: *Secuencia de transiciones de fase inducidas por la variación de la presión en el In_2O_3 hasta 50 GPa.*

En la **Figura 4** y en la **Tabla 1** se muestra la dependencia en presión del volumen de la celda unidad por fórmula unidad de los cuatro polimorfos encontrados de In_2O_3 (c-In_2O_3, o1-In_2O_3, o3-In_2O_3 y rh-In_2O_3) hasta una presión máxima de 50 GPa a temperatura ambiente y los resultados experimentales y teóricos (*ab initio*) del ajuste con una ecuación de estado de segundo orden de Birch-Murnaghan (B_0' = 4).

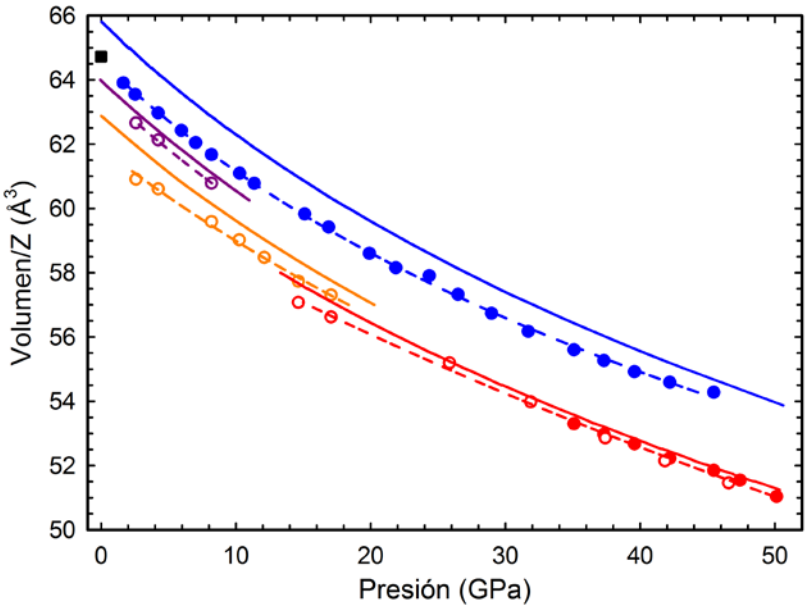

Figura 4: *Dependencia con la presión del volumen de la celda unidad por fórmula unidad en los cuatro polimorfos de In_2O_3, concretamente, c-In_2O_3 (azul), o1-In_2O_3 (rojo), o3-In_2O_3 (naranja) y rh-In_2O_3 (violeta) a temperatura ambiente. Los datos experimentales, los datos teóricos y los ajustes con la ecuación de estado de segundo orden de Birch-Murnaghan están representados con círculos, línea continua y línea discontinua, respectivamente.*

Polimorfo	Origen	V_0/Z (Å^3)	B_0 (GPa)	B_0'
c-In_2O_3	Experimental	64.28(13)	184(10)	4.0
	Teórico	65.72(2)	169.4(12)	4.0
o1-In_2O_3	Experimental	61.9(3)	189(40)	4.0
	Teórico	62.9(1)	169.6(14)	4.0
o3-In_2O_3	Experimental	61.2(7)	194(10)	4.0
	Teórico	61.8(2)	185.4(12)	4.0

Tabla 1: *Ajuste experimental y teórico del volumen de la celda unidad por fórmula unidad (V_0/Z), módulo de compresibilidad (B_0) empleando la ecuación de estado de segundo orden de Birch-Murnaghan (B_0' = 4) para los tres polimorfos de In_2O_3 con suficientes datos experimentales (c-In_2O_3, o1-In_2O_3 y o3-In_2O_3) para realizar los ajustes.*

Una posterior recompresión de la muestra recuperada del primer ciclo de presión a temperatura ambiente (rh-In_2O_3) muestra la transición de fase a o3-In_2O_3. Por lo tanto, o3-

In_2O_3 es claramente la fase posterior a la fase corindón, es decir, la fase de alta presión entre las fases *R-3c* y *Pbcn*. La diferencia entre las transiciones de fases observadas experimentalmente y las predichas por los cálculos teóricos pueden ser atribuidas a la presencia de grandes barreras cinéticas en las transiciones de fase en este compuesto a temperatura ambiente.

Para intentar recuperar o3-In_2O_3 de forma metaestable en condiciones ambiente comenzando con el material en volumen c-In_2O_3, hemos realizado diferentes experimentos de dispersión Raman en función de la presión bajo condiciones no hidrostáticas usando aceite silicona como medio transmisor de presión e incluso sin medio transmisor de presión hasta 27.2 y 39.6 GPa, respectivamente. Los resultados obtenidos han sido los siguientes: Primero, en el proceso de subida en presión, la fase c-In_2O_3 se transforma en o1-In_2O_3 a través de la fase intermedia o3-In_2O_3. Esto contrasta con los resultados obtenidos en condiciones cuasi hidrostáticas cuando se empleó MEW (16:3:1) o helio como medio transmisor de presión. En ambos casos, la muestra se transformaba directamente de c-In_2O_3 a o1-In_2O_3. Segundo, aunque o3-In_2O_3 estuvo coexistiendo con rh-In_2O_3 hasta 0.7 GPa en el proceso de bajada en presión cuando se empleó un medio transmisor de presión no hidrostático, no se pudo recuperar o3-In_2O_3 como una fase metaestable en condiciones ambiente. En este contexto, una opción para futuros experimentos sería realizar un nuevo ciclo de presión hasta 50 GPa en las peores condiciones de hidrostaticidad, es decir, sin medio transmisor de presión, permitiendo obtener en el proceso de bajada en presión la fase pura de o3-In_2O_3 a la presión de 4 GPa. A esa presión, se podrían implementar dos estrategias. La primera estrategia consistiría en hacer una bajada drástica (quenching) en presión en la muestra hasta alcanzar la presión ambiente, mientras que la segunda podría ser una bajada rápida (quenching) en temperatura de la muestra introduciendo la celda de diamante en un tanque de nitrógeno líquido, para posteriormente disminuir la presión lentamente hasta alcanzar la presión ambiente, con el objetivo de recuperar de forma pura o3-In_2O_3 en condiciones ambiente de presión y temperatura.

Después de muchas síntesis, se ha podido recuperar la estructura romboédrica tipo corindón en el In_2O_3 (rh-In_2O_3) como una fase metaestable en condiciones ambiente, empleando prensas de gran volumen como la prensa MA Sumitomo (1200 toneladas) y la prensa PE (200 toneladas) para generar condiciones extremas de presión y temperatura. El mayor inconveniente a la hora de conseguir dicha fase metaestable fue las reacciones químicas de la muestra de partida (c-In_2O_3) con los materiales que tenía a su alrededor a altas temperaturas. En los primeros intentos de síntesis a altas presiones y altas temperaturas, el c-In_2O_3

reaccionó con la cápsula de h-BN formándose la estructura romboédrica tipo corindón de $InBO_3$ (rh-$InBO_3$). Para evitar este problema, se decidió introducir la muestra de partida (c-In_2O_3) en una cápsula metálica. Inicialmente, se probó con cápsulas de platino y molibdeno, pero en ambos casos se observaron reacciones químicas. Finalmente, se logró evitar la reacción química usando una cápsula de renio, consiguiendo sintetizar de forma pura la fase de rh-In_2O_3.

La **Figura 5** resume las condiciones de presión y temperatura que nos permitieron recuperar la fase rh-In_2O_3 como una fase metaestable en condiciones ambiente.

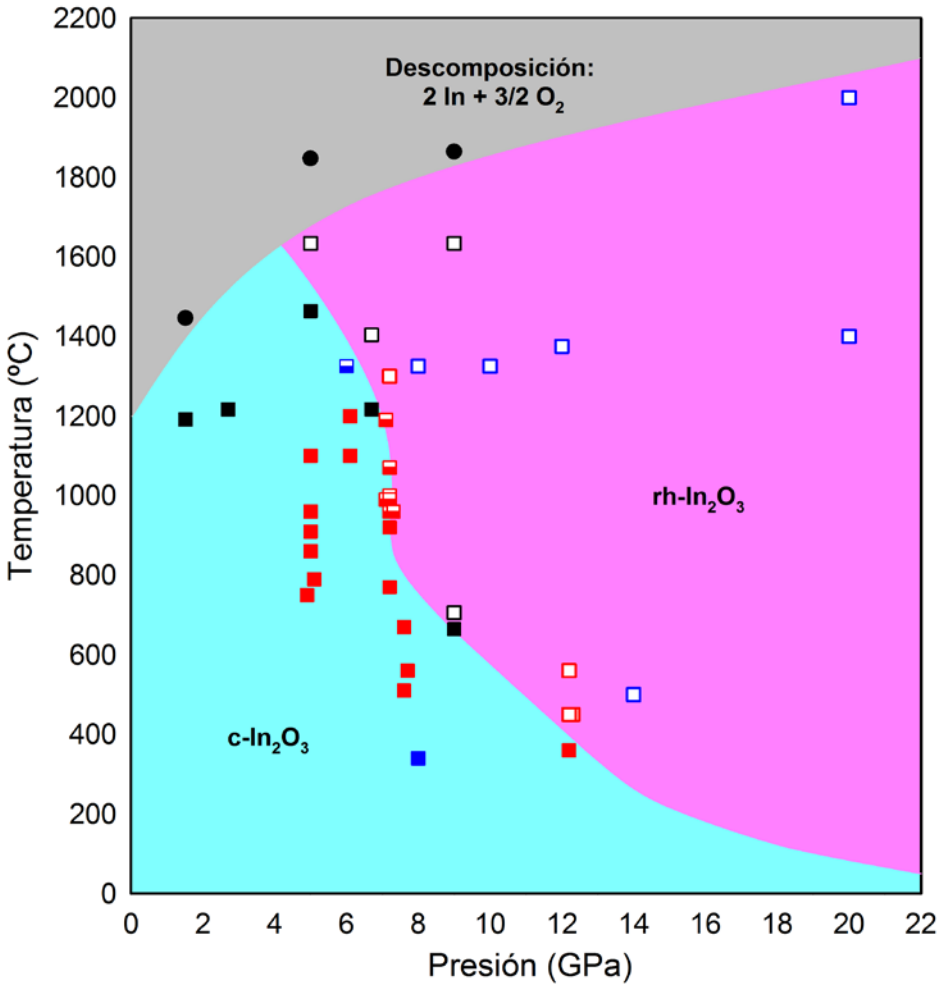

Figura 5: *"Diagrama de fases de presión-temperatura" obtenido para todas las síntesis realizadas a alta presión y alta temperatura comenzando con c-In_2O_3. Las áreas delimitadas con los colores cian, rosa y gris son para las siguientes fases propuestas c-In_2O_3 (cuadrados rellenos), rh-In_2O_3 (cuadrados vacíos) y la descomposición del In_2O_3 (círculos rellenos), respectivamente. Los símbolos en rojo y azul corresponden a los datos experimentales obtenidos en la Universidad de Valencia y en el BGI, respectivamente. Sin embargo, los símbolos en negro hacen referencia a los datos publicados por H. Saitoh et al* ***[39]****.*

Los mejores cristales recuperados de las síntesis de alta presión y alta temperatura de rh-In_2O_3 (desde el punto de vista de la calidad de los espectros Raman) han sido obtenidos en la región de 12 GPa y entre 500 y 600 ºC como se puede observar en la **Figura 6**. La estabilidad térmica de diversos cristales de rh-In_2O_3 ha sido estudiada a través de las medidas de dispersión Raman. Se ha podido comprobar que la estructura tipo corindón del In_2O_3 es estable hasta 500 ºC a presión ambiente.

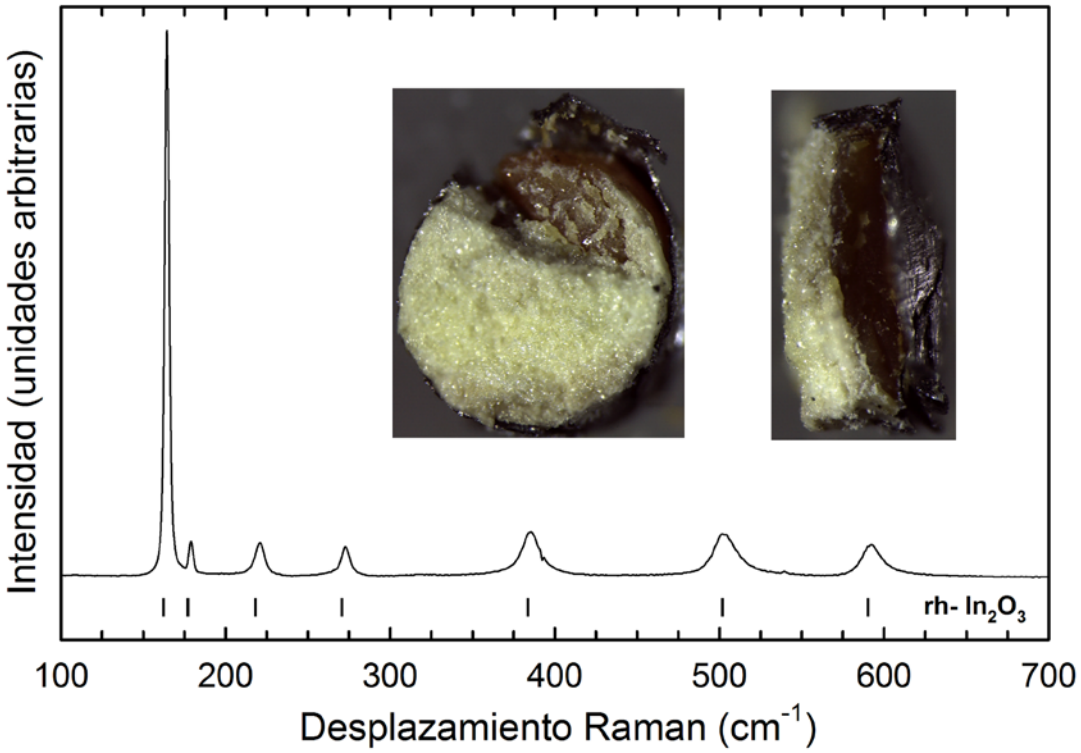

Figura 6: *Espectro Raman de la muestra recuperado situada en el punto medio del horno, correspondiente a la fase rh-In_2O_3 (amarillo claro). La fase c-In_2O_3 (naranja) es observada en los extremos (arriba y abajo) del horno de renio.*

Con la finalidad de analizar la estabilidad de rh-In_2O_3 en función de la presión, se ha empelado una muestra sintetizada a 12 GPa y 1375 ºC (la mejor muestra obtenida hasta el momento de rh-In_2O_3) y posteriormente recocida a 300 ºC durante 3 h para mejorar su calidad cristalina. Las medidas de XRD en función de la presión nos han permitido obtener de forma precisa la ecuación de estado experimental de la fase tipo corindón del In_2O_3 en concordancia con los cálculos teóricos. Para rh-In_2O_3 se ha obtenido un módulo de bulk menor que para los siguientes materiales isomorfos: rh-Al_2O_3 y rh-Ga_2O_3 como se aprecia en la **Tabla 2**.

Este resultado sugiere la posibilidad de usar Cr^{3+} dopado con rh-In_2O_3 a temperatura ambiente como un sensor de presión más sensible que el rubí, por lo menos hasta 14 GPa. El incremento del parámetro de la elongación cuadrática en rh-In_2O_3 al aumentar la presión sugiere la presencia de una inestabilidad mecánica de esta estructura a altas presiones (ver

Figura 7). Este resultado está en concordancia con la menor estabilidad en presión de rh-In_2O_3 que rh-Al_2O_3, lo que se constata mediante la transición de fase de rh-In_2O_3 a o3-In_2O_3 a mucha menor presión (en torno a 14 GPa según medidas de XRD y Raman) que en rh-Al_2O_3.

	Fase	V_0/Z (Å^3)	B_0 (GPa)	B_0'	Método	Tipo EoS
Al_2O_3	R-3c	42.51	257 (6)	4	Exp. (XRD)[a]	BM2
	R-3c	42.8(4)	257 (1)	4	Teo. (GGA-PBEsol)[b]	BM2
Ga_2O_3	R-3c	48.16 (4)	223 (2)	4	Exp. (XRD)[c]	BM2
	R-3c	47.24	243	4.0	Teo. (LDA)[c]	BM3
In_2O_3	R-3c	62.87 (3)	176 (7)	4	Exp. (XRD)[b]	BM2
	R-3c	63.993 (13)	161.3 (2.0)	4	Teo. (GGA-PBEsol)[b]	BM2

[a]Referencia 39. [b]Referencia 62. [c]Referencia 36.

Tabla 2: *Comparación entre los valores teóricos y experimentales del volumen de la celda unidad por fórmula unidad (V_0/Z), el módulo de compresibilidad (B_0) y su derivada (B_0') a presión ambiente para la estructura tipo corindón (R-3c) de los compuestos isomorfos Al_2O_3, Ga_2O_3 y In_2O_3. La última columna indica si los ajustes de las ecuaciones de estado se han realizado usando la ecuación de segundo grado de Birch−Murnaghan (BM2) o la ecuación de tercer grado de Birch−Murnaghan (BM3).*

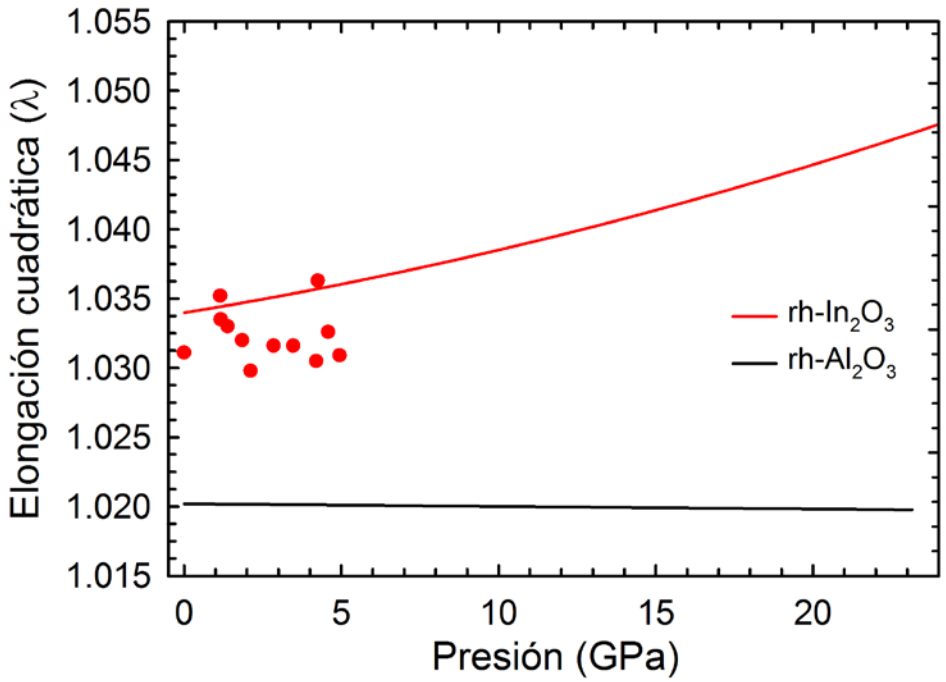

Figura 7: *Dependencia de la elongación cuadrática (λ) en función de la presión para los compuestos rh-In_2O_3 y rh-Al_2O_3.*

Se han realizado numerosos intentos para sintetizar rh-In_2O_3 dopado con Cr^{3+} a altas presiones y altas temperaturas, pero no se ha observado ninguna señal de luminiscencia en las muestras recuperadas. Las muestras de partida se obtuvieron mezclando manualmente en un mortero polvos de c-In_2O_3 y de rh-Cr_2O_3. Este método manual, dada la pequeñísima proporción de rh-

Cr_2O_3, es lo que probablemente no nos ha permitido alcanzar una distribución homogénea de Cr en la muestra de partida. Esta podría ser una razón por la que el cromo no se ha incorporado finalmente en la red cristalina de rh-In_2O_3. Se ha comenzado a colaborar con un grupo de Química de la Universidad de Valencia (Prof. Eduardo Martínez Tamayo) para conseguir una mejor distribución de cromo en la muestra de partida (c-In_2O_3) para las síntesis a altas presiones y altas temperaturas. Por lo tanto, esperamos que en un futuro cercano seamos capaces de realizar nuevos intentos para sintetizar diferentes dopados de Cr^{3+} en rh-In_2O_3.

Finalmente, se ha estudiado tanto el comportamiento estructural como vibracional de nanocristales de rh-In_2O_3, sintetizados por colaboradores de la India, hasta 30 GPa. Estos resultados han sido comparados con los resultados obtenidos en el material en volumen y con las simulaciones teóricas. Las medidas de XRD en polvo de los nanocristales de rh-In_2O_3 nos han permitido obtener de forma más precisa una ecuación de estado experimental para este compuesto, mostrando un buen acuerdo entre los experimentos realizados en el material en volumen de rh-In_2O_3 y los cálculos teóricos. Los coeficientes de presión de los fonones activos Raman medidos en los nanocristales de rh-In_2O_3 confirman un módulo de bulk similar a los medidos en el material en volumen de rh-In_2O_3. Además, las medidas de dispersión Raman muestran una transición de fase desde rh-In_2O_3 a o3-In_2O_3 a una presión mayor (20 GPa) que en el material en volumen. Sin embargo, esa transición de fase no ha sido observada en medidas de XRD en polvo incluso hasta 30 GPa. El origen de esta discrepancia radica en tres posibles efectos: Primero, las medidas de dispersión Raman son más sensibles a los cambios locales que las medidas de XRD. Segundo, el tamaño nanométrico de las muestras da lugar a un ensanchamiento de los picos de XRD comparado con los obtenidos en el material en volumen. Además, el hecho de que muchos picos de la fase romboédrica (*R-3c*) y ortorrómbica (*Pbca*) sean coincidentes en el rango de presiones entre 20 y 30 GPa, dificulta la observación de la transición de fase. Tercero, se ha observado recientemente que transformaciones a altas presiones en nanocristales pueden verse afectadas por defectos tanto de la superficie como del volumen. En la bajada en presión, los nanocristales de rh-In_2O_3 fueron observados por debajo de 8 GPa, al igual que ocurría en el material en volumen. Finalmente, hay que destacar que la diferencia entre la estabilidad estructural observada entre los nanocristales y el material en volumen de rh-In_2O_3, a pesar de tener una compresibilidad similar, nos permitiría extender las posibles aplicaciones de este compuesto a rangos de presiones más elevados. Estos efectos son importantes en futuros estudios con la posibilidad

de dopar los nanocristales de rh-In_2O_3 con Cr^{3+} para conseguir un sensor de presión más sensible que el rubí por lo menos hasta 20 GPa.

Chapter 1

Introduction

The nature is awesome, but limited. To my mind, nothing has more potential than applying the ingenuity of the humans to modify what surrounds us and create something completely new.

Condensed Matter Physics is a field gaining importance in modern Physics. In virtue of the successes achieved in Condensed Matter Physics, enormous advances in quantum electronics, semiconductors and material science have resulted in many technological applications breakthroughs that have changed our lives dramatically in the last 50 years. One of the branches of Condensed Matter Physics is the study of the properties of matter under extreme conditions of pressure and temperature. This study aims at understanding the forces acting inside a solid that govern their structural, elastic, vibrational, optical, electric and magnetic properties and allow us to reproduce the processes and phenomena that occur inside the Earth and other planets among others. Thanks to these studies, we can help to understand the physical, chemical, geological and even biological phenomena occurring under variable pressures and temperatures.

Traditionally, experiments performed in laboratories were the main responsible to provide most of the information about the properties of matter. However, in the last decades the development of computer science with theoretical methods of calculations from first principles or *ab initio* methods, perfected in collaboration with experimental scientists, have become an indispensable tool not only to understand materials properties but also to design new materials and predicting their properties provoking a quick development in the study of

HP-HT techniques. First principles or *ab initio* methods are modern calculations based in the well-established quantum theory and require only the a priori knowledge of the types of atoms present in the material, their approximate location in real space (structural symmetry) and their interactions.

The cubic bixbyite-type structure is present in several binary oxides, like In_2O_3, Sc_2O_3 and Mn_2O_3. In fact, apart from In_2O_3, many binary oxides such as ZnO, SnO_2, and TiO_2 has been widely studied for optoelectronic devices due to its special properties as a TCO **[1–3]**. The widespread use of cubic bixbyite-type structure of Indium oxide (c-In_2O_3) in industrial processes covers the fabrication of window layers in solar cells **[3–5]**, light-emitting diodes **[6–9]**, electrochromic windows **[10]**, liquid-crystal displays **[11, 12]** and gas sensors **[13–17]**. However, the scarcity and high cost to obtain indium metal has led to the study of new systems, like Sn-doped In_2O_3 (ITO) and $In_{2-2x}Zn_xSn_xO_3$ ($x \leq 0.4$, also named ZITO or IZTO), in order to cut the price of its production process **[18–20]**.

Several polymorphs of In_2O_3 are known. At ambient conditions, In_2O_3 crystallizes in the cubic bixbyite-type structure (space group (SG) *Ia-3*, No. 206, Z = 16) **[21, 22]**, the most well-known phase, which is common to most rare-earth sesquioxides. However, the other lesser known polymorphs of In_2O_3 like the rhombohedral corundum-type (SG *R-3c*, No. 167, Z = 6), orthorhombic Rh_2O_3−II type (SG *Pbcn*, No. 60, Z = 4), and orthorhombic α-Gd_2S_3-type (SG *Pnma*, No. 62, Z = 4) **[23−44]** could be obtained by the application of pressure and temperature. In the cubic, rhombohedral, and Rh_2O_3-II structures, cations are sixfold-coordinated; however, cation coordination increases to seven and eight in the α-Gd_2S_3 structure.

HTs have systematically been used in HP studies in order to induce phase transitions delayed or even impeded in In_2O_3 at room temperature due to the presence of kinetic effects **[36, 37, 40, 41, 43, 45]**. As regards the studies of c-In_2O_3 under pressure, it has been reported that c-In_2O_3 remains stable up to 6 GPa and 1450 ºC **[46]**. Moreover, in the 1960s it has been reported that c-In_2O_3 subjected to pressures of 6.5 GPa and temperatures between 880 and 1300 ºC result in the growth of rhombohedral corundum-type structure of In_2O_3 (rh-In_2O_3) when retrieved at ambient conditions **[23, 25]**. In recent years, rh-In_2O_3 has been synthesized at ambient conditions in a metastable way in different nanostructures and thin films **[27, 28, 30–35, 38, 41, 47–50]**. Even, the rh-In_2O_3 has also been found by applying shock waves in the pressure range of 15–25 GPa to cubic In_2O_3 **[26]**.

The great interest to obtain rh-In_2O_3 as a metastable phase at ambient conditions is because it is expected to show better properties than c-In_2O_3, like better stability and higher conductivity **[21, 51]**. These properties made rh-In_2O_3 especially suitable for the use in solar cell, catalysis and gas sensors.

Yusa *et al*. observed by XRD measurements the Rh_2O_3-II phase as post corundum phase in In_2O_3 at 7 GPa and 1630 ºC and the α-Gd_2S_3 phase as post-Rh_2O_3-II phase above 40 GPa and 1730 ºC **[36, 37]**.

Apparent contradictory results at HP and room temperature, like the observance of rh-In_2O_3 as the HP phase of c-In_2O_3, proposed by Liu *et al.* **[52]** and Qi *et al.* **[53]** through a bulk and nanocrystalline study, respectively, have motivated us to perform a much deeper study of the polymorphism of In_2O_3 at room temperature up to higher pressures. Actually, another controversy is the possibility to obtain the orthorhombic Rh_2O_3−II type (o1-In_2O_3) as a metastable phase at ambient conditions by means of HP-HT treatments **[40, 41, 43]**. The isolation of o1-In_2O_3 at ambient pressures would open a new avenue for tuning the materials properties **[54]**.

The properties of In_2O_3 nanocrystals are receiving increasing attention in the last years because their properties are practically unknown. Significant research efforts have been made for successful preparation of size and shape controlled In_2O_3 nanocrystals **[53, 55, 56]**. Moreover, vibrational properties of In_2O_3 nanostructures have started to be also investigated **[57, 58]**.

The main objective of this thesis work is to study the pressure and temperature stability of several polymorphs of bulk and nanocrystalline In_2O_3 and to know the optimal conditions of pressure and temperature synthesis, starting from c-In_2O_3 to get rh-In_2O_3 as a metastable phase at ambient conditions.

The manuscript has been divided into eight chapters in the following way:

In chapter 2, we make a brief theoretical introduction to most concepts used throughout this thesis work. Thus, the basics of XRD, the EoS and some notions about the light-matter interaction in order to understand the phenomena of non-resonant RS and optical absorption are discussed.

Chapter 3 is dedicated to the description of the details of both the experimental methods and techniques and the theoretical *ab initio* calculations. As regards the experimental methods, the crystal growth technique using a large volume press used for HP-HT syntheses is presented, including the pressure and temperature calibrations; concretely, for the 200 tons PE press and the Sumitomo 1200 tons MA apparatus. Besides, two different types of DAC, like the membrane-type DAC and the ALMAX-Boehler-type DAC, and the different pressure scales employed are also described. The final part of this chapter is devoted to detail the different characterization techniques of as-grown materials at ambient and extreme conditions of pressure and temperature, like SEM, angle-dispersive XRD at ALBA synchrotron radiation source, RS spectroscopy and how their results are compared to theoretical *ab initio* calculations.

The following chapters are devoted to the presentation of the results obtained in our study that where published in international journals.

In chapter 4, we report a joint experimental and theoretical vibrational study of bulk (nanocrystalline) c-In_2O_3 under compression up to 31.6 (30.0) GPa. Experiments were performed using a 16:3:1 mixture of MEW as a PTM. Thanks to *ab initio* calculations, we have been able to assign the symmetry of 16 (8) observed Raman-active modes in bulk (nanocrystalline) c-In_2O_3 and compare the evolution of the experimental and theoretical Raman-active mode frequencies with pressure.

In chapter 5, we report a joint experimental and theoretical structural (XRD) and vibrational (RS) study of bulk c-In_2O_3 under HP-HT. Two different pressure cycles with different PTM were performed. In the first one, XRD and RS experiments were performed in bulk powder c-In_2O_3 compressed up to approximately 50 GPa and also during downstroke to ambient conditions, where the sample recovered at ambient pressure was rh-In_2O_3. In a second upstroke, XRD (RS) experiments were performed on recovered rh-In_2O_3 up to 22.2 (33.0) GPa.

In the downstroke process of the first pressure cycle, we discovered a new polymorph of In_2O_3 at HP. The new polymorph (o3-In_2O_3) crystallizes in the orthorhombic Rh_2O_3−III structure with *Pbca* space group (No. 61). In order to recover this polymorph as a metastable phase at ambient conditions, we performed a RS experiment in the worst hydrostatic conditions, i.e., without PTM, and realised that under non-hydrostatic conditions bulk c-In_2O_3 undergoes a phase transition to rh-In_2O_3.

In chapter 6, we describe all the syntheses that we performed employing the large volume presses (Sumitomo 1200 tons MA press and 200 tons PE press) to generate HP-HT conditions in order recover the rh-In_2O_3 as a metastable phase at ambient conditions. Once we obtained pure rh-In_2O_3 as a metastable phase, we carry out a structural and vibrational study under pressure up to 15.9 and 30 GPa, respectively, with the aim of determine the pressure stability range for this phase. Moreover, the thermal stability through different crystals annealed of rh-In_2O_3 at room pressure has also been studied by means of RS measurements. The smaller bulk modulus obtained for rh-In_2O_3, compared with rh-Al_2O_3, suggests the possibility to use Cr^{3+}-doped rh-In_2O_3 at ambient temperature as a more sensitive pressure sensor than ruby at least up to 14 GPa.

In chapter 7, we present a study of the structural and vibrational properties of rh-In_2O_3 nanocrystals up to 30 GPa and compare them to those of the bulk material and theoretical simulations. An increase of the pressure stability range (at least up to 20 GPa) in the rh-In_2O_3 nanocrystals compared with the bulk material (14 GPa) has been observed.

Finally, the manuscript is finished with chapter 8 devoted to the conclusions. We will summarize all the results obtained in this thesis work and give some future perspectives and open topics to be investigated in different polymorphs of In_2O_3.

Chapter 2

Theoretical foundations

In this chapter we are going to explain the theoretical concepts necessary to understand the physical properties studied in c-In_2O_3 and rh-In_2O_3 at ambient and HP. We will start describing the XRD theory emphasizing the fundamentals of powder diffraction. We will continue with the analytical EoS employed to fit our experimental and theoretical unit-cell volume per formula unit and lattice parameters. Finally, we will conclude with the description of the interaction between light and matter in order to understand the phenomena of non-resonant RS and optical absorption.

2.1. X-ray diffraction

A German physicist named Wilhelm Röntgen discovered the X-rays in 1895. X-rays are a form of electromagnetic radiation comprised between the ultraviolet light and gamma rays. Approximately, X-rays have wavelengths located between 0.1 and 100 Å, corresponding to frequencies ranging from $3 \cdot 10^{16}$ to $3 \cdot 10^{19}$ Hz and to energies from 100 eV to 100 keV as we can observe in **Figure 2.1**.

In classical physics, the diffraction phenomenon is described as the interference of waves according to the Huygens-Fresnel principle. This phenomenon is exhibited when a wave encounters an obstacle or a slit that is comparable in size to its wavelength. Since a range of the electromagnetic radiation corresponding to X-rays presents a wavelength which is about the same size of the separation between atoms (~1 Å), XRD is a technique that allow the study of the atomic structure of materials.

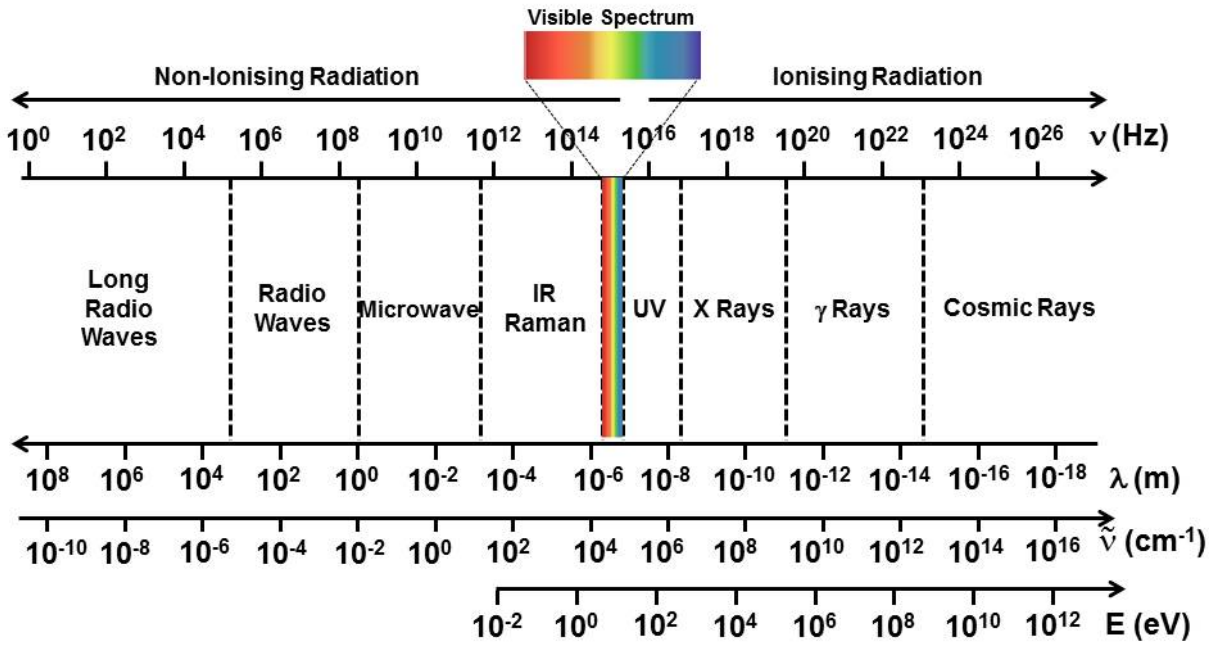

Figure 2.1: *The electromagnetic radiation spectrum.*

In 1912, during the meeting of the German Physical Society, Max von Laue announced his discovery of XRD in crystals as in a three-dimensional diffraction grating **[64]**. The application of XRD to the study of materials has been used in two main areas: the fingerprint characterization of crystalline materials and the determination of their structure. Each crystalline solid has a characteristic XRD pattern, which may be used as a fingerprint for its identification. Once the material has been identified, X-ray crystallography may be used to determine its structure, i.e. the distribution of the atoms and the interatomic distances and angles between them. Therefore, XRD is one of the most powerful characterization tool used in solid state physics, chemistry and materials science.

In this theoretical introduction we will describe only the process of coherent scattering in the XRD from periodic lattices. Moreover, we will consider the kinematical theory of diffraction in which a beam scattered once is not allowed to be scattered again before it leaves the crystal **[65]**.

2.1.1. Scattering by electrons, atoms and lattices

When a wave interacts with a point object, the initial wave is scattered and the outcome of this interaction is a new wave, which spreads in all directions. An elastic scattering is produced when no energy loss occurs in the interaction, i.e. the resultant wave has the same frequency as the incident wave. In three dimensions, the elastically scattered wave is

spherical. When two or more points are involved, they all produce spherical waves with the same λ, which interfere with each other simply by adding their amplitudes. Therefore, constructive and destructive interferences will be produced by scattering of waves in a periodic array of points.

It is important to note that X-rays scatter from electrons. More precisely, the active scattering center for X-rays is not the nuclei of the atoms but the electron density, which is periodically distributed in the crystal lattice. The origin of the electromagnetic wave elastically scattered by electrons can be better understood by recalling the fact that electrons are charged particles. Thus, an oscillating electric field from the incident wave exerts a force on the electric-charge (electron) forcing the electron to oscillate with the same frequency as the electric-field component of the electromagnetic wave. The oscillating electron accelerates and decelerates in concert with the varying amplitude of the electric field vector, and emits electromagnetic radiation, which spreads in all directions. In this respect, the elastically scattered X-ray beam is simply radiated by the oscillating electron which has the same frequency as the incident wave.

Considering electrons as stationary points and disregarding the dependence of the scattered intensity on the scattering angle, each electron interacts with the incident X-ray wave producing a spherical elastically scattered wave with a phase difference (φ) between any pair of neighboring waves as we can see in **Figure 2.2**.

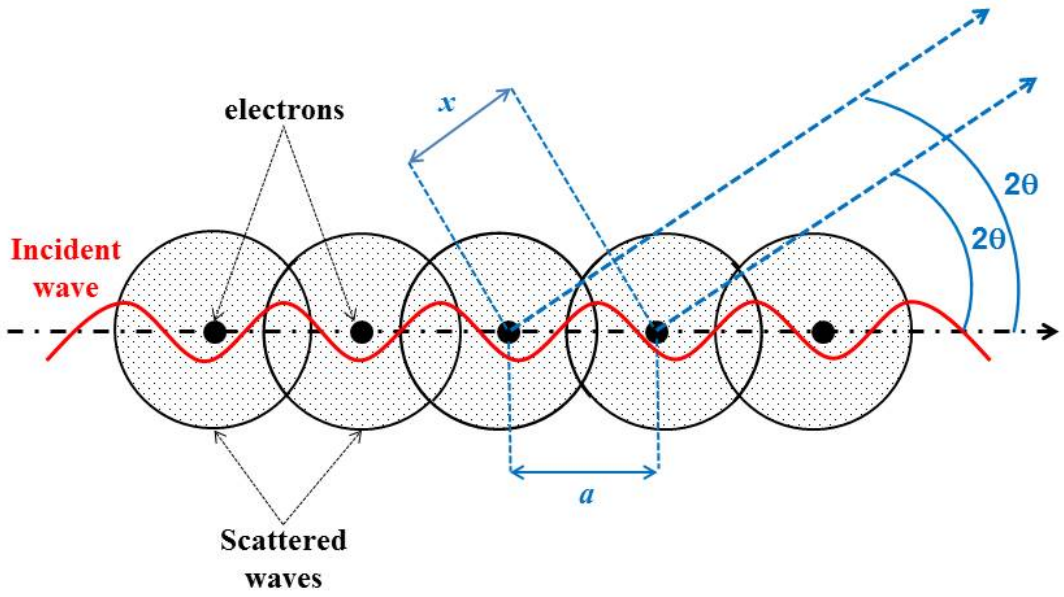

Figure 2.2: *Five equally spaced electrons producing five spherical waves as a result of elastic scattering of the single incident wave.*

$$\varphi = 2\pi\frac{a-x}{\lambda} = 2\pi\frac{a(1-\cos 2\theta)}{\lambda} = \frac{4\pi a\, sin^2\theta}{\lambda} \quad \textbf{(2.1)}$$

For a one dimensional periodic structure, the intensity diffracted by the row of N equally spaced electrons as a function of the phase difference is proportional to the interference function.

$$I(\varphi) \sim \frac{sin^2 N\varphi}{sin^2\varphi} = N^2, when\ \varphi = h\pi, and\ h = \cdots, -2, -1, 0, 1, 2, \ldots \quad \textbf{(2.2)}$$

We now consider an atom instead of a stationary electron. The majority of atoms and ions consist of multiple electrons distributed around a nucleus (see **Figure 2.3**).

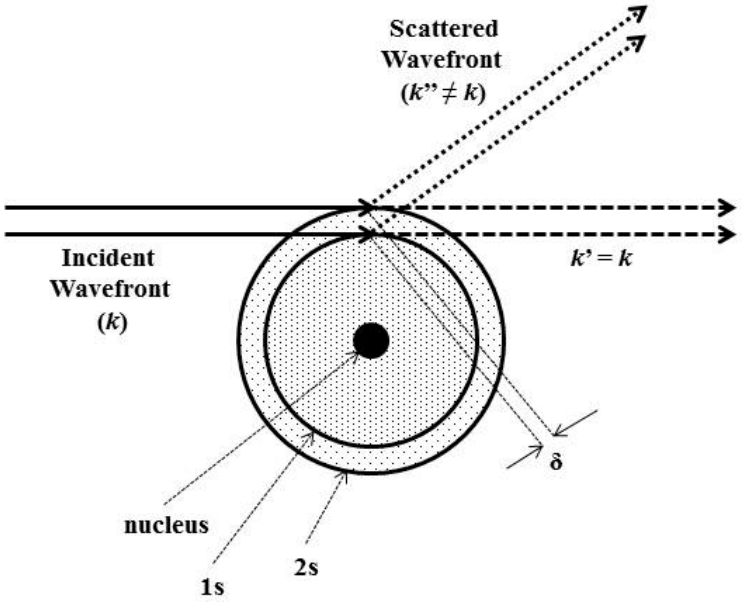

Figure 2.3: *Schematic of the elastic scattering of X-rays by s electrons illustrating the introduction of a path difference (δ) into the wavefront with a propagation vector k'', which is different from the propagation vector, k, of the incident beam.*

The intensity scattered in the direction of the propagation vector (*k*') of the incident wavefront (2θ = 0) is proportional to the total number of core electrons in the atom. For any other angle (2θ > 0), the propagation vector of the scattered waves (*k*'') is different from the propagation vector of the incident waves (*k*). The presence of core electrons results in the introduction of a certain path difference (δ) between the individual waves in the resultant wavefront. The intrinsic angular dependence of the X-ray amplitude scattered by an atom is called the atomic scattering function (*f*), and its behavior is shown in **Figure 2.4** (left) as a function of the phase angle (φ).

Therefore, the wave intensity obtained from diffraction in N atoms as a function of the phase difference is given by the product of the interference function and the square of the atomic scattering function.

$$I(\varphi) \sim f^2(\varphi) \frac{sin^2 N\varphi}{sin^2 \varphi} \quad \textbf{(2.3)}$$

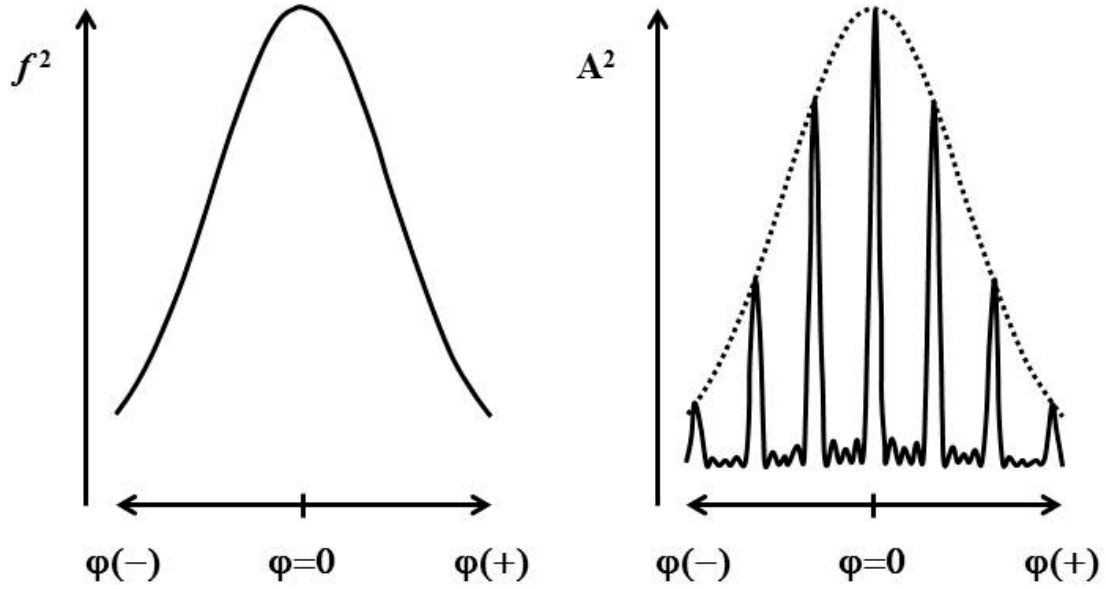

Figure 2.4: *Schematic showing the dependence of the intensity scattered by an atom, i.e., the atomic scattering factor, $f^2 \sim A^2$, as a function of the phase angle (left), and the resultant decrease of the intensity of the diffraction pattern from the row of five regularly spaced atoms, also as a function of the phase angle (right).*

It is worth noting that the radial distribution of core electrons in an atom is the responsible for the reduction of the intensity when the phase difference increases; i.e., when the diffraction angle increases.

A crystal contains approximately an infinite number of scattering points ($N \sim \infty$), which are systematically arranged in three dimensions producing a discrete diffraction pattern with sharp diffraction peaks (delta function) observed only in specific directions. In three dimensions, three integers (*h*, *k* and *l*), commonly called Miller indices are required to define the positions of maximum intensity in the diffraction space

$$I(\varphi) \sim f^2(\varphi) \frac{sin^2 N_1 h\pi}{sin^2 h\pi} \frac{sin^2 N_2 k\pi}{sin^2 k\pi} \frac{sin^2 N_3 l\pi}{sin^2 l\pi} \quad \textbf{(2.4)}$$

where N_1, N_2 and N_3 are the total numbers of the identical atoms in the corresponding directions. Furthermore, when the unit cell contains more than one atom, the individual

atomic scattering function *f*(φ) should be replaced by the whole unit cell called the structure factor or the structure amplitude (F). As a result, the intensity of the diffraction pattern produced by a crystal lattice as a function of the diffracted angle may be defined as

$$I(\varphi) \sim \mathrm{F}^2(\varphi) \frac{sin^2 U_1 h\pi}{sin^2 h\pi} \frac{sin^2 U_2 k\pi}{sin^2 k\pi} \frac{sin^2 U_3 l\pi}{sin^2 l\pi} \quad \textbf{(2.5)}$$

where U_1, U_2 and U_3 are the numbers of the unit cells in the corresponding directions. In general the intensities of discrete points (*hkl*) in the reciprocal space are given as:

$$I(hkl) \sim \mathrm{F}^2(hkl) \frac{sin^2 U_1 h\pi}{sin^2 h\pi} \frac{sin^2 U_2 k\pi}{sin^2 k\pi} \frac{sin^2 U_3 l\pi}{sin^2 l\pi} \quad \textbf{(2.6)}$$

2.1.2. Geometry of diffraction by a lattice

Direct and reciprocal spaces are used to understand the geometry of diffraction by a lattice. In the direct space the physical concepts are more intuitive than in reciprocal space. However, the reciprocal space is extremely useful for the visualization of diffraction patterns.

2.1.2.1. Laue Equations

Max Von Laue described the relationships between the directions of the incident and diffracted beams with the three simultaneous equations commonly known as Laue equations:

$$\begin{aligned} a(cos\Psi_1 - cos\varphi_1) &= h\lambda \\ b(cos\Psi_2 - cos\varphi_2) &= k\lambda \\ c(cos\Psi_3 - cos\varphi_3) &= l\lambda \end{aligned} \quad \textbf{(2.7)}$$

where *a*, *b* and *c* are the dimensions of the unit cell, ψ_{1-3} and $\varphi_{1\text{-}3}$ are the angles that the incident and diffracted beams, respectively, form with the parallel row of atoms in three independent directions and λ is the wavelength of the used radiation. Sharp diffraction peaks can only be observed when all equations in **(2.7)** are satisfied as we can observe in **Figure 2.5**.

Laue equations give the most general representation of a three-dimensional diffraction pattern and they may be used in the form of (**2.7**) to describe the geometry of diffraction from a single crystal.

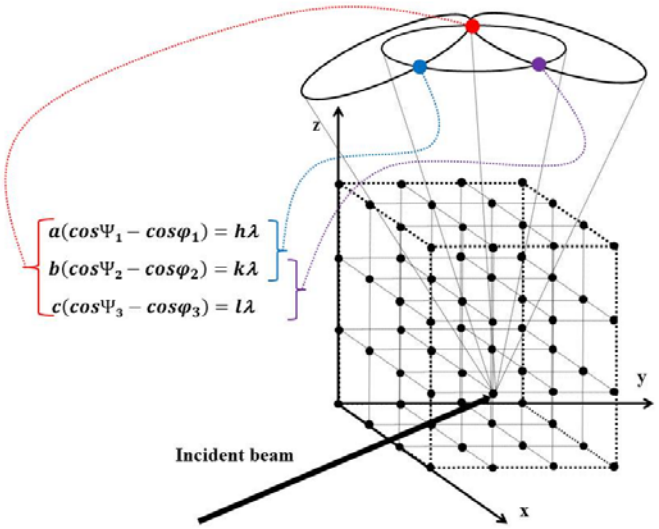

Figure 2.5: *Graphical illustration of Laue equation. Each of the three cones satisfies one of the three equations, while the intersecting cones satisfy either two or all three equations simultaneously. A sharp diffraction peak is only observed in the direction of a point where three Laue equations are simultaneously satisfied.*

2.1.2.2. Bragg's Law

W.H. Bragg and W.L. Bragg established a relationship among the diffraction angle, wavelength and interplanar spacing. All planes with identical triplets of Miller indices are parallel to one another and they are equally spaced. Thus, each plane in a set (*hkl*) may be considered as a separate scattering object and the diffraction from a set of equally spaced objects is only possible at specific angles. The possible θ angles are established from Bragg's law, which is derived geometrically in **Figure 2.6**.

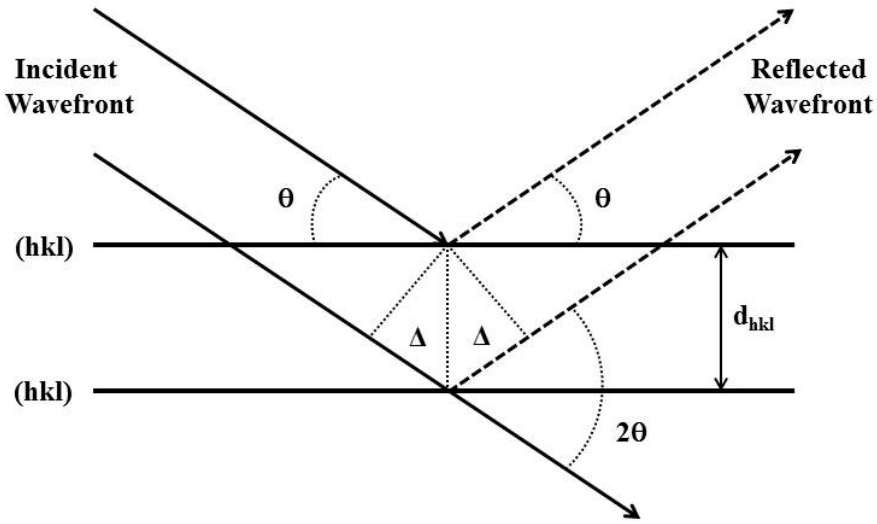

Figure 2.6: *Geometrical illustration of Bragg's law.*

Consider an incident wavefront with parallel propagation vectors, which form an angle θ with the planes (*hkl*). The reflected wavefront will also consist of parallel waves, which form the same angle θ with all planes. The path differences (Δ) introduced between a pair of waves, both before and after they are reflected by the neighboring planes, are determined by the interplanar distance as:

$$\Delta = d_{hkl} \sin\theta \quad \textbf{(2.8)}$$

The total path difference is 2Δ, and the constructive interference is observed when:

$$2\Delta = n\lambda \quad \textbf{(2.9)}$$

where *n* is an integer (order of reflections) and λ is the wavelength of the incident wavefront. This simple geometrical analysis results in the Bragg's law:

$$2d_{hkl} \sin\theta = n\lambda \quad \textbf{(2.10)}$$

2.1.2.3. Reciprocal Lattice and Ewald's Sphere

Paul Peter Ewald introduced the best visual representation of the diffraction phenomenon by taking into account the reciprocal lattice. The incident wave is defined with a wavevector (k_0) and wavelength (λ), related by the following expression:

$$|k_0| = \frac{1}{\lambda} \quad \textbf{(2.11)}$$

Since the wavelength remains constant in an elastic scattering, the scattered wave is characterized by a different wavevector (k_1), which has the same length as k_0.

$$|k_1| = |k_0| = \frac{1}{\lambda} \quad \textbf{(2.12)}$$

The angle between k_0 and k_1 is 2θ as we could observe in **Figure 2.7**.

Locating the vector k_0 in such a way that it ends in the original point of the reciprocal lattice (fixed vector) and overlapping the origins of both wavevectors (k_0 and k_1) results in a lattice vector (d^*) of the reciprocal space. This observation indicates that a signal of diffraction in the direction of k_1 will be observed only when its end coincides with a point in the reciprocal lattice. This procedure describes what angles (2θ, $2\theta'$...) will produce a Bragg's reflection**.** Considering that k_0 and k_1 have identical lengths regardless of the direction of k_1 and their ends are equidistant from a common point, therefore, all possible orientations of k_1 delineate a

sphere in three dimensions. This sphere is called the Ewald's sphere, and it is shown schematically in **Figure 2.8**. Obviously, the radius of the Ewald's sphere is the same as the length of k_0.

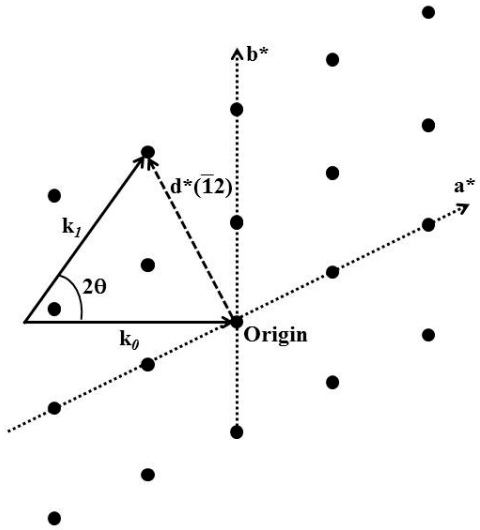

Figure 2.7: *The incident (k_0) and diffracted (k_1) wavevectors overlapped with the two-dimensional reciprocal lattice, which is based on the unit vectors a* and b* being the origin of the reciprocal lattice the end of k_0.*

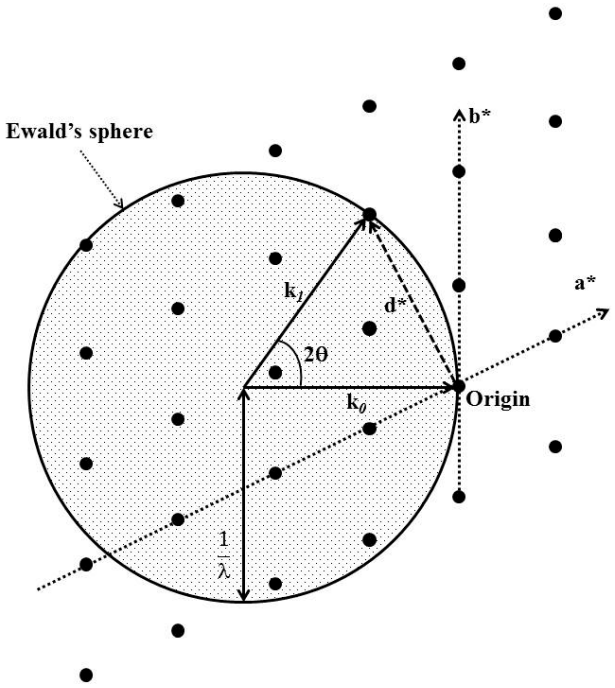

Figure 2.8: *The visualization of diffraction using the Ewald's sphere with radius 1/λ and the two-dimensional reciprocal lattice with unit vectors* a* *and* b*. *The origin of the reciprocal lattice is located on the surface of the sphere at the end of* k_0. *Diffraction can only be observed when a reciprocal lattice point, other than the origin, intersects with the surface of the Ewald's sphere.*

The Ewald's sphere is a simple geometrical arrangement of the reciprocal lattice. The three vectors (k_0, k_1 and d^*_{hkl}) in a straightforward and elegant fashion yields Bragg's equation. From **Figure 2.7** and **Figure 2.8**, it is clear that vector k_1 is the sum of two vectors (k_0 and d^*_{hkl}).

$$k_1 = k_0 + d^*_{hkl} \tag{2.13}$$

Knowing that d^* could be expressed as:

$$|d^*| = \frac{1}{d} \tag{2.14}$$

and employing **(2.12)** we obtain the Bragg's Law.

$$|k_1| \sin\theta = |k_0| \sin\theta = \frac{1}{2}|d^*| \rightarrow \boldsymbol{2d \sin\theta = \lambda} \tag{2.15}$$

2.1.3. Powder diffraction pattern

The experiment of powder diffraction is the cornerstone of a truly basic materials characterization technique because the scattered intensity of a powder sample can be measured as a function of a simple independent variable (Bragg angle). This experiment yields a powder diffraction pattern that has been used to provide accurate information about the structure of materials. The quality of the powder diffraction pattern is usually limited by the nature and the energy of the available radiation, by the resolution of the instrument, and by the physical and chemical conditions of the sample. Many materials can only be prepared in a polycrystalline form being the powder diffraction experiment the only realistic option for a reliable determination of the crystal structure of such materials **[66]**. The other option is single crystal diffraction which is not going to be discussed in the following.

What makes the powder diffraction experiment so powerful is that different structural features of a material have different effects on various parameters of its powder diffraction pattern. For example, the presence of a crystalline phase is manifested as a set of discrete intensity maxima (different Bragg reflections), each with a specific intensity and location. When atomic parameters, for example, coordinates of atoms in the unit cell or populations of different sites in the crystal lattice are altered, this change affects relative intensities and/or positions of the characteristic Bragg peaks of this phase. If changes are microscopic, such as when grain size is reduced below a certain limit, or when the material has been strained or

deformed, then the shapes of Bragg's peaks become affected in addition to their intensities and positions.

Once the number of grains in the irradiated volume is large and their orientations are completely random, the same is true for the reciprocal lattices associated with each crystallite. Thus, the ends of the identical reciprocal lattice vectors, d^*_{hkl}, become arranged on the surface of the Ewald's sphere in a circle perpendicular to the incident wavevector (k_0). The corresponding scattered wavevectors (k_1), are aligned along the surface of the cone, as shown in **Figure 2.9**. The apex of the cone coincides with the center of the Ewald's sphere, being the cone axis parallel to k_0, and the solid cone angle 4θ.

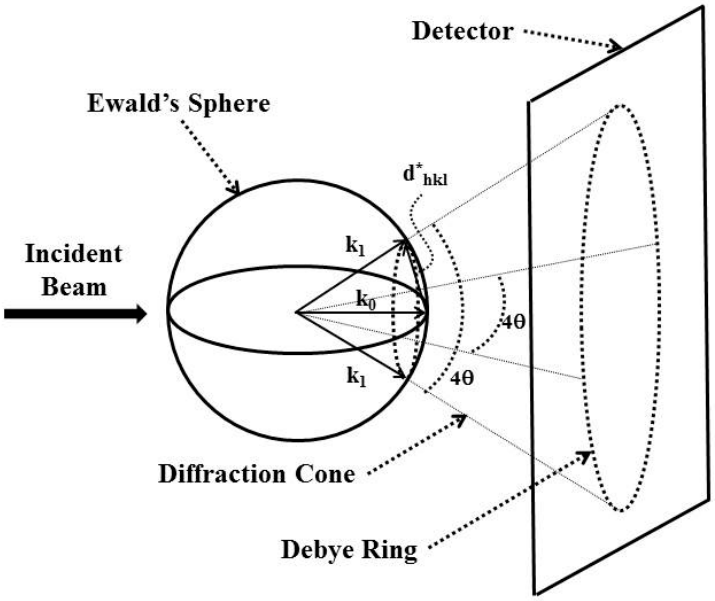

Figure 2.9: *The origin of the powder diffraction cone as a result of the infinite number of completely randomly oriented identical reciprocal lattice vectors (d^*_{hkl}) forming a circle with their ends placed on the surface of the Ewald's sphere, thus producing a powder diffraction cone and the corresponding Debye ring on a flat detector. The detector is perpendicular to both the direction of the incident beam and cone axis, and the radius of the Debye ring in this geometry is proportional to tan 2θ.*

Assuming that the number of crystallites approaches infinity, the density of the scattered wavevectors (k_1) becomes constant on the surface of the cone. Therefore, the diffracted intensity will be constant around the circumference of the cone base when measured by a planar area detector as we can observe in **Figure. 2.9**. Similar rings but with different intensities and diameters are formed by other independent reciprocal lattice vectors, and these are commonly known as the Debye rings. As an example, **Figure 2.10** shows the Debye rings for the four lowest Bragg angles in the diffraction pattern of a polycrystalline copper sample

using Cu $K\alpha_1$ radiation. Assuming that the diffracted intensity is evenly distributed around the base of each cone, there is usually no need to measure the intensity of the entire Debye ring, being an advantage of this technique.

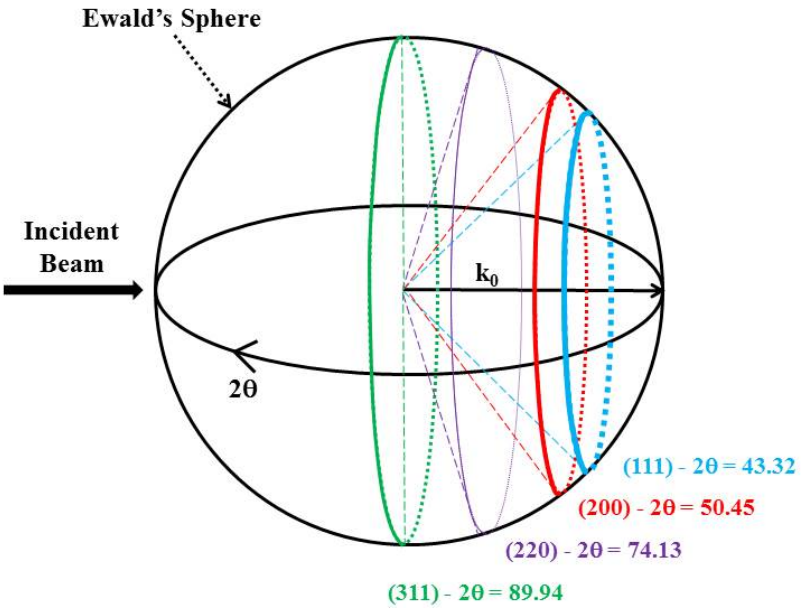

Figure 2.10: *The schematic of the powder diffraction cones produced by a polycrystalline copper sample using Cu $K\alpha_1$ radiation. Each cone is marked with the corresponding triplet of Miller indices.*

In powder diffraction, the scattered intensity is customarily represented as a function of a single independent variable called Bragg angle or 2θ. This type of plot is standard and it is called a powder diffraction pattern. In some instances, the diffracted intensity may be plotted versus the interplanar distance (d), the q-value ($q = 1/d^2 = d^{*2}$) and the $\sin\theta/\lambda$ (or the Q-value, which is different from $\sin\theta/\lambda$ by a factor of 4π). The scattered intensity is usually represented as the total number of the accumulated counts, counting rate (cps) or in arbitrary units. Regardless of which units are chosen to plot the intensity, the patterns are visually identical because the intensity scale remains linear, and because the intensity measurements are usually relative, not absolute. In rare instances, the intensity is plotted as a common or a natural logarithm, or a square root of the total number of the accumulated counts, in order to better visualize both the strong and weak Bragg peaks on the same plot. The use of these two nonlinear intensity scales increases the visibility of the noise.

Furthermore, various horizontal scales alternative to the Bragg angle are employed. For example, d-spacing is most commonly used in the time-of-flight (ToF) experiments. According to the de Broglie equation:

$$\lambda = \frac{h}{mv} \quad \textbf{(2.16)}$$

since the wavelength is the inverse of the velocity of the particle (neutron). The ToF from the specimen to the detector is therefore, directly proportional to *d*. This scale, however, reduces the visual resolution in the low *d* range (equivalent to high Bragg angle range) when used in combination with XRD data. The second scale is $1/d = 2\sin\theta/\lambda$. It results in only slightly reduced resolution at high Bragg angles when compared to the 2θ scale. Recalling that $1/d = d^*$, this type of plot is a one-dimensional projection of the reciprocal lattice and it is best suited for direct comparison of powder diffraction data collected using different wavelengths. The similarity of these two diffraction patterns is especially impressive after comparing them when both are plotted versus 2θ. The third is the *q*-values scale, where $q = 1/d^2 = 4\sin^2\theta/\lambda^2$, which provides the best resolution at high Bragg angles when compared to other wavelength independent scales. This scale results in the equally spaced Bragg peaks when the crystal system is cubic. In cases of lower-symmetry crystal systems, only certain types of Bragg peaks are equally spaced along the *q*-axis and in some instances, the *q*-scaled powder diffraction pattern may be used to assign indices and/or examine the relationships between the lattice parameters of the material with the unknown crystal structure.

We assumed that the diffracted intensity is observed as infinitely narrow diffraction maxima (delta functions). Actually, the Ewald's sphere has finite thickness due to wavelength aberrations and reciprocal lattice points are far from infinitesimal shapeless points. They may be reasonably imagined as small diffuse spheres. Therefore, Bragg peaks always have nonzero widths as a function of 2θ, which is illustrated quite well in **Figure 2.11** by the powder diffraction pattern of c-In_2O_3 measured at ALBA synchrotron.

The best way to appreciate and understand how structural information is encoded in a powder diffraction pattern is to consider the latter as a set of discrete diffraction peaks (Bragg reflections) superimposed over a continuous background. The background may be used to extract information about the crystallinity of the specimen and few other parameters about the material. Disregarding the background, the structure of a typical powder diffraction pattern may be described by the following components: positions, intensities and shapes of multiple Bragg reflections.

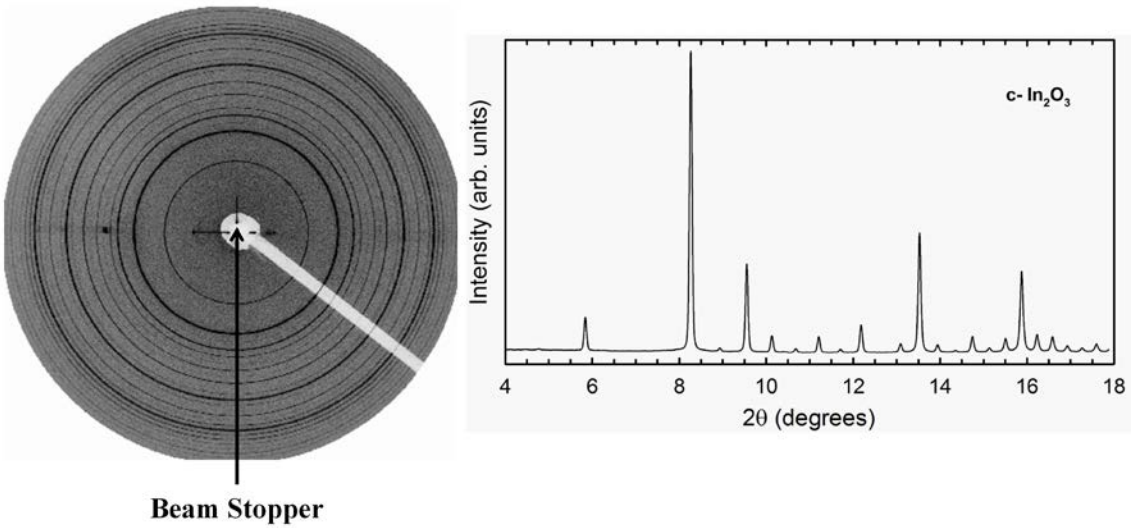

Figure 2.11: *Synchrotron XRD pattern of a polycrystalline sample of c-In_2O_3 recorded with a flat CCD area detector placed perpendicular to the incident X-ray beam with a wavelength of 0.4246 Å.* The *measured intensity is proportional to the degree of darkening. The diffuse white line extending from the center of the image to the bottom right corner is the projection of the wire holding the beam stop needed to protect the detector from being damaged by the high intensity incident beam. The integration has been performed in the entire CCD detector area except some masks like the beam stopper and some strange dots.*

There are two kinds of crystallographic (structural) parameters, which essentially define the makeup of every powder diffraction pattern. These are the unit cell dimensions and the atomic structure (both the unit cell content and spatial distributions of atoms in the unit cell). Thus, a powder diffraction pattern can be constructed (or simulated) as follows:

First, Bragg peaks positions are established from the Bragg's law as a function of the wavelength and the interplanar distances. Solving 2θ in **(2.15)** we obtain:

$$2\theta_{hkl} = 2\sin^{-1}\left(\frac{\lambda}{2d_{hkl}}\right) \qquad \textbf{(2.17)}$$

where d_{hkl} depends of each crystal system **[67]** as we can observe in the following equations:

Cubic: $$\frac{1}{d^2} = \frac{h^2+k^2+l^2}{a^2} \qquad \textbf{(2.18)}$$

Tetragonal: $$\frac{1}{d^2} = \frac{h^2+k^2}{a^2} + \frac{l^2}{c^2} \qquad \textbf{(2.19)}$$

Hexagonal: $$\frac{1}{d^2} = \frac{4}{3}\frac{h^2+hk+k^2}{a^2} + \frac{l^2}{c^2} \qquad \textbf{(2.20)}$$

Orthorhombic:
$$\frac{1}{d^2} = \frac{h^2}{a^2} + \frac{k^2}{b^2} + \frac{l^2}{c^2} \quad \textbf{(2.21)}$$

Monoclinic:
$$\frac{1}{d^2} = \frac{h^2}{a^2 \sin^2\beta} + \frac{k^2}{b^2} + \frac{l^2}{c^2 \sin^2\beta} + \frac{2hl\cos\beta}{ac\ \sin^2\beta} \quad \textbf{(2.22)}$$

Triclinic:
$$\frac{1}{d^2} = \frac{\left[\begin{array}{l} \frac{h^2}{a^2\sin^2\alpha} + \frac{2kl}{bc}(\cos\beta\cos\gamma - \cos\alpha) + \\ + \frac{k^2}{b^2\sin^2\beta} + \frac{2hl}{ac}(\cos\alpha\cos\gamma - \cos\beta) + \\ + \frac{l^2}{c^2\sin^2\gamma} + \frac{2hk}{ab}(\cos\alpha\cos\beta - \cos\gamma) \end{array}\right]}{(1 - \cos^2\alpha - \cos^2\beta - \cos^2\gamma + 2\cos\alpha\cos\beta\cos\gamma)} \quad \textbf{(2.23)}$$

The usefulness of the reciprocal lattice concept may be once again demonstrated here by illustrating how from **(2.18)** to **(2.23)** can be derived in the reciprocal space employing reciprocal lattice vectors. When the derivation is performed in the direct space, the geometrical considerations becomes quite complex. Consider a reciprocal lattice as shown in **Figure 2.12**. Any reciprocal lattice vector, d^*_{hkl}, is a sum of three non-coplanar vectors (a^*,b^* and c^* are the unit vectors of the reciprocal lattice and h, k, and l are integers):

$$d^*_{hkl} = ha^* + kb^* + lc^* \quad \textbf{(2.24)}$$

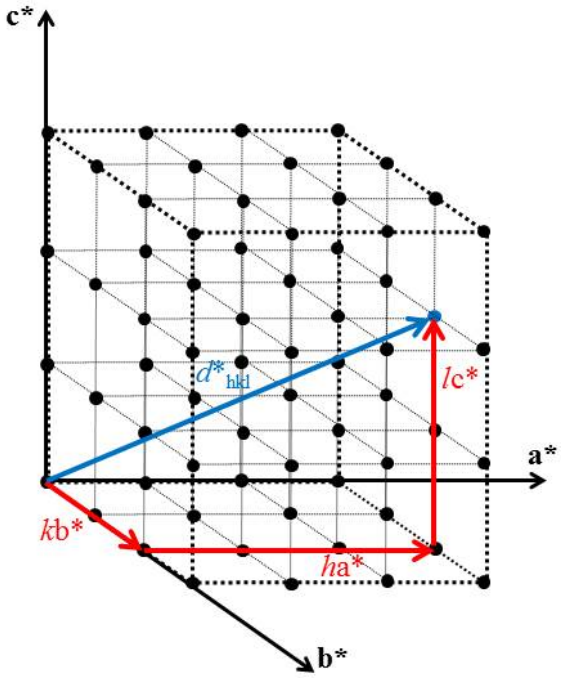

Figure 2.12: *The illustration of a reciprocal lattice vector, d^*_{hkl}, as a vectorial sum of three basis unit vectors, a*, b* and c* multiplied by h, k and l, respectively.*

The equation **(2.25)** shows the relation between the direct and reciprocal space.

$$d^* = \frac{1}{d};\ a^* = \frac{1}{a}; b^* = \frac{1}{b};\ c^* = \frac{1}{c} \qquad \textbf{(2.25)}$$

Second, the intensity of diffraction maxima is a function of the periodicity of the scattering centers (unit cells) and therefore, the intensities can be calculated for individual Bragg peaks from the structural model. The latter requires the knowledge of the coordinates of atoms in the unit cell together with other relevant atomic and geometrical parameters. There are three different factors to determine the peak intensity: (a) "structural factors" which depend on the internal (or atomic) structure of the crystal, which is described by relative positions of atoms in the unit cell, their types and other characteristics, such as thermal motion and population parameters; (b) "specimen factors" owing to its shape and size, preferred orientation, grain size and distribution, microstructure and other parameters of the sample; and (c) "instrumental factors" such as radiation and detector properties, type of focusing geometry, and slit and monochromator geometry.

In summary, the integrated intensity in a powder diffraction pattern is expressed as the following product:

$$I_{hkl} = K \cdot p_{hkl} \cdot L_\theta \cdot P_\theta \cdot A_\theta \cdot T_{hkl} \cdot E_{hkl} \cdot |F_{hkl}|^2 \qquad \textbf{(2.26)}$$

where K is the scale factor, p_{hkl} is the multiplicity factor (number of symmetrically equivalent reflections), L_θ is the Lorentz multiplier, P_θ is the polarization factor, A_θ is the absorption multiplier, T_{hkl} is the preferred orientation factor, E_{hkl} is the extinction multiplier and F_{hkl} is the structure factor.

Third, the shape of Bragg peaks is usually represented by a bell-like function, the so-called peak-shape function. The latter is weakly dependent on the crystal structure and is the convolution of various individual functions, established by the instrumental parameters and to some extent by the properties of the specimen. The shape of each peak can be modeled using instrumental and specimen characteristics, but actually *ab initio* modeling is difficult and most often it is performed using various empirically selected peak-shape functions and parameters. If the radiation is not strictly monochromatic, that is, when both $K\alpha_1$ and $K\alpha_2$ components are present in the diffracted beam, the resultant peak should include contributions from both components as shown in **Figure 2.13**. Peak area is a function of the full width at

half maximum, which varies with Bragg angle. Individual peaks should have their areas proportional to intensities of individual Bragg reflection.

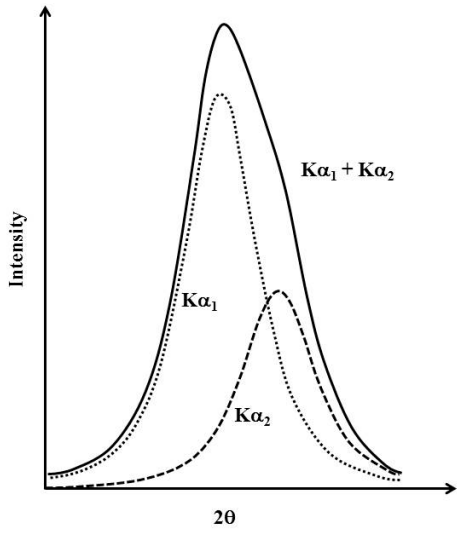

Figure 2.13: *Two individual peak-shape functions corresponding to monochromatic $K\alpha_1$ and $K\alpha_2$ wavelengths (dotted lines) and the resulting combined peak-shape function for a $K\alpha_1/K\alpha_2$ doublet as the sum of two peaks (solid line). Since both $K\alpha_1$ and $K\alpha_2$ peaks correspond to the same d^*_{hkl}, their positions, θ_1 and θ_2, are related as $\sin\theta_1/\lambda K\alpha_1 = \sin\theta_2/\lambda K\alpha_2$.*

Finally, the resultant powder diffraction pattern is a sum of the individual peak-shape functions and the background, sometimes assumed constant for simplicity.

Therefore, it is generally quite easy to simulate the powder diffraction pattern when the crystal structure of the material is known (peak-shape parameters are empirical and the background, typical for a given instrument, may be measured). The inverse process; that is, the determination of the crystal structure from powder diffraction data **[68]** is much more complex. First, individual Bragg peaks should be located on the pattern, and both their positions and intensities determined by fitting to a certain peak-shape function, including the background. Second, peak positions are used to establish the unit cell symmetry, parameters and content. Third, peak intensities are used to determine space-group symmetry and coordinates of atoms **[69]**. Fourth, the entire diffraction pattern is used to refine all crystallographic and peak-shape function parameters, including the background.

2.2. Equations of State

Matter in solid state differs from the gaseous and liquid states by a more compact and symmetrical distributions of atoms. In solids, the typical distance between atoms is about the

same as thus size of the atoms themselves. Therefore, considerable forces act within a solid. The binding energy of the atoms in a crystal is of the same order of magnitude as the binding energy of the valence electrons in an atom but it is less than the binding energy of the inner-shell electrons. Therefore, we may conclude that the forces in a solid are primarily due to the interactions of the outer electrons and that the inner atomic electron shells are practically unaffected by the forces acting on the atoms in a solid.

The relationships established between the thermodynamic variables volume (*V*) and temperatures (*T*) of a system and the first derivative of the free energy with respect to volume, as pressure (*P*), give raise to what are known as the EoS of the system. In static HP science, the EoS are the isothermal *P*-*V* relationship or the relation between P and the different lattice parameters of the material once these lattice parameters are experimentally or theoretically obtained from diffraction experiments and *ab initio* calculations, respectively. Moreover, from these key relationships, many other thermodynamic variables related to second derivatives of the energy with respect to different variables, such as the heat capacity, can be obtained.

A brief review of EoS provides a general background useful for understanding the analysis available to the HP experimental data discussed herein. While the conceptualization of an EoS is straightforward, its broad application can be limited, particularly in regards to the transferability of an EoS to fundamentally different materials (molecular, polymeric, ionic, etc.). Therefore, EoS and their application become essential for insight into not only macroscopic *P*-*V*-*T* behaviour but also the basic forces in condensed matter.

2.2.1. Murnaghan equation of state

The isothermal compressibility (χ) of a material can be defined as the relative change of the volume with respect to the change in pressure at constant temperature:

$$\chi = -\frac{1}{V}\left(\frac{\partial V}{\partial P}\right)_T \qquad \textbf{(2.27)}$$

Since the volume decreases at increasing pressure, a minus sign is added in order to express compressibility with positive values. The isothermal bulk modulus (*B*) of a material can be defined as the inverse of the compressibility:

$$B = -V\left(\frac{\partial P}{\partial V}\right)_T \qquad \textbf{(2.28)}$$

The Murnaghan equation is based on the assumption that *B* is a linear function of pressure at any temperature.

$$B = B_0 + B_0' P \tag{2.29}$$

Using the equations **2.28** and **2.29** and integrating at constant *T* it is obtained:

$$ln\left(\frac{V_0}{V}\right) = \frac{1}{B_0'} ln\left(1 + \frac{B_0'}{B_0} P\right) \tag{2.30}$$

where V_0 is the original volume of the sample. Solving the volume from equation **2.30** we obtained the Murnaghan EoS:

$$V = V_0 \left[1 + \frac{B_0'}{B_0}\right]^{\frac{-1}{B_0'}} \tag{2.31}$$

This EoS describes well the compression of solids in a certain pressure interval provided that the relative volume $\frac{V}{V_0} > 90\%$ **[70]**.

2.2.2. Birch-Murnaghan equation of state

The most commonly EoSs used to describe the compression of ionic-covalent solids are the Birch-Murnaghan equations. Besides expanding the bulk modulus in pressure, the relationship between a material's free energy and its volume can also be used to develop an EoS. For an isothermal close system, the change in Helmholtz free energy (F) with volume relates to pressure through:

$$P = -\left(\frac{\partial F}{\partial V}\right)_T \tag{2.32}$$

Birch expanded the free energy in terms of Eulerian strain as:

$$F = af^2 + bf^3 + cf^4 + \cdots \tag{2.33}$$

being:

$$f = \frac{1}{2}\left[\left(\frac{V_0}{V}\right)^{\frac{2}{3}} - 1\right] \tag{2.34}$$

This expansion coupled with **(2.32)** allowed for the derivation of the Birch-Murnaghan EoS. Expanding the Helmholtz free energy to a quadratic dependence in strain yielded the second-order Birch-Murnaghan (BM2) EoS which takes the form:

$$P = \frac{3B_0}{2}\left[\left(\frac{V_0}{V}\right)^{\frac{7}{3}} - \left(\frac{V_0}{V}\right)^{\frac{5}{3}}\right] \quad \textbf{(2.35)}$$

Including the cubic term in the Helmholtz free energy, the resultant third-order Birch-Murnaghan (BM3) EoS is:

$$P = \frac{3B_0}{2}\left[\left(\frac{V_0}{V}\right)^{\frac{7}{3}} - \left(\frac{V_0}{V}\right)^{\frac{5}{3}}\right]\left[1 + \frac{3}{4}(B_0' - 4)\left(\left(\frac{V_0}{V}\right)^{\frac{2}{3}} - 1\right)\right] \quad \textbf{(2.36)}$$

It can be seen that the BM3 EoS reduces to the BM2 EoS when $B_0' = 4$.

2.3. Raman Spectroscopy

The inelastic scattering of light was predicted by Adolf Smekal in 1923 **[71]**. In 1922, an Indian physicist C.V. Raman published his work on the "Molecular Diffraction of Light," the first of a series of investigations with his collaborators that ultimately led to his discovery on February 28, 1928 of the radiation effect that bears his name. The Raman effect was first reported by C.V. Raman and K. S. Krishnan **[72]**, and independently by Grigory Landsberg and Leonid Mandelstam, on February 21, 1928. That is why in the former Soviet Union the priority of Raman was always disputed. In Russian scientific literature this effect is usually referred to as "combination scattering" or "combinatory scattering". Raman received the Nobel Prize in 1930 for his work on the scattering of light **[73]**.

2.3.1. Fundamentals of non-resonant Raman scattering

Raman spectroscopy is an optical technique based on the inelastic scattering of monochromatic light, usually a laser in the UV-VIS-NIR range, which is used to detect vibrational, rotational, and other atomic-level collective motions in materials **[72]**. Raman spectroscopy is a complementary tool to XRD which is commonly used in materials science in order to obtain the fingerprint by which atoms and molecules can be identified once the structure is known, since Raman modes are characteristic of both the chemical and structural properties of the material. However, it can also be used to discriminate between different crystalline phases if chemical information is known.

RS consists in the inelastic scattering of light by matter. Therefore, contrary to XRD, which consists of elastic scattering of electromagnetic waves, in Raman scattering there is a difference in energy between the ongoing and outgoing electromagnetic wave. The shift in energy between the ongoing and outgoing waves gives information about the vibrational modes in the system. The energy of the molecule can be separated into three additive components associated with the motion of the electrons in the molecule, the vibrations of the constituent atoms, and the rotation of the molecule as:

$$E_{total} = E_{el} + E_{vib} + E_{rot} \quad \textbf{(2.37)}$$

The basis for this separation lies in the fact that electronic transitions occur on a much shorter timescale compared with the rotational transitions that occurs on a much longer timescale.

If a molecule is placed in an electromagnetic field, such as light, a transfer of energy between the field and the molecule will occur when Bohr's frequency condition is satisfied:

$$\Delta E = hv \quad \textbf{(2.38)}$$

where ΔE is the difference in energy between two quantized states, *h* is the Planck constant and ν is the frequency of light. **Figure 2.1** shows the region of the electromagnetic spectrum where ΔE is indicated in ν, λ, $\tilde{v}$ and E. The vibrational transitions which are observed in IR or Raman spectra appear in the 10^2-10^4 cm^{-1} region, and originate from vibrations of nuclei constituting molecules. Rotational transitions occur in the 1-10^2 cm^{-1} region (microwave region) because rotational levels are relatively close to each other, whereas electronic transitions are observed in the 10^4-10^6 cm^{-1} region (UV–VIS region) because their energy levels are far apart. However, such division is somewhat arbitrary, for pure rotational spectra may appear in the far-infrared region if transitions to higher excited states are involved, and pure electronic transitions may appear in the near-infrared region if electronic levels are closely spaced. **Figure 2.14** illustrates transitions of the three types mentioned for a diatomic molecule. As **Figure 2.14** shows, rotational intervals tend to increase as the rotational quantum number J increases, whereas vibrational intervals tend to decrease as the vibrational quantum number ν increases. The dashed line below each electronic level indicates the "zero-point energy" that must exist even at absolute zero, as a result of Heisenberg's uncertainty principle:

$$E_0 = \frac{1}{2}hv \quad \textbf{(2.39)}$$

It should be emphasized that not all transitions between these levels are possible. To see whether the transition is allowed or forbidden, the relevant selection rule must be examined. This, in turn, is determined by the symmetry of the molecule.

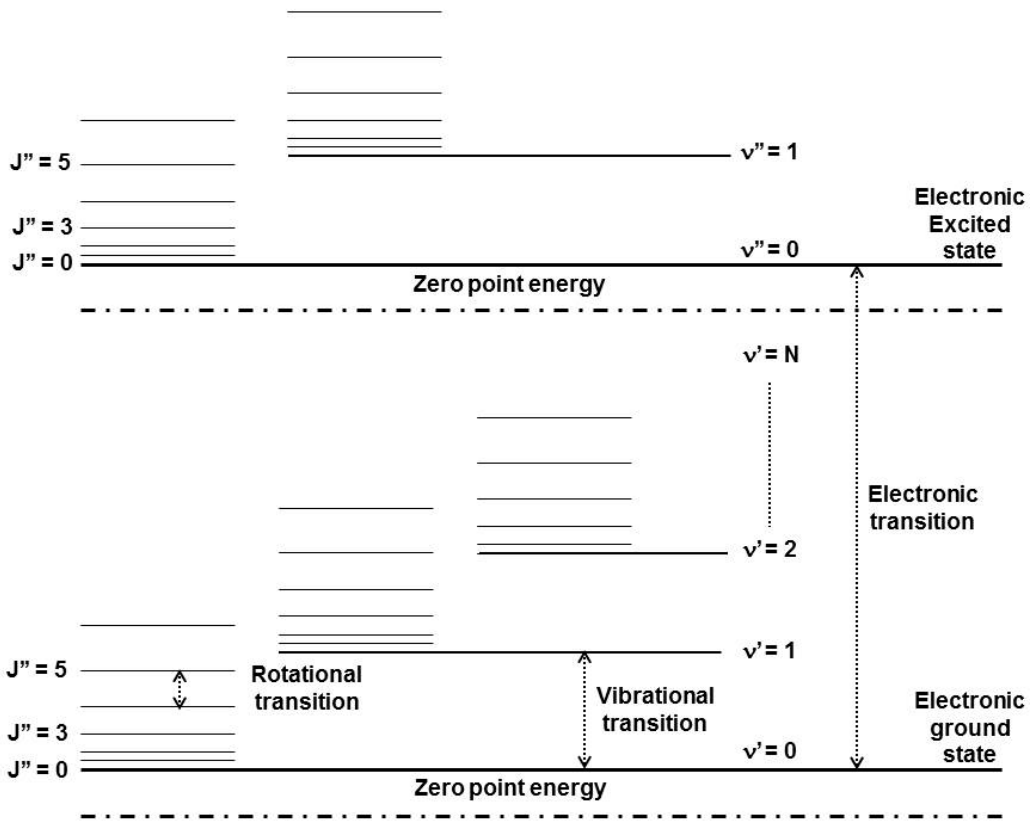

Figure 2.14: *The illustrative energy level of a diatomic molecule*

Electronic spectra are very complicated because they are accompanied by vibrational as well as rotational fine structure. The rotational fine structure in the electronic spectrum can be observed if a molecule is simple and the spectrum is measured in the gaseous state under high resolution. The vibrational fine structure of the electronic spectrum is easier to observe than the rotational fine structure, and can provide structural and bonding information about molecules in electronic excited states. The selection rule allows any transitions corresponding to $\Delta\nu = \pm 1$ if the molecule is assumed to be a harmonic oscillator. Under ordinary conditions, however, only the fundamentals that originate in the transition from $\nu = 0$ to $\nu = 1$ in the electronic ground state can be observed. This is because the Maxwell–Boltzmann distribution law requires that the ratio of population at $\nu = 0$ and $\nu = 1$ state is given by:

$$R = \frac{P(v=1)}{P(v=0)} = e^{-\frac{\Delta E_v}{kT}} \quad \textbf{(2.40)}$$

where ΔE_v is the vibrational frequency (cm^{-1}) and kT = 208 cm^{-1} at room temperature.

As stated previously, vibrational transitions can be observed as IR or Raman spectra. However, the physical origins of these two vibrational spectroscopies are markedly different. On the one hand, IR spectra correspond to absorption of IR photons by transitions to vibrational levels showing a change in the dipolar moment of the molecule with respect to the electronic ground state. On the other hand, Raman spectra have their origin in the change of the electronic polarization of the molecule caused by UV, VIS, and NIR light. If a molecule is irradiated by monochromatic light of frequency ν (laser), then, because of electronic polarization induced in the molecule by this incident beam, the light of frequency ν ("Rayleigh scattering") as well as that of frequency $\nu \pm \nu_i$ ("Raman scattering") is scattered, where ν_i represents a vibrational frequency of the molecule. Thus, Raman spectra are presented as light signals detected as shifts from the incident frequency in the UV, VIS, and NIR region.

The advent of lasers revolutionized Raman spectroscopy in the 60's of the 20th century. Although RS is much weaker than Rayleigh scattering (by a factor of 10^{-3}-10^{-12}), it is still possible to observe the former by using a strong exciting source. The origin of Raman spectra can be explained by an elementary classical theory. Consider a light wave of frequency ν with an electric field strength E. Since E oscilates at frequency ν, we can write

$$E = E_0 cos(2\pi\nu t) \quad \textbf{(2.41)}$$

where E_0 is the amplitude and *t* the time. If a diatomic molecule is irradiated by this light, a dipole moment P given by

$$P = \alpha E = \alpha E_0 \cos(2\pi\nu t) \quad \textbf{(2.42)}$$

is induced. Here α is a proportionality constant and is called the polarizability. If the molecule is vibrating with frequency ν_i, the nuclear displacement q is written as

$$q = q_0 \cos(2\pi\nu_i t) \quad \textbf{(2.43)}$$

where q_0 is the vibrational amplitude. For small amplitudes of vibration, α is a linear function of q. Thus, we can write

$$\alpha = \alpha_0 + \left(\frac{\partial \alpha}{\partial q}\right)_0 q \qquad \textbf{(2.44)}$$

Here, α_0 is the polarizability at the equilibrium position, and $\left(\frac{\partial \alpha}{\partial q}\right)_0$ is the rate of change of α with respect to the change in q, evaluated at the equilibrium position. If we combine the equations **2.42** and **2.44**, we have

$$P = \alpha_0 E_0 \cos(2\pi \nu t) + \frac{1}{2}\left(\frac{\partial \alpha}{\partial q}\right)_0 q_0 E_0 \{\cos[2\pi(\nu + \nu_i)t] + \cos[2\pi(\nu - \nu_i)t]\} \qquad \textbf{(2.45)}$$

According to classical theory, the first term describes an oscillating dipole that radiates light of frequency ν (Rayleigh scattering). The second term gives the RS of frequencies $\nu + \nu_i$ (anti-Stokes) and $\nu - \nu_i$ (Stokes). If $\left(\frac{\partial \alpha}{\partial q}\right)_0$ is zero, the second term vanishes. Thus, the vibration is not Raman-active unless the polarizability changes during the vibration.

A revision of the application of Raman spectroscopy in HP science can be found in several texts **[74-77]**.

2.3.2. Resonant versus non-resonant Raman scattering

In the case of resonant RS **[78]**, the exciting frequency is chosen so as to fall inside the electronic absorption band. The degree of resonance enhancement varies as a function of the exciting frequency and reaches a maximum when the exciting frequency coincides with that of the electronic absorption maximum. It is possible to change the exciting frequency continuously by pumping dye lasers with powerful gas or pulsed lasers.

Figure 2.15 illustrates the mechanisms of normal (non-resonant) and RR scattering. In the former, the energy of the exciting line falls far below (sometimes well above) that required to excite the first electronic transition. In the latter, the energy of the exciting line coincides with that of an electronic transition. If the exciting line is close to but not inside an electronic absorption band, the process is called preresonance RS. If the photon is absorbed and then emitted during the process, it is called RF. Although the conceptual difference between RR scattering and RF is subtle, there are several experimental differences which can be used to distinguish between these two phenomena. For example, in RF spectra all lines are depolarized, whereas in RR spectra some are polarized and others are depolarized. Additionally, RR bands tend to be broad and weak compared with RF bands **[79, 80]**.

In the case of Stokes lines, the molecule at $\nu = 0$ is excited to the $\nu = 1$ state and the scattered light has a frequency ν-ν_1. However, the Anti-Stokes lines arise when the molecule initially in the $\nu = 1$ state reverts to the $\nu = 0$ state and scattered radiation of frequency ν+ν_1 is observed. Since the population of molecules is larger at $\nu = 0$ than at $\nu = 1$ (Maxwell–Boltzmann distribution law), the Stokes lines are always stronger than the anti-Stokes lines. Thus, it is customary to measure Stokes lines in Raman spectroscopy.

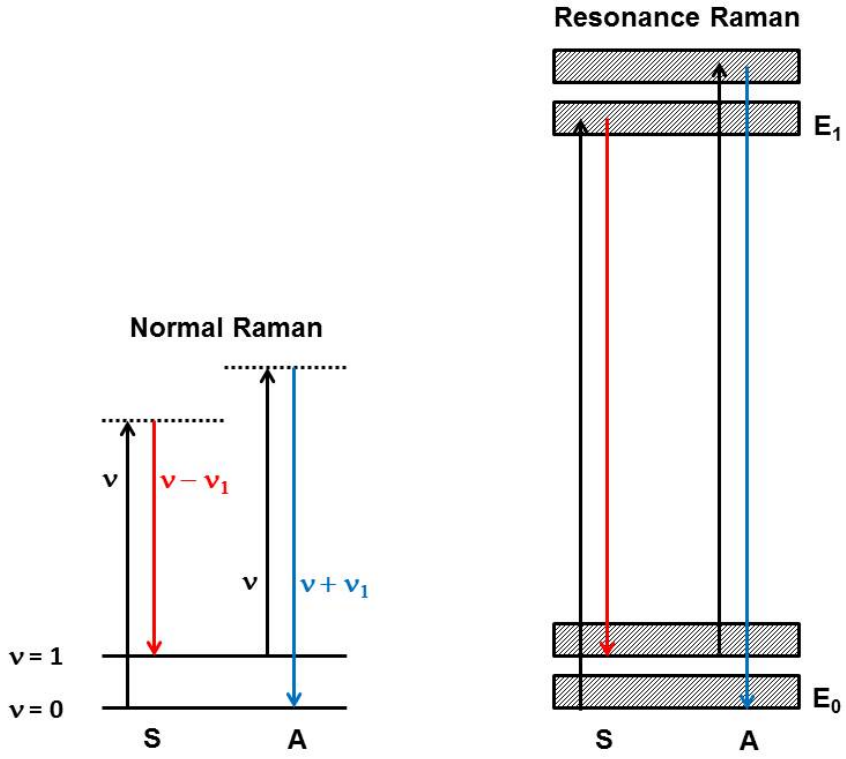

Figure 2.15: *Mechanisms of normal and resonance Raman scattering. S and A denote Stokes and anti-Stokes scattering, respectively. The shaded areas indicate the broadening of rotational and vibrational levels in the liquid and solid states*

It is currently possible to cover the whole range of electronic transitions continuously by using excitation lines from a variety of lasers and Raman shifters **[81]**. In particular, the availability of excitation lines in the UV region has made it possible to carry out UV RR spectroscopy **[82]**. In RR spectroscopy, the excitation line is chosen inside the electronic absorption band. This condition may cause thermal decomposition of the sample by local heating. To minimize thermal decomposition, several techniques have been developed. These include the rotating sample technique, the rotating (or oscillating) laser beam technique, and their combinations with low-temperature techniques **[81-83]**. It is always desirable to keep laser power at a low value so that thermal decomposition is minimal. This will also minimize photodecomposition, which occurs depending on laser lines in some compounds.

2.4. Optical absorption

During the propagation of light through matter several interactions can take place, like refraction, scattering, absorption and luminescence phenomena **[84]**. Basically, refraction consists of a change in the direction of wave propagation and is caused by a change in the wave propagation velocity at different media. Scattering is caused by elastic and inelastic collision between light and different entities inside matter and results in light exiting virtually in every direction. However, absorption is caused by the annihilation of the part of the incident photons in matter by collision with atoms so the photon energy is totally transferred to the material. In this way, absorption causes and attenuation of the intensity of the incident beam. Finally, luminescence is caused by the spontaneous emission of light after the process of absorption by the atoms and it can result in either coherent or incoherent emission of light in any direction.

Semiconductors are materials that can behave either as metals or as insulators depending on several factors. The reason is that there is a gap of energy between the VBM, with all electronic states occupied (ground states), and the CBM, with all electronic states unoccupied (excited states). In general, at T = 0 K VB electrons in semiconductors are tightly bound to the ions and cannot move freely along the material thus behaving as insulators. However, at temperatures above 0 K, VB electrons can be promoted to the CB where they are free to move along the sample as in a metal. In this context, it looks reasonable to wonder about the consequences of irradiating such a material with light of a given frequency able to promote the valence electrons of a semiconductor to an excited state.

2.4.1. Direct and indirect absorption

A transition of an electron from the VB to the CB can occur when a photon of light with energy higher than the semiconductor band-gap energy is absorbed in the material and the electron takes the energy of the photon. Taking into account the nature of the band-gap, semiconductors can be classified as direct or indirect band-gap semiconductors. On the one hand, in direct band-gap semiconductors, such as GaAs, the CBM coincides with the VBM in k-space. Therefore, in a direct band-to-band transition of electrons between the VBM and the CBM the electron momentum must be kept constant (see **Figure 2.16 (left)**). This characteristic is easily obeyed since photons corresponding to the UV-VIS-NIR region have a very small moment. On the other hand, in indirect band-gap semiconductors, such as Si and

Ge, the wavevector of the CBM and the VBM in k-space is different. Consequently, transition of electrons between VBM and CBM involve a change in the electron momentum so indirect transitions cannot proceed just by the absorption of a photon and occur with the assistance of a phonon (either by absorption or emission of a lattice vibration) which provides the difference in moment between the electron at the initial and final k points (see **Figure 2.16 (right)**. These different locations in k-space of VBM and CBM are due to the difference between the tight binding states of electrons and lattice atoms. Of course, the energy is conserved in both direct and indirect transitions.

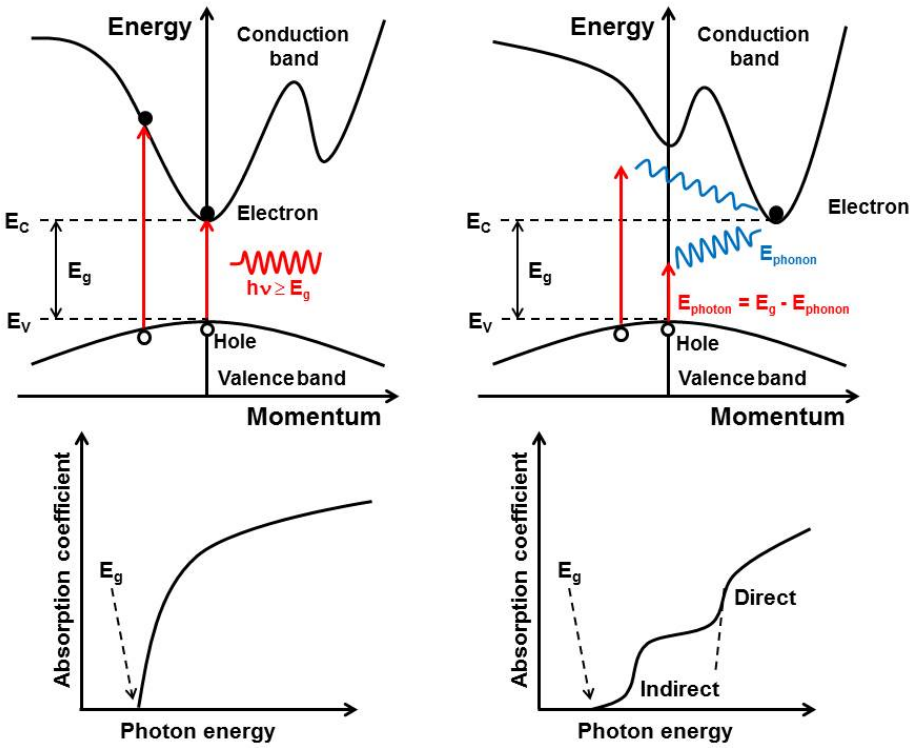

Figure 2.16: *Simplified illustration of the fundamental absorption processes in direct (left) and indirect (right) band-gap semiconductors.*

The physical phenomena related with the fundamental transition processes in semiconductors are spontaneous emission, stimulated emission, and absorption and are summarized in **Figure 2.17**.

These physical phenomena (absorption, spontaneous and stimulated emission) are closely related to one another and were explained by A. Einstein in 1916 and 1917 **[85, 86]**. The probability of indirect transitions is much smaller than the direct transitions because of the requirement of a third particle (phonon). Consequently, direct band-gap semiconductors are usually better absorbers (electron is promoted to the CB leaving a hole in the VB) and

emitters (through band-to-band recombination of electrons and holes; i.e., the electron of the CB recombines with the hole in the VB) than indirect band-gap semiconductors. This explains why they are commonly used in light-emitting devices. **Figure 2.18** shows the scheme for the band-to-band recombination in direct and indirect semiconductors.

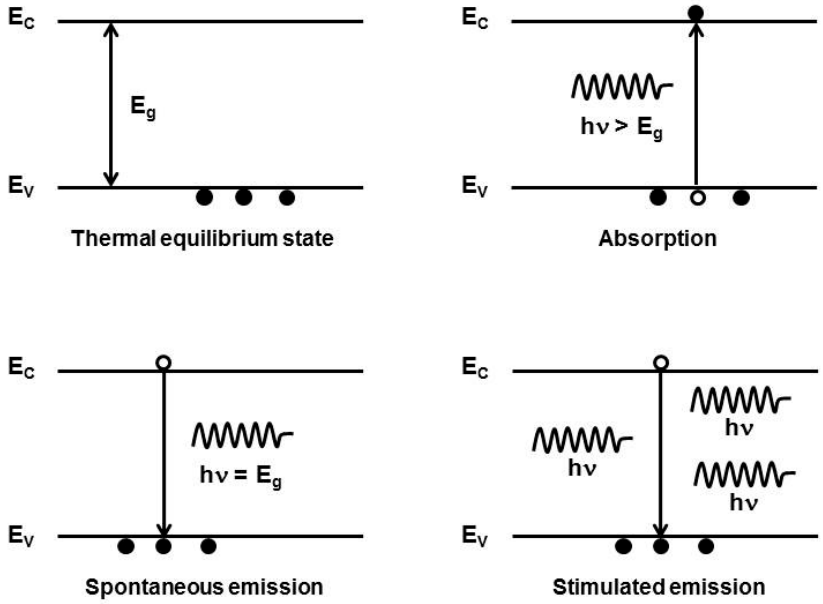

Figure 2.17: *The fundamental transition processes in semiconductors. Filled circles correspond to electronic filled states while empty circles represent electronic empty states.*

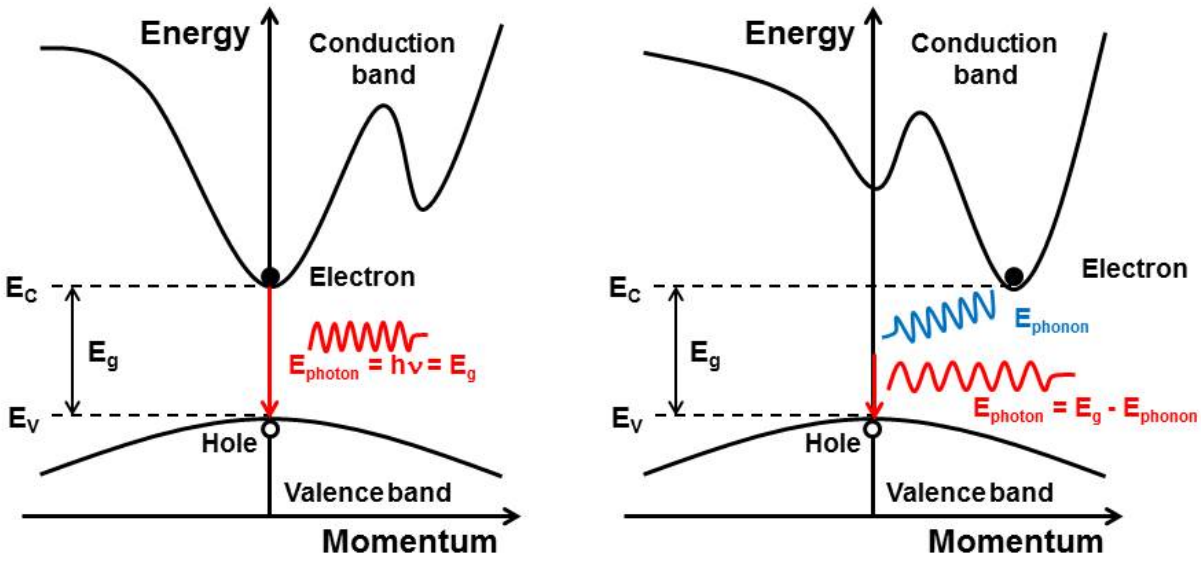

Figure 2.18: *Band-to-band recombination processes in (a) direct and (b) indirect band-gap semiconductors.*

The fundamental absorption corresponds to the excitation of electrons from the VB to the CB. Consequently, when the semiconductor is illuminated, light having an energy higher than the

band-gap energy of the semiconductor is absorbed and light having an energy less than the band-gap energy passes through the semiconductor without being absorbed (see **Figure 2.16**).

The energy at which the fundamental absorption starts is called the absorption edge. At energies near the absorption edge, the absorption coefficient (α) as a function of the incident photon energy (hν) is expressed for a direct transition:

$$\alpha_{CV} \sim \left(hv - E_g\right)^{\frac{1}{2}} \quad \textbf{(2.46)}$$

and for an indirect transition:

$$\alpha_{CV(In)} \sim \left(hv - E_g \pm E_{phonon}\right)^2 \quad \textbf{(2.47)}$$

where E_g and E_{phonon} are the band-gap and phonon energy, respectively. In indirect band-gap semiconductors the absorption process changes from indirect to direct as photon energy increases (see **Figure 2.16**). As evident from equations **2.46** and **2.47**, the absorption coefficient at the near absorption edge increases more rapidly in direct band-gap semiconductors than in indirect band-gap semiconductors. At the absorption edge, the absorption coefficient is small because the density of states at the edge of the conduction band is low. As the photon energy increases, the electron can transit to a higher energy level in the CB, at which the density of states is larger. Thus the absorption coefficient increases exponentially and tends to saturate.

Chapter 3

Experimental methods and techniques and theoretical *ab initio* calculations

In this chapter we are going to describe the experimental set-ups and the techniques employed to study the physical properties of the studied materials, like c-In_2O_3 and rh-In_2O_3 at ambient and HPs.

During this thesis work, we used the PE and the MA large volume presses to synthesize new phases of In_2O_3 at extreme conditions of pressure and temperature. We have characterized the starting materials and synthesized samples through SEM, XRD, Raman and optical spectroscopy. Additionally, we used a DAC to generate static HP and to study some physical properties as a function of pressure. In the following sections, we will briefly review these techniques. Moreover, we will conclude with a brief description of the theoretical *ab initio* calculations.

3.1. Crystal growth technique using a large volume press

3.1.1. Paris-Edinburg press

The PE press is a two-opposed anvil large-volume apparatus, designed to minimize both size and weight, allowing an easy set-up and use in large-scale facilities. It was initially developed for *in situ* neutron scattering experiments under pressure **[87-90]**. Later on, it has been adapted to perform a large variety of *in situ* measurements under HP and HT such as XRD **[91-93]**, inelastic neutron and X-ray scattering **[94]** and ultrasonic studies **[95, 96]** among

others. However, we employed basically the PE press to synthetize metastable phases of several compounds at extreme conditions of pressure and temperature.

The PE press presents some advantages over other large volume presses for *in situ* measurements. Indeed, unlike MA systems, PE press has a wide angular range accessible. This angular range can change depending on the model. For example, the V3 model has an angular aperture of 60º in the horizontal plane and 15º in the vertical plane, allowing a large variety of *in situ* scattering experiments under HP. Other advantages of the PE press are the lightness (~50 kg) with reduced dimensions and easily detachable. As mentioned before, these advantages offer a great flexibility in setting up this press on all kind of large-scale facilities, especially in experiments with synchrotron radiation.

There are several models and sizes of the PE press, but all of them work with the same principle. At the University of Valencia and for this thesis work we have used a VX3 PE press, shown in **Figure 3.1**.

Figure 3.1: *VX3 PE located at the Applied Physics department at the University of Valencia.*

Figure 3.2 shows in detail the cross section of the VX3 PE and its main components.

PE presses of type VX have two opposite very large angular apertures. Each aperture presents 140º horizontally and 60º vertically. In addition, the hydraulic ram can be unscrewed and replaced by other rams (for example with low temperature capability or with rear access). The

VX3 model has an outer diameter of 230 mm and a height of 290 mm. The oil pressure is applied via a hand pump (280 MPa capability) connected to the lower part of the press through a flexible HP pipe. As the maximum oil pressure that can be applied is 200 MPa (2000 bar) and the piston has a cross section of ~ 100 cm^2, therefore, the PE press has a maximum load capacity of 200 tonnes. Thus, the maximum generated force by this VX3 press is 2 MN, which is an exceptional performance, taking into account its mass and dimensions.

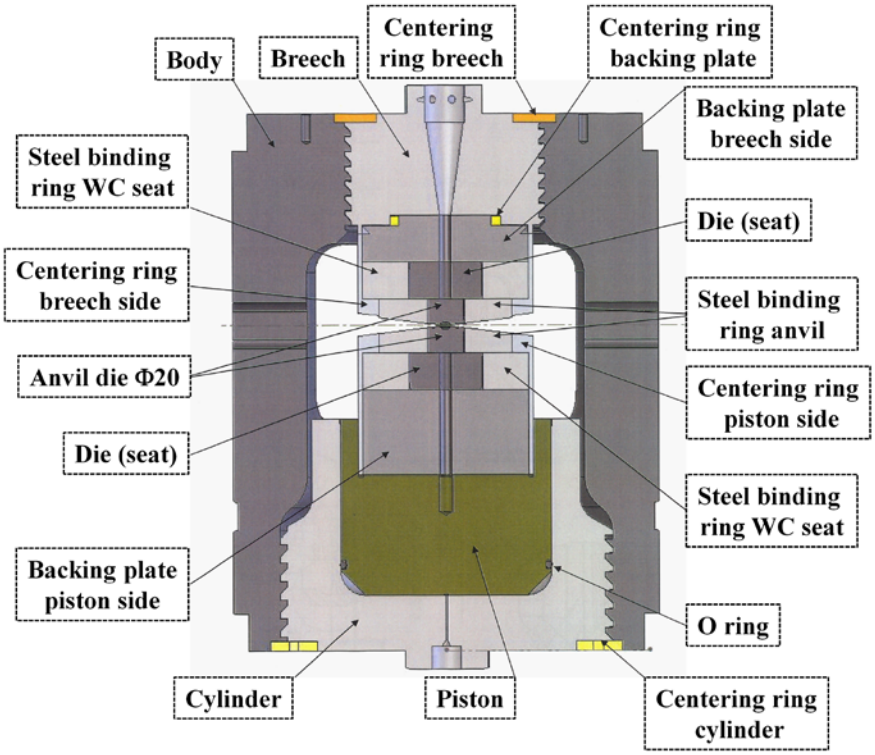

Figure 3.2: *Main components of the VX3 PE* ***[97]****.*

The force applied to the rear faces of the anvils is transmitted to the sample assembly on a much smaller surface, which results in the multiplication of the pressure. We can do an order of magnitude calculation to get a rough idea. Because of the surface ratio between the piston and the sample assembly is roughly 100, that means that with an oil pressure of 100 MPa (1000 bar) we can reach a static pressure on the sample of 10 GPa approximately.

To generate HP conditions, oil is injected into a chamber which increases the oil pressure and pushes a piston upwards. This piston pushes the lower anvil against a fixed opposed upper anvil thus generating a uniaxial compression in the sample assembly located between these two opposed anvils as we could observe in **Figure 3.3**.

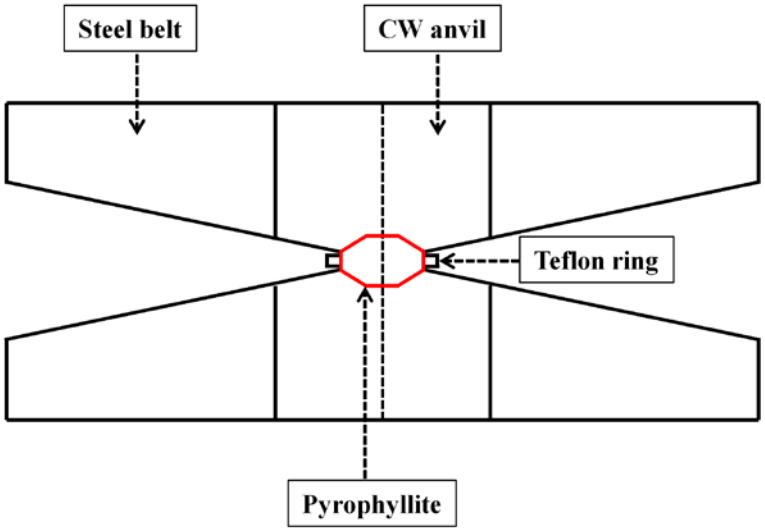

Figure 3.3: *Two opposite CW anvils compress the pyrophyllite gasket.*

Figure 3.4 shows the experimental set-up to carry out a HP-HT synthesis employing a VX3 PE. Specifically, the hydraulic hand pump to generate HP, the current source to generate HT, the thermocouple reading to register the synthesis temperature, the water cooling system to refrigerate both anvils and the protection box to prevent possible accidents of an unexpected explosion.

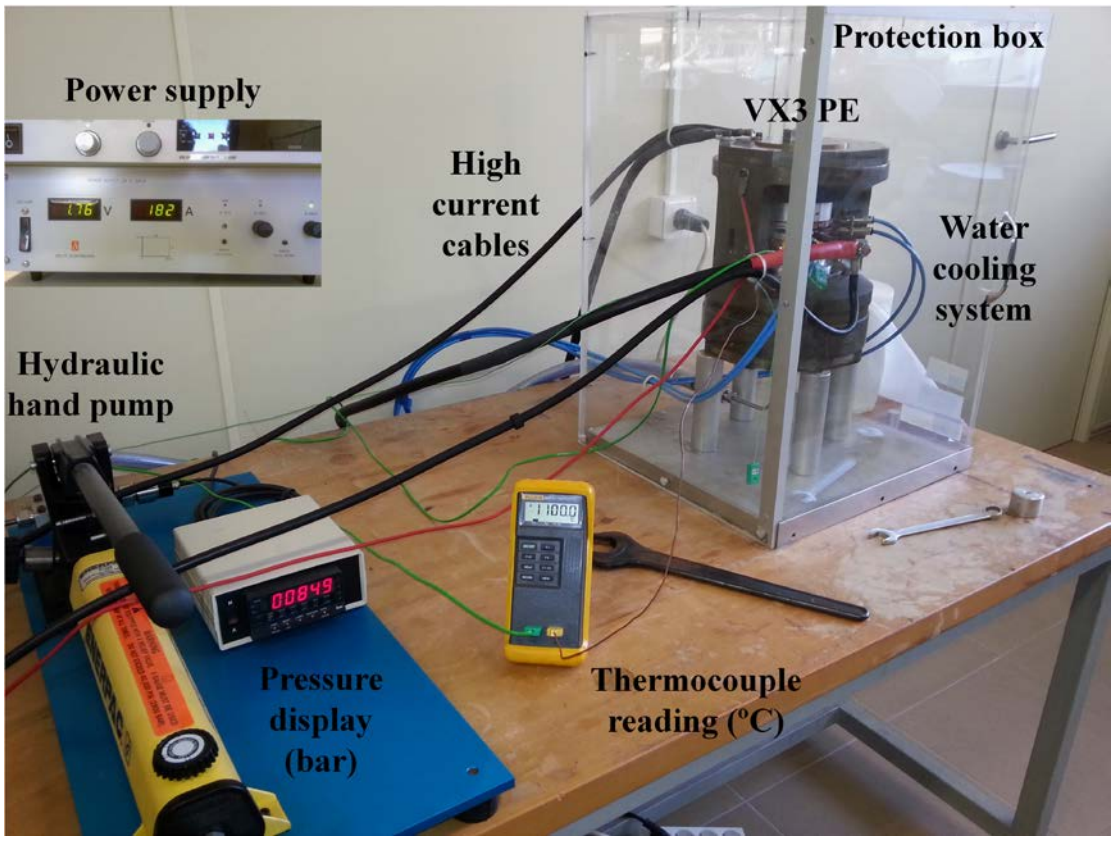

Figure 3.4: *Experimental set-up for a HP-HT synthesis employing a VX3 PE.*

3.1.1.1. The anvils

There are two types of anvils that could be employed for HP-HT synthesis using the VX3 PE as we could observe in **Figure 3.5**. On the one hand, the WC anvils with a conical shape cavity are embedded in a hardened steel ring, with a radial tension of 1 GPa with the aim of increase the compressive strength. On the other hand, the SD anvils are embedded in WC ring, and this, in turn, is embedded in a hardness steel ring.

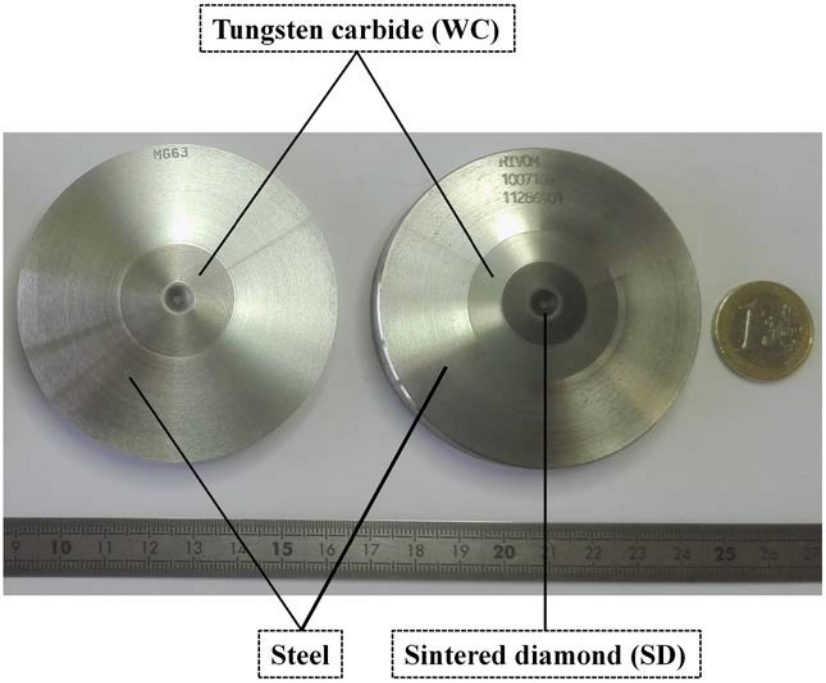

Figure 3.5: *5mm WC (left) and SD (right) anvils. A metallic rule and a one euro coin are shown for size comparison.*

The central anvil cavity can have different diameters (ϕ = 10 mm, 7 mm, and 5mm) as we could observe in **Figure 3.6**. Depending on the synthesis pressure that we want to reach and the volume sample that we want to recover we will employ different anvils sizes as we could observe in **Table 3.1**. With the larger WC anvils the amount of sample compressed is around 10 mm^3 to a maximum pressure of 6 GPa, whereas with the smaller WC anvils the amount of sample compressed is around 1 mm^3 and pressures up to 12 GPa can be attained. Besides, HTs up to 1500 ºC can be usually attained with a graphite furnace.

In order to avoid the dilation of the anvils, keep stable the mechanical elements and avoid the embrittlement of CW anvils, a good water cooling system is required. **Figure 3.7** shows the home-made water cooling system built by Diego Gómez Hernández, technician in the Applied Physics department.

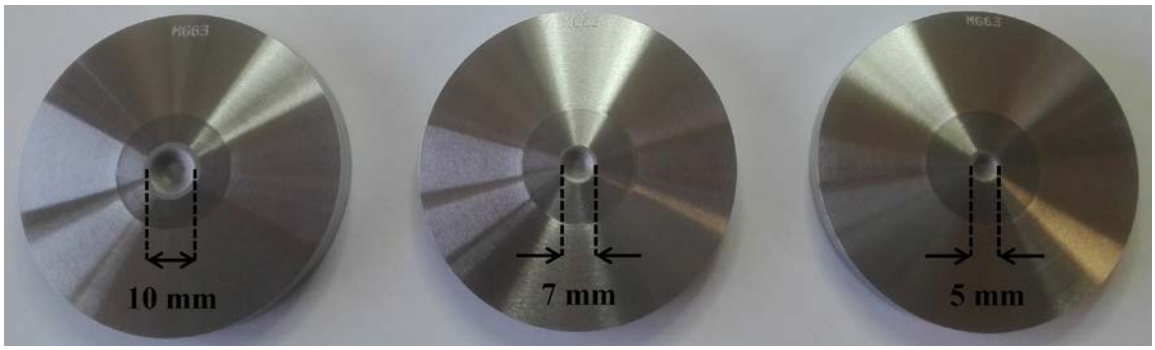

Figure 3.6: *Different diameter WC anvils.*

Anvil material	Anvil size (mm)	Maximum HP synthesis (GPa)	Volume sample (mm^3)
WC	10	~ 6	~10
WC	7	~ 8	~ 4
WC	5	~ 12	~ 1
SD	5	~ 20	~ 1

Table 3.1: *Approximate values of maximum pressure and compressed volumes, for different anvil materials and sizes.*

Figure 3.7: *Home-made water cooling system. Blue arrows indicate the water flow.*

3.1.1.2. The sample assembly

The sample assembly was loaded into a pyrophyllite gasket, held by a Teflon ring, which is compressed between two CW anvils (see **Figure 3.3**). The pyrophyllite gasket was previously machined and then fired to 950ºC during 90 minutes. This thermal treatment improves the mechanical (strength increase) and thermal (better thermal insulation) properties of the gasket.

The Teflon ring is around the pyrophyllite. Its main function is to hold the extruded material and increase the performance to reach higher pressures during the synthesis.

Sample was placed inside a hollow h-BN cylinder and covered with an upper and a lower h-BN disk. Afterwards, this h-BN capsule is located in a high resistivity graphite furnace. The h-BN capsule isolates electrically the sample from heater and serves together with graphite as the PTM. The current passes through a steel ring, in contact with the anvils. Molybdenum disks are used to improve the electrical contact with the graphite furnace. A schematic drawing could be observed in **Figure 3.8**.

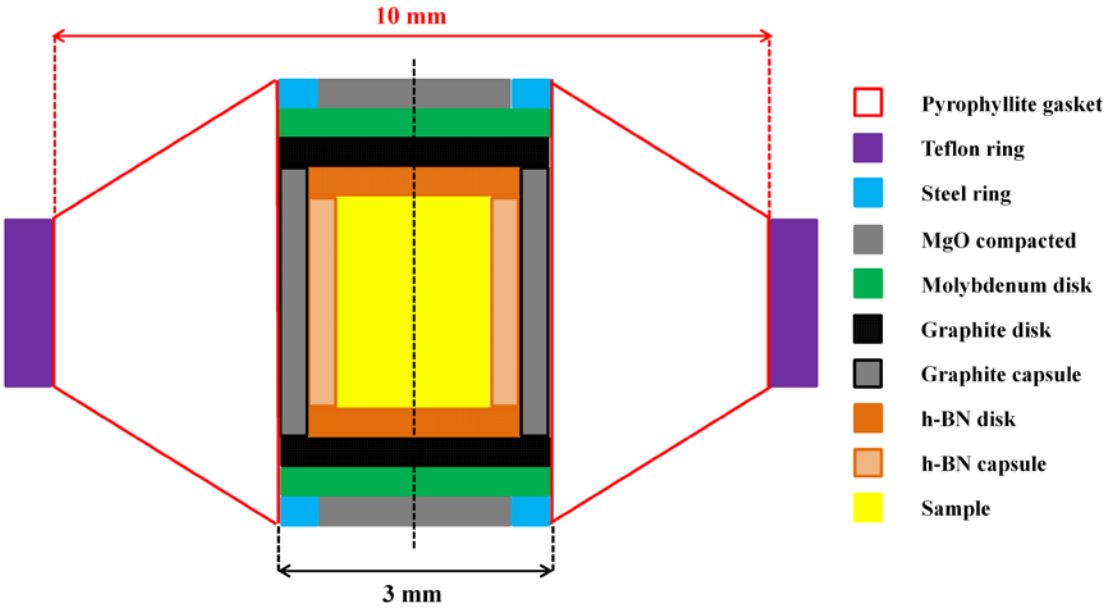

Figure 3.8: *Sample assembly for HP-HT synthesis.*

A picture of all involved elements in the sample assembly is shown in **Figure 3.9**.

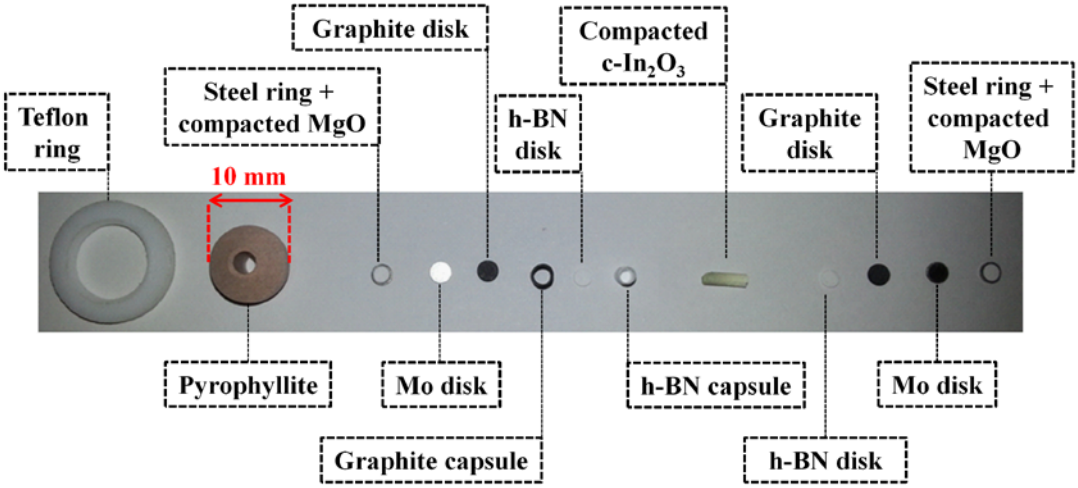

Figure 3.9: *Involved elements in the sample assembly for HP-HT synthesis.*

One of the goals of this thesis work was to synthesize the rh-In_2O_3. In the first attempt, it was employed the same set-up as describe in the **Figure 3.8**, using c-In_2O_3 as starting material. But for synthesis temperatures above 1000ºC, we observed corundum-type structure with *R-3c* SG (No. 167) of $InBO_3$ due to the reaction between the h-BN capsule and the c-In_2O_3. In order to avoid this problem, we used a metallic (Pt, Mo or Re) capsule to isolate the sample from the h-BN container (see **Figure 3.10**). The best results to synthesize rh-In_2O_3 were obtained with the Re capsule.

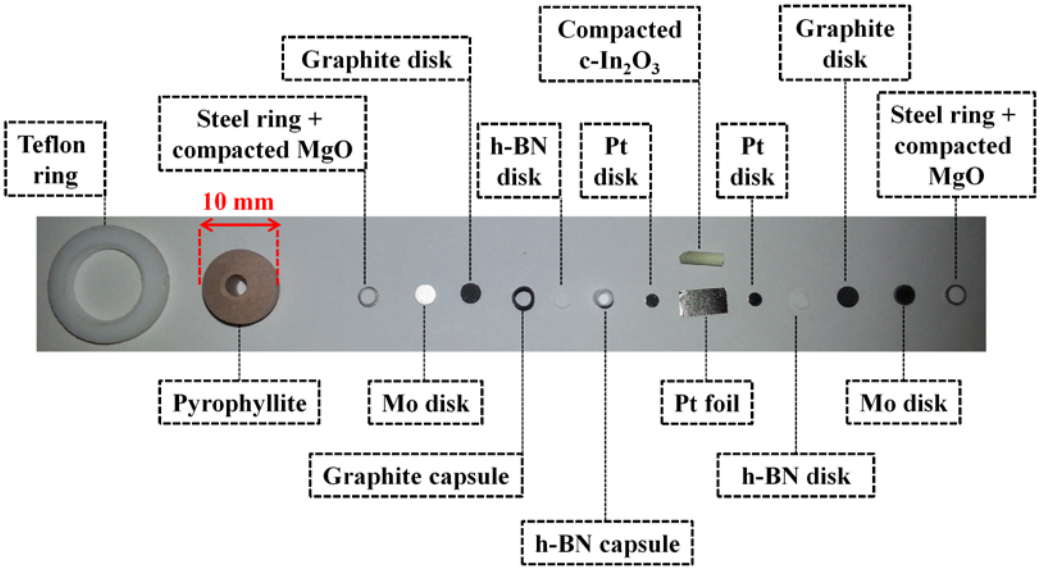

Figure 3.10: *Elements of the sample assembly for HP-HT synthesis to prevent the formation of the corundum-type structure of $InBO_3$.*

In the **Figure 3.11** we show the tool used to compact the In_2O_3 sample inside the metallic capsule.

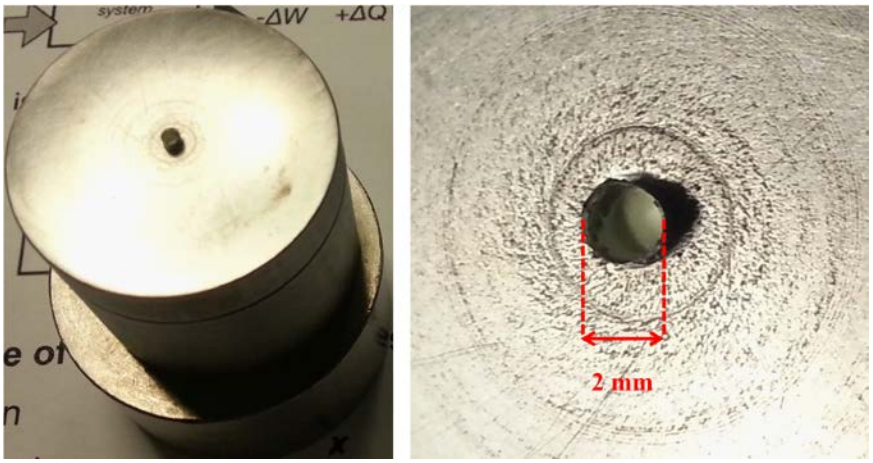

Figure 3.11: *Metal capsule compactor (left) at BGI. A zoom of the Re capsule is shown (right).*

3.1.1.3. Pressure calibration

The variation of the two-point resistance behaviour of several samples with different phase transition like HgSe **[98, 99]**, HgTe **[99, 100]**, CdSe **[101]**, CdTe **[101]**, $Cd_{0.8}Zn_{0.2}Te$ **[102]** and InAs **[103]** under pressure has been used to calibrate the pressure at sample location with the load pressure (oil pressure applied to the press piston by the hydraulic hand pump). For these compounds, phase transitions from semiconductor to semimetal, semimetal to semiconductor or semiconductor to metal were observed under pressure.

For example, **Figure 3.12** shows the two-point resistance measurement of HgSe and HgTe in a 10 mm pyrophyllite gasket without using a Teflon ring. The first experiments were made without Teflon ring, but at some point, we decided to use systematically the Teflon ring because it reduces the gasket extrusion and improves the pressure performance.

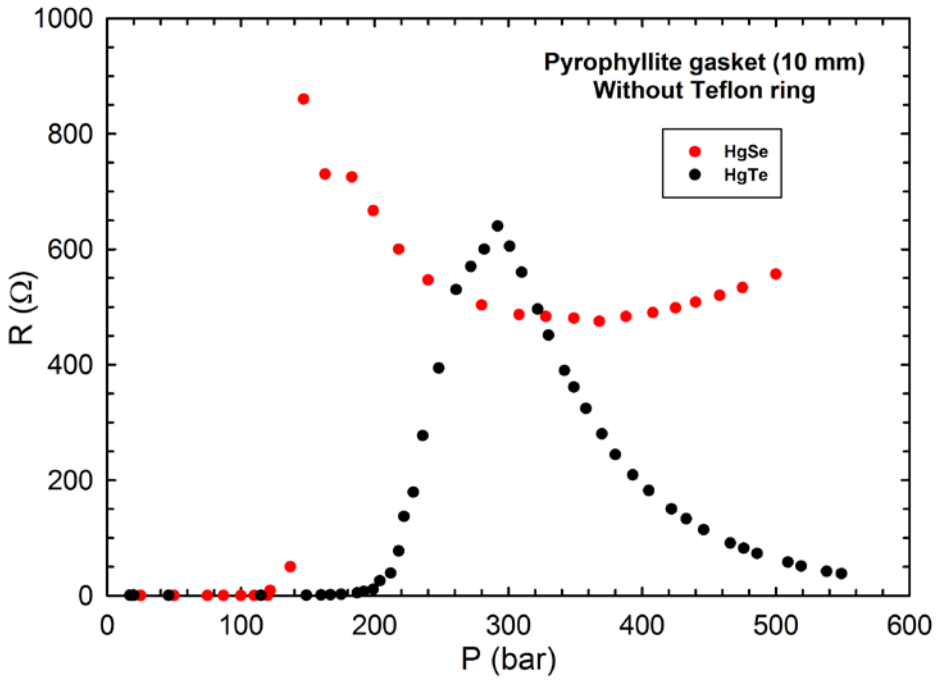

Figure 3.12: *Two-point resistance measurement of HgSe (red circles) and HgTe (black circles) under pressure in a 10 mm pyrophyllite gasket without employing the Teflon ring.*

HgSe transform from semimetal to semiconductor at 0.7 GPa. That pressure is reached at an oil pressure about 122 bar. The same transition (semimetal to semiconductor) occurs in the HgTe but at the pressure of 1.3 GPa (200 bar).

Table 3.2 summarized the transition-type and the phase transition pressure of each compound (HgSe, HgTe, CdTe, $Cd_{0.8}Zn_{0.2}Te$ and InAs) and the pressure load (oil pressure) for which we

observe the onset of the electrical transition. For these experiments we used a 10 mm pyrophyllite gasket.

Transition-type				With Teflon ring	Without Teflon ring
Compound	**From**	**To**	**P (GPa)**	**P_{Oil} (bar)**	**P_{Oil} (bar)**
HgSe	Semimetal	Semiconductor	0.7		122
HgTe	Semimetal	Semiconductor	1.3		200
HgTe	Semiconductor	Metal	2.6		290
CdTe	Semiconductor	Semimetal	3.3		323
$Cd_{0.8}Zn_{0.2}Te$	Semiconductor	Semimetal	5.5	510	
InAs	Semiconductor	Metal	6.9	860	

Table 3.2: *Pressure-load calibration for 10 mm pyrophyllite gasket, using different calibrants and the corresponding phase transitions.*

Other example could be observed in **Figure 3.13**, where it is showed the two-point resistance measurement of $Cd_{0.8}Zn_{0.2}Te$ in a 7 mm pyrophyllite gasket using a Teflon ring. In that case, the sample transforms from semiconductor to semimetal at 5.5 GPa (~327 bar).

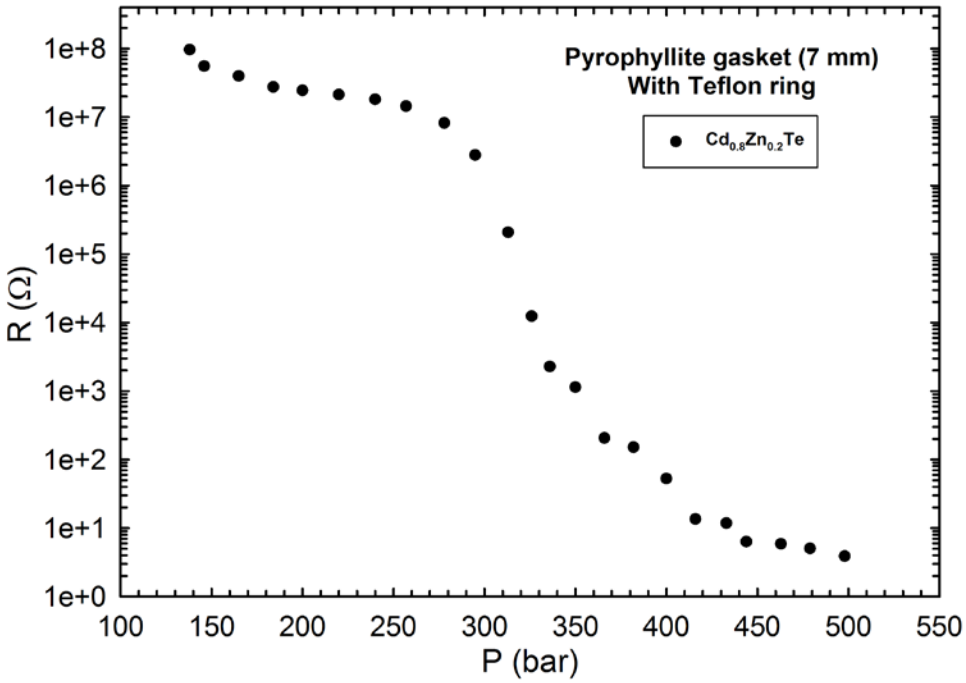

Figure 3.13: *Two-point resistance measurement of $Cd_{0.8}Zn_{0.2}Te$ under pressure in a 7 mm pyrophyllite gasket using a Teflon ring.*

Table 3.3 summarized the transition-type and the phase transition pressure of each compound (HgSe, HgTe, CdSe, CdTe, $Cd_{0.8}Zn_{0.2}Te$ and InAs) with the oil pressure, observing the electrical transition in a 7 mm pyrophyllite gasket.

Compound	Transition-type		P (GPa)	With Teflon ring	Without Teflon ring
	From	To		P_{Oil} (bar)	P_{Oil} (bar)
HgSe	Semimetal	Semiconductor	0.7		68
HgTe	Semimetal	Semiconductor	1.3		117
CdSe	Semiconductor	Semiconductor	2.5		158
HgTe	Semiconductor	Metal	2.6		214
CdTe	Semiconductor	Semimetal	3.3		224
$Cd_{0.8}Zn_{0.2}Te$	Semiconductor	Semimetal	5.5	327	
InAs	Semiconductor	Metal	6.9	598	

Table 3.3 *Pressure-load calibration for 7 mm pyrophyllite gasket, using different calibrants and the corresponding phase transitions.*

Our experimental results obtained through the pressure calibration for the 10 and 7 mm pyrophyllite gaskets are represented in **Figure 3.14** and **Figure 3.15**, respectively and compared with experimental data obtained by Dr. Yann Le Godec in XRD experiments.

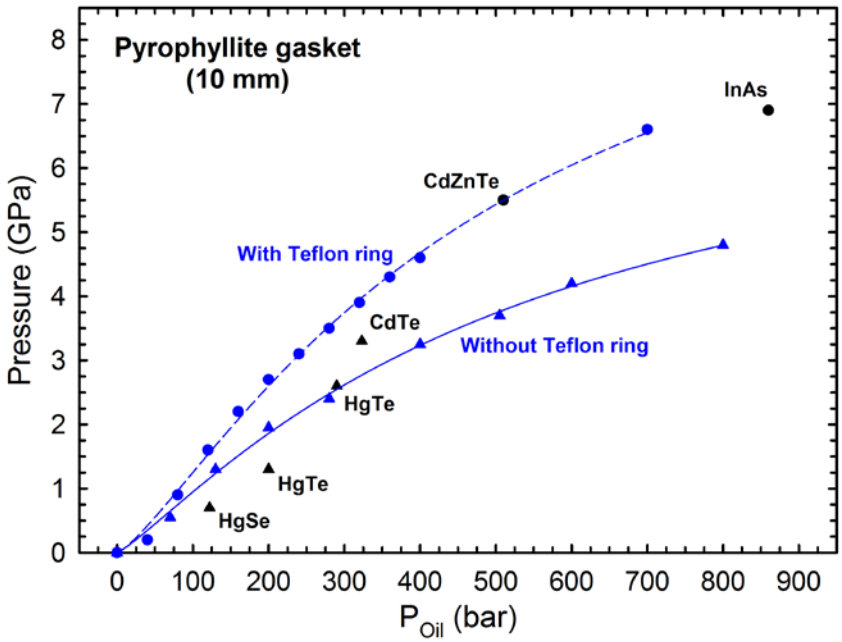

Figure 3.14: *Pressure-load calibration for a 10 mm pyrophyllite gasket. Black and blue symbols are related with the pressure calibration performed at the University of Valencia and the obtained by Dr. Yann Le Godec through the XRD experiments, respectively. Triangles (circles) and the blue solid (dashed) line are associated with the pressure calibration without (with) Teflon ring. Symbols and lines are associated to the experimental data and to the fits of the three parameters logistic regression, respectively.*

The experimental data obtained by Dr. Yann Le Godec (blue circles and triangles) are fitted with three parameters logistic regression. This mathematical regression presents the following form:

$$P\ (GPa) = \frac{a}{1+\left(\frac{P_{Oil}\,(bar)}{x_0}\right)^b} \qquad \textbf{(3.1)}$$

where *a*, *b* and x_0 are the three free fitting parameters. **Table 3.4** summarized the experimental pressure calibration obtained by Dr. Yann Le Godec.

As we could observe, in the lower oil pressure range (0 – 400 bar) of the **Figure 3.14** there is a disagreement, at least for the 10 mm pyrophyllite gasket, between the calibration that we perform employing the two-point resistance measurement at the University of Valencia with the calibration obtained by Yann Le Godec in XRD experiments. A possible explanation could be that we employed powder samples that were not sufficiently compacted and therefore, the contact between grains was worst at low pressures. It implies that the phase transitions, observed through the two-point resistance measurement, will be detected at higher pressures. However, although the data by Dr. Yann Le Godec were provided after the first HP-HT synthesis starting from c-In_2O_3, the pressure synthesis did not have to be modified because both pressure calibrations are in good agreement in the upper oil pressure range (500 – 900 bar).

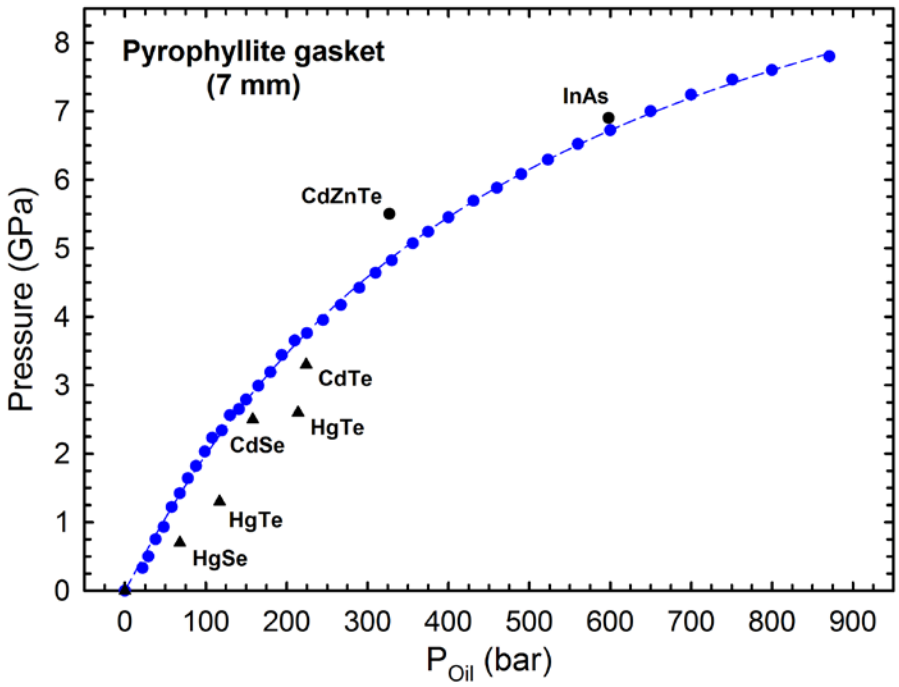

Figure 3.15: *Pressure-load calibration for a 7 mm pyrophyllite gasket. Black and blue symbols correspond to pressure calibration performed at the University of Valencia and the one obtained by Dr. Yann Le Godec in XRD experiments, respectively. Triangles (circles) correspond to pressure calibration without (with) Teflon ring. Blue dashed line corresponds to the fit of X-ray data.*

Parameter	ϕ = 10 mm		ϕ = 7 mm
	Without Teflon ring	With Teflon ring	With Teflon ring
***a* (GPa)**	7.8 (8)	10.6 (1.0)	12.2 (3)
b	-1.18 (9)	-1.28 (8)	-1.03 (2)
***x_0* (bar)**	530 (100)	480 (70)	490 (30)

Table 3.4: *Experimental pressure calibration obtained by Dr. Yann Le Godec in XRD experiments showing values of fitting parameters.*

We employed the pressure calibration of the 5 mm boron epoxy gasket (see **Figure 3.16**), published in the PhD thesis of Dr. Guillaume Morard **[104]**, to have an idea of the pressure synthesis employing the 5 mm pyrophyllite gasket.

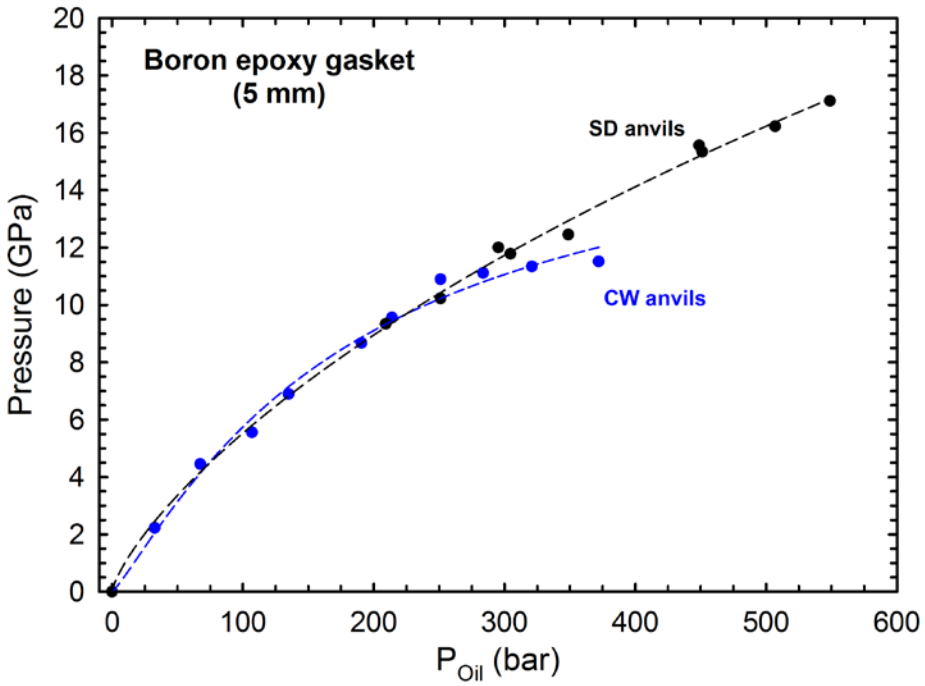

Figure 3.16: *Pressure-load calibration for a 5 mm boron epoxy gasket. Blue (black) circles are related with the employment of CW (SD) anvils. Symbols and lines correspond to the experimental data and to the fit of the three parameters logistic function, respectively.*

Table 3.5 summarizes the results (fitting values) of the three-parameter logistic regression of the pressure calibration for the 5 mm boron epoxy gasket represented in **Figure 3.16**.

Parameter	ϕ = 5 mm	
	CW anvils	SD anvils
***a* (GPa)**	17.1 (1.9)	87 (16)
b	-1.17 (18)	-0.76 (19)
***x_0* (bar)**	180 (50)	3500 (800)

Table 3.5: *Pressure calibrations of the 5 mm boron epoxy gasket obtained by Dr. Guillaume Morard using the CW and the SD anvils.*

3.1.1.4. Temperature calibration

Figure 3.17 shows the set-up employed for temperature calibration. The sample is replaced by an h-BN solid cylinder and a K-type thermocouple is introduced till the center. A steel tube is inserted till touching the outer wall of the graphite capsule in order to protect the thermocouple. The thermocouple is slightly shifted vertically with the aim of lay down better into the lower CW anvil. Moreover, in order to avoid the breaking of the thermocouple, we made a radial groove in this CW anvil as we could observe in **Figure 3.18**.

Figure 3.19 shows different temperature calibration at different oil pressures for a 10 mm pyrophyllite gasket.

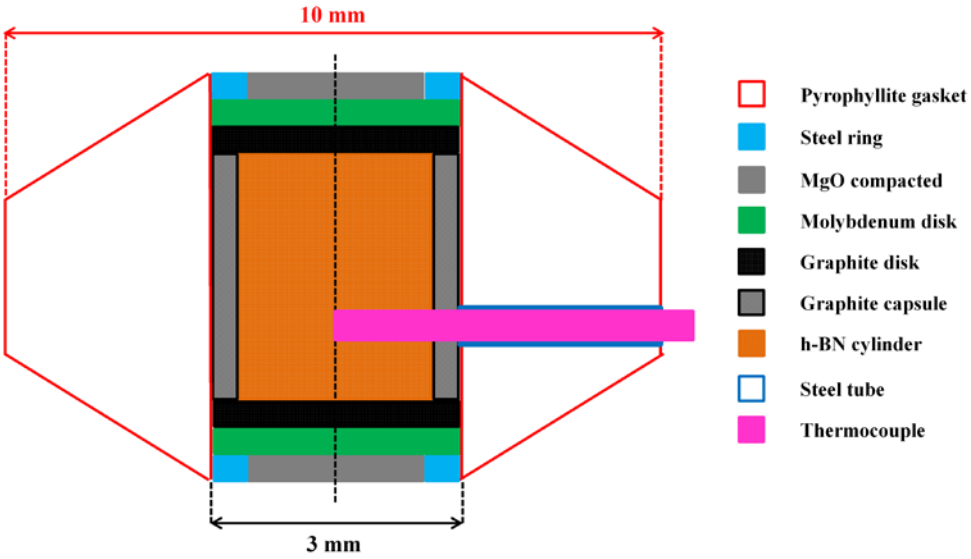

Figure 3.17: *Sample assembly used for temperature calibration of 10 mm pyrophyllite gasket.*

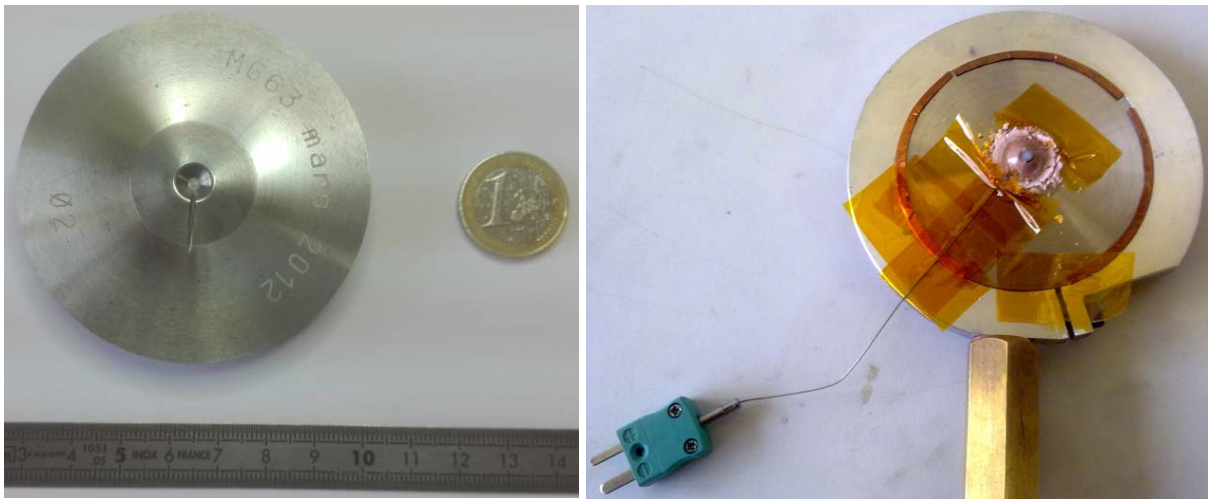

Figure 3.18: *Radial groove in this CW anvil (left) and complete set-up after decompression (right).*

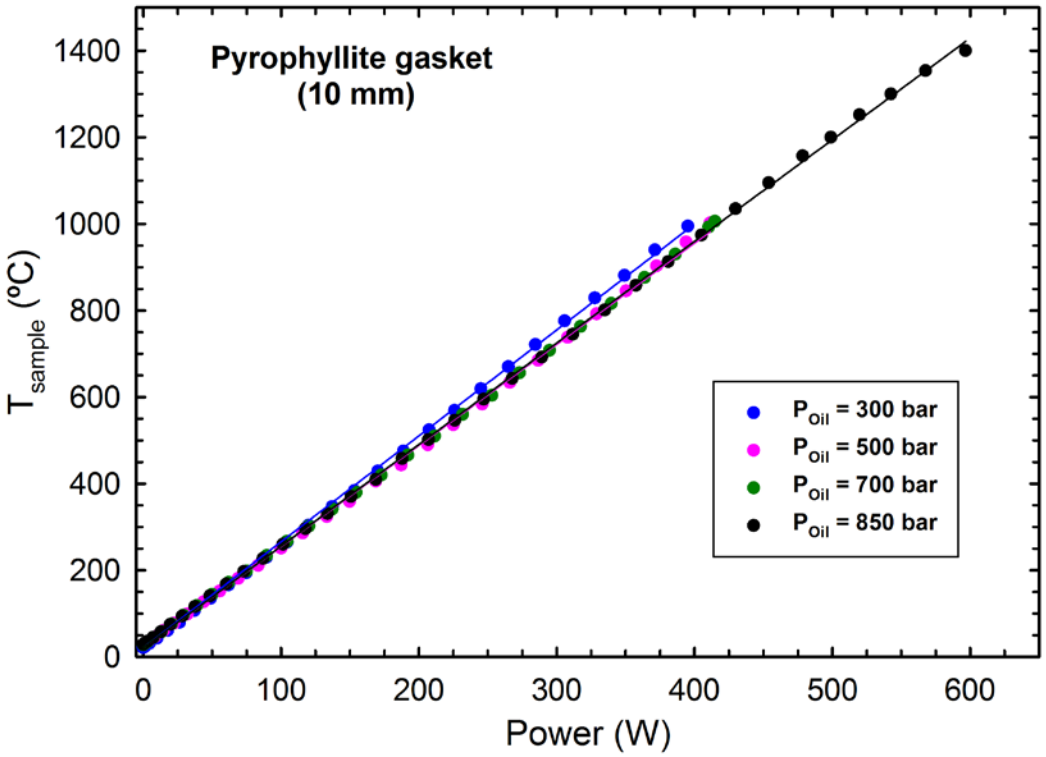

Figure 3.19: *Power-temperature calibration for different oil pressure loads for a 10 mm pyrophyllite gasket.*

The experimental data corresponding with the power supplied by the current source and the sample temperature registered by the thermocouple were fitted with a linear regression (**3.2**) and summarized in **Table 3.6**.

$$T(ºC) = T_0 + a\,P(W) \qquad \textbf{(3.2)}$$

P_{Oil} (bar)	P (GPa)	T_0 (± 0.1ºC)	a (ºC/W)
300	~ 3.8	21.0	2.447 (11)
500	~ 5.4	21.0	2.337 (13)
700	~ 6.6	21.0	2.346 (8)
850	~ 7.2	21.0	2.347 (7)

Table 3.6: *Linear regressions of the temperature calibration at different pressures for the 10 mm pyrophyllite gasket*

"T_0" was the room temperature in the experiment. Therefore, the slope was the only free parameter in the linear fit. As observed, the slope does not change too much with pressure. **Figure 3.20** shows the sample assembly used for temperature calibration of 7 mm pyrophyllite gasket.

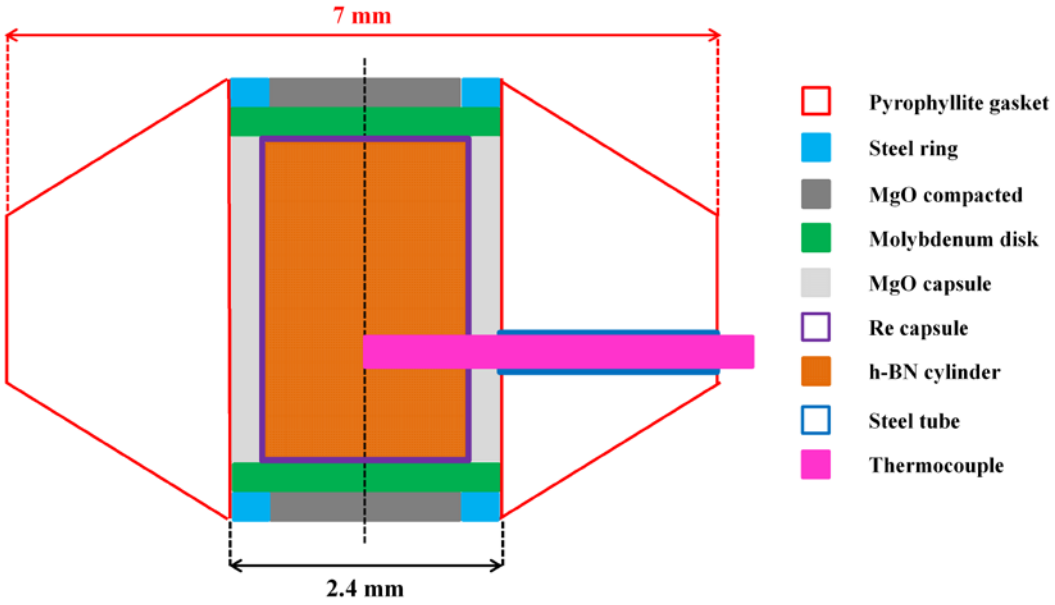

Figure 3.20: *Sample assembly used for temperature calibration of 7 mm pyrophyllite gasket.*

Different Re thickness foil (12.5 μm and 25 μm) were used as furnace. **Figure 3.21** shows the power-temperature calibration for a12.5 μm Re heater.

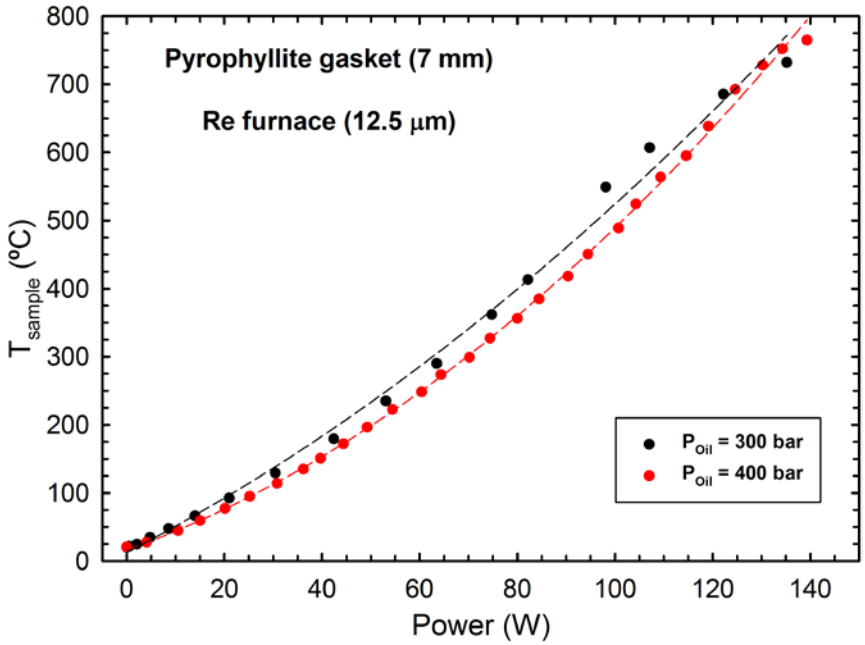

Figure 3.21: *Power-temperature calibration for different oil pressures in a 7 mm pyrophyllite gasket employing a 12.5 μm Re foil as furnace.*

The experimental data corresponding with the power supplied by the current source and the sample temperature registered by the thermocouple were fitted with a quadratic regression (**3.3**) and summarized in **Table 3.7**.

$$T(ºC) = T_0 + a\,P(W) + b\,P^2(W^2) \quad \textbf{(3.3)}$$

P_{Oil} (bar)	P (GPa)	T_0 (ºC)	*a* (ºC/W)	*b* (ºC^2/W^2)
300	~ 4.6	20 (9)	3.5 (4)	0.016 (3)
400	~ 5.5	21 (4)	2.44 (14)	0.022 (1)

Table 3.7: *Quadratic regression of the temperature calibration at different pressures for a 7 mm pyrophyllite gasket employing a 12.5 μm Re foil as furnace.*

As we could observe, the 12.5 μm Re capsule start to be unstable around 140 W (~ 750 ºC). For that reason, we decided to increase the thickness of the Re capsule to 25 μm. The temperature calibration obtained is exhibited in **Figure 3.22**.

The experimental data corresponding with the power supplied by the current source and the sample temperature registered by the thermocouple were fitted with a quadratic regression **(3.3)** and summarized in **Table 3.8**.

The sample assembly used for 5 mm pyrophyllite gasket was quite similar as the employed for the sample assembly of 7 mm pyrophyllite gasket (see **Figure 3.20**), except that we didn't use the MgO capsule. The metallic Re furnace remained with the same dimensions as the set-up used for the 7 mm pyrophyllite gasket. Therefore, we used the same temperature calibration as described in **Figure 3.21** and **Figure 3.22** for the 12.5 μm and 25 μm Re foil furnace, respectively.

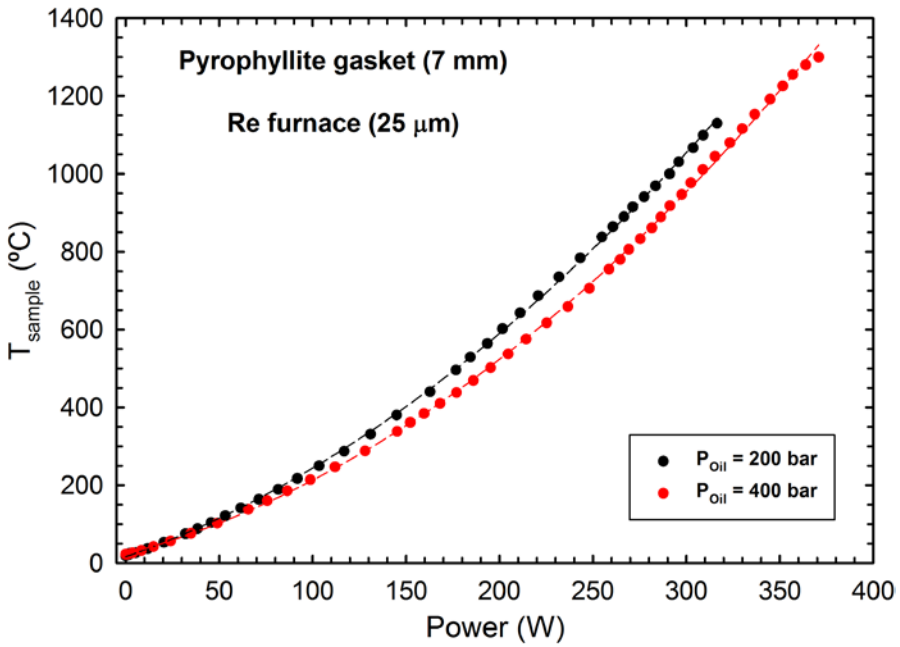

Figure 3.22: *Power-temperature calibration for different oil pressures in a 7 mm pyrophyllite gasket employing a 25 μm Re foil as furnace.*

P_{Oil} (bar)	P (GPa)	T_0 (ºC)	*a* (ºC/W)	*b* (ºC^2/W^2)
200	~ 3.5	20.4 (1.9)	1.63 (3)	0.0060 (2)
400	~ 5.5	22 (3)	1.31 (4)	0.0060 (2)

Table 3.8: *Quadratic regression of the temperature calibration at different pressures for a 7 mm pyrophyllite gasket employing a 25 μm Re capsule.*

3.1.2. Multi-anvil press

During my research stay at the Bayerisches Geoinstitut (BGI) in Bayreuth (Germany), I had the opportunity to use a Kawai-type MA apparatus **[105]**. Specifically, I employed the Sumitomo 1200 tons MA press (see **Figure 3.23**) to perform HP-HT synthesis.

The sample pressure is generated by a two-stage anvil compression system as we could observe in **Figure 3.24**. Firstly a hydraulic ram drives six first-stage anvils via guide blocks. Subsequently, the six first-stage anvils, forming a cubic cavity, compress eight second-stage anvils. Different second-stage anvil like CW, c-BN and SD could be used depending on the pressure conditions for the synthesis. Finally, the second-stage anvils compress an octahedral cell assembly whose dimensions also depends on the pressure conditions needed for the experiment.

Figure 3.23: *Sumitomo 1200 tons multi-anvil press.*

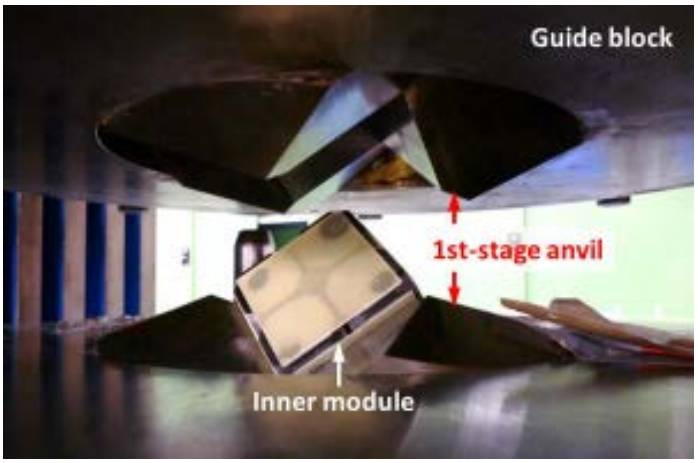

Figure 3.24: *Pressure system generation in the Sumitomo 1200 tons (Kawai-type) multi-anvil press* ***[106]****.*

3.1.2.1. The sample assembly

We employed two different assemblies depending on of the extreme conditions of pressure and temperature needed for the synthesis **[107]**. The different set-ups (10/5 and 18/11) have different cubes and truncation edge lengths. On the one hand, the 10/5 set-up was used for synthesis at pressure and temperature higher than 13 GPa and 1300-1400ºC, respectively. This assembly is loaded into a 10 mm MgO:Cr octahedron which is compressed between eight c-BN anvils, separated by pyrophyllite gaskets as we can see in **Figure 3.25**.

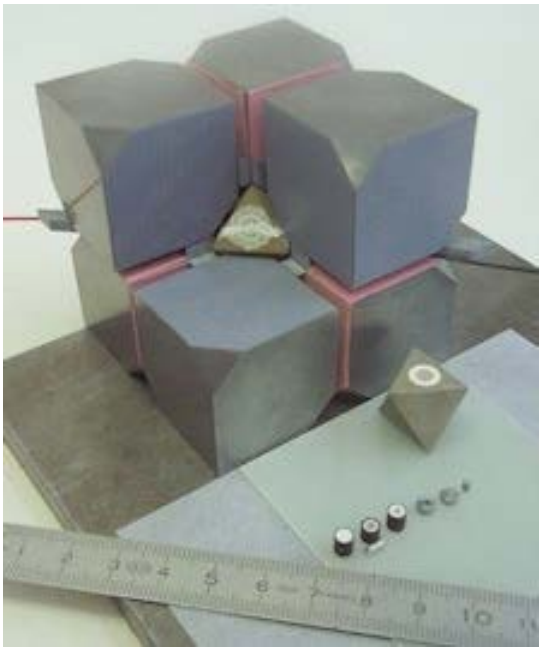

Figure 3.25: *Essential elements and spatial arrangement for a sample assembly employing a 10 mm MgO:Cr octahedra compressed between eight c-BN anvils in the 10/5 multi-anvil configuration* ***[108]****.*

The sample was compacted and placed inside a 25 μm thickness Re capsule to synthesize rh-In_2O_3. This metallic capsule was located in a high resistivity $LaCrO_3$ furnace, using MgO cylinder as a spacer. The MgO cylinder isolates electrically the metal capsule from the heater and serves together with $LaCrO_3$ as a pressure-transmitting medium. The hard Al_2O_3 cylinder is used for protection of the thermocouple. The thermocouple passes through cavities drilled in the upper electrically conducting disk with a hole, and covered by a similar but shorter MgO:Cr cylinder to keep these parts inside the octahedron. The electrical contacts are used to lead the current to the $LaCrO_3$ furnace. In **Figure 3.26** it can be observed in more detail all necessary elements to perform a HP-HT synthesis in a MA press.

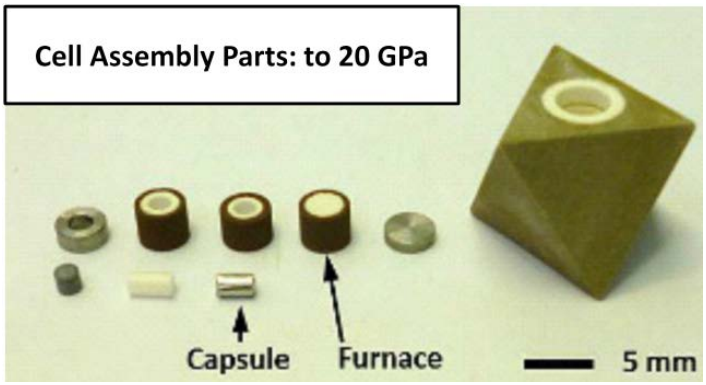

Figure 3.26: *Essential elements to perform a HP and HT synthesis in a 10/5 multi-anvil configuration* ***[107]****.*

The distribution of all the elements that take part inside the octahedron in the 10/5 multi-anvil set-up are shown in **Figure 3.27**.

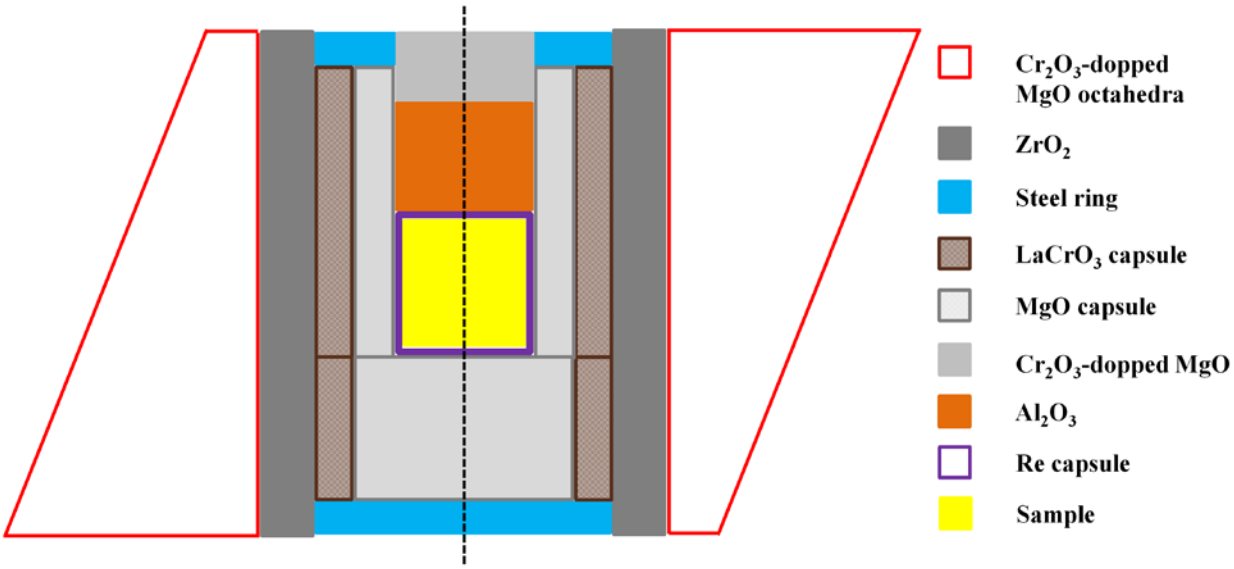

Figure 3.27: *Sample assembly used for HP-HT synthesis employing the 10/5 configuration.*

On the other hand, the 18/11 set-up was employed for synthesis at pressure and temperature lower than 14 GPa and 1300-1400ºC, respectively. Apart of size, the difference between 18/11 and 10/5 set-ups are the furnace material for the HP-HT synthesis and the electrical contact employed. Firstly, this assembly was loaded into a 18 mm MgO:Cr octahedra which was compressed between eight tungsten carbide anvils in the 18/11 multi-anvil configuration. Secondly, a high resistivity graphite furnace (divided in three parts) is employed instead of $LaCrO_3$ (divided in two parts) furnace. Thirdly, we employed directly two graphite disks instead of two steel rings to lead the current to the graphite furnace as we could observe in **Figure 3.28**.

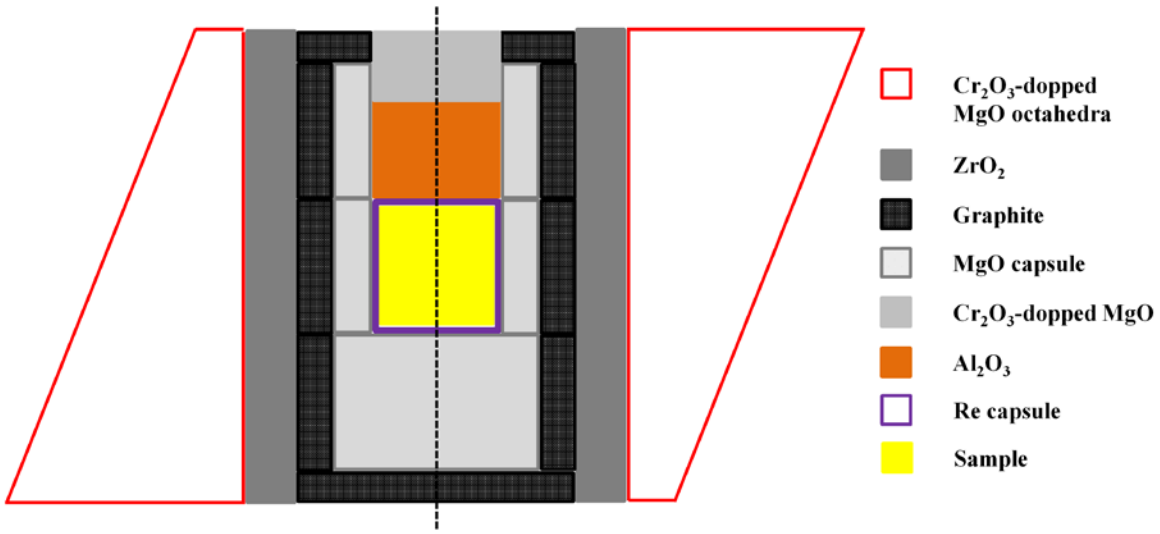

Figure 3.28: *Sample assembly used for HP-HT synthesis employing the 18/11 configuration.*

3.1.2.2. Pressure calibration

Table 3.9 and **Table 3.10** are employed to determine the pressure during the experiments with 18/11 and 10/5 configurations, respectively.

P(GPa)	1	2	3	4	5	6	7	8	9	10	11	12	13	14
Ton	48	96	144	192	242	294	350	406	466	532	600	680	774	886
Bar	28	56	84	112	141	172	204	237	272	310	350	397	452	517

Table 3.9: *Pressure calibrations for the Sumitomo 1200 tons MA press employing 18/11 configuration.*

P(GPa)	13	14	15	16	17	18	19	20
Ton	350	370	390	412	470	550	650	770
Bar	204	216	228	240	274	321	379	439

Table 3.10: *Pressure calibrations for the Sumitomo 1200 tons MA press employing 10/5 configuration.*

3.1.2.3. Temperature calibration

To generate HT conditions, the current flows from the first-stage anvil to the second one, and then, it passed through the sample assembly. As we mention before, the current flows from the steel ring to the $LaCrO_3$ furnace in the 10/5 configuration and from the graphite disk to the graphite furnace in the 18/11 configuration.

Figure 3.29 shows different temperature calibrations of the 10/5 MA configuration using the $LaCrO_3$ heater performed by several scientists at BGI. To estimate the HT conditions during the synthesis we employed the green solid line marked as "Re, graphite (Gr) capsule".

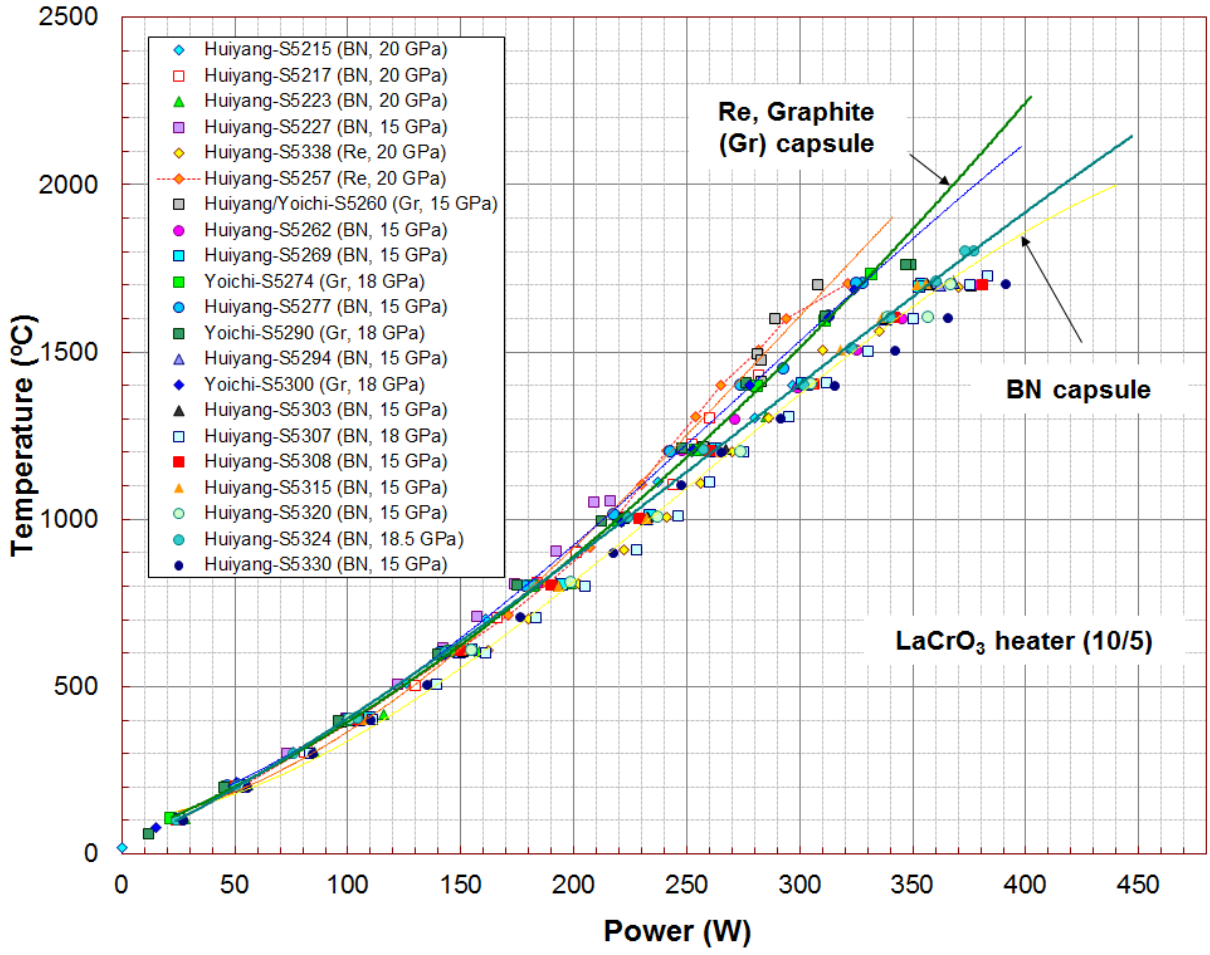

Figure 3.29: *Different temperature calibration for the Sumitomo 1200 tons MA press in the 10/5 MA configuration using the $LaCrO_3$ heater.*

Figure 3.30 shows different temperature calibrations of the 18/11 MA configuration using the graphite heater performed by several scientists at BGI. To estimate the HT conditions during the synthesis we employed the black solid line corresponding to an average of all calibrations curves.

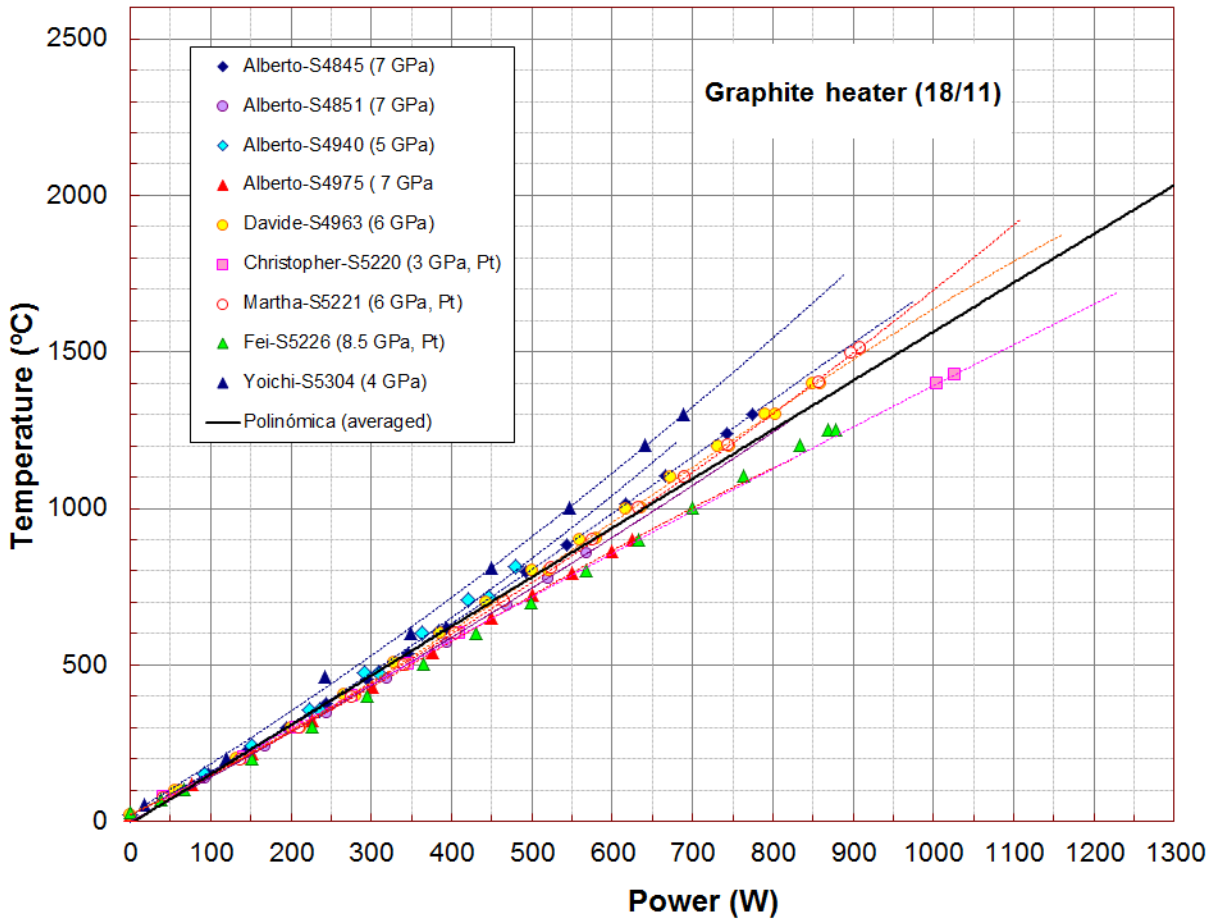

Figure 3.30: *Different temperature calibration for the Sumitomo 1200 tons MA press in the 18/11 MA configuration using the graphite heater.*

3.2. High-pressure measurements

3.2.1. The diamond-anvil cell

The DAC is the most appropriate device to reach pressures larger than 1 Mbar (100 GPa) when a big sample volume (~mm^3) is not required. Diamond has great properties to be employed as an anvil material. On the one hand, it is one of the hardest and uncompressible materials to generate HPs without considerable deformation or fracture. On the other hand, it remains transparent for a very wide range of energies, specifically, from infrared till hard X-rays (energies larger than 10 KeV). That gives access to a very large variety of *in situ* spectroscopy techniques to characterise the behaviour of samples under extreme pressure conditions.

Basically, the DAC that we employed in our experiments consists of two identical opposed brilliant-cut diamonds with truncated tips that are pushed one against the other with a metallic gasket in between (see **Figure 3.31**). This gasket, previously pre-indented, has a hole in the

center where the sample is placed together with a pressure calibrant. Normally, we employed small ruby balls (around 2μm diameter size) as pressure gauge for optical spectroscopy, RS and angle-dispersive powder XRD **[109]**. On certain occasions, especially in synchrotron measurements (angle-dispersive powder XRD), we used copper powder **[110]** as a pressure sensor instead of ruby balls in order to optimize the measurement time. Together with the sample and the pressure calibrant, a liquid or gas was loaded in the hole of the gasket as PTM to ensure quasi-hydrostaticity **[111]**.

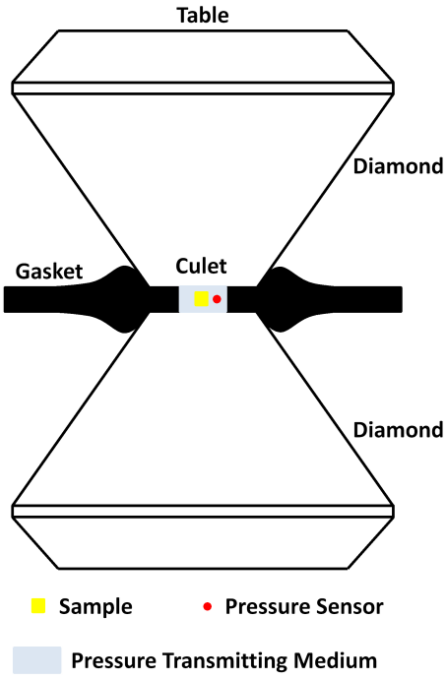

Figure 3.31: *Essential elements of a DAC.*

In this work, we have used basically a membrane-type DAC designed at the University of Paris **[59]**, as well as an ALMAX-Boehler-type DAC **[60, 61]**. The differences between DACs basically come from the way in which the force is applied on the diamonds to increase pressure. In the membrane-type DAC, diamonds are fixed to the carbide seats of the piston and body, respectively. The piston is introduced into the body and the whole DAC is closed with a screwed tap containing a gas membrane (it is a three-piece DAC). To increase pressure on the sample, pressurized helium is introduced into the membrane chamber causing the expansion of the membrane which pushes the piston against the body, therefore, both diamonds are pushed together thus compressing the sample chamber; i.e., the compressing mechanism is internal through external gas pressure increase. In the ALMAX-Boehler-type DAC, diamonds sit on carbide seats that are held to two steel disks (it is a two-piece DAC). To increase pressure on the sample, three screws push together the two diamonds in both steel

disks by bending the inner part of both disks where diamonds are attached; i.e., the compressing mechanism is external since the three screws have to be manually operated from the outside of the DAC.

An advantage of using the membrane-type DAC with respect to the ALMAX-Boehler-type DAC; i.e., the internal pressurizing mechanism vs. the external one, is that the former DAC does not have to be moved during the experiment for pressure increase or decrease, unlike the later DAC. Therefore, it is very convenient to employ this cell in a synchrotron experiment because of the time saving in the centering and alignment procedure of the DAC with the x-ray beam. However, the ALMAX-Boehler-type DAC has a bigger aperture angle (up to $4\theta = 90^{o}$) than the membrane-type DAC, and this is interesting in angle dispersive XRD experiments because it allows observing a higher number of Bragg reflections.

3.2.2. Pressure calibration

There are different ways to measure the pressure at the sample location. The most common technique employed consists of using the luminescence properties of the ruby (α-Al_2O_3:Cr^{3+}). Basically, by impinging a laser beam on the ruby produces two thin and intense luminescence peaks called R_1 and R_2. The most intense peak (R_1) is located at a wavelength of 694.38 nm at ambient conditions. As pressure is applied, both luminescence peaks shift towards lower energies, i.e., larger wavelengths, as can be seen in **Figure 3.32**.

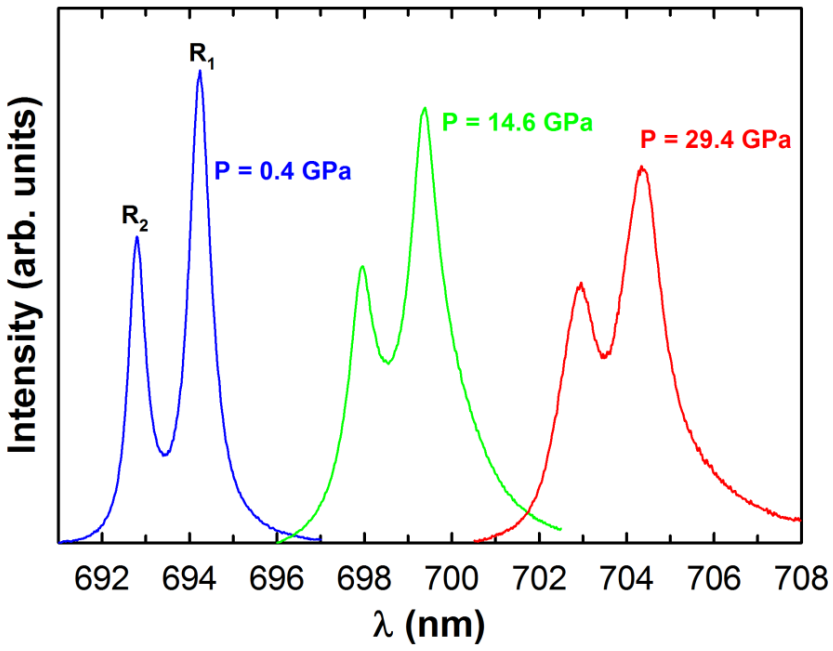

Figure 3.32: *Ruby luminescence at different pressures.*

There are different ruby pressure scales, depending on the pressure range **[109, 112-115]**. During this thesis work, we performed experiments from ambient pressure till 50 GPa. Due to the pressure range studied, we decided to employ the equation **(3.4)**, proposed by Mao *et. al* **[115]** to determine the pressure inside the pressure chamber.

$$P(GPa) = \frac{1904}{7.665}\left\{\left[1 + \left(\frac{\lambda - \lambda_0}{\lambda_0}\right)\right]^{7.665} - 1\right\} \quad \textbf{(3.4)}$$

where λ_0 and λ are the wavelength of the R_1 luminescence peak at atmospheric and at certain pressure, respectively.

Another way to measure the pressure inside a DAC is through the EoS of a known material used as calibrant (which is mixed with the sample to be measured) **[110]**. Generally, copper powder was employed in angle-dispersive powder XRD experiments to optimize the synchrotron measurement time. We could employ this calibrant when the Bragg reflections of copper do not overlap with the Bragg reflections of the sample, as we could observe in the Rietveld refinement of the rh-In_2O_3 at 1.2 GPa shown in **Figure 3.33**. The Bragg reflections of copper are showed with asterisk marks (*). As pressure is applied the Bragg reflections shift toward higher angles due to the decrease of the lattice parameters of the unit cell.

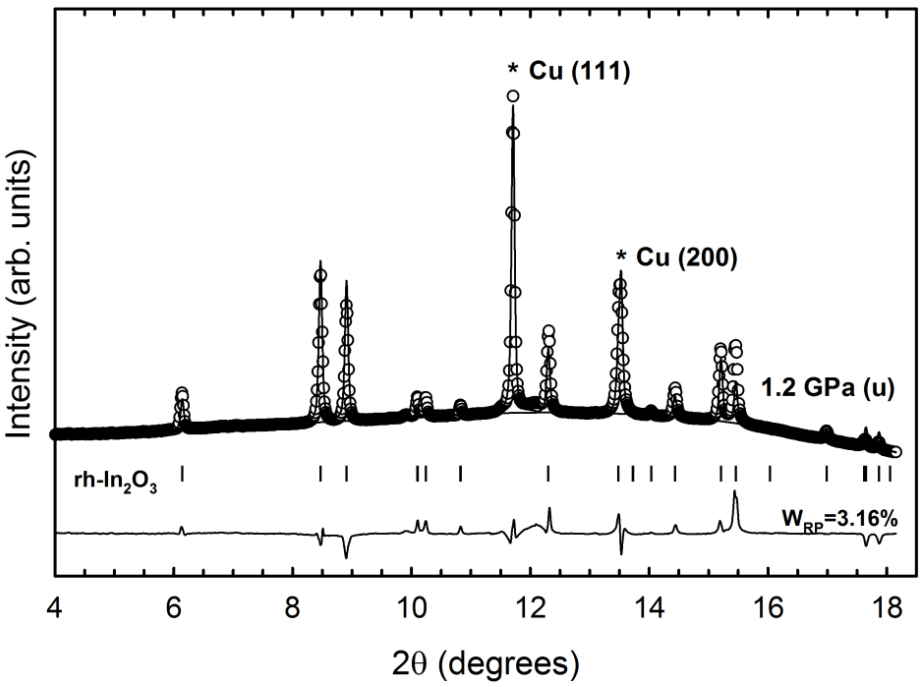

Figure 3.33: *Rietveld refinement of the experimental angle-dispersive XRD pattern was performed on upstroke (u) at 1.2 GPa. The Bragg reflections of rh-In_2O_3 structure and cubic Cu (*) was taken into account to perform the Rietveld refinement.*

3.3. Characterization of as-grown materials at ambient and extreme conditions of pressure and temperature

3.3.1. Scanning electron microscopy

The SEM is a technique used to determine the morphology and the chemical composition of the starting powder and the synthesized samples at HP-HT conditions in the micrometric and nanometric scales. The electronic microscope presents a better resolution than the optic microscope because it employs electrons (shorter wavelength compared with visible light) as radiation source.

In accordance with the Abbe equation **(3.5)**, the resolution of a microscope (r) is proportional to the wavelength of the illumination source (λ) and inversely proportional to the numerical aperture (NA)

$$r = \frac{0.612\,\lambda}{NA} \qquad \textbf{(3.5)}$$

On the one hand, the NA is a dimensionless number that characterizes the range of angles for which the optical system captures light. In the case of electronic microscope, the NA ($NA = 10^{-2} – 10^{-3}$) is several orders of magnitude lower than in the optical microscope ($NA > 1.4$). On the other hand, the wavelength associated to an accelerated electron by a potential difference can be estimated by the De Broglie relation **[116]** showed in the equation **(3.6).**

$$\lambda = \frac{h}{p} = \frac{h}{\sqrt{2m_e eV}} \qquad \textbf{(3.6)}$$

where h is the Planck's constant, p, m_e and e are the linear momentum, mass and charge of the electrons, respectively. In the SEM, the electrons are accelerated in the range from 0.2 to 30 keV. Therefore, this equipment could have a theoretical resolution of a few nanometers.

When an electron beam (primary electrons) impinges onto the surface of the sample, the electrons penetrate and diffuse into the material forming an interaction within a teardrop-shaped volume, which extends from less than 100 nm to approximately 5 μm into the surface. The penetration depth onto the material depends of the primary electrons energy, the atomic number and the density (ρ) of the material **[117]**. During the diffusion process, the primary electrons can interact as individual particles, with the atoms of the sample in an elastic or inelastic manner. In the elastic process, the primary electrons preserve their kinetic energy. This phenomenon is observed when the primary electrons are backscattered due to their

collisions with the atomic nuclei of the surface sample. However, in the inelastic process, the primary electrons give up some of its energy causing the excitation of the material. This excitation into the material can produce the emission of secondary electrons, Auger electrons, X-rays and cathodoluminescence as we can observe in **Figure 3.34**.

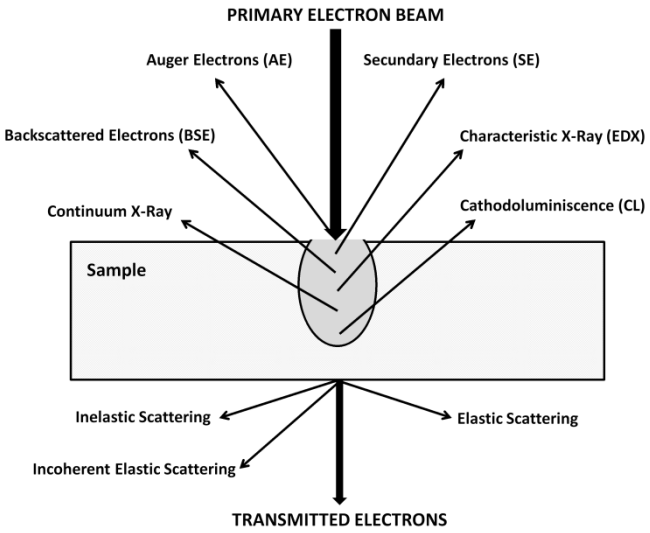

Figure 3.34: *The process involved in the interaction of the primary electrons with the sample in a SEM.*

The SEM used secondary electrons to create the image. These electrons typically have energies below 50 eV and are ejected from the k-shell of atoms which are close to the area of the surface of the material where the primary electron beam is focused. Therefore, secondary electrons give high resolution information about the topography of the surface of the sample.

The primary electrons are produced by two methods. On the one hand, it is used the thermionic emission where the cathode is heat up to certain temperature and the electrons acquire bigger energy than the work function; i.e., the energy to remove an electron from a solid. On the other hand, it is employed the field emission through the tungsten (W) and lanthanum hexaboride (LaB_6) cathodes. This method consists of circulate an intense electric current through the cathode to remove the electrons from the sample. Once the electrons are produced, they are accelerated thanks to the electric potential difference present in the microscope column. Afterwards, the electron beam is focused with the help of several electromagnetic lenses, called also condenser lenses to a spot about 0.4 to 5 nm in diameter. The SEM equipment should work in high vacuum ($\sim 10^{-6}$ torr) to reduce the electron dispersion produced by the collisions of the electrons with the air inside the apparatus. Magnetic coils were employed to perform the scanning of the electron beam onto the *x* and *y*

directions of the surface sample. Finally, the emitted secondary electrons are collected by a detector. This signal is amplified and then processed as video signal to form the image. In these devices, the collection and signal processing are synchronized with the scanning beam on the sample, being the image constructed point by point. In the SEM, the sample is placed on a carbon tape that is adhered on a metal sample holder in order to avoid charge accumulation on the surface of the sample, which can cause a deviation of the incident beam and prevent optimal image acquisition.

3.3.2. Synchrotron radiation sources

The investigation of matter under extreme conditions is one of the main issues addressed at synchrotron radiation sources. Changes in physical properties of matter may be directly correlated with changes in the distribution of the constituent atoms and interatomic distances. The determination of structural changes of materials tested at HP and HT is of great importance in various domains, like materials science and geophysics. We performed experiments in ALBA **[118]**, a third generation synchrotron light source located at Cerdanyola del Vallès in Barcelona (Spain). This large facility consists of a combination of a linear accelerator, a booster (circular accelerator) and a storage ring with insertion devices as high brilliance beam line sources. The linear accelerator and the booster accelerate electrons close to the speed of light reaching 3 GeV. The electrons are then injected into a storage ring with a perimeter of 270 metres, optimised to produce a continuum of wavelengths of electromagnetic radiation, from IR to X-rays.

3.3.2.1. Angle-dispersive powder x-ray diffraction (MSPD beamline at ALBA synchrotron)

The MSPD beamline is devoted to high-resolution powder diffraction and HP powder diffraction using DAC. Therefore, to accommodate the different experimental techniques there are two experimental end stations. The MSPD beamline operates with X-rays whose energies are between 8 and 50 keV. This energy range adequately covers the desirable range for almost any powder diffraction experiment. Moreover, it is possible to perform both total scattering experiments, and diffraction at HP, for which it is not only desirable but sometimes necessary to have X-rays with energies beyond 30 keV. Other important technical specifications of MSPD beamline are the flux at sample of approximately $4 \cdot 10^{12}$ photons/s with an energy resolution of $2 \cdot 10^{-4}$ and beam variable size at sample from 1.5 x 5 mm^2 to

15 x 15 μm^2 for high-resolution powder diffraction and HP powder diffraction experiments, respectively.

Figure 3.35 shows a schematic drawing of the beam going through the optical elements of the MSPD beamline till it reaches the HP station.

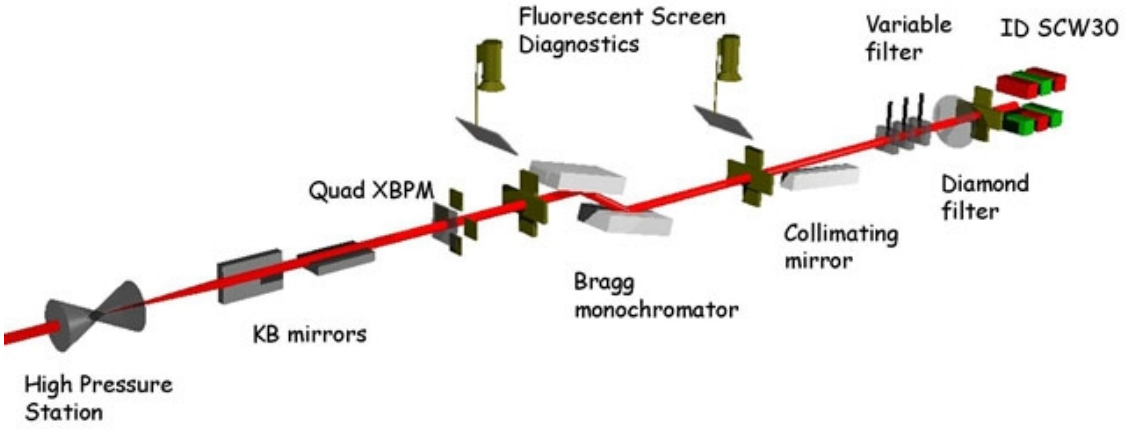

Figure 3.35: *Optical elements of the MSPD beamline* ***[119]****.*

A superconducting wiggler (SCW30) is the selected insertion device for MSPD beamline at ALBA synchrotron. It consists in a series of magnets, normally distributed in a Halbach array, designed to periodically laterally deflect a beam of charged particles inside a storage ring of a synchrotron. These deflections create a change in acceleration which in turn produces emission of broad synchrotron radiation tangent to the curve. The collimating mirror collimates the beam in a vertical direction by a mechanical bender, increasing the energy resolution. The glancing angle of the mirror is 2 mrad. It has three stripes, each one with different coatings (Pt, Rh, Si) to adapt reflectivity and harmonic suppression to be within the different energy ranges. Although the monochromator is externally water cooled, it serves to reduce the heat load on the monochromator. A Si (111) crystal monochromator was used. To preserve energy resolution and flux at the sample under high heat load, the crystals are externally cooled with liquid nitrogen. By doing this both thermal expansion is reduced as well as the conductivity of the silicon is increased compared to room-temperature values. For HP and total-scattering experiments it is important to have access to considerably high levels of energy. For this setup, the mirror can be moved to be out of the beam path. In its place, a KB-mirror system using multilayers can be inserted which serves to focus the beam on HP station. The KB-mirror is applicable in the energy range of about 20-50 keV and can also be

used together with the collimating mirror. They are placed 1.1m and 0.7m upstream from HP station on a granite table. **Figure 3.36** shows some elements of the HP station. Among them, we can appreciate a Rayonix CCD detector and a support that allows rotating the DAC to improve the quality of the angle-dispersive XRD pattern. A beam stopper is introduced between the DAC and the CCD camera to avoid the direct x-ray beam on the detector. A webcam is installed in the HP station to control the position of all experimental devices from outside of the experimental hutch with the aim of having greater control and a saving of time.

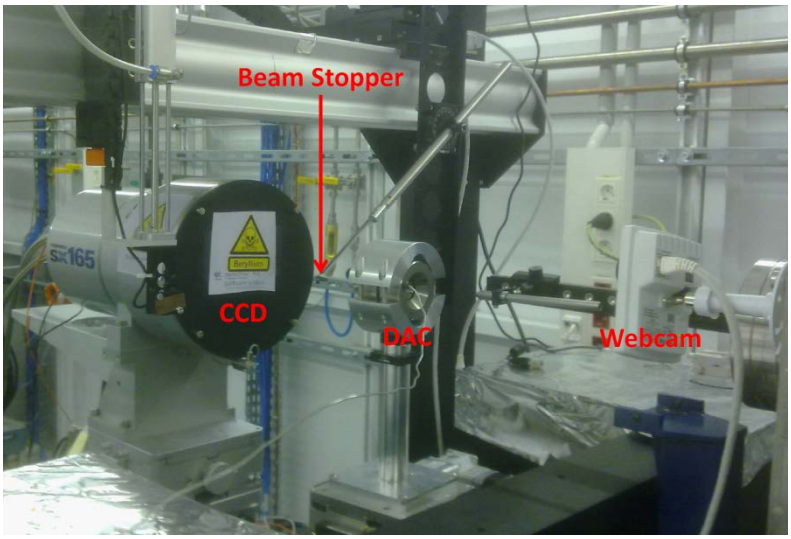

Figure 3.36: HP station at MSPD beamline in ALBA synchrotron.

Usually, lanthanum hexaboride (LaB_6) is employed to calibrate the distance between the sample and the CCD detector (refine distance). FIT2D software **[120]** is used to obtain the refined distance and to perform the integration of the 2-D diffractions images. Lattice parameters of XRD patterns were obtained with Rietveld refinements performed using POWDERCELL **[121]** and GSAS **[122]** program packages.

3.3.3. Raman Scattering

RS spectroscopy consists in the excitation of vibrations in matter with light and the collection of the inelastic signal scattered by the sample using an optical spectrometer.

The commercial equipments employed for RS measurements at ambient conditions were the Horiba Jobin-Yvon LabRam HR UV spectrometer located at the Polytechnic University of Valencia and the home-made Raman set-up available at the University of Valencia as we can see in **Figure 3.37** and **Figure 3.38**, respectively. Both equipments use a thermoelectrically cooled multichannel CCD detector with a resolution below 2 cm^{-1}. Most of the RS

measurements at ambient temperature and different pressures have been performed using the Polytechnic University of Valencia equipment.

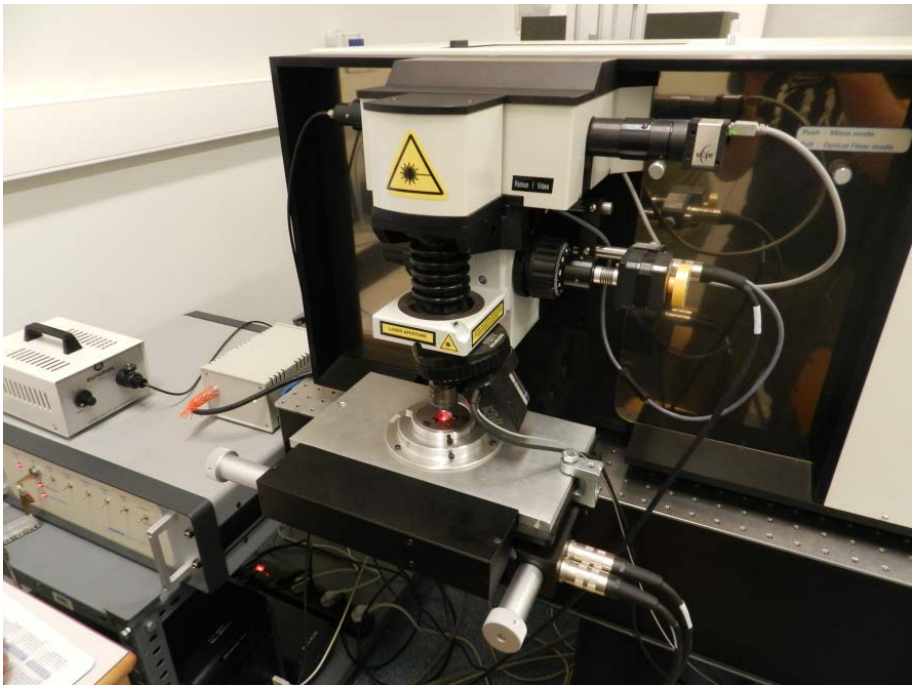

Figure 3.37: *RS equipment employed at the* Polytechnic University of Valencia

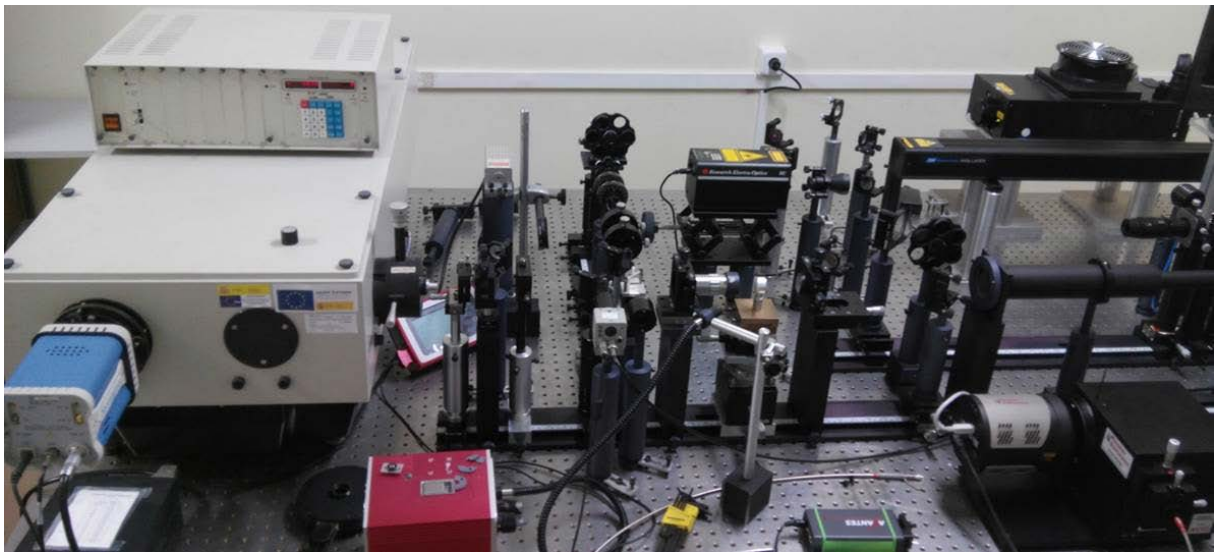

Figure 3.38: *Home-made RS equipment employed at the University of Valencia.*

Figure 3.39 shows a scheme of the instrumentation employed in a typical confocal system of micro-Raman spectroscopy like the Polytechnic University of Valencia and the University of Valencia equipment.

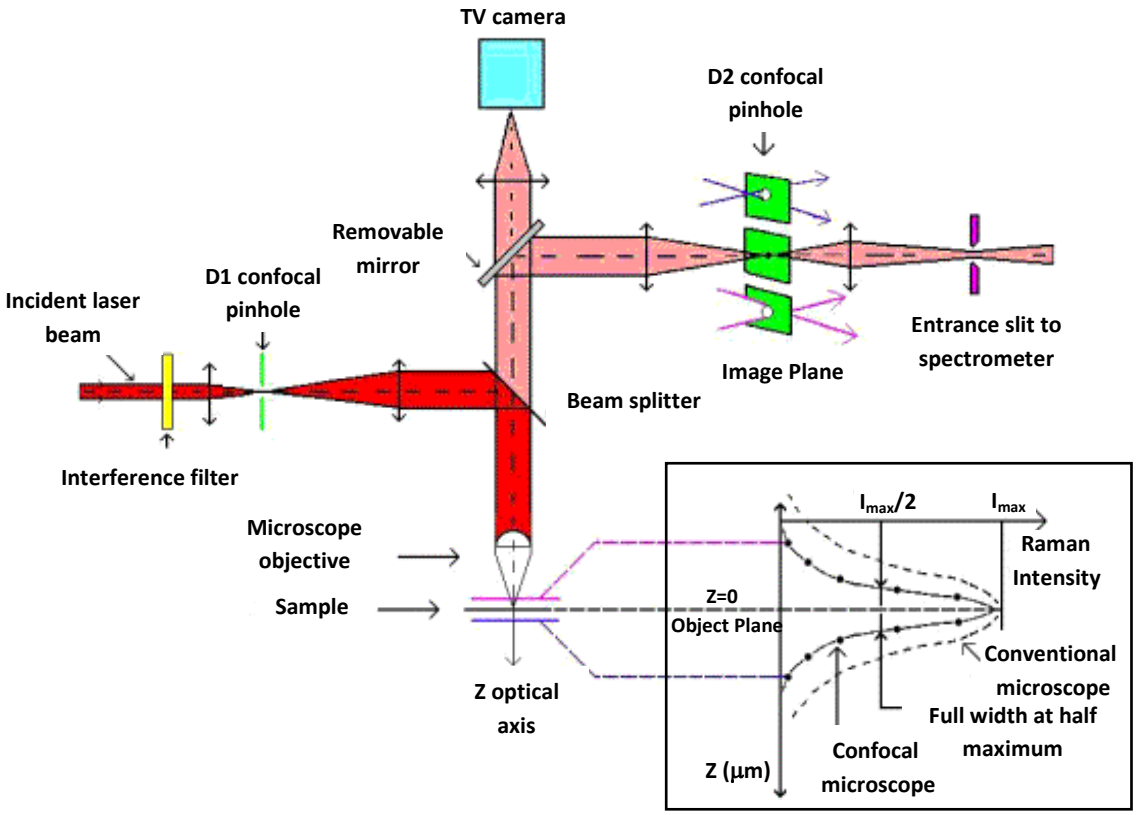

Figure 3.39: *Schematic diagram of the laser focusing, sample viewing and scattered light collection geometry usually employed in micro-Raman spectroscopy.* ***Inset*** *shows the signal collected from the focal plane and from outside the focal plane at the entrance slit of the spectrometer in the confocal set-up* **[77]**.

The samples were excited using HeNe (632.8 nm) and solid state (532 nm) lasers since a high intensity and highly monochromatic light source is needed in order to get a good signal to noise ratio in RS measurements. An interference filter is located after the gas laser in order to filter undesired laser lines present in the emitted light of almost all kind of lasers. The most recent interference filters allow laser light be monochromatized to 1-3 cm^{-1}.

In order to excite RS in a sample inside a DAC, the laser light must be focused onto the sample through the diamond windows. For that purpose, refractive microscope objectives with large or ultra-large working distance (10-30 cm) are commonly used.

The light containing the Raman signal emitted by the sample exits the DAC through the diamond windows. The configuration used is the backscattering geometry; i.e., the same microscope objective is employed both to excite and collect the Raman signal. This configuration limits the type of selection rules that can be used to study RS of compressed samples.

The light collected by the microscope objective is composed of the incident laser light reflected by the diamond windows and the sample, the elastic scattered light from the sample and the diamond window (Rayleigh signal mainly with the same wavelength of the laser), and the inelastic scattered light from the sample and the window (Raman signal with slightly different wavelengths than the incident laser light). Reflected and Rayleigh scattering light must be eliminated in order to detect the weak Raman signal. In our experimental set-up, this is performed using Edge filters. These are band filters that block all wavelengths close to the laser line and at higher energies while transmitting the Raman signal at smaller energies than the laser excitation line. Therefore, they permit observation of Stokes (long wavelengths), but not of anti-Stokes (short wavelengths) scattered light while blocking the laser line within 50 cm^{-1} from the laser line. The Raman filter is located between the removable mirror (which allows optical inspection of the sample with a camera) and the lens that focuses light into the image plane of the confocal system, as we can see in **Figure 3.39**.

In order to collect only the Raman signal coming from the focal plane of the sample a confocal microscopic setup is used. This confocal system consists of two pinhole spatial filters (D1 and D2) which allow focusing and spatially filtering the laser beam (D1) and the Raman signal (D2).

Finally, the Raman scattered light is focused onto the entrance slit of the spectrometer. As we have mentioned before, the spectrometer employed is a Horiba Jobin Yvon LabRam HR UV. The light signal is dispersed using a diffraction grating and then analysed with a multichannel detector. We used a thermoelectrically cooled multichannel CCD detector with a resolution below 2 cm^{-1} and with a high signal-to-noise ratio for the detection of weak Raman signals.

RS spectra have been analyzed by fitting Raman peaks with a Voigt profile by fixing the Gaussian line width to the experimental set-up resolution in order to obtain the three free parameters of the Lorentzian profile of the Raman-active phonon peak.

3.3.4. Optical spectroscopy

The optical properties of some rh-In_2O_3 synthesized samples were studied by absorption spectroscopy at room temperature. For this purpose, some of the as-grown or annealed crystals were polished down to about 15 μm. To carry out optical measurements we employed the equipment available at the BGI in Bayreuth. Specifically, we used a Bruker IFS 125 Fourier transform infrared spectrometer together with an all-reflecting microscope (Bruker IR

scope I). The spot size on the sample was limited to a diameter of 50 to 60 μm by an aperture in the rear focal plane of the 15-fold Cassegrain objective. Measurements were carried out from 2000 to 10000 cm^{-1} using a tungsten source, a Si-coated CaF_2 beam splitter and a narrow-band MCT detector and from 10000 to 30000 cm^{-1} using the same tungsten light source, but with a quartz beam splitter with dielectric coating and a Si diode detector. In each spectral range several hundred scans were accumulated.

3.4. Theoretical *ab initio* calculations

In an ever increasing need for the design of new materials to improve the desired properties for particular applications, modern simulations of new materials are mandatory since experiments, despite necessary to show the real properties of the material, cannot cover the whole range of possibilities with different chemical compositions and structures in a reasonable time. First principles or *ab initio* methods are modern calculations based in the well-established quantum theory and require only the a priori knowledge of the types of atoms present in the material and its approximate location in real space (structural symmetry). With this information, interactions can be calculated with the help of quantum mechanics and statistical mechanics theories so that the energy of the system can be minimized to find the properties of the ground state. Unlike empirical theories, *ab initio* methods lack adjustable parameters to experimental data, and they have predictive power, i.e. not only reproduce experimental results but also can predict them. Thanks to the great advances that have occurred recently in the field of computing, these methods of first principles have been applied to the study of complex solids.

One of the most important achievements of *ab initio* calculations is the correct description of the structural properties of a solid. Thus, it has been possible to explain the solid-solid phase transitions induced by pressure and the prediction of new solids at high pressures using only atomic numbers and atomic masses **[123]**.

The total-energy *ab initio* calculations presented in this thesis thanks to the collaboration with the professors A. Muñoz and P. Rodríguez-Hernández are mainly based on the Density Functional Theory (DFT) and the approximation of pseudopotentials. Specifically, the total energy and lattice dynamics *ab initio* calculations were performed within the framework of the density functional theory (DFT) **[124]** with the pseudopotential method and the projector augmented wave (PAW) scheme **[125]** using the first-principles code called Vienna Ab initio Simulation Package (VASP) **[126, 127]**. In this work, *ab initio* calculations have been

performed with the exchange and correlation energy evaluated either in the local-density approximation (LDA) **[128]** or in the generalized-gradient approximation (GGA) **[129]**. In the latter case, either the Perdew-Burke-Enzerhof (PBE) **[129]** or the recent Perdew-Burke-Enzerhof for solids (PBEsol) **[130]** prescriptions has been used.

Lattice-dynamics *ab initio* calculations presented in this thesis were performed at the zone center (Γ point) of the Brillouin zone (BZ) using the direct force constant (or supercell) approach **[132]**. In this method, the construction of the dynamical matrix at the Γ point of the BZ involves separate calculations of the forces in which a fixed displacement from the equilibrium configuration of the atoms within the cell is considered. Highly converged results on forces calculated in preceding total-energy *ab initio* calculations are required for an accurate calculation of the dynamical matrix. The use of crystal symmetries aids by reducing the number of independent displacements from the equilibrium configuration, and consequently the computational effort required to study the different structures considered. Diagonalization of the dynamical matrix provides both the frequencies of the normal vibrational modes, the symmetry of the modes and their polarization vectors. These results enable us to assign the Raman-active modes observed in the different structures of materials the symmetry of the modes and polarization vectors are not easily accessible in HP experiments.

Chapter 4

High-pressure lattice dynamical study of bulk and nanocrystalline In_2O_3

4.1. Abstract

The effect of pressure on the vibrational properties of bulk and nanocrystalline powders of c-In_2O_3 has been investigated at room temperature by means of RS up to 31.6 and 30 GPa, respectively. We have been able to follow the pressure dependence of up to sixteen and seven Raman modes in bulk and nanocrystalline c-In_2O_3, respectively. The experimental frequencies and pressure coefficients of the Raman-active modes of bulk cubic In_2O_3 at ambient pressure are in good agreement with those predicted by our theoretical *ab initio* calculations. Furthermore, a comparison of our experimental data with our calculations for the Raman modes in rhombohedral corundum and orthorhombic Rh_2O_3-II structures, as well as with already reported Raman modes of rh-In_2O_3 at room pressure, indicate that RS measurements provide no experimental evidence of the cubic to rhombohedral or cubic to orthorhombic phase transitions either in bulk material or in nanocrystals up to 30 GPa.

4.2. Introduction

In_2O_3 is an attractive semiconductor material that it is employed as a TCO in many industrial applications **[1, 2]** because of its wide direct (3.75 eV) and indirect (3.10 eV) band-gaps **[21, 132–134]** and its high charge-carrier mobility. Due to these characteristics, In_2O_3 has been used in several applications, like the production of solar cells **[3, 4]**, light-emitting diodes **[6–**

8], liquid-crystal displays **[11,12]** and gas sensors **[13–15]**. The improvement in performance of those applications and the development of new applications can also be envisaged in nanomaterials with controlled size and shape **[135–137]**. In this context, significant research efforts have been made for successful preparation of size-controlled In_2O_3 nanocrystals, hereafter named nano In_2O_3 **[53, 55, 56]**.

At ambient conditions, In_2O_3 crystallizes in the cubic bixbyite-type structure (space group (SG) *Ia-3*, No. 206, Z = 16) **[21, 22]**, which is common to most rare-earth sesquioxides. However, several HP phases are reported for this compound, like the rhombohedral corundum-type structure (SG *R-3c*, No. 167, Z = 6) **[25]**, the orthorhombic Rh_2O_3-II structure (SG *Pbcn*, No. 60, Z = 4) **[36]**, and the orthorhombic α-Gd_2S_3 structure (SG *Pnma*, No. 62, Z = 4) **[37]**. In the cubic, rhombohedral, and Rh_2O_3-II structures, cations are sixfold-coordinated; however, cation coordination increases to seven and eight in the α-Gd_2S_3 structure. In recent years, the rh-In_2O_3 has been synthesized at ambient conditions in a metastable way in different nanostructures and thin films **[27, 28, 30–35, 38, 41, 47–50]**. In particular, the corundum phase is expected to show better properties than the bixbyite phase, like better stability and more conductivity **[21, 51]**; therefore, it is of great interest to study the various pressure induced phases of In_2O_3.

The properties of c-In_2O_3 have been thoroughly investigated at ambient conditions. In particular, its vibrational properties in bulk as well as in thin films have been studied since the 1970s **[138–143]**. More recently, corundum-type In_2O_3 has been reported and characterized at ambient conditions by RS, evidencing the differences between the Raman-active modes of the cubic and rhombohedral phases **[28, 38, 144]**. On the other hand, the properties of In_2O_3 nanocrystals are receiving increasing attention in the last years, and recently, the vibrational properties of In_2O_3 nanostructures have started to be also investigated **[57, 58]**.

As regards the studies of bulk c-In_2O_3 under pressure, it has been reported that c-In_2O_3 retains its cubic structure till 6 GPa and 1450 ºC **[46]**; on the other hand, it has been reported that cubic In_2O_3 subjected to pressures of 6.5 GPa and temperatures between 880 and 1300 ºC result in the growth of rh-In_2O_3 when retrieved at ambient conditions **[23, 25]**. The rh-In_2O_3 has also been found by applying shock waves in the pressure range of 15–25 GPa to c-In_2O_3 **[26]**. More recently, Yusa *et al.* observed by XRD measurements the Rh_2O_3-II phase as post corundum phase in In_2O_3 at 7 GPa and 1630 ºC and the α-Gd_2S_3 phase as post-Rh_2O_3-II phase above 40 GPa and 1730 ºC **[36, 37]**. Finally, Liu *et al.* carried out both powder XRD and RS

studies up to 27.8 and 26.2 GPa, respectively. They have shown that the compound remains stable up to 15.3 GPa, when it undergoes a phase transition to the corundum structure **[52]**. On the other hand, c-In_2O_3 nanocrystals have been less studied under pressure than bulk c-In_2O_3. In particular, Qi *et al.* performed powder XRD measurements up to 40 GPa at room temperature in c-In_2O_3 nanocrystals with average size of 6 nm. They showed that c-In_2O_3 nanocrystals remain stable to 23.6 GPa, pressure at which they undergo a phase transition to the corundum structure **[53]**.

In this paper, we report RS measurements of bulk and nanocrystalline powders of c-In_2O_3 at ambient temperature. Unlike previous works, that report the existence of six Raman-active modes out of the twenty-two expected ones **[52, 142, 143]**, we show up to sixteen (seven) Raman-active modes of the cubic phase in bulk (nano) In_2O_3. Additionally, we report the pressure dependence of the Raman-active mode frequencies of the cubic phase in bulk (nano) up to 31.6 (30.0) GPa. Both the frequencies at ambient pressure and the pressure coefficients measured for the Raman-active modes of the cubic phase are in good agreement with our lattice-dynamics *ab initio* calculations in the bulk material. We will show that our RS measurements do not provide clear evidence of the cubic to rhombohedral or cubic to orthorhombic phase transitions either in bulk material or in nanocrystals up to 30 GPa.

4.3. Experimental details

Commercial c-In_2O_3 powder (99.99% pure) from Sigma-Aldrich Inc. and as-grown nanocrystals of c-In_2O_3 were used in this work. The nanocrystals of c-In_2O_3 were prepared by nonhydrolytic alcoholysis ester elimination reaction of indium acetate in a procedure similar to that reported earlier **[56]**. Starting reagents for the preparation were indium acetate, oleyl alcohol, oleic acid, and methanol. About 0.5 mg of indium acetate along with 40 ml oleyl alcohol and 2.5 ml of oleic acid were taken in a 100 ml volume three-necked flask. The reaction flask was evacuated to a vacuum level of 2 mbar and heated slowly to 100 ºC and held for 1 h. After the evacuation, the vacuum was cut off and slowly argon was introduced to the reaction flask. The reaction system was heated to 220 ºC under flowing argon atmosphere and maintained at this temperature for 4 h. The reaction solution was then cooled to 60 ºC, and excess of methanol (40 ml) was added to precipitate the nanocrystals. The precipitate was separated by centrifugation.

In_2O_3 nanocrystalline powder was characterized at ambient pressure by powder XRD collected on a Panalytical X-pert pro diffractometer using CuKα radiation **(Figure 4.1)**. All the observed reflections can be attributed to c-In_2O_3 with a unit cell parameter a = 10.1214(8) Å and unit-cell volume per formula unit V/Z = 64.806 (13) $Å^3$. The obtained unit cell parameter and unit-cell volume per formula unit are in agreement with those reported earlier in the literature **[56, 145]**. The size of crystallites of nano c-In_2O_3 was obtained from the full width at half maximum (FWHM) of the (222) Bragg peak using the Scherrer relation with a shape factor of 0.9. The average crystallite size of the nanocrystals is about 9 ± 3 nm.

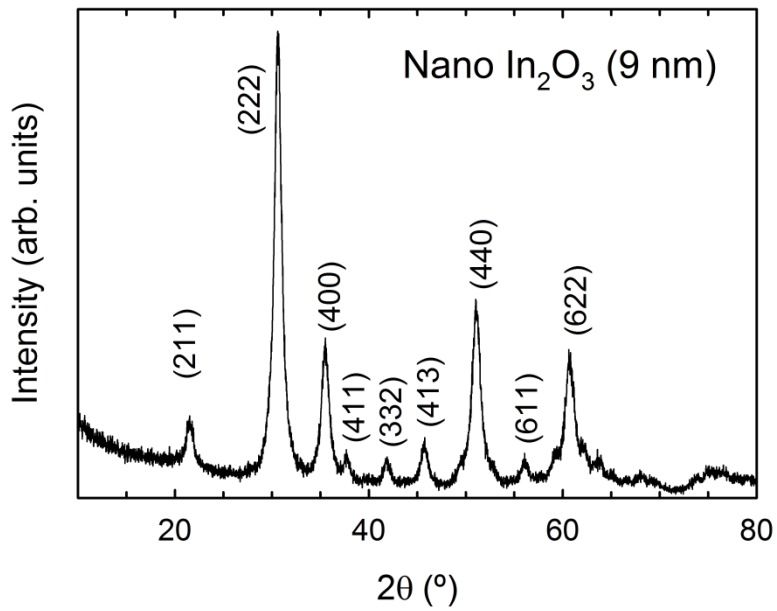

Figure 4.1: *XRD data of nanocrystalline c-In_2O_3 obtained at 1 atm.*

RS measurements were performed at room temperature in a backscattering geometry using the 632.8 nm laser line and a Horiba Jobin-Yvon LabRam HR UV spectrometer in combination with a thermoelectrically cooled multichannel CCD detector with a resolution below 2 cm^{-1}. HP Raman measurements in bulk and nanocrystalline powders of c-In_2O_3 up to 31.6 and 30 GPa, respectively, were performed in a membrane-type DAC using a 50x large working distance objective and laser power below 10 mW. We used a mixture of MEW in the proportion 16:3:1 as a quasihydrostatic PTM and a few ruby balls of about 2 μm in diameter evenly distributed in the pressure chamber as a pressure sensor. The pressure was determined using the ruby fluorescence scale **[109]**. The experimental phonons have been analyzed by fitting, when possible, Raman peaks with a Voigt profile (Lorentzian convoluted with a Gaussian) where the Gaussian linewidth (1.5 cm^{-1}) has been fixed to the experimental setup resolution.

4.4. *Ab initio* calculations details

We have performed *ab initio* total-energy calculations within the DFT **[124]** using the plane-wave method and the pseudopotential theory with the VASP **[126, 146–148]**. We have used the PAW **[125, 127]** implemented in this package to take into account the full nodal character of the all-electron charge density in the core region. Basis set including plane waves up to an energy cutoff of 520 eV were used in order to achieve highly converged results and accurate description of the electronic and dynamical properties. The description of the exchange-correlation energy was described with the GGA with the PBEsol prescription **[132]**. A dense special k-points sampling for the BZ integration was performed in order to obtain very well converged energies and forces. At each selected volume, the structures were fully relaxed to their equilibrium configuration through the calculation of the forces and the stress tensor. It allows to obtain the relax structures at the theoretical pressures defined by the calculated stress. In the relaxed equilibrium configuration, the forces on the atoms are less than 0.006 eV/Å, and the deviation of the stress tensor from a diagonal hydrostatic form is less than 1 kbar (0.1 GPa). The application of DFT-based total-energy calculations to the study of semiconductors properties under HP has been reviewed in **Ref. 123**, showing that the phase stability, electronic, and dynamical properties of compounds under pressure are well described by DFT.

We have also performed lattice dynamics calculations of the phonons at the zone center (Γ point) of the BZ. Our theoretical results enable us to assign the Raman modes observed for the different phases. Furthermore, the calculations provide information about the symmetry of the modes and polarization vectors. Highly converged results on forces are required for the calculation of the dynamical matrix. We use the direct force constant approach **[149]**. The construction of the dynamical matrix at the Γ point of the BZ is particularly simple and involves separate calculations of the forces in which a fixed displacement from the equilibrium configuration of the atoms within the primitive unit cell is considered. Symmetry aids by reducing the number of such independent displacements, reducing the computational effort in the study of the analyzed structures considered in this work. Diagonalization of the dynamical matrix provides both the frequencies of the normal modes and their polarization vectors. This allows us to identify the irreducible representation and the character of the phonons modes at the Γ point.

4.5. Results and discussion

Since the primitive cell of c-In_2O_3 contains 8 formula units, group theory predicts that this structure should have 120 vibrational modes with the following representation:

$$\Gamma = 4A_g(R) + 4E_g(R) + 14T_g(R) + 5A_u + 5E_u + 17T_u(IR) \quad \textbf{(4.1)}$$

where E and T (also noted F in the literature) modes are double and triple degenerated, the 22 gerade (g) modes are Raman-active (R) modes, 16 T_u modes are infrared (IR)-active modes, the A_u and E_u are silent modes, and one T_u mode corresponds to acoustic vibrations.

Figures 4.2 (a) and **(b)** show unpolarized Raman spectra at room temperature in bulk and nano c-In_2O_3, respectively. Unlike previous works where a maximum of seven Raman modes (109, 135, 305, 366, 495, 513, and 629 cm^{-1}) have been observed **[52, 58, 142, 143]**; we have observed up to sixteen Raman-active modes of bulk c-In_2O_3 powder at room conditions. The Raman spectrum is dominated by the stretching mode at 131 cm^{-1} and by the broad mode at 306 cm^{-1}.

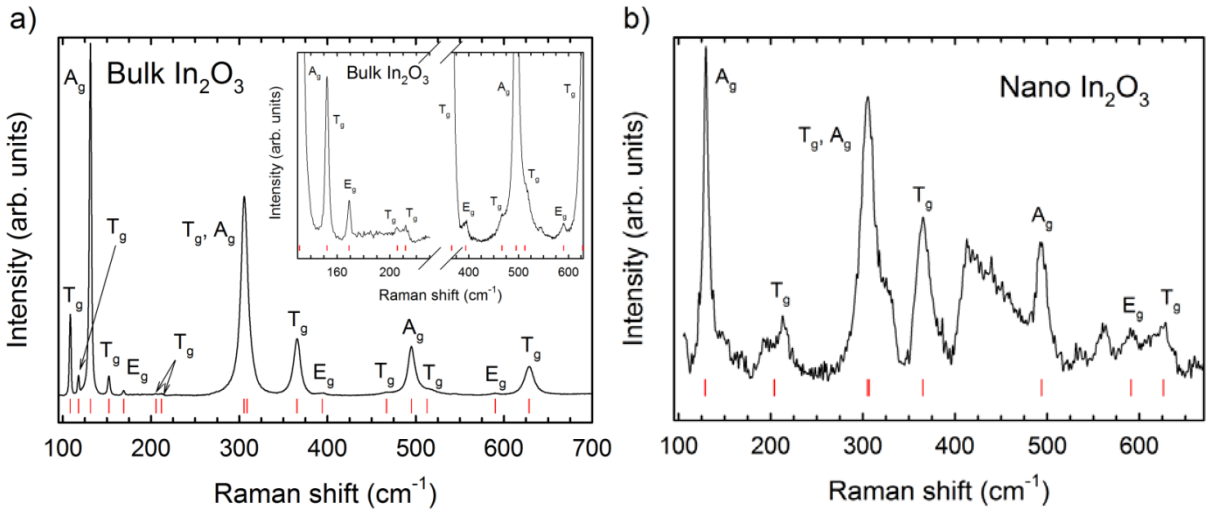

Figure 4.2: (a) *Unpolarized RS spectrum of bulk c-In_2O_3 at room conditions. Inset: Show the spectral regions with smaller intensity Raman modes.* ***(b)*** *Unpolarized RS spectrum of c-In_2O_3 nanocrystal. Vertical red lines show the theoretically predicted Raman-mode frequencies at room pressure for bulk c-In_2O_3 that have been observed experimentally.*

Table 4.1 summarizes the zero-pressure experimental frequencies and pressure coefficients of the Raman-active modes in bulk and nano c-In_2O_3. Our frequencies at ambient pressure are in good agreement with the theoretical frequencies of the Raman-active modes obtained from our *ab initio* calculations and with the Raman-active modes already reported in the literature

[58, 138, 142, 143]. Furthermore, thanks to our *ab initio* calculations we have assigned the symmetry of the different observed Raman modes [see **Figure 4.2 (a)** and **(b)**]. As regards nano c-In_2O_3, only seven modes have been clearly observed at ambient pressure. Their frequencies are rather close to those of bulk c-In_2O_3, as can be seen in **Table 4.1**, since our nanoparticles have around 9 nm and phonon confinement effects are likely negligible for particles above 4 nm **[150]**.

Raman modes of c-In_2O_3

	***Ab initio* calculations**			**In_2O_3 bulk powder**			**Nanocrystals of In_2O_3**			**Literature**
Mode (Sym)	ω_0 (cm^{-1})	$\frac{\partial\omega}{\partial P}$ $\left(\frac{cm^{-1}}{GPa}\right)$	$\frac{\partial^2\omega}{\partial P^2}$ $\left(\frac{cm^{-1}}{GPa^2}\right)$	ω_0 (cm^{-1})	$\frac{\partial\omega}{\partial P}$ $\left(\frac{cm^{-1}}{GPa}\right)$	$\frac{\partial^2\omega}{\partial P^2}$ $\left(\frac{cm^{-1}}{GPa^2}\right)$	ω_0 (cm^{-1})	$\frac{\partial\omega}{\partial P}$ $\left(\frac{cm^{-1}}{GPa}\right)$	$\frac{\partial^2\omega}{\partial P^2}$ $\left(\frac{cm^{-1}}{GPa^2}\right)$	ω_0 (cm^{-1})
Tg	106 (1)	0.01 (1)	-0.008 (2)	108 (1)	0.07 (3)	-0.006 (2)				109[a]
Tg	114 (1)	0.3 (1)	-0.006 (2)	118 (1)	0.4 (1)	-0.009 (3)				
Ag	128 (1)	0.8 (1)	-0.009 (3)	131 (1)	1.0 (1)	-0.02 (1)	129 (2)	1.2 (1)	-0.03 (1)	131,[b] 135[a, b]
Tg	148 (1)	1.2 (1)	-0.01 (1)	152 (1)	1.4 (1)	-0.02 (1)				
Eg	165 (1)	1.1 (1)	-0.008 (2)	169 (1)	0.8 (1)					
Tg	199 (1)	1.8 (1)	-0.02 (1)	205 (3)	1.3 (1)					
Tg	204 (1)	1.5 (1)	-0.01 (1)	211 (3)	3.0 (2)					
Tg	302 (2)	2.2 (2)	-0.01 (1)	306 (2)	2.4 (2)	-0.03 (1)	306 (3)	2.5 (2)	-0.03 (1)	306,[b, c] 307,[a, b] 308[d]
Ag	302 (2)	3.1 (2)	-0.03 (1)	306 (2)	4.0 (3)	-0.06 (2)	307 (3)	3.3 (2)	-0.02 (1)	
Eg	308 (2)	3.1 (2)	-0.02 (1)							
Tg	312 (2)	2.6 (2)	-0.02 (1)							
Tg	356 (3)	3.9 (3)	-0.03 (1)	365 (2)	4.3 (3)	-0.06 (2)	365 (5)	4.9 (3)	-0.08 (3)	365,[b, d, e] 366,[a, c]
Tg	379 (3)	3.9 (3)	-0.03 (1)							
Eg	385 (3)	3.6 (3)	-0.02 (1)	396 (4)	3.3 (2)					
Tg	438 (3)	3.0 (3)	-0.02 (1)							
Tg	447 (3)	4.3 (3)	-0.03 (1)	467 (4)						
Ag	476 (4)	3.4 (3)	-0.02 (1)	495 (2)	3.7 (3)	-0.04 (1)	494 (3)	3.8 (2)	-0.03 (1)	495,[a, b, c] 496,[b] 504,[d]
Tg	499 (4)	5.0 (3)	-0.03 (1)	513 (4)						
Tg	520 (4)	4.7 (3)	-0.02 (1)							
Eg	565 (4)	5.2 (3)	-0.03 (1)	590 (4)	5.2 (4)		591 (6)	3.1 (4)		
Ag	576 (4)	5.4 (3)	-0.03 (1)							602[b]
Tg	600 (4)	5.4 (3)	-0.03 (1)	628 (2)	6.0 (2)	-0.09 (3)	626 (6)	5.4 (4)		627,[b] 628,[e] 630,[c] 631,[a] 637,[d]

[a]*Reference 58.* [b]*Reference 143.* [c]*Reference 142.* [d]*Reference 138.* [e]*Reference 57.*

Table 4.1: *Experimental Raman-mode frequencies at room pressure and their pressure coefficients in bulk and nanocrystalline cubic In_2O_3. Experimental parameters have been obtained by fitting measured data to linear $\omega = \omega_0 + \left(\frac{d\omega}{dP}\right)P$ or quadratic $\omega = \omega_0 + \left(\frac{d\omega}{dP}\right)P + \left(\frac{d^2\omega}{dP^2}\right)P^2$ expressions. Theoretical Raman-mode frequencies at room pressure and their pressure coefficients in bulk cubic In_2O_3 along with previously reported Raman-mode frequencies at room pressure are also shown for comparison.*

On the one hand, **Figures 4.3 (a)** and **(b)** show selected Raman spectra of bulk c-In_2O_3 at different pressures and the pressure dependence of the Raman mode frequencies up to 31.6 GPa, respectively.

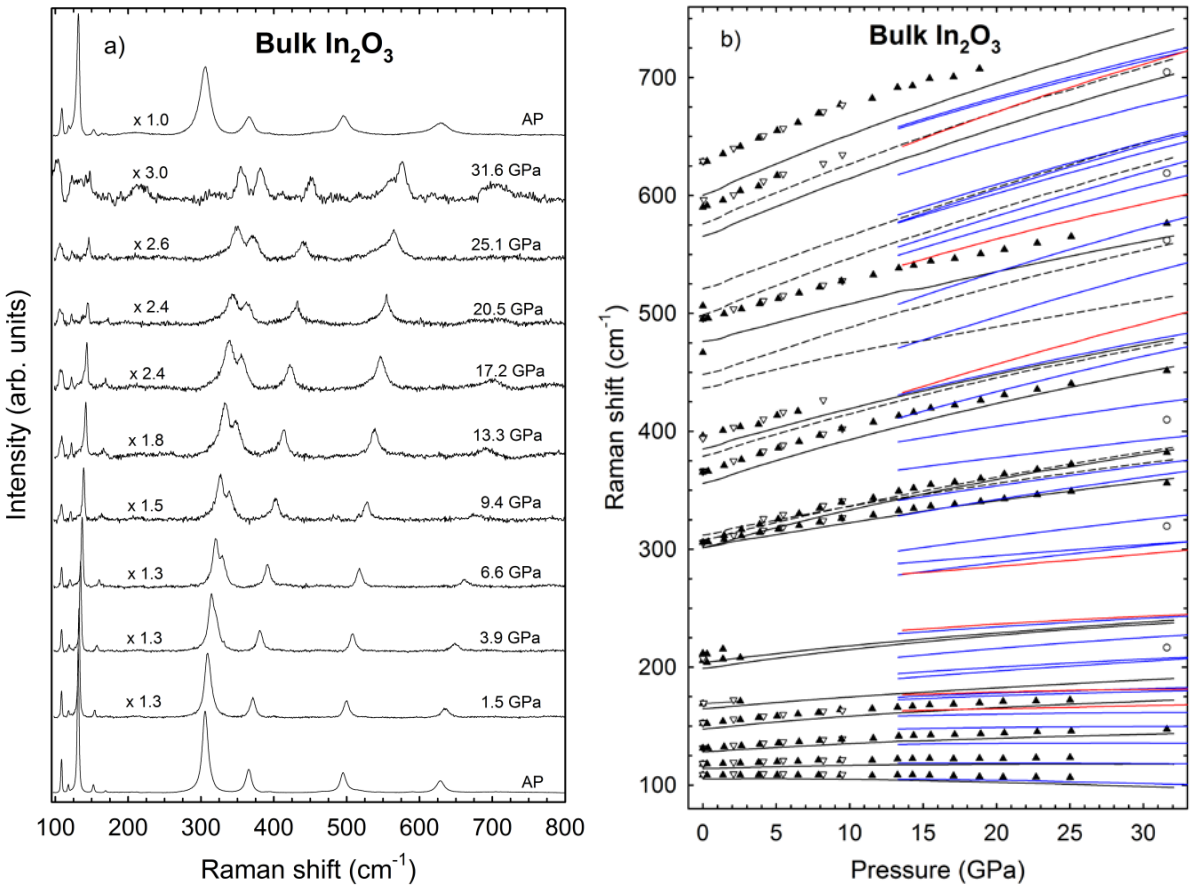

Figure 4.3: (a) *Selected Raman spectra of bulk c-In_2O_3 at different pressures up to 31.6 GPa.* ***(b)*** *Pressure dependence of the Raman-mode frequencies of bulk c-In_2O_3. Symbols correspond to experimental data. Filled (empty) black triangles up (down) correspond to upstroke (downstroke). Empty circles correspond with new peaks observed at 31.6 GPa, not related to the cubic phase. Black solid (dashed) lines represent theoretical data for observed (not observed) Raman-active modes in bulk cIn_2O_3. Red (blue) lines are theoretical data for Raman-active modes of the rhombohedral corundum (orthorhombic Rh_2O_3-II) phase in bulk In_2O_3.*

On the other hand, **Figures 4.4 (a)** and **(b)** show selected Raman spectra of nano c-In_2O_3 at different pressures and the pressure dependence of the Raman mode frequencies up to 30 GPa, respectively. When comparing **Figures. 4.3 (a)** and **4.4 (a)** one can appreciate that the Raman spectra of bulk c-In_2O_3 have better quality than that of nano c-In_2O_3. In both bulk and nano c-In_2O_3, all Raman-active mode frequencies increase with pressure in a monotonous way till the maximum pressure attained in the experiment. Therefore, apparently no phase transition seems to occur neither in bulk nor in nano c-In_2O_3 up to 30 GPa. Furthermore, on

releasing pressure, the Raman spectrum of bulk c-In_2O_3 is similar to the initial one but with peaks slightly broadened. A similar Raman spectrum, but with less defined features was obtained in the recovered sample of nano c-In_2O_3 at room pressure. It can be also observed that the peak widths of the Raman modes in the nanocrystalline sample are much larger than in the bulk leading to a possible overlapping of several Raman-active modes.

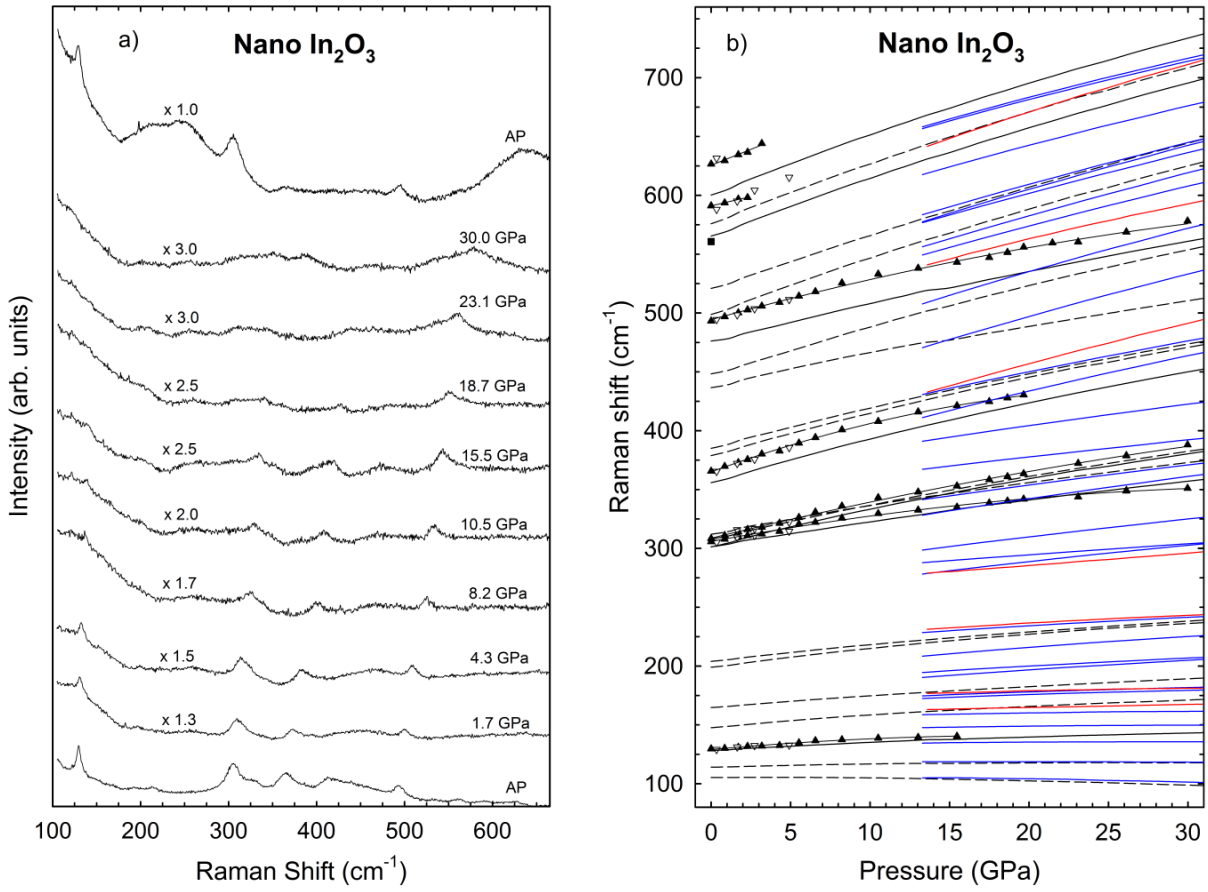

Figure 4.4: ***(a)*** *Selected Raman spectra of c-In_2O_3 nanocrystals at different pressures up to 30 GPa.* ***(b)*** *Pressure dependence of the Raman-mode frequencies of c-In_2O_3 nanocrystals. Symbols correspond to experimental data. Filled (empty) black triangles up (down) correspond to upstroke (downstroke). Filled black square (around 560 cm^{-1}) do not corresponds to a first-order Raman mode. Black solid (dashed) lines represent theoretical data for observed (not observed) Raman-active modes in bulk c-In_2O_3. Red (blue) lines are theoretical data for Raman-active modes of the rhombohedral corundum (orthorhombic Rh_2O_3-II) phase in bulk In_2O_3.*

Figures 4.3 (b) and **4.4 (b)** show the experimental pressure dependence of the first-order Raman-active mode frequencies for bulk and nano c-In_2O_3, respectively. These figures also include the theoretical pressure dependence of the Raman-active modes in the bulk bixbyite phase for comparison. As observed, most of the Raman modes exhibit a non-linear blue-shift with pressure which is also in good agreement with our *ab initio* calculations up to the highest

pressure attained in these experiments. Most of the Raman modes show a sublinear dependence of the frequency vs. pressure till 30 GPa, which is not observed when frequency is plotted vs. the relative volume variation, $\Delta V/V_0$, as we could observe in **Figure 4.5**. This result suggests that the Grüneisen parameter of the Raman modes in c-In_2O_3 is almost constant along the pressure range between ambient pressure and 30 GPa. Therefore, this means that there is no change in the force of the bondings what suggests that there is no charge redistribution between In and O atoms up to 30 GPa. Additionally, it can be appreciated that all the calculated frequencies are slightly underestimated due to the underestimation of the cohesion energy in the GGA approximation. The underestimation of experimental frequencies by GGA calculations is less than 5%; therefore, higher frequencies show larger experimental-theoretical differences than lower frequencies **[151]**. On the basis of the comparison of our experimental and theoretical frequencies, we propose that the peaks of the Raman-active modes centred at 395.8 and 589.7 cm^{-1} should have E_g symmetry [see **Figure 4.2 (a)**]. Similarly, the symmetry proposed for the Raman-active mode in c-In_2O_3 nanocrystals centred in 591.1 cm^{-1} is also E_g [see **Figure 4.2 (b)**].

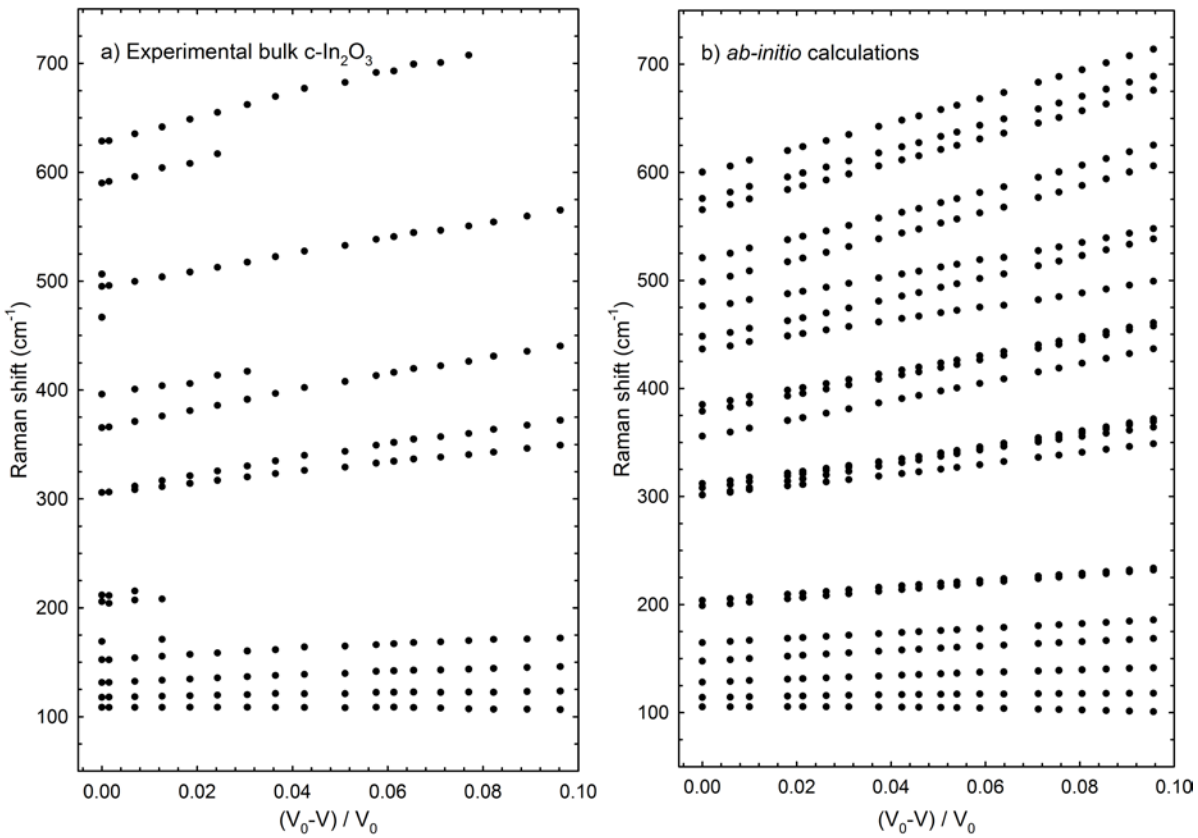

Figure 4.5: *Experimental (a) and theoretical (b) Raman modes evolution as a function of the relative volume variation in bulk c-In_2O_3.*

An interesting feature of the Raman spectra of bulk c-In_2O_3 is the splitting of the broad peak near 306 cm^{-1} into two peaks, observed for pressures above 1.5 GPa. The broadening of this peak is evident in the Raman spectrum at 3.9 GPa [see **Figure 4.3 (a)**]. According to our calculations up to four Raman-active modes should appear in the region near 300 cm^{-1} for the c-In_2O_3. Note that out of the four predicted Raman modes in this region, three have similar pressure coefficients while the lowest in frequency has a smaller pressure coefficient (see **Figure 4.3 (b)** and **Table 4.1**). Therefore, we ascribe the splitting observed above 1.5 GPa to two Raman-active modes of the cubic phase almost degenerate in frequency at room pressure that have very different pressure coefficients. In nano c-In_2O_3 [**Figure 4.4 (b)**], the splitting of the broad peak at 306 cm^{-1} was observed above 4 GPa; i.e., later than for bulk c-In_2O_3. A possible explanation for this behavior could be the larger overlapping of the two modes near 306 cm^{-1} in nanocrystals compared to the bulk, which prevents the observation of this splitting at smaller pressures.

In a previous work, Liu *et al.* observed the splitting of the modes near 306 cm^{-1} above 12.2 GPa and attributed it to the onset of a phase transition from the cubic bixbyite-type to the rhombohedral corundum-type structure **[52]**. With this interpretation, their HP RS data matched with the observation of a new XRD peak above 15.3 GPa that they attributed to the rhombohedral phase. Furthermore, both experimental results seemed to agree with prior theoretical predictions that considered that a cubic-to-rhombohedral phase transition could be observed in In_2O_3 above 3.8 GPa **[21]**. Curiously, the observation of the cubic-to-rhombohedral phase transition was also claimed in a recent paper both on bulk and 6-nm-size nanocrystals **[53]**. However, our theoretical calculations do not predict the cubic-to-rhombohedral phase transition up to around 15 GPa in good agreement with previous calculations of Gurlo *et al.* **[41]**. Furthermore, in agreement with Gurlo *et al.*, we have found that our calculations predict the cubic-to-orthorhombic Rh_2O_3-II phase transition to occur at pressures even lower than those for the cubic-to-rhombohedral transition; however, no report for the cubic-to-orthorhombic pressure-induced phase transition has been claimed at room temperature to our knowledge. Therefore, we consider that the splitting of the two Raman modes near 306 cm^{-1} as pressure increases does not constitute an evidence of the phase transition of In_2O_3 from the cubic-to-rhombohedral phase transition since this splitting is expected for two degenerate modes of the cubic phase at ambient pressure according to our *ab initio* calculations.

A curious feature of the Raman spectra of bulk c-In_2O_3 at different pressures is that, despite there is a general decrease of intensity of the Raman modes with increasing pressure, there is an increase of the relative peak intensity of the peak at 495 cm^{-1} with respect to the most intense A_g peak near 105 cm^{-1}. This behaviour is in contrast with that of other peaks that decrease in intensity or even disappear at low pressures. It can be noted that a broad band appears as a shoulder in the low-frequency side of the 495 cm^{-1} peak above 9.4 GPa. In fact, similar broad bands, but less clearly observed, are also developed above 9.4 GPa in the low-frequency side of the peaks at 306 and 365 cm^{-1}. Similar broad bands were already reported by Liu *et al.* above 12.8 GPa and were attributed to the onset of a phase transition to the rhombohedral phase with some disorder, as it was previously observed in corundum-type Ga_2O_3 **[152]**. However, we must highlight that these bands do not correspond to Raman-active modes predicted by our theoretical calculations neither for the cubic phase nor for the rhombohedral or orthorhombic phases. Furthermore, we must note that neither our Raman spectra nor those obtained by Liu *et al.* above 15 GPa resemble to those measured for the rhombohedral phase of In_2O_3 at ambient pressure **[28, 38]**. Therefore, on the basis of our RS measurements, our lattice dynamics calculations and the experimental evidence of Raman modes of the rhombohedral phase at ambient conditions, we cannot confirm either the cubic-to-rhombohedral or the cubic-to-orthorhombic phase transitions below 30 GPa but just the existence of some features that suggest the onset of a phase transition to an unknown structure.

Taking into account *ab initio* calculations, one could explain the observation of two XRD peaks near 6.4º and 9º above 15 GPa in both bulk and nanocrystals **[52, 53]** and the absence of new Raman modes around that pressure by invoking that they are signs of the onset of a phase transition to the rhombohedral phase. However, a rather high kinetic barrier occurs for the cubic-to-rhombohedral or cubic-to-orthorhombic phase transitions **[153, 154]**. In fact, data of previous authors show that the phase transition is far from complete even at 30 GPa **[52, 53]**. In this sense, high kinetic barriers would allow the cubic phase being present at least till 30 GPa. Additionally, if the polarizability of the corundum phase is smaller than that of the cubic phase, the RS of the corundum phase could be of smaller intensity than that of the cubic phase and this would explain the absence of Raman-active modes of the corundum phase above 15 GPa while XRD peaks of the HP phase are observed above that pressure.

Finally, we have to mention that several new Raman peaks are observed in the spectrum of bulk In_2O_3 at 31.6 GPa whose frequencies are plotted in **Figure 4.3 (b)** with open circles.

These peaks are too weak to be clearly identified with any possible HP phase; however, they indicate that, as far as RS concerns, the phase transition seems to take place above 30 GPa. We need to reach higher pressures to shed more light on the nature of the pressure-induced phase transitions in c-In_2O_3 at room temperature.

4.6. Conclusions

We report an accurate Raman spectrum at room conditions of bulk c-In_2O_3, showing up to sixteen Raman-active modes. Thanks to *ab initio* calculations we have been able to assign the symmetry of most of the observed Raman-active modes in bulk and nanocrystalline c-In_2O_3. We have also reported the pressure dependence of the Raman-active mode frequencies in both bulk and nanocrystalline c-In_2O_3 up to 31.6 and 30 GPa, respectively. The pressure dependence of the experimental Raman modes shows a considerable non-linear pressure dependence that matches with the theoretical predictions. We have found no clear sign of a phase transition to the rhombohedral corundum-type structure neither in the bulk nor in the nanocrystals of c-In_2O_3 till 30 GPa. Instead, we have found a considerable broadening of some Raman modes above 15 GPa that could be indicative of the onset of a phase transition. New modes appear in the Raman spectrum of bulk In_2O_3 above 30 GPa that seem to indicate that the phase transition occurs above this pressure in this compound at room temperature.

Chapter 5

Pbca-type In_2O_3: The high-pressure post-corundum phase at room temperature

5.1. Abstract

HP powder XRD and RS measurements in c-In_2O_3 have been performed at room temperature. On increasing pressure c-In_2O_3 undergoes a transition to the orthorhombic Rh_2O_3−II structure and on decreasing pressure Rh_2O_3−II-type In_2O_3 undergoes a transition to a previously unknown phase with *Pbca* space group which is isostructural to Rh_2O_3−III. On further decrease of pressure, we observed a phase transition to the metastable rhombohedral corundum-type In_2O_3 near room conditions. Recompression of the metastable corundum-type In_2O_3 at room temperature leads to a transition to the Rh_2O_3−III phase, thus showing that the Rh_2O_3−III phase is the post-corundum phase at room temperature. Our results are supported by theoretical *ab initio* calculations. Furthermore, they show that the Rh_2O_3−III phase could be present in other sesquioxides, thus prompting to a revision of the pressure−temperature phase diagrams of sesquioxides.

5.2. Introduction

In_2O_3 is an attractive sesquioxide employed as a gas sensor **[13, 14, 155]**, in thermoelectrics **[156, 157]**, and in particular, when doped with Sn or F, as a TCO in many optoelectronic

applications including solar cells, light-emitting diodes, and liquid-crystal displays **[5, 8, 12, 158]**. In_2O_3 crystallizes in the cubic bixbyite (C-type) structure (SG *Ia-3*, No. 206, Z = 16) and for many years it was known in another metastable structure at ambient conditions, the rhombohedral corundum-type structure (SG *R-3c*, No. 167, Z = 6) which was obtained after application of extreme conditions of pressure and temperature **[23, 25, 26]**.

The discovery of the post-perovskite ($CaIrO_3$) phase **[159]** in $MgSiO_3$ led to a major revision of the pressure-temperature phase diagrams in many ABO_3 compounds including sesquioxides ($A = B$). Theoretical works in In_2O_3 analyzed several structures and suggested the existence of the post-perovskite phase **[21, 160]**, which, consequently, triggered considerable experimental efforts in order to find this phase at HP-HT **[36, 37, 40, 41, 43]**. Noteworthy, experiments showed that the post-perovskite phase is not stable at HP in In_2O_3. Instead, two new HP phases were discovered: the orthorhombic Rh_2O_3−II (SG *Pbcn*, No. 60, Z = 4), and the orthorhombic α-Gd_2S_3 phase (SG *Pnma*, No. 62, Z = 4) **[36, 37, 40, 41, 43]**. This last phase was initially unexpected and theoretical calculations showed that it was predicted to be the more stable phase **[37]** at pressures beyond 35 GPa. Hereafter, the cubic, rhombohedral, Rh_2O_3−II and α-Gd_2S_3 phases of In_2O_3 will be named c-In_2O_3, rh-In_2O_3, o1-In_2O_3, and o2-In_2O_3, respectively.

Recently, several attempts have been performed in order to obtain in a metastable way o1-In_2O_3 at room conditions by means of HP and HT treatments **[40, 41, 43]**, and a theoretical work has recently commented on the possible applications of o1-In_2O_3 **[54]**. HT have systematically been used in these experimental HP studies in order to induce phase transitions delayed or even impeded in In_2O_3 at room temperature due to the presence of kinetic effects **[36, 37, 40, 41, 43, 45]**. In the last years, HP studies of In_2O_3 at room temperature have also been reported yielding some contradictory results **[52, 53, 161]**. A phase transition from c-In_2O_3 to rh-In_2O_3 between 12 and 25 GPa in bulk and nanocrystalline In_2O_3 was reported **[52, 53]**, whereas no sign of phase transition up to 30 GPa neither in bulk nor in nanocrystalline c-In_2O_3 was found in the latest work **[161]** in good agreement with previous results **[40]**.

These contradictory results at HP and room temperature have motivated us to perform a much deeper study of the polymorphism of In_2O_3 at room temperature up to higher pressures (50 GPa) with both powder XRD and RS measurements. Our work shows that on increasing pressure c-In_2O_3 undergoes a phase transition to o1-In_2O_3 at room temperature without undergoing a phase transition to rh-In_2O_3. Furthermore, on decreasing pressure we find that

o1-In_2O_3 undergoes a phase transition to a previously unknown structure of In_2O_3, the orthorhombic Rh_2O_3−III phase **[162]** (SG *Pbca*, No. 61, Z = 8), hereafter named o3-In_2O_3, prior to the phase transition to rh-In_2O_3, which is the metastable phase at room conditions. Our theoretical *ab initio* calculations suggest that o3-In_2O_3 (see **Figure 5.1**) is competitive in a certain range of pressures with c-In_2O_3, rh-In_2O_3, and o1-In_2O_3. These phases were already theoretically simulated by several authors who did not consider o3-In_2O_3 **[37, 44]**.

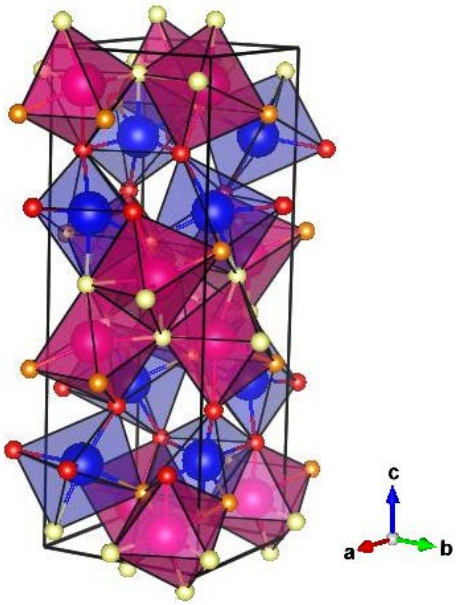

Figure 5.1: *Orthorhombic Pbca-type In_2O_3 (o3-In_2O_3). Blue and pink atoms represent the two inequivalent In atoms, while red, yellow, and orange atoms represent the three inequivalent O atoms. InO_6 octahedra are shown in the figure.*

5.3. Experimental section

c-In_2O_3 powders of high purity (99.99%) were commercially obtained from Sigma-Aldrich Inc. However, rh-In_2O_3 powders were obtained on downstroke from c-In_2O_3 powders pressurized to 50 GPa at room temperature.

HP angle-dispersive powder XRD experiments at room temperature up to 50 GPa for c-In_2O_3 and up to 25 GPa for rh-In_2O_3 were conducted in a membrane-type DAC. Either a 16:3:1 MEW mixture or He gas were used as quasihydrostatic PTM. Pressure inside the DAC was estimated from the EoS of copper **[110]**. Experiments were performed at the BL04-MSPD beamline of the ALBA synchrotron **[118]** with an incident monochromatic wavelength of 0.4246 Å focused to 20 × 20 μm. No pinhole was used to cut the X-ray beam tail what explains the presence of the gasket in our XRD patterns. Images covering a 2θ range up to 15°

were collected using a SX165 CCD located at 270 mm from sample. One-dimensional diffraction profiles of intensity as a function of 2θ were obtained by integration of observed intensities with the Fit2D software **[120]**. Lattice parameters of powder XRD patterns were obtained with Rietveld refinements performed using POWDERCELL **[121]** and GSAS **[122]** program packages.

RS measurements at room temperature excited either with 532.0 or with 632.8 nm laser lines and laser power below 10 mW were performed in a backscattering geometry using a Horiba Jobin-Yvon LabRam HR UV spectrometer in combination with a thermoelectrically cooled multichannel CCD detector (resolution below 2 cm^{-1}). HP RS measurements in bulk power of c-In_2O_3 up to 50 GPa and of rh-In_2O_3 up to 33 GPa were performed inside the DAC. A 16:3:1 MEW mixture was used as a PTM and a few ruby balls of about 2 μm in diameter evenly distributed in the pressure chamber were employed as a pressure sensor **[109]**.

Ab initio total-energy calculations were performed within the DFT using the plane wave method and the pseudopotential theory with the VASP **[126, 146−148]**. Lattice-dynamics calculations of the phonons at the zone center (Γ point) of the BZ were performed using the direct force constant approach. The reader can consult **Ref. 161** for further theoretical details.

5.4. Results and discussion

Powder XRD patterns on the upstroke up to 50 GPa (**Figure 5.2 (a)**) can be clearly indexed below 35 GPa with the Miller indexes of the Bragg reflections for c-In_2O_3 (see Rietveld refinement of the XRD pattern at 1.7 GPa with R_{wp} = 3.5% in **Figure 5.3**). The onset of a HP phase transition starts above 35.1 GPa. This phase transition is completed above 46 GPa and the XRD pattern fully corresponds to o1-In_2O_3 (see XRD pattern at 50.1 GPa in **Figure 5.3**). This result is in good agreement with references **[36, 37, 40, 41, 43, 45]** and in disagreement with references **[52, 53]**. Note that at 50.1 GPa there is a large experimental broadening of the XRD peaks, likely due to the poor crystalline quality of the *Pbcn*-type phase at HP and room temperature. The peaks obtained by Le Bail refinement agree with the position of the experimental Bragg features, but the difference between the widths of both of them causes a big mismatch in the difference spectrum, as we can clearly observe by comparison.

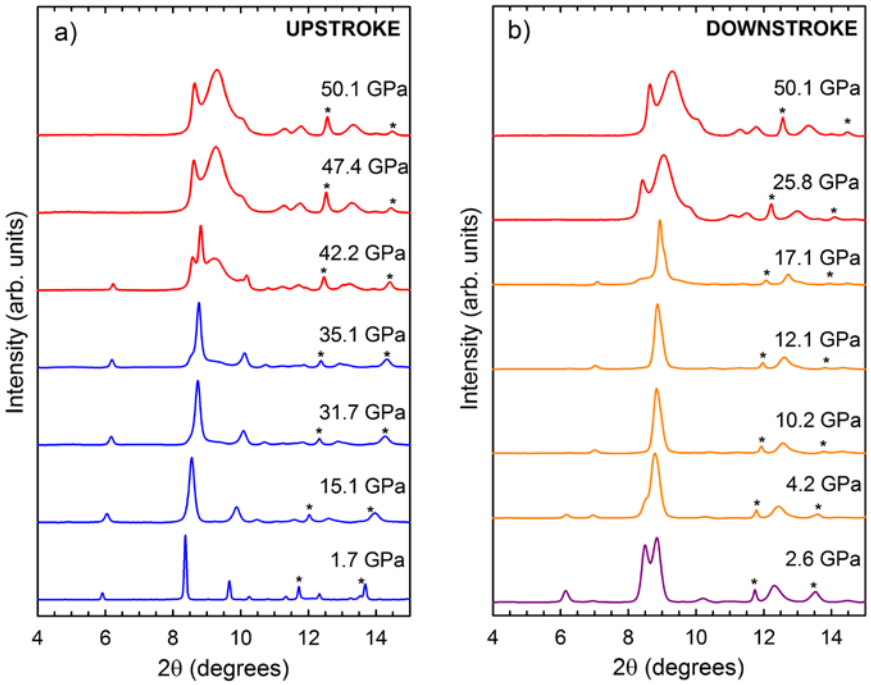

Figure 5.2: *Room temperature XRD powder patterns of c-In_2O_3 at selected pressures with helium as PTM on upstroke up to 50 GPa (a) and on downstroke down to 2.6 GPa (b). Colours indicate the XRD patterns with mainly c-In_2O_3 (blue), o1-In_2O_3 (red), o3-In_2O_3 (orange), and rh-In_2O_3 (violet) phases. Asterisks denote the diffraction maxima of copper at each pressure.*

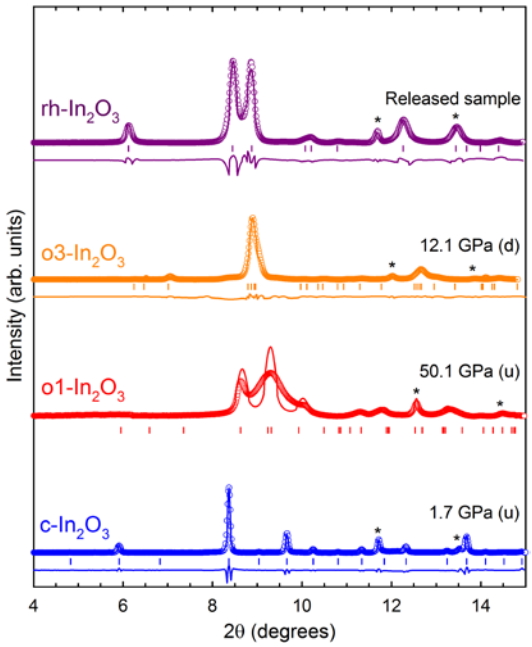

Figure 5.3: *Refinements of the experimental XRD patterns on upstroke (u) at 1.7 GPa with the c-In_2O_3 structure and at 50.1 GPa with the o1-In_2O_3 structure and on downstroke (d) at 12.1 GPa with the o3-In_2O_3 structure and at 1 atm with the rh-In_2O_3 structure. Residuals of the Rietveld refinements are plotted below the experimental (circles) and fitted (lines) XRD profiles (except for the o1-In_2O_3 phase, where a LeBail refinement has been performed).*

We want to stress that the pressure for the onset of the transition from c-In_2O_3 to o1-In_2O_3 on upstroke decreases with decreasing hydrostatic conditions from 35 GPa with helium to 31 GPa when the experiment was performed with the MEW mixture. These results clearly indicate that the post-cubic phase of In_2O_3 at room temperature under reasonable hydrostatic conditions is not the corundum-type phase, as it was assumed in previous works at room temperature **[52,53]**, but the orthorhombic Rh_2O_3–II (SG *Pbcn*) structure. Curiously, our *ab initio* calculations (at T = 0 K) indicate that o1-In_2O_3 should be the most stable phase above 8 GPa (see **Figure 5.4**) and below 36 GPa (α-Gd_2S_3-type In_2O_3 is the most stable one above this pressure in good agreement with previous calculations **[37, 44]**). The disagreement between experiments and calculations can be explained by the existence of a high kinetic energy barrier for the transformation from c-In_2O_3 to o1-In_2O_3 as already commented by several authors **[36, 37, 40, 41, 43, 45]**. These high kinetic energy barriers could be studied in future experiments combining pressure with a moderate heating to help the sample to overcome the kinetic barriers in the structural transition.

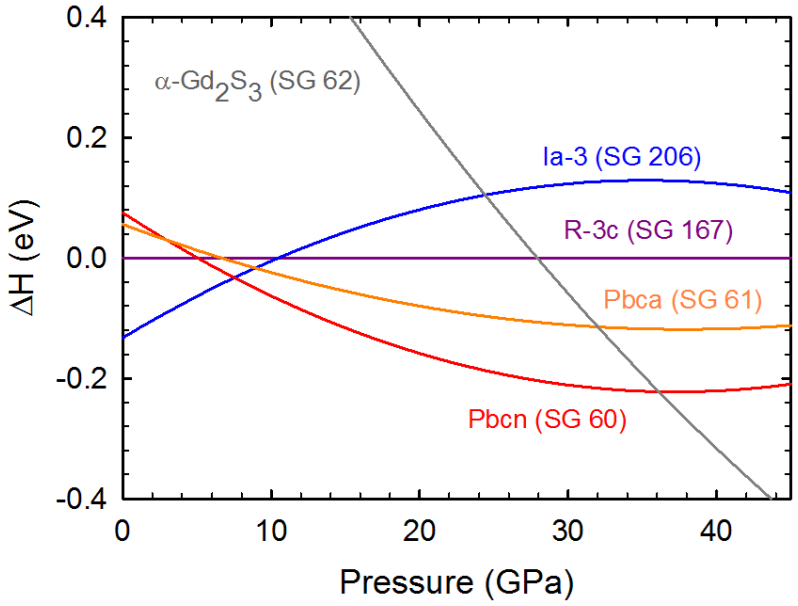

Figure 5.4: *Calculated enthalpy-pressure diagram for In_2O_3 polymorphs with respect to the corundum-type rhombohedral R-3c phase (violet): cubic Ia-3 (blue), orthorhombic Pbca (orange), orthorhombic Pbcn (red), and orthorhombic α-Gd_2S_3 (gray). The curve for the P2/c phase goes on top of that of the R-3c phase and it is not plotted.*

Powder XRD patterns on downstroke from 50 GPa (**Figure 5.2 (b)**) show that o1-In_2O_3 is stable in the region between 50 and 20 GPa. Below 20 GPa, a phase transformation to a previously unknown phase occurs. The XRD pattern at 17.1 GPa corresponds mainly to the new phase with some remnant peaks of o1-In_2O_3. However, at 12.1 GPa the XRD pattern

corresponds entirely to the new phase. Finally, on decreasing pressure below 4.2 GPa another phase transition occurs, which resulted in the observation of rh-In_2O_3 at room pressure (see Rietveld refinement in the released sample with R_{wp}=2.3% in **Figure 5.3**), in good agreement with previously reported results **[40, 41, 43]**.

In order to look for candidate structures of the new phase discovered on downstroke, which is intermediate between rh-In_2O_3 and o1-In_2O_3, we resorted to *ab initio* total-energy calculations of a number of structures already found or suggested to occur in ABO_3 compounds, including sesquioxides (*A* = *B*). In particular, we focused in structures that could be intermediate between the *R-3c* and the *Pbcn* phases, like the monoclinic *P2/c*, which was suggested to constitute a diffusionless pathway between both *R-3c* and *Pbcn* structures **[43, 163]**. Curiously, our calculations showed that the most competitive phase with the cubic *Ia-3*, rhombohedral *R-3c*, and orthorhombic *Pbcn* phases is not the monoclinic *P2/c* structure, which follows an enthalpy vs pressure curve that matches with that of the *R-3c* phase at all pressures, but the orthorhombic *Pbca* phase, which is isostructural to Rh_2O_3−III (see **Figure 5.4**).

Due to the large number of variables, the atomic positions were assumed to be fixed to those theoretically calculated in order to perform a pseudo-Rietveld refinement (R_{wp} = 2.8%) of the XRD pattern at 12.1 GPa on downstroke with the *Pbca* phase (o3-In_2O_3) is shown in **Figure 5.3**. The structure obtained by this refinement was deposited into the FIZ-Karlsruhe database (ICSD number: 426846). The experimental values of the lattice parameters and atomic positions for o3-In_2O_3 at 12.1 GPa are shown in **Tables 5.1 (a) and (b)**, respectively. Several differences can be noted between the XRD pattern of o3-In_2O_3 and those of o1-In_2O_3 and rh-In_2O_3. On the one hand, the o3-In_2O_3 shows a peak below 8° that it is not present in the o1-In_2O_3. On the other hand, one broad peak is observed above 9° in o3-In_2O_3, corresponding to several close reflections, while two narrow peaks are observed in rh-In_2O_3. In fact, our XRD pattern at 2.6 GPa on downstroke (see **Figure 5.2 (b)**) can be indexed with a mixture of rh-In_2O_3 (70%) and o3-In_2O_3 (30%). In this respect, we must note that a moderate heating at these conditions resulted in an increase of the proportion of rh-In_2O_3 at the expense of o3-In_2O_3. This information can be helpful for future experiments in order to recover a pure *Pbca* phase at room conditions.

Appendix 5.1 shows two Raman studies under pressure starting from bulk powder c-In_2O_3 with different pressure transmitting media. In one experiment, we used silicone oil and in the

other one, we did not employ any PTM, i.e., the c-In_2O_3 was compressed under non hydrostatic conditions.

	a (Å)	b (Å)	c (Å)
Experimental	5.380 (1)	5.515 (1)	15.513 (1)
Theoretical	5.433	5.569	15.626

Table 5.1 (a): *Experimental (from pseudo-Rietveld refinement) and theoretical values of the lattice parameters obtained for the o3-In_2O_3 (Pbca) at 12.1 GPa.*

Atom	Wyckoff site	x	y	z
In1	8c	0.0003	0.7887	0.4304
In2	8c	0.9976	0.7352	0.1827
O1	8c	0.3594	0.8722	0.2014
O2	8c	0.2063	0.5157	0.3755
O3	8c	0.1458	0.6550	0.0529

Table 5.1 (b): *Due to the large number of variables, the atomic positions were assumed to be fixed to those theoretically calculated in order to perform a pseudo-Rietveld refinement of the XRD pattern at 12.1 GPa.*

The unit cell of o3-In_2O_3 (see **Figure 5.1**) contains 8 formula units and all 5 atoms (two In and three O) are in 8c Wyckoff positions. The structure can be understood as a distorted bixbyite-like structure where In is octahedrally coordinated as well as in c-In_2O_3, rh-In_2O_3, and o1-In_2O_3. Octahedral connectivity in the mentioned In_2O_3 polymorphs, however, is rather complicated and varies from corner-, through edge-, to face-sharing connections.

A more comprehensive description of the structure of the four polymorphs can be obtained from the analysis of the second-neighbor coordination sphere of metallic atoms **[164−166]**. In the cation subarray of c-In_2O_3, each In is surrounded by 12 In (d < 3.85 Å) forming a slightly distorted cuboctahedron, like that existing in elemental indium. Furthermore, six of the 12 In–In interatomic distances (4 × 3.35 Å, 2 × 3.37 Å) are comparable to those of metallic In (4 × 3.25 Å, 8 × 3.37 Å), relating the topology and dimensions of oxide and the parent element, as previously reported **[167]**. At higher pressures, two additional In−In equatorial contacts in the cuboctahedra increase the coordination number to 14 (d < 4.05 Å) in o1-In_2O_3. During downstroke, the tendency of the structure is to reduce the number of second neighbors; however, the coordination number in o3-In_2O_3 is also 14 as in o1-In_2O_3, but in a more distorted configuration than in o1-In_2O_3. Finally, after releasing pressure, metastable rh-In_2O_3 shows 13 In−In distances below 4 Å (1 × 2.42 Å corresponding to the face-sharing

octahedra). In summary, the understanding of the four polymorphs taking into account the second-neighbor coordination is consistent with the irreversible transformation of metastable rh-In_2O_3 upon heating into the thermodynamically stable c-In_2O_3 at room conditions.

Despite the four room temperature polymorphs of In_2O_3 up to 50 GPa have 6-fold-coordinated In, they have different densities since their unit-cell volumes per formula unit *(V/Z)* decrease in the sequence *V/Z* (*Ia-3*) > *V/Z* (*R-3c*) > *V/Z* (*Pbca*) > *V/Z* (*Pbcn*), as can be deduced from their EoS plotted in **Figure 5.5**. The corresponding densities for the *Ia-3*, *R-3c*, *Pbca*, and *Pbcn* phases are 7.179(1), 7.255(1), 7.449(1), and 7.536(1) g/cm^3, respectively. The experimental and theoretical parameters of the EoS of the four polymorphs can be found in **Table 5.2**.

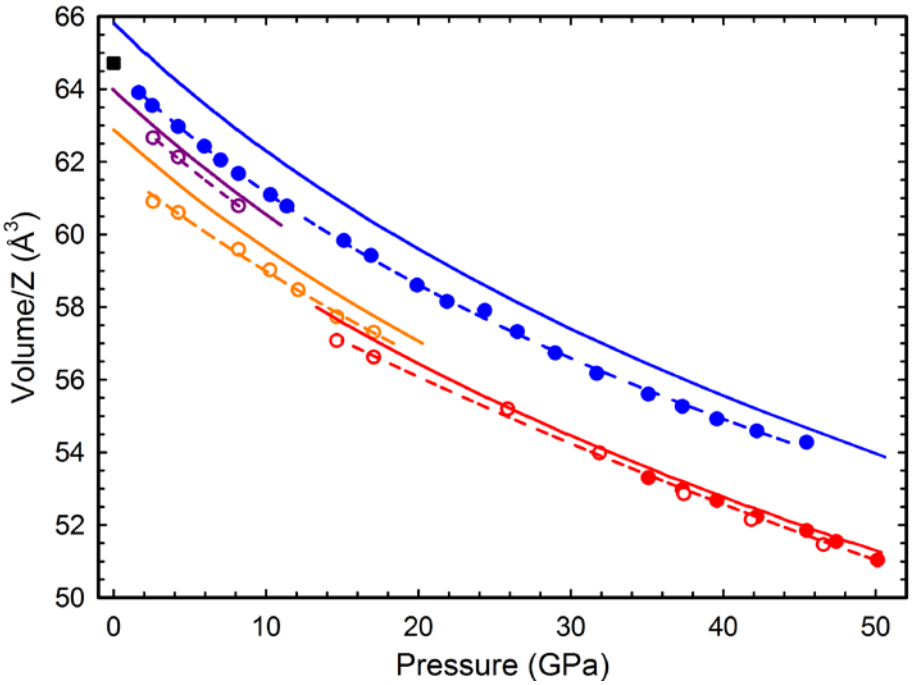

Figure 5.5: *Experimental (circles) and calculated (solid lines) pressure dependences of the unit-cell volume per formula unit (V/Z) for c-In_2O_3 (blue), rh-In_2O_3 (violet), o3-In_2O_3 (orange), and o1-In_2O_3 (red) phases. Upstroke (downstroke) depicted by full (empty) symbols.*

The phase transitions on upstroke from c-In_2O_3 to o1-In_2O_3 up to 50 GPa and on downstroke from o1-In_2O_3 to o3-In_2O_3 and from o3-In_2O_3 to rh-In_2O_3, that we have determined by XRD, have been also confirmed by means of RS measurements (see **Figure 5.6 (a)** and **(b)**). On upstroke, our RS measurements locate the onset of the transformation from c-In_2O_3 to o1-In_2O_3 at 31.6 GPa. Below this pressure, 16 Raman-active modes of bulk c-In_2O_3 were observed whose frequencies and pressure dependences agree with those recently published **[161]**. Above 31.6 GPa, new peaks appear and the Raman spectrum already corresponds

entirely to o1-In_2O_3 above 34.5 GPa. The Raman spectrum of the o1-In_2O_3 is dominated by two well-defined modes at 439 and 719 cm^{-1} (at 31.6 GPa) and by broad bands located in the regions between 180 and 280, 300−350, and 610−690 cm^{-1}.

Polymorph	Origin	V_0/Z (Å^3)	B_0 (GPa)	B_0'
c-In_2O_3	Experimental	64.28 (13)	184 (10)	4.0
	Theoretical	65.72 (2)	169.4 (12)	4.0
o1-In_2O_3	Experimental	61.9 (3)	189 (40)	4.0
	Theoretical	62.9 (1)	169.6 (14)	4.0
o3-In_2O_3	Experimental	61.2 (7)	194 (10)	4.0
	Theoretical	61.8 (2)	185.4 (12)	4.0

Table 5.2: *Experimental and theoretical values of the unit-cell volume per formula unit (V_0/Z), bulk modulus (B_0), and pressure derivative (B_0') at room pressure for the three Polymorphs c (Ia-3), o1 (Pbcn), and o3 (Pbca) of In_2O_3. Data for the rh (R-3c) phase are not given due to the lack of enough experimental data. Both experimental and theoretical data have been fitted to a second-order Birch-Murnaghan equation of state (B_0' fixed to 4).*

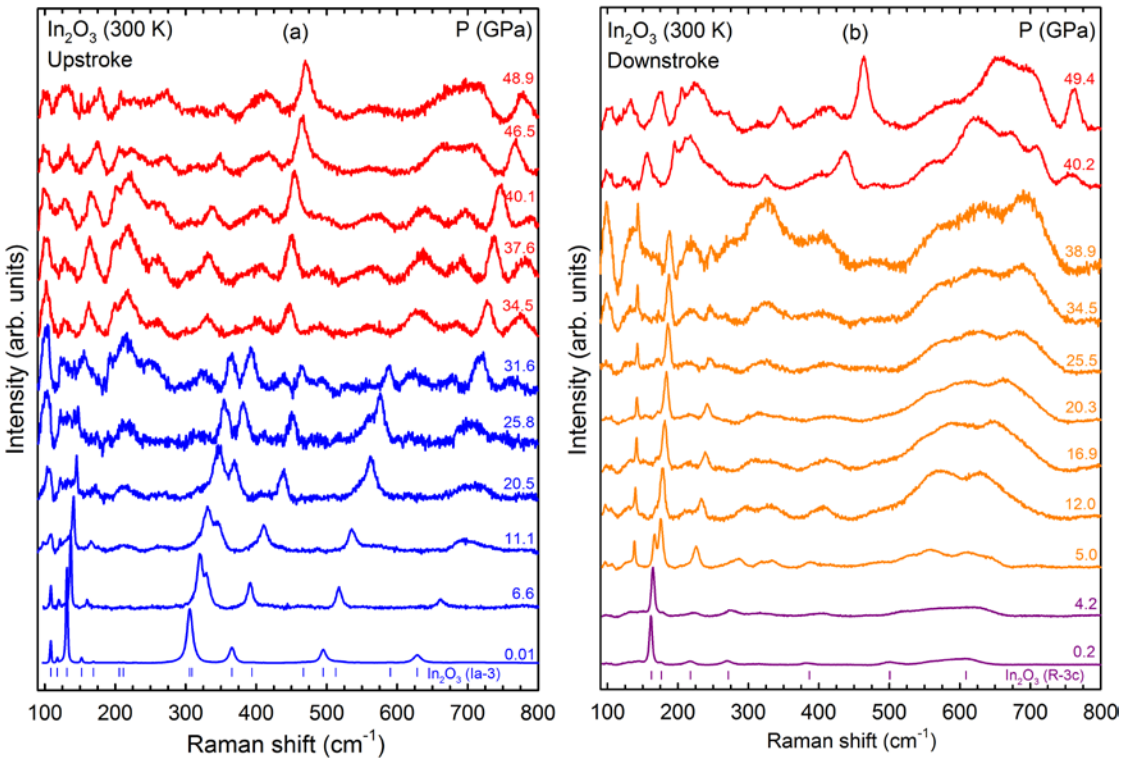

Figure 5.6: *Selected Raman spectra of bulk powder In_2O_3 at different pressures on upstroke up to 50 GPa (a) and on downstroke down to ambient pressure (b). A mixture of 16:3:1 MEW was used as a PTM. Colors indicate spectra mainly corresponding to cubic Ia-3 (blue), orthorhombic Pbcn (red), orthorhombic Pbca (orange), and rhombohedral R-3c (violet) phases. The frequencies of the main Raman-active peaks of the corundum-type phase at room conditions are indicated in the bottom of part b.*

On downstroke from 50 GPa, RS measurements show changes in the Raman spectrum below 40 GPa and below 5 GPa. Above 40 GPa, the Raman spectrum corresponds to o1-In_2O_3; however, below this pressure the Raman modes of the new phase appear. In particular, the Raman spectrum of the new phase is dominated by three rather narrow bands around 135, 180, and 240 cm^{-1}, which can be observed down to 5.0 GPa. These modes have been attributed to o3-In_2O_3 since their frequencies and pressure coefficients are consistent with our results from lattice-dynamical *ab initio* calculations. At 5.0 GPa, new Raman peaks appear and at 1.2 GPa the Raman modes of the *Pbca* phase are no longer seen. The Raman spectrum at 0.2 GPa consists of seven Raman modes which match perfectly with those theoretically expected and experimentally measured in rh-In_2O_3 at room conditions **[38]**. **Appendix 5.2** shows in detail the pressure dependence of the Raman-mode frequencies of the c-In_2O_3 and its HP phases (o1-In_2O_3, o3-In_2O_3 and rh-In_2O_3) on upstroke up to 50 GPa and on downstroke to ambient pressure.

In order to understand further the sequence of pressure-induced phase transitions observed in In_2O_3 at room temperature we performed HP measurements in rh-In_2O_3 samples recovered from pressurizing c-In_2O_3 samples to 50 GPa. Room temperature XRD measurements at selected pressures up to 25 GPa are shown in **Figure 5.7 (a)**. All XRD patterns can be indexed by a mixture of rh-In_2O_3 and o3-In_2O_3. Below 15 GPa, rh-In_2O_3 is dominant, while above this pressure the dominant phase is o3-In_2O_3. On decreasing pressure from 25 GPa to 1 atm, the recovered sample was completely in the rh-In_2O_3 phase. Room temperature RS measurements were performed in the recovered sample up to 33 GPa during a second upstroke (see **Figure 5.7 (b)**). Below 12.4 GPa, only Raman peaks of rh-In_2O_3 were present, while above this pressure new peaks appeared that reveal a gradual phase transition with coexistence of both phases until 26 GPa. Between 26 and 33 GPa, only Raman modes of o3-In_2O_3 were observed. On decreasing pressure, the rh-In_2O_3 phase is again metastable obtained at room conditions. All these results evidence the good agreement between our XRD and RS data.

Appendix 5.3 shows a more detailed study of the XRD and RS experiments performed during the second upstroke.

One question that naturally arises is why the *Pbca* phase is not observed on upstroke from the *Ia-3* phase and it is observed on downstroke from the *Pbcn* phase. The explanation is still not clear, but it is likely that the phase transition from the cubic *Ia-3* phase to the *Pbca* phase at

room temperature is hindered by the presence of a high kinetic energy barrier. This high kinetic energy barrier is present between the cubic phase and the three HP phases (*R-3c*, *Pbca*, and *Pbcn*) as suggested in previous works. In this way, a certain heating is needed to observe the transition to these three HP phases on upstroke and the *Pbca* was not previously observed in HP-HT experiments likely because the right conditions of pressure and temperature were not matched. On the other hand, if the barriers between the three HP phases are not so high, the transformation between the three of them can be experimentally observed on downstroke at room temperature from the original *Pbcn* phase.

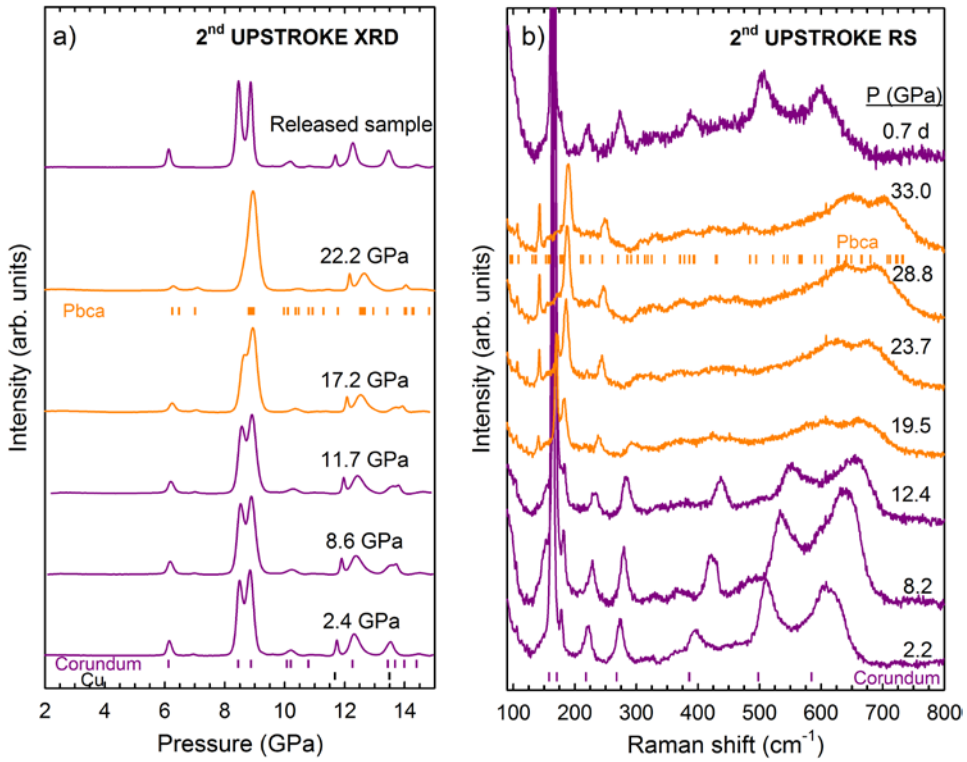

Figure 5.7: *Selected XRD patterns up to 25 GPa (a) and RS spectra up to 33 GPa (b) of rh-In_2O_3. Spectra mainly corresponding to R-3c and Pbca, phases are represented in violet and orange, respectively. Ticks at the bottom of XRD (RS) patterns of 2.4 (2.2) and 22.2 (33.0) GPa mark the positions of the diffraction (Raman) peaks of the dominating rh-In_2O_3 and o3-In_2O_3 phases at each pressure, respectively.*

To sum up the results obtained in this work, **Scheme 5.1** displays the sequence of pressure-induced phase transitions in In_2O_3 at room temperature up to 50 GPa. In this work, the four known polymorphs of In_2O_3 with the same coordination for In atoms were obtained starting from the cubic polymorph by compression and decompression at room temperature. To our knowledge, it is the first time that this phenomenon has been observed. We want to comment that the scheme of pressure-induced phase transitions here proposed for In_2O_3 at room

temperature is in disagreement with many previous reports and prompts for a revision of previous results. As already commented, the observed phase transition from c-In_2O_3 to o1-In_2O_3 above 35 GPa is in disagreement with previous results which suggested that the R-3c phase is the post-cubic phase **[52, 53]**. A careful analysis of XRD peaks assigned by Liu *et al.* **[52]** and Qi *et al.* **[53]** to the *R-3c* phase suggests the possibility to assign them also to the *Pbcn* phase. Note that data of the HP phase reported by Liu *et al.* and Qi *et al.* show no XRD peak at small angles, as we have already commented we have observed for the *Pbcn* phase. Therefore, we think that these authors already found the phase transition from c-In_2O_3 to o1-In_2O_3, even at smaller pressures than in this work, likely due to the presence of slightly non-hydrostatic conditions in their experiments. We also want to note that RS data of the HP phase reported by Liu *et al.* are not consistent with the *R-3c* phase, as it was already commented by Garcia-Domene *et al.* **[161]**. In fact, if the XRD data of Qi *et al.* **[53]** are reinterpreted on this basis, these authors indeed provided evidence for the metastable recovery of the o1-In_2O_3 at room pressure at least in nanocrystals.

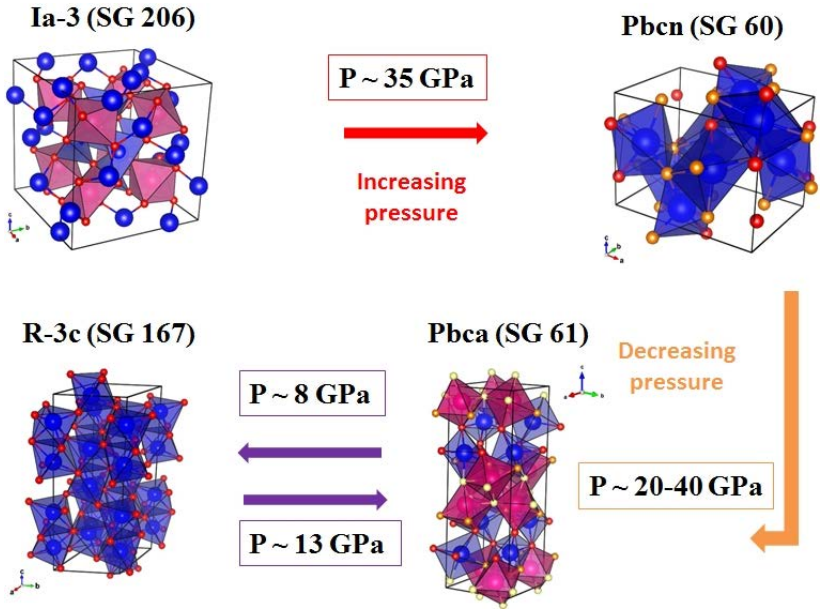

Scheme 5.1: *Sequence of Pressure-Induced Phase Transitions in In_2O_3 up to 50 GPa. Atoms in different Wyckoff sites are depicted by different colors: In (blue and pink) and O (red, yellow and orange).*

On the other hand, the observed phase transition from rh-In_2O_3 to o3-In_2O_3 above 12 GPa is apparently in disagreement with results of Gurlo *et al.*, who pointed out that no phase transition was observed in rh-In_2O_3 up to 30 GPa at room temperature **[40]**. Nevertheless, a close analysis of the room temperature XRD patterns reported by these authors at 24 and 30 GPa show that they are quite different from those of the rh-In_2O_3 at room pressure and that

they exhibit similarities with those of the o3-In_2O_3 structure shown in this work. However, our results and those of Gurlo *et al.* could be slightly different because, unlike us, they used nanocrystalline rh-In_2O_3 powder in their HP study. Finally, we have to note that Bekheet *et al.* have recently reported the stabilization of an orthorhombic phase of In_2O_3 at 1 atm after pressurizing rh-In_2O_3 at 9 GPa and 600°C **[43]**. These authors have identified it as the o1-In_2O_3 phase; however, our results suggest that the o3-In_2O_3 phase could be indeed recovered as a metastable phase at 1 atm since its enthalpy is even smaller than that of o1-In_2O_3 at ambient pressure. Therefore, further studies are needed to fully understand the structural HP-HT behavior of In_2O_3. We hope the results here reported will trigger such studies.

5.5. Conclusions

We report the discovery of a new polymorph of In_2O_3 at HP. The new polymorph (o3-In_2O_3) crystallizes in the Rh_2O_3−III structure and has been found to be the post-corundum phase; i.e., the HP phase between the *R-3c* and the *Pbcn* phases. This discovery has far-reaching implications for the understanding of the pressure−temperature diagram of In_2O_3 and of other sesquioxides. It must be stressed that a structure with *Pbca* space group was previously found as a HT phase of Rh_2O_3 (Rh_2O_3−III) **[24]**. Other sesquioxides have also been found in this space group, but are not isostructural to Rh_2O_3−III. This is the case of the poorly known α-Mn_2O_3 **[168]**, which has been recently postulated to be the low-temperature phase of Mn_2O_3 **[169]**, and the other is mineral *panguite*, recently found in the Allende meteorite **[170]** and mainly composed of Ti_2O_3. These results show that structures belonging to the *Pbca* space group are the less known and understood phases of sesquioxides and that they could be found in other corundum-type sesquioxides. In fact, our preliminary calculations indicate that the Rh_2O_3−III phase could be relevant in other corundum-type sesquioxides, like Al_2O_3, Ga_2O_3, V_2O_3, Cr_2O_3, and Fe_2O_3 at HP. Therefore, we stress that detailed experimental studies on upstroke and downstroke should be performed to confirm its presence in other sesquioxides.

Appendix 5.1: Raman studies under pressure of bulk powder c-In_2O_3 with silicone oil and without pressure transmitting medium.

Three additional HP-RS experiments have been performed starting from bulk powder c-In_2O_3 with different pressure-transmitting media: silicone oil and without PTM (experiments 1 and 2). In experiments 1 and 2, we created the worst hydrostatic conditions inside the pressure chamber of the DAC with the aim to explore the possibility to get the o3-In_2O_3 as a metastable phase at room conditions.

Figure A5.1.1 shows the HP-RS spectra measured with silicon oil on upstroke and the pressure dependence of the Raman-active mode frequencies. The maximum pressure reached in the experiment was 27.0 GPa.

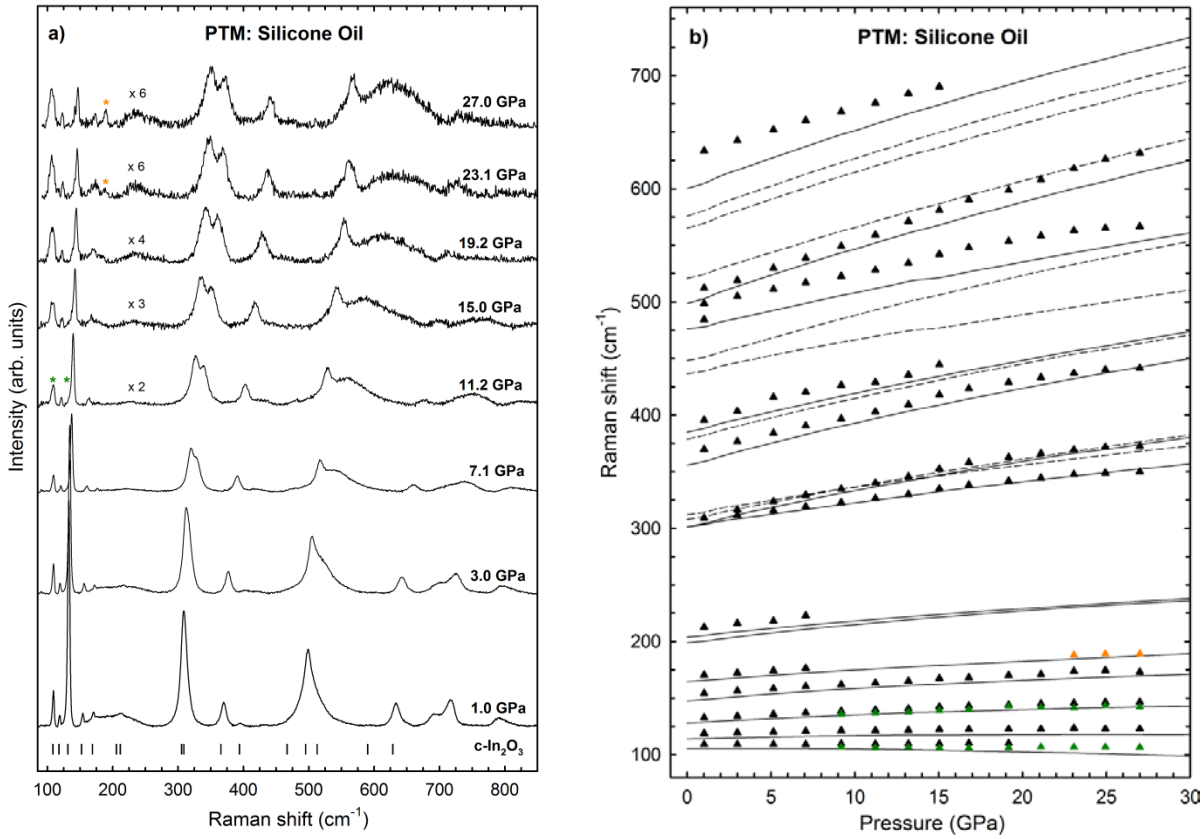

Figure A5.1.1: *Selected Raman spectra starting from bulk powder c-In_2O_3 at different pressures on upstroke up to 27.0 GPa* ***(a)*** *and the pressure dependence of the Raman-active mode frequencies* ***(b)****. The experiment was performed with silicone oil as a PTM. Black vertical marks correspond with the frequencies of the main Raman-active modes of the experimental c-In_2O_3 phase (a). Green and orange asterisks denote the widening of some c-In_2O_3 Raman modes and the appearance of the most intense Raman-active mode of the o3-In_2O_3 phase, respectively. Triangles up correspond to experimental data and solid (dashed) lines represent theoretical data for observed (not observed) Raman-active modes in bulk c-In_2O_3.*

The appearance of two peaks at 9.2 GPa located at 107 and 136 cm^{-1}, denoted with a green asterisk in the **Figure A5.1.1**, can be related with the uniaxial stresses rupture of the local translational symmetry and could activate a new Raman mode, that in principle is not Raman active, or the density of states. The positions of both peaks have an insignificant variation with pressure.

The evolutions with pressure of the experimental c-In_2O_3 Raman-active modes have a good agreement with the theoretical predictions. The c-In_2O_3 structure remains stable until 21.1 GPa. However, at 23.1 GPa, a new Raman-active mode start to appear which we have attributed to the most intense Raman-active mode of the o3-In_2O_3 structure (see orange asterisk in the **Figure A5.1.1**). Therefore, our results seem to suggest that the c-In_2O_3 start to transform into the o3-In_2O_3 before undergoing a transformation into the o1-In_2O_3 structure, unlike what happen with the c-In_2O_3 in more hydrostatic conditions where a direct c-In_2O_3 to o1-In_2O_3 phase transition occurs.

Figure A5.1.2 and Figure A5.1.3 show two Raman studies under pressure of bulk powder c-In_2O_3 in the worst hydrostatic conditions, i.e., without PTM in the pressure chamber of the DAC.

In the upstroke process, the widening of Raman-active modes of the cubic phase give rise two new peaks located at 109 and 133 cm^{-1} that appear above 2.7 and 6.9 GPa, respectively. The new Raman-active modes start to increase in intensity compared to the rest of Raman-active modes of each Raman spectra. This phenomenon is observed until 27.2 GPa, the maximum pressure reached in experiment 1. Both Raman-active modes have the same behaviour with pressure as the observed employing silicone oil as a PTM, with the exception that both Raman-active modes are observed at lower pressures than in the case of employing silicone oil as a PTM. Therefore, this experiment could confirm our hypothesis about the rupture of the local translational symmetry due compression under non-hydrostatic conditions.

The most intense Raman-active mode associated to the o3-In_2O_3 structure located at 188 cm^{-1} denoted with an orange asterisk in **Figure A.5.1.2** appeared at 19.5 GPa. This Raman-active mode increases in intensity, compared with the rest of Raman-active modes, until the maximum pressure reached in the experiment (27.2 GPa). Although the lowest frequency A_g Raman-active mode of the c-In_2O_3 phase disappeared from the Raman spectra at 27.2 GPa, other Raman-active modes of the c-In_2O_3 remained, like the T_g and A_g situated at 355 cm^{-1} and 379 cm^{-1}, respectively. Therefore, the Raman spectra at 27.2 GPa could be explained as a

combination of the o3-In_2O_3 and the c-In_2O_3 structure. In summary, this RS study also confirms the occurrence of the c-In_2O_3 to o3-In_2O_3 phase transition under non-hydrostatic conditions.

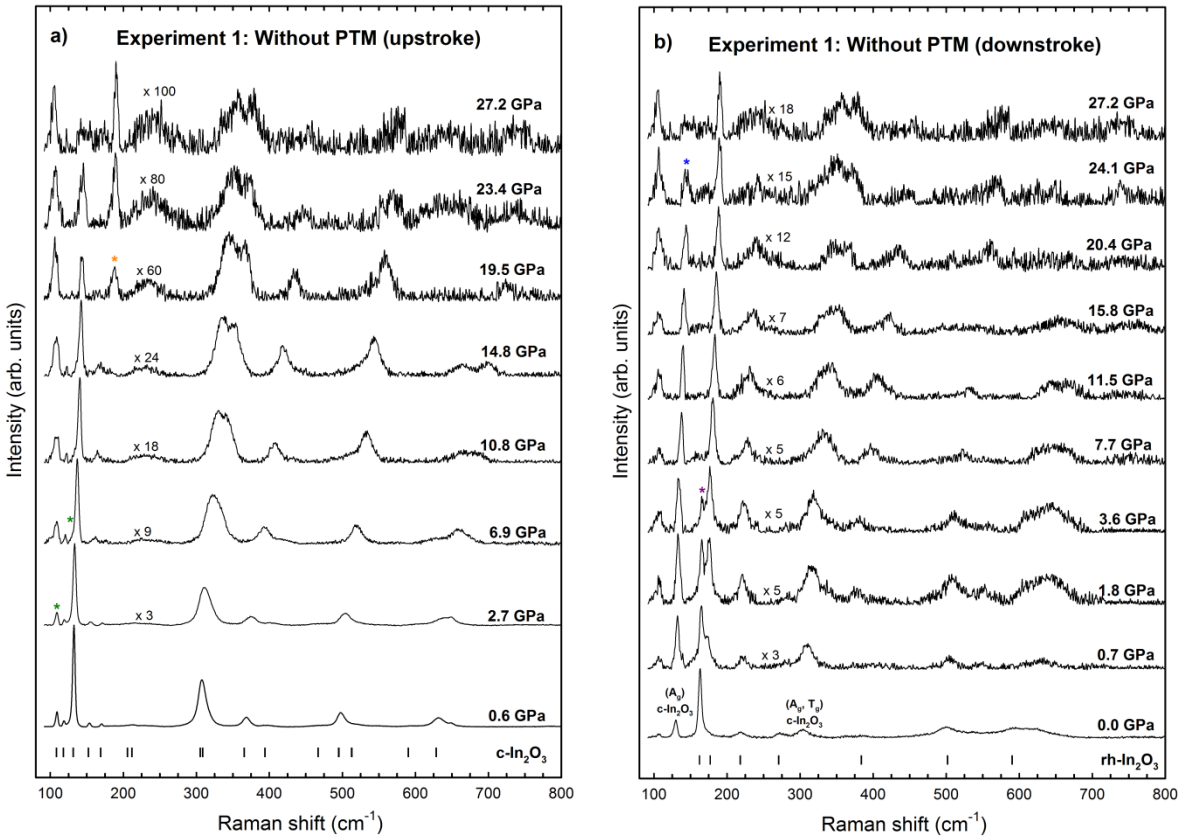

Figure A5.1.2: *Selected Raman spectra starting from bulk powder c-In_2O_3 at different pressures on upstroke up to 27.2 GPa* ***(a)*** *and on downstroke down to ambient pressure* ***(b)****. The experiment was performed without PTM. Black vertical marks correspond with the frequencies of the main Raman-active peaks of the experimental cubic bixbyite-type phase (a) and corundum-type phase (b) at room conditions. Green, orange, blue and purple asterisk denote the onset pressure for the widening of some c-In_2O_3 Raman modes and the appearance of the most intense Raman-active mode of the o3-In_2O_3,* c-In_2O_3 *and rh-In_2O_3 phase, respectively.*

In the downstroke process, the most intense Raman-active mode of c-In_2O_3 was observed again at 24.1 GPa (see blue asterisk in **Figure A.5.1.2**). Both phases c-In_2O_3 and o3-In_2O_3 coexist until 7.7 GPa, however, the o3-In_2O_3 starts to transform into the rh-In_2O_3 structure at 3.6 GPa. An evidence of this transformation is the appearance of the lowest and most intense A_{1g} Raman-active mode of rh-In_2O_3 located at 166 cm^{-1} (see purple asterisk in **Figure A.5.1.2**). Therefore, the three phases are coexisting at least down to 0.7 GPa. At ambient pressure, the Raman spectra could be explained mostly with a mixture of rh-In_2O_3 with some minor part of c-In_2O_3.

Experiment 2 was thought to complete the transformation of the c-In_2O_3 into the o1-In_2O_3 structure, its HP phase at least under hydrostatic conditions. **Figure A5.1.3** shows the Raman spectra up to 39.6 GPa, the maximum pressure reached in the experiment.

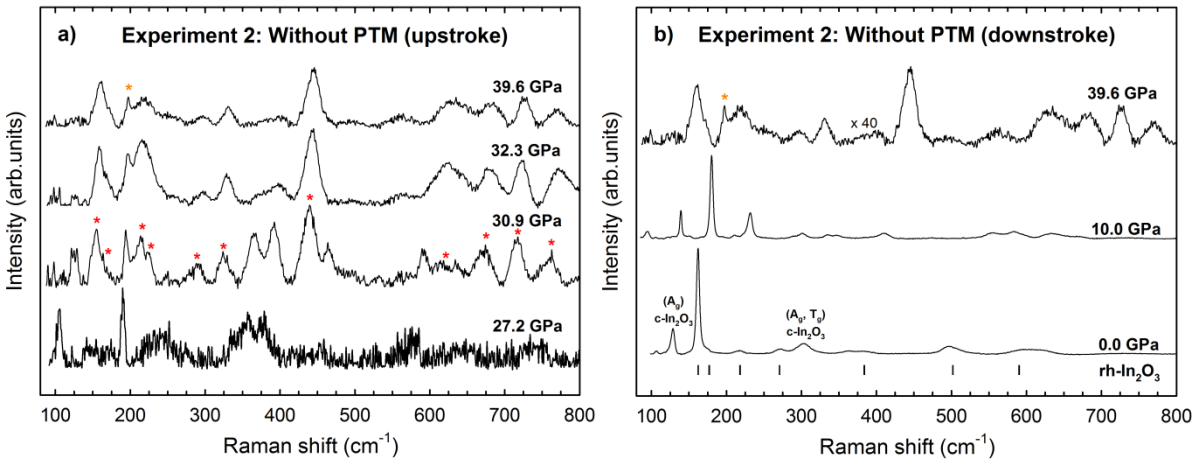

Figure A5.1.3: *Selected Raman spectra starting from bulk powder c-In_2O_3 at different pressures on upstroke up to 39.6 GPa* ***(a)*** *and on downstroke down to ambient pressure* ***(b)****. The experiment was performed without PTM. Black vertical marks correspond with the frequencies of the main Raman-active peaks of the experimental corundum-type phase (b) at room conditions. Orange and red asterisks denote the Raman-active mode associated to the o3-In_2O_3 and o1-In_2O_3 structure, respectively.*

Figure A5.1.3 (a) shows the HP-RS spectra during the upstroke process in experiment 2. For comparison, the Raman spectra at 27.2 GPa corresponds to the RS spectrum of experiment 1 taken at the highest pressure. We could observe at 30.9 GPa the appearance of new Raman-active modes corresponding to the o1-In_2O_3 structure (see red asterisks in **Figure A5.1.3 (a)**), thus leading to the coexistence of the three phases (c-In_2O_3, o3-In_2O_3 and o1-In_2O_3). At the maximum pressure of the experiment (39.6 GPa), the Raman spectra could be explained mostly with the o1-In_2O_3 phase, but not completely, because the most intense Raman-active mode of the o3-In_2O_3 phase was still observed (see orange asterisk in **Figure A5.1.3 (a)**).

In the downstroke process, the Raman spectra could be explained as a combination of the o3-In_2O_3 and the c-In_2O_3 structure down to 10.0 GPa. However, at ambient conditions, the dominant structure it is again the rh-In_2O_3, although it coexists with the c-In_2O_3. The fact that we had some proportion of c-In_2O_3 sample at 10.0 GPa and ambient pressure (1 atm) means that some parts of the samples remain at the c-In_2O_3 phase at the maximum pressure reached in the experiment (39.6 GPa).

Figure A5.1.4 shows the pressure dependence of the Raman-active mode frequencies starting from c-In_2O_3 in experiments 1 and 2 without PTM. A good agreement is observed between the experimental and theoretical Raman-active modes with the evolution of pressure of the c-In_2O_3 structure.

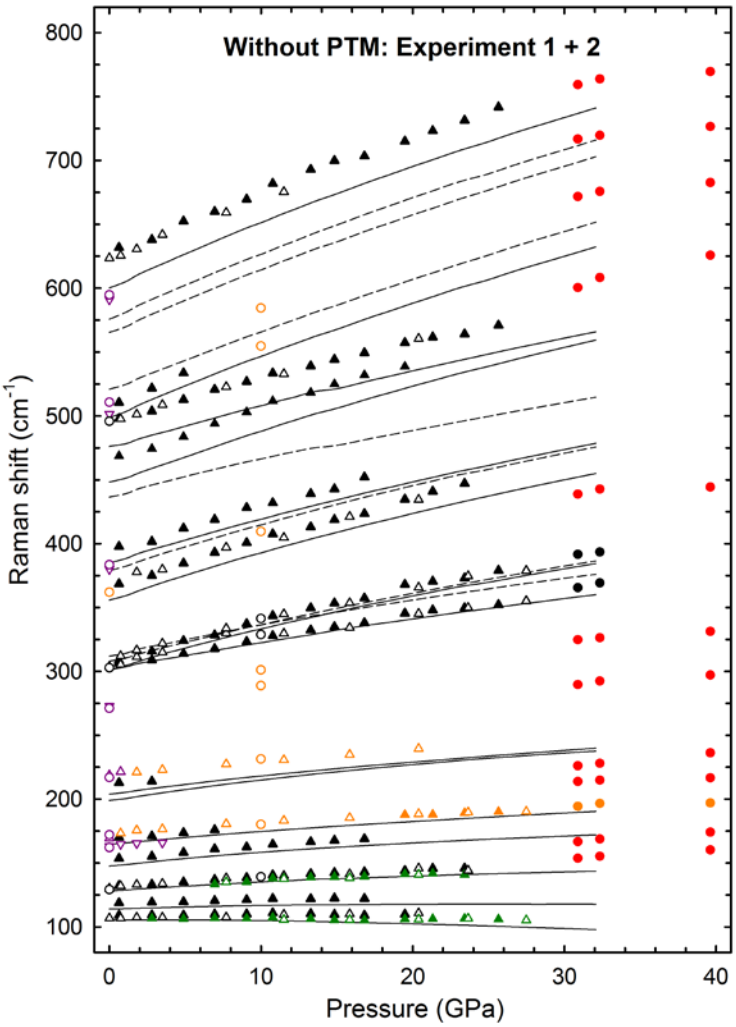

Figure A5.1.4 *shows the pressure dependence of the Raman-mode frequencies starting from c-In_2O_3 of the two Raman experiment performed without PTM. Symbols correspond to experimental data. Triangles (circles) are related with the first (second) experiment and filled (empty) symbols with the upstroke (downstroke) process. Solid (dashed) lines represent theoretical data for observed (not observed) Raman-active modes in bulk c-In_2O_3. Black, orange, red and purple colours are related with the c-In_2O_3, o3-In_2O_3, o1-In_2O_3 and rh-In_2O_3 structure. The green colour denotes a widening of some c-In_2O_3 Raman modes.*

Table A5.1.1 shows the experimental Raman-mode frequencies at room pressure and their pressure coefficient of c-In_2O_3 using three different pressure transmitting media. Specifically, the Raman experiments have been performed with MEW in the proportion 16:3:1, silicone oil and without PTM.

Raman modes of c-In_2O_3									
	M-E-W (16:3:1) (0 – 25 GPa)			Silicone Oil (0 – 27 GPa)			Without PTM (0 – 27 GPa)		
Mode (Sym)	ω_0 (cm^{-1})	$\frac{\partial\omega}{\partial P}$ $\left(\frac{cm^{-1}}{GPa}\right)$	$\frac{\partial^2\omega}{\partial P^2}$ $\left(\frac{cm^{-1}}{GPa^2}\right)$	ω_0 (cm^{-1})	$\frac{\partial\omega}{\partial P}$ $\left(\frac{cm^{-1}}{GPa}\right)$	$\frac{\partial^2\omega}{\partial P^2}$ $\left(\frac{cm^{-1}}{GPa^2}\right)$	ω_0 (cm^{-1})	$\frac{\partial\omega}{\partial P}$ $\left(\frac{cm^{-1}}{GPa}\right)$	$\frac{\partial^2\omega}{\partial P^2}$ $\left(\frac{cm^{-1}}{GPa^2}\right)$
Tg	108 (1)	0.07 (3)	-0.006 (2)	109.2 (2)	0.01 (4)	0.003 (2)	108.7 (5)	0.25 (11)	-0.011 (5)
Tg	118 (1)	0.4 (1)	-0.009 (3)	118.5 (2)	0.35 (3)	-0.007 (2)	118.3 (4)	0.42 (10)	-0.010 (5)
Ag	131 (1)	1.0 (1)	-0.02 (1)	131.7 (2)	0.85 (3)	-0.010 (2)	131.1 (4)	0.96 (8)	-0.014 (3)
Tg	152 (1)	1.4 (1)	-0.02 (1)	152.8 (6)	1.14 (10)	-0.012 (3)	152.3 (4)	1.34 (10)	-0.020 (6)
Eg	169 (1)	0.8 (1)		169.4 (2)	0.96 (4)		169.1 (6)	0.96 (13)	
Tg	205 (3)	1.3 (1)							
Tg	211 (3)	3.0 (2)		211.1 (9)	1.58 (19)		212.6 (5)		
Tg	306 (2)	2.4 (2)	-0.03 (1)	305.4 (1.0)	2.18 (16)	-0.017 (5)	303.0 (9)	2.46 (15)	-0.020 (5)
Ag	306 (2)	4.0 (3)	-0.06 (2)	304.6 (1.1)	3.88 (19)	-0.048 (7)	305.2 (1.1)	3.95 (18)	-0.044 (6)
Eg									
Tg									
Tg	365 (2)	4.3 (3)	-0.06 (2)	364.2 (1.4)	4.15 (23)	-0.044 (8)	366.0 (1.2)	3.88 (23)	-0.019 (9)
Tg									
Eg	396 (4)	3.3 (2)		392 (3)	4.3 (8)	-0.07 (5)	394.0 (1.7)	3.7 (5)	-0.02 (3)
Tg									
Tg	467 (4)						463.4 (1.5)	4.8 (4)	-0.043 (17)
Ag	495 (2)	3.7 (3)	-0.04 (1)	493.7 (1.5)	3.6 (3)	-0.030 (8)	494.6 (8)	3.92 (14)	-0.038 (5)
Tg	513 (4)			504.1 (1.5)	5.3 (3)	-0.017 (9)	506.9 (5)	5.40 (16)	
Tg									
Eg	590 (4)	5.2 (4)							
Ag									
Tg	628 (2)	6.0 (2)	-0.09 (3)	629.2 (4)	4.61 (12)	-0.036 (7)	626.6 (1.8)	5.2 (3)	-0.031 (11)

Table A5.1.1*: Experimental Raman-mode frequencies at room pressure and their pressure coefficient of c-In_2O_3 using three different pressure transmitting media. The pressure range of the fit is also shown.*

The conclusions that we could reach after performing these experiments employing silicone oil or without PTM are: i) c-In_2O_3 transforms into o1-In_2O_3 through an intermediate o3-In_2O_3 phase, unlike when MEW (16:3:1) was used as PTM that transforms directly c-In_2O_3 into o1-In_2O_3; ii) we could not recover the o3-In_2O_3 as a metastable phase at ambient conditions.

In this context, we are thinking in new experiments, like performing a new cycle pressure till 50 GPa in the worst hydrostatic conditions, i.e., without PTM with the purpose to get pure o1-In_2O_3 at 50 GPa. In the downstroke process, we expected to have the pure o3-In_2O_3 structure close to the ambient pressure (around 4 GPa). At that pressure, we wanted to check two options. The first one is to quench the sample in pressure and the other one is to decrease the

temperature of the DAC and after that decrease very slowly the pressure till reach the ambient pressure with the aim of get pure o3-In_2O_3.

Appendix 5.2: Raman study of the c-In_2O_3 and its HP phases (Pbcn, Pbca and R-3c)

As we mention in **(4.1)**, the primitive cell of cubic bixbyite structure (c-In_2O_3) with space group (No. 206) contains 8 formula units. Group theory predicts that this structure should have 120 vibrational modes with the following representation:

$$\Gamma = 4A_g(R) + 4E_g(R) + 14T_g(R) + 16T_u(IR) + 5A_u + 5E_u + T_u \qquad \textbf{(A5.2.1)}$$

where E and T (also noted F in the literature) modes are double and triple degenerated, respectively, the 22 gerade (g) modes are Raman-active (R) modes, the 16 ungerade (u) modes are infrared-active (IR) modes, the A_u and E_u are silent modes, and one T_u mode corresponds to the three acoustic vibrations.

The orthorhombic Rh_2O_3-II structure (o1-In_2O_3) with *Pbcn* space group (No. 60) has 4 formula units. Group theory predicts that this structure should have 60 vibrational modes with the following representation:

$$\Gamma_{60} = 7A_g(R) + 8B_{1g}(R) + 7B_{2g}(R) + 8B_{3g}(R) + 7B_{1u}(IR) + 6B_{2u}(IR) + 7B_{3u}(IR) + \\ + 7A_u + B_{1u} + B_{2u} + B_{3u} \qquad \textbf{(A5.2.2)}$$

Specifically, there are 30 Raman-active (R) modes (A_g, B_{1g}, B_{2g} and B_{3g}), 20 infrared-active (IR) modes (B_{1u}, B_{2u} and B_{3u}), 7 silent modes (A_u) and 3 acoustic vibrations (B_{1u}, B_{2u}, and B_{3u}).

The primitive cell of orthorhombic Rh_2O_3−III (o3-In_2O_3) structure with *Pbca* space group (No. 61) contains 8 formula units. Group theory predicts that this structure should have 120 vibrational modes with the irreducible representation,

$$\Gamma_{120} = 15A_g(R) + 15B_{1g}(R) + 15B_{2g}(R) + 15B_{3g}(R) + 14B_{1u}(IR) + 14B_{2u}(IR) + \\ + 14B_{3u}(IR) + 15A_u + B_{1u} + B_{2u} + B_{3u} \qquad \textbf{(A5.2.3)}$$

where there are 60 Raman-active (R) modes (A_g, B_{1g}, B_{2g} and B_{3g}), 42 modes infrared-active (IR) modes (B_{1u}, B_{2u} and B_{3u}), 15 silent modes (A_u) and 3 acoustic vibrations (B_{1u}, B_{2u}, and B_{3u}).

Finally, the corundum-type structure (rh-In_2O_3) with *R-3c* space group (No. 167) has a primitive unit cell with 2 formula units. Group theory predicts that this structure should have 30 vibrational modes with the irreducible representation **[171]**,

$$\Gamma_{30} = 2A_{1g}(R) + 5E_g(R) + 2A_{2u}(IR) + 4E_u(IR) + 2A_{1u} + 3A_{2g} + A_{2u} + E_u \qquad \textbf{(A5.2.4)}$$

thus resulting 7 Raman-active (R) modes (A_{1g} and E_g), 6 infrared-active (IR) modes (A_{2u} and E_u), 5 silent (A_{1u} and A_{2g}) modes, and 3 acoustic modes (A_{2u} and E_u).

Figure A5.2.1 shows the pressure dependence of the Raman-mode frequencies starting from c-In_2O_3 on upstroke up to 50 GPa and on downstroke to ambient pressure, employing MEW in the proportion 16:3:1 as a PTM. A good agreement is observed between the experimental and theoretical data. Thanks to the *ab initio* calculations, we could assign some of the symmetries in some Raman-active modes of the HP phases of c-In_2O_3; i.e., the o1-In_2O_3, the o3-In_2O_3 and the rh-In_2O_3 phases.

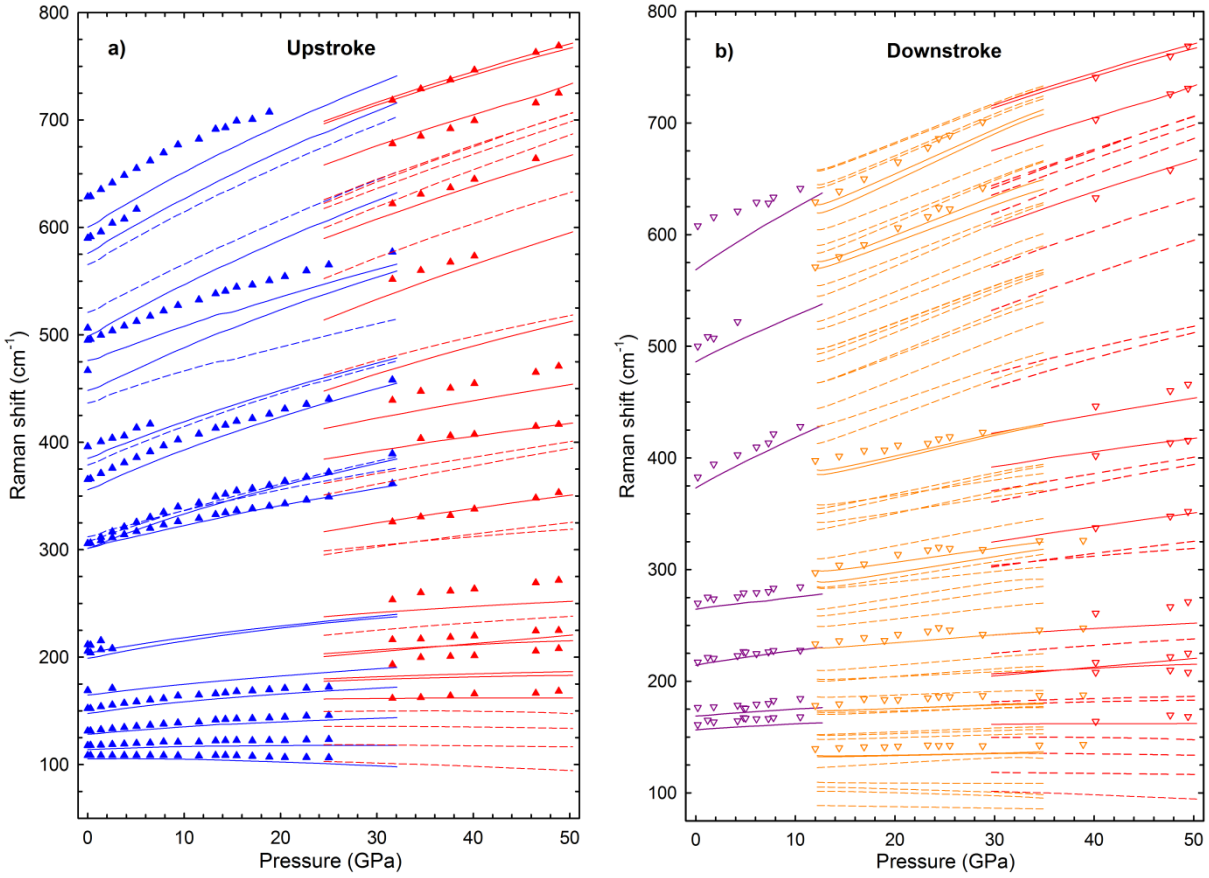

Figure A5.2.1 *Pressure dependence of the Raman-mode frequencies starting from c-In_2O_3 employing MEW in the proportion 16:3:1 as a PTM. Symbols correspond to experimental data. Triangles up (down) are related with the upstroke (downstroke) process. Solid (dashed) lines represent theoretical data for observed (not observed) Raman-active modes in bulk c-In_2O_3 and its HP phases. Blue, red, orange and purple colours correspond to c-In_2O_3, o1-In_2O_3, o3-In_2O_3, and rh-In_2O_3, respectively.*

Table A5.2.1, Table A5.2.2, Table A5.2.3 and **Table A5.2.4** show the experimental zero-pressure Raman-active mode frequencies and their pressure coefficient for c-In_2O_3, o1-In_2O_3, o3-In_2O_3, and rh-In_2O_3, respectively. Experimental parameters have been obtained by fitting measured data to the linear expression:

$$\omega = \omega_0 + \left(\frac{d\omega}{dP}\right) P \qquad \textbf{(A5.2.5)}$$

or the quadratic expression:

$$\omega = \omega_0 + \left(\frac{d\omega}{dP}\right) P + \left(\frac{d^2\omega}{dP^2}\right) P^2 \qquad \textbf{(A5.2.6)}$$

Raman modes of c-In_2O_3

	***Ab initio* calculations (0 – 32 GPa)**			**In_2O_3 bulk powder (0 – 32 GPa)**			**Literature**
Mode (Sym)	$\boldsymbol{\omega_0}$ $\left(\mathbf{cm^{-1}}\right)$	$\frac{\partial\omega}{\partial P}$ $\left(\frac{\mathbf{cm^{-1}}}{\mathbf{GPa}}\right)$	$\frac{\partial^2\omega}{\partial P^2}$ $\left(\frac{\mathbf{cm^{-1}}}{\mathbf{GPa^2}}\right)$	$\boldsymbol{\omega_0}$ $\left(\mathbf{cm^{-1}}\right)$	$\frac{\partial\omega}{\partial P}$ $\left(\frac{\mathbf{cm^{-1}}}{\mathbf{GPa}}\right)$	$\frac{\partial^2\omega}{\partial P^2}$ $\left(\frac{\mathbf{cm^{-1}}}{\mathbf{GPa^2}}\right)$	$\boldsymbol{\omega_0}$ $\left(\mathbf{cm^{-1}}\right)$
Tg	105.49 (7)	0.01 (2)	-0.008 (1)	108.4 (2)	0.07 (3)	-0.006 (2)	109[a]
Tg	114.16 (7)	0.31 (2)	-0.006 (1)	117.8 (2)	0.42 (3)	-0.009 (1)	
Ag	128.30 (9)	0.76 (2)	-0.009 (1)	131.2 (2)	0.95 (3)	-0.015 (1)	131,[b] 135[a, b]
Tg	147.9 (2)	1.17 (2)	-0.013 (1)	152.2 (2)	1.39 (4)	-0.024 (1)	
Eg	164.87 (8)	1.05 (2)	-0.008 (1)	169.0 (8)	0.8 (1)		
Tg	199.03 (8)	1.76 (2)	-0.017 (1)	204.8 (8)	1.3 (5)		
Tg	204.2 (2)	1.50 (2)	-0.012 (1)	211.1 (8)	3.0 (9)		
Tg	301.53 (9)	2.23 (2)	-0.013 (1)	306.3 (5)	2.13 (8)	-0.014 (3)	306,[b, c] 307,[a, b] 308[d]
Ag	301.6 (2)	3.41 (3)	-0.03 (1)	307.6 (9)	3.5 (2)	-0.032 (5)	
Eg	307.9 (2)	3.05 (2)	-0.019 (1)				
Tg	312.4 (2)	2.56 (2)	-0.018 (1)				
Tg	355.9 (2)	3.94 (3)	-0.027 (1)	366.4 (7)	3.9 (2)	-0.036 (4)	365,[b, d, e] 366,[a, c]
Tg	378.8 (2)	3.87 (2)	-0.027 (1)				
Eg	385.3 (2)	3.60 (2)	-0.022 (1)	395.8 (9)	3.3 (3)		
Tg	437.6 (5)	2.97 (7)	-0.019 (2)				
Tg	447.2 (2)	4.33 (3)	-0.026 (1)	467 (2)			
Ag	475.8 (3)	3.35 (5)	-0.017 (1)	495.1 (4)	3.66 (6)	-0.034 (2)	495, [a, b, c] 496,[b] 504,[d]
Tg	498.9 (2)	5.03 (3)	-0.028 (1)	506 (2)			
Tg	520.4 (2)	4.73 (3)	-0.020 (1)				
Eg	565.2 (2)	5.18 (3)	-0.028 (1)	589.7 (7)	5.2 (3)		
Ag	576.1 (2)	5.39 (3)	-0.033 (1)				602[b]
Tg	600.4 (2)	5.40 (3)	-0.032 (1)	627.5 (7)	6.0 (2)	-0.10 (2)	627,[b] 628,[e] 630,[c] 631,[a] 637,[d]

[a]*Reference 58.* [b]*Reference 143.* [c]*Reference 142.* [d]*Reference 138.* [e]*Reference 57.*

***Table A5.2.1**: Experimental and theoretical Raman-active mode frequencies of c-In_2O_3 at room pressure and their pressure coefficients.*

Theoretical Raman-mode frequencies at room pressure and their pressure coefficients in the four phases (c-In_2O_3, o1-In_2O_3, o3-In_2O_3 and rh-In_2O_3) are also shown for comparison with the experimental data. The fits to **equations A5.2.5** and **A5.2.6** have been performed in the whole pressure interval of each phase. In o1-In_2O_3 and o3-In_2O_3, there are several

experimental Raman-active modes that could not be assigned to the theoretical ones unequivocally because they were to close.

o1-In_2O_3					
	***Ab initio* calculations (25 – 50 GPa)**			**Experimental (31 – 50 GPa)**	
Mode (Sym)	$\omega_0\ (cm^{-1})$	$\frac{\partial\omega}{\partial P}\left(\frac{cm^{-1}}{GPa}\right)$	$\frac{\partial^2\omega}{\partial P^2}\left(\frac{cm^{-1}}{GPa^2}\right)$	$\omega_0(cm^{-1})$	$\frac{\partial\omega}{\partial P}\left(\frac{cm^{-1}}{GPa}\right)$
B_{1g}	107.3 (5)	-0.10 (3)	-0.003 (1)		
B_{3g}	119.5 (3)	-0.01 (2)	-0.001 (1)		
A_g	132.8 (3)	0.21 (2)	-0.004 (1)		
B_{3g}	140.6 (9)	0.56 (5)	-0.008 (1)		
B_{2g}	157.1 (5)	0.22 (3)	-0.002 (1)	150 (2)	0.37 (5)
B_{1g}	166.6 (3)	0.57 (2)	-0.005 (1)	172 (5)	0.73 (11)
A_g	168.6 (3)	056 (2)	-0.004 (1)		
B_{3g}	181.1 (4)	0.80 (2)		198 (2)	0.55 (4)
B_{1g}	182.0 (6)	1.06 (3)	-0.008 (1)		
B_{2g}	194.0 (4)	1.27 (3)	-0.008 (1)		
A_g	217.0 (3)	0.98 (2)	-0.006 (1)	225 (4)	0.96 (9)
B_{2g}	258.4 (3)	1.67 (2)	-0.007 (1)		
B_{3g}	270.8 (5)	1.32 (3)	-0.007 (1)		
A_g	275.8 (5)	1.85 (3)	-0.007 (1)	275 (4)	1.58 (10)
B_{2g}	301.9 (8)	2.16 (5)	-0.006 (1)		
B_{1g}	318.3 (8)	1.90 (4)	-0.005 (1)		
B_{1g}	342.9 (1.2)	1.87 (7)	-0.008 (1)	370 (3)	0.95 (6)
B_{3g}	364.0 (7)	2.18 (4)	-0.008 (1)	386 (4)	1.73 (9)
B_{3g}	364.1 (7)	3.85 (4)	-0.018 (1)		
B_{2g}	388.3 (7)	3.43 (4)	-0.017 (1)		
B_{1g}	418.7 (9)	4.23 (5)	-0.014 (1)	471 (3)	2.55 (9)
B_{3g}	453.5 (1.5)	4.48 (8)	-0.018 (1)		
A_g	500.1 (7)	3.96 (4)	-0.013 (1)	533 (4)	2.80 (11)
B_{3g}	503.8 (1.5)	4.15 (8)	-0.010 (1)		
B_{2g}	527.8 (9)	3.92 (5)	-0.010 (1)		
A_g	525.0 (1.7)	4.33 (10)	-0.014 (1)		
B_{1g}	533.2 (1.2)	4.10 (7)	-0.013 (1)		
B_{2g}	576 (4)	3.6 (3)	-0.010 (3)	592 (4)	2.70 (9)
B_{3g}	607.5 (1.0)	4.07 (6)	-0.018 (1)	628 (4)	2.90 (9)
B_{1g}	609.3 (1.2)	4.07 (7)	-0.017 (1)		

***Table A5.2.2**: Experimental and theoretical Raman-active mode frequencies of o1-In_2O_3 at room pressure and their pressure coefficients.*

o3-In_2O_3						
	***Ab initio* calculations (11 – 35 GPa)**			**Experimental (11 – 39 GPa)**		
Mode (Sym)	$\omega_0(cm^{-1})$	$\frac{\partial\omega}{\partial P}\left(\frac{cm^{-1}}{GPa}\right)$	$\frac{\partial^2\omega}{\partial P^2}\left(\frac{cm^{-1}}{GPa^2}\right)$	$\omega_0(cm^{-1})$	$\frac{\partial\omega}{\partial P}\left(\frac{cm^{-1}}{GPa}\right)$	$\frac{\partial^2\omega}{\partial P^2}\left(\frac{cm^{-1}}{GPa^2}\right)$
A_g	60.3 (3)	-0.20 (2)				
B_{1g}	63.3 (4)	0.17 (2)				
B_{3g}	90.5 (3)	-0.15 (3)				
B_{2g}	100.7 (2)	0.17 (2)	-0.009 (1)			

Ag	109.1 (6)	0.29 (3)				
B2g	109.8 (4)	-0.04 (2)				
B3g	110 (4)	1.2 (5)	-0.018 (9)			
B1g	130.5 (4)	0.14 (2)		135.2 (1.0)	0.46 (8)	-0.007 (2)
B3g	135.3 (9)	-0.26 (9)	0.009 (2)			
B2g	145 (2)	0.2 (2)				
Ag	148.7 (6)	0.23 (2)				
B1g	148.4 (4)	0.31 (2)				
B1g	166.4 (6)	0.32 (3)				
Ag	169.6 (5)	0.20 (2)				
B2g	170.3 (3)	0.27 (2)		176.7 (1.7)	0.32 (7)	
B3g	169.5 (3)	0.31 (2)				
Ag	182.4 (5)	0.27 (2)				
B2g	192.6 (7)	0.60 (3)				
B3g	197.1 (6)	0.37 (3)				
B1g	201.1 (7)	0.68 (3)				
Ag	221.4 (5)	0.66 (2)		231 (3)	0.50 (12)	
B2g	237.2 (8)	0.94 (3)				
B3g	243.5 (7)	1.19 (3)				
B1g	249 (2)	1.24 (8)				
B1g	272.6 (1.2)	0.85 (5)				
Ag	267.7 (1.6)	1.31 (6)				
B3g	272.2 (1.7)	1.31 (7)		289 (4)	1.07 (15)	
B2g	284.2 (1.4)	1.16 (5)				
Ag	289.4 (8)	1.61 (3)				
B3g	312.8 (7)	1.88 (3)				
B1g	326.2 (1.1)	1.28 (4)				
Ag	326.5 (9)	1.90 (4)				
B3g	332.9 (1.0)	1.77 (4)				
B2g	341.9 (1.2)	1.27 (5)				
B2g	360.3 (1.6)	1.98 (6)		380.1 (1.7)	1.50 (8)	
B1g	365.4 (1.6)	1.87 (6)				
Ag	373.5 (1.2)	3.20 (5)				
B3g	391.7 (1.3)	2.95 (5)				
B2g	401.8 (1.2)	3.44 (5)				
Ag	427.2 (1.5)	3.24 (6)				
B1g	424.2 (1.3)	3.48 (5)				
Ag	443.1 (1.2)	3.49 (5)				
B2g	452.7 (1.4)	3.27 (6)				
B3g	458.0 (1.7)	3.18 (7)				
B1g	473.9 (1.5)	3.33 (6)				
B3g	478.9 (1.3)	3.51 (5)				
B2g	499.2 (1.6)	3.67 (6)				
Ag	512.9 (1.6)	3.33 (7)				
B3g	530.4 (1.4)	3.17 (6)		523 (3)	4.04 (14)	
Ag	535 (2)	3.30 (9)				
B1g	538.1 (1.6)	3.65 (6)				
B2g	548.1 (1.6)	3.39 (7)				
B3g	561.8 (1.8)	3.40 (7)				
Ag	570 (3)	3.98 (10)		574 (4)	4.50 (9)	
B3g	579 (2)	3.81 (8)				
B2g	597.4 (1.8)	3.58 (7)				
B1g	600 (2)	3.57 (8)				
B1g	615.5 (1.6)	3.33 (6)				
B2g	616.2 (1.8)	3.36 (7)				

***Table A5.2.3**: Experimental and theoretical Raman-active mode frequencies of o3-In_2O_3 at room pressure and their pressure coefficients.*

rh-In_2O_3							
	***Ab initio* calculations (0 – 11 GPa)**			**Experimental (0 – 11GPa)**			**Literature[a]**
Mode (Sym)	ω_0 (cm^{-1})	$\frac{\partial\omega}{\partial P}\left(\frac{cm^{-1}}{GPa}\right)$	$\frac{\partial^2\omega}{\partial P^2}\left(\frac{cm^{-1}}{GPa^2}\right)$	ω_0 (cm^{-1})	$\frac{\partial\omega}{\partial P}\left(\frac{cm^{-1}}{GPa}\right)$	$\frac{\partial^2\omega}{\partial P^2}\left(\frac{cm^{-1}}{GPa^2}\right)$	ω_0 (cm^{-1})
A_{1g}	156.48 (7)	0.65 (3)	-0.012 (2)	161.2 (5)	1.07 (18)	-0.040 (17)	164
E_g	168.78 (8)	0.73 (3)	-0.010 (2)	175 (6)	0.78 (11)		
E_g	214.38 (9)	1.54 (3)	-0.023 (2)	216.9 (6)	1.8 (3)	-0.07 (2)	221.8
E_g	264.72 (17)	1.11 (7)	-0.005 (5)	269.8 (1.1)	1.8 (4)	-0.04 (4)	273
							309
E_g	373.32 (13)	4.91 (5)	-0.040 (4)	383 (3)	5.0 (1.1)	-0.07 (9)	385
A_{1g}	486.35 (16)	4.46 (6)	-0.033 (4)	498.3 (1.1)	5.5 (5)		504.5
E_g	568.66 (13)	6.14 (5)	-0.059 (4)	608.5 (1.3)	3.1 (2)		596

[a]*Reference 28*

***Table A5.2.4**: Experimental and theoretical Raman-active mode frequencies of rh-In_2O_3 at room pressure and their pressure coefficients.*

Appendix 5.3: Study of the second upstroke XRD and RS experiment.

Figure A5.3.1 shows the pressure dependence of the *a* and *c* lattice parameters and **Figure A5.3.2** displays the pressure dependence of the unit-cell volume per formula unit of the rh-In_2O_3 structure during the second upstroke.

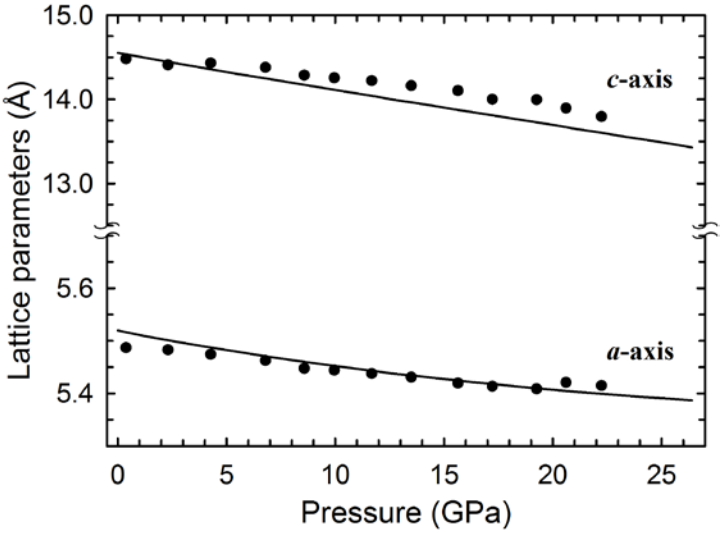

Figure A5.3.1 *Pressure dependence of the a and c lattice parameters of the rh-In_2O_3 structure. Full circles are related with the experimental data on the upstroke and solid lines with the theoretical ab initio calculations.*

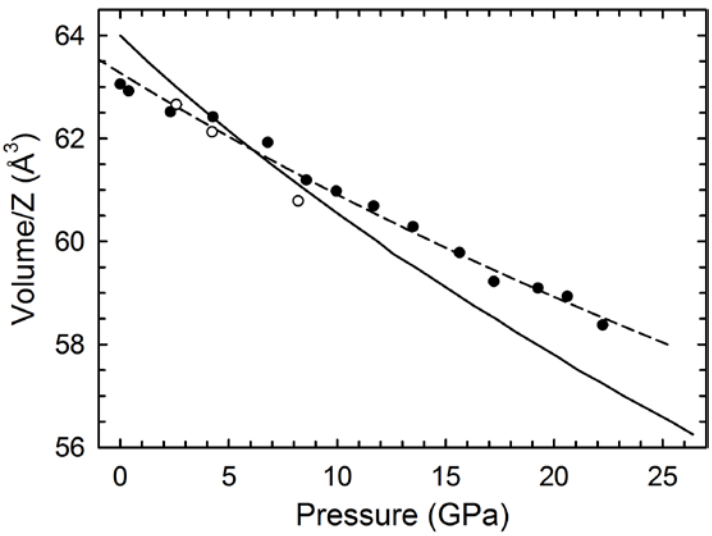

Figure A5.3.2 *Pressure dependence of the unit-cell volume per formula unit in the rh-In_2O_3 structure. Full (empty) circles are related with the upstroke (downstroke) process. Dash (solid) lines are related with the fit of 2nd (3rd) order Birch-Murnaghan equation.*

Table A5.3.1 resumes all the experimental and theoretical fits of the 2nd and 3rd Birch-Murnaghan equations. Previous results published in the literature are also shown for

comparison. The large experimental bulk modulus obtained compared with other experiments and with the *ab initio* calculations could be attributed to the high stress suffered by the sample during both HP cycles of pressure.

rh-In_2O_3				
V_0/Z (Å^3)	B_0 (GPa)	B_0'	Method	EoS type
63.27 (15)	240 (30)	4	Exp. (XRD)[a]	BM2
	213 (8)	4.62	Exp. (XRD)[b]	BM3
	215.2 (1.9)	4.74	Exp. (XRD)[c]	BM3
63.971 (10)	165.9 (9)	3.38 (7)	Theo. (GGA-PBEsol)[a]	BM3
64.04 (3)	158 (2)	4	Theo. (GGA-PBEsol)[a]	BM2
62.82	183.6	4.62	Theo. (LDA)[d]	BM3
63.25	182	3.0	Theo. (LDA)[e]	BM3
62.46	176	4.24	Theo. (LDA)[f]	BM3

[a]Reference 172. [b]Reference 52. [c]Reference 53. [d]Reference 21. [e]Reference 36. [f]Reference 173.

***Table A5.3.1**: Theoretical and experimental unit-cell volume per formula unit, bulk modulus, and its pressure derivative for the corundum-type structure (R-3c) of In_2O_3 at room pressure.*

Figure A5.3.3 shows the pressure dependence of the Raman-active mode frequencies of the RS experiment corresponding to the second upstroke as discussed in **section 5.4**, called "Results and discussion". Specifically, correspond to the analysis of the Raman spectra showed in **Figure 5.7(b)**.

Table A5.3.2 and **Table A5.3.3** show the experimental Raman-active mode frequencies at room pressure and their pressure coefficients for rh-In_2O_3 and o3-In_2O_3. Experimental parameters have been obtained by fitting measured data to a linear **(equation A5.2.5)** or a quadratic expression **(equation A5.2.6)**. Theoretical Raman-active mode frequencies at room pressure and their pressure coefficients for rh-In_2O_3 and o3-In_2O_3 along with previously reported Raman-active mode frequencies at room pressure for rh-In_2O_3 are also shown for comparison. The fits to **equations A5.2.5** and **A5.2.6** have been performed in the whole pressure interval of each phase. In o3-In_2O_3 there are some experimental Raman-active modes that could not be assigned to the theoretical ones unequivocally because they were too close to each other.

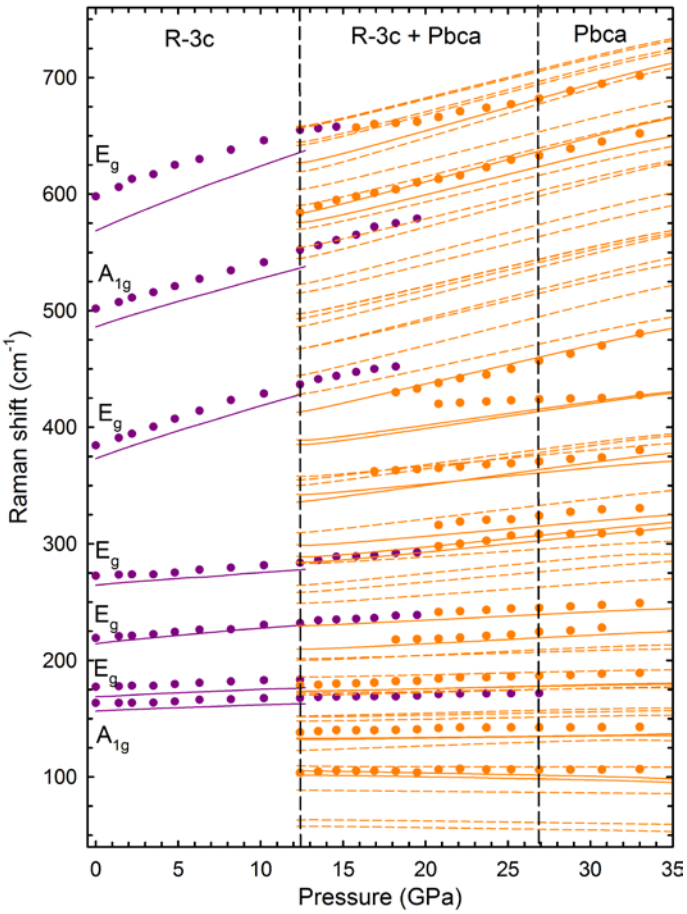

Figure A5.3.3. *Pressure dependence of the Raman-active mode frequencies of rh-In_2O_3 during the second upstroke. Symbols (lines) correspond to experimental (theoretical) data. Solid (dashed) lines represent theoretical data for observed (not observed) Raman-active modes. Violet (orange) colours correspond to the rh-In_2O_3 (o3-In_2O_3) structure. The symmetry of the rh-In_2O_3 Raman-active modes is assigned.*

rh-In_2O_3							
	***Ab initio* calculations (0 – 12.5 GPa)**			**Experimental (0 – 27 GPa)**			**Literature[a]**
Mode (Sym)	ω_0 (cm^{-1})	$\frac{\partial\omega}{\partial P}$ $\left(\frac{cm^{-1}}{GPa}\right)$	$\frac{\partial^2\omega}{\partial P^2}$ $\left(\frac{cm^{-1}}{GPa^2}\right)$	ω_0 (cm^{-1})	$\frac{\partial\omega}{\partial P}$ $\left(\frac{cm^{-1}}{GPa}\right)$	$\frac{\partial^2\omega}{\partial P^2}$ $\left(\frac{cm^{-1}}{GPa^2}\right)$	ω_0 (cm^{-1})
A_{1g}	156 (1)	0.65 (3)	-0.012 (2)	162.9 (3)	0.46 (5)	-0.004 (2)	164
E_g	169 (1)	0.73 (3)	-0.010 (2)	176.9 (3)	0.58 (13)	0.11 (5)	
E_g	214 (1)	1.54 (3)	-0.023 (2)	218.9 (4)	1.13 (10)	-0.004 (5)	221.8
E_g	265 (1)	1.11 (6)	-0.005 (5)	271.8 (6)	0.82 (14)	0.016 (7)	273
							309
E_g	373 (2)	4.91 (5)	-0.040 (4)	383.4 (5)	5.43 (14)	-0.089 (7)	385
A_{1g}	486 (2)	4.46 (6)	-0.033 (4)	501.8 (6)	4.01 (14)	0.001 (7)	504.5
E_g	569 (2)	6.14 (5)	-0.059 (4)	598.5 (9)	5.9 (3)	-0.012 (3)	596

[a]*Reference 28.*

Table A5.3.2*: Experimental and theoretical Raman-active mode frequencies of rh-In_2O_3 at room pressure and their pressure coefficients.*

o3-In_2O_3						
	***Ab initio* calculations (11 – 35 GPa)**			**Experimental (11 – 39 GPa)**		
Mode (Sym)	$\omega_0(\mathbf{cm^{-1}})$	$\frac{\partial\omega}{\partial P}\left(\frac{\mathbf{cm^{-1}}}{\mathbf{GPa}}\right)$	$\frac{\partial^2\omega}{\partial P^2}\left(\frac{\mathbf{cm^{-1}}}{\mathbf{GPa^2}}\right)$	$\omega_0(\mathbf{cm^{-1}})$	$\frac{\partial\omega}{\partial P}\left(\frac{\mathbf{cm^{-1}}}{\mathbf{GPa}}\right)$	$\frac{\partial^2\omega}{\partial P^2}\left(\frac{\mathbf{cm^{-1}}}{\mathbf{GPa^2}}\right)$
B_{2g}	100.7 (2)	0.17 (2)	-0.009 (1)	103.1 (7)	0.12 (3)	
A_g	109.1 (6)	0.29 (3)				
B_{1g}	130.5 (4)	0.14 (2)		130.9 (1.3)	0.77 (12)	-0.013 (3)
B_{3g}	135.3 (9)	-0.26 (9)	0.009 (2)			
B_{3g}	169.5 (3)	0.31 (2)		172.2 (6)	0.54 (3)	
B_{2g}	170.3 (3)	0.27 (2)				
B_{1g}	201.1 (7)	0.68 (3)		201.6 (1.3)	0.84 (5)	
A_g	221.4 (5)	0.66 (2)		228.6 (5)	0.62 (2)	
A_g	267.7 (1.6)	1.31 (6)		279 (5)	1.00 (17)	
B_{3g}	272.2 (1.7)	1.31 (7)				
B_{2g}	284.2 (1.4)	1.16 (5)		291 (3)	1.22 (8)	
B_{3g}	312.8 (7)	1.88 (3)		343.8 (1.7)	1.03 (7)	
B_{1g}	326.2 (1.1)	1.28 (4)				
B_{2g}	360.3 (1.6)	1.98 (6)		408.7 (1.1)	0.56 (4)	
B_{1g}	365.4 (1.6)	1.87 (6)				
A_g	373.5 (1.2)	3.20 (5)		368 (3)	3.34 (10)	
A_g	535 (2)	3.30 (9)		546.3 (1.0)	3.22 (5)	
B_{1g}	538.1 (1.6)	3.65 (6)				
B_{3g}	579 (2)	3.81 (8)		644 (6)	-0.08 (5)	0.055 (11)

***Table A5.3.3**: Experimental and theoretical Raman-active mode frequencies of o3-In_2O_3 at room pressure and their pressure coefficients.*

Chapter 6

Synthesis and high-pressure study of corundum-type In_2O_3

6.1. Abstract

This work reports the HP-HT synthesis of pure rh-In_2O_3 from its most stable polymorph, c-In_2O_3, using a MA press. Structural and vibrational properties of rh-In_2O_3 have been characterized by means of angle-dispersive powder XRD and RS measurements at HPs which have been compared to structural and lattice dynamics *ab initio* calculations. The EoS and the pressure dependence of the Raman-active modes of the corundum-type phase are reported and compared to those of rh-Al_2O_3 (known as corundum or α-Al_2O_3). It can be concluded that rh-In_2O_3 is stable under compression up to 14 GPa (see **Scheme 6.1**) and it gradually transforms to the o3-In_2O_3 between 14 and 26 GPa. The bulk modulus, axial compressibilities, and the pressure range of stability of the corundum-type phase in group-IIIA sesquioxides A_2O_3 (*A* = Al, Ga, and In) are discussed.

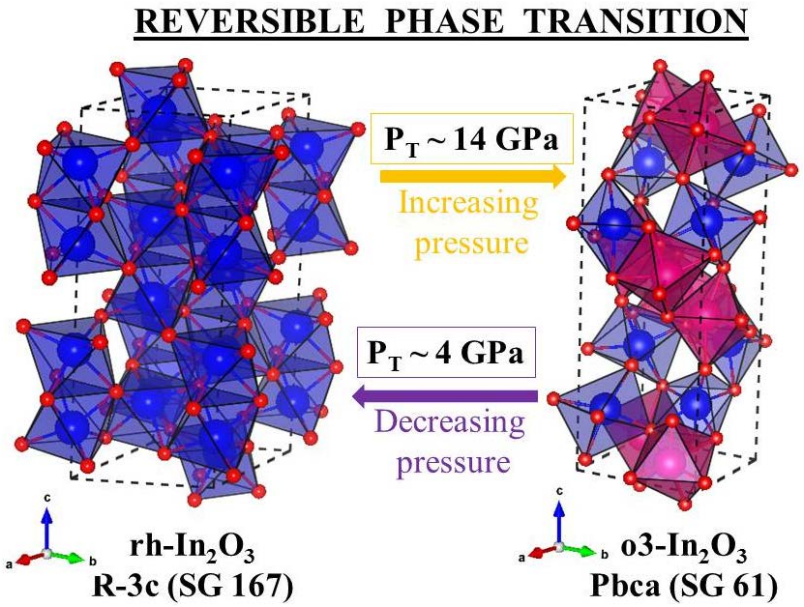

Scheme 6.1: *Stability pressure range of rh-In_2O_3.*

6.2. Introduction

The properties of the HP phases of In_2O_3, some of which can be obtained in a metastable form at ambient conditions, are largely unknown despite their important applications **[40−44]**. In particular, a decrease on the bulk modulus is expected for the corundum-type structure of sesquioxides A_2O_3 (A = Al, Ga, In) on increasing the cation ionic radius. In fact, Cr^{3+}-doped Ga_2O_3 was already postulated as a possible substitute of ruby (Cr^{3+}-doped Al_2O_3) for pressure sensor **[174]**. Similarly, corundum-type Cr^{3+}-doped In_2O_3 could be more sensitive than ruby as pressure calibrant. With this aim, the knowledge of the EoS and stability range of rh-In_2O_3 is mandatory. In this regard, the EoS of rh-In_2O_3 has been studied by means of theoretical calculations **[21, 36, 173]**, but the experimental determination of its bulk modulus at ambient pressure has only been estimated by extrapolation of HP data to ambient pressure **[52, 53]**. Furthermore, there is a controversy regarding the pressure range of stability of rh-In_2O_3. Gurlo et al. showed that rh-In_2O_3 is stable at ambient temperature between ambient pressure and 30 GPa **[40, 42]**; however, in a recent study we have reported that rh-In_2O_3 undergoes a transformation to o3-In_2O_3 above 12.4 GPa at room-temperature **[172]**.

In this paper, we focus on the structural and vibrational properties of rh-In_2O_3 under pressure. For that purpose, we have synthesized rh-In_2O_3 in a MA press and characterized it by angle-dispersive powder XRD and RS measurements at HP. Experimental structural and vibrational properties of rh-In_2O_3 have been analyzed with the help of theoretical *ab initio* calculations.

Our study has allowed us to obtain the bulk modulus of rh-In_2O_3 at ambient pressure in a more accurate way and shows that the corundum-type phase is only stable up to 14 GPa, because it undergoes a phase transition to the o3-In_2O_3. These results are in good agreement with our previous work **[173]**. A comparison between the properties of rh-In_2O_3 and rh-Al_2O_3 at different pressures is discussed and extended to other sesquioxides.

6.3. Experimental details

Pure rh-In_2O_3 was synthesized from commercial c-In_2O_3 (99.99% pure from Sigma-Aldrich Inc.) as starting material using a Sumitomo 1200 tons MA press to generate HP-HT conditions. c-In_2O_3 was compacted and placed inside a 25 μm thickness Re capsule. This metallic capsule was located in a high resistivity graphite furnace, using a MgO cylinder as a spacer. The MgO cylinder isolates electrically the metal capsule from the heater and serves together with graphite as PTM. The sample assembly is loaded into a 18 mm MgO:Cr octahedra which is compressed between eight tungsten carbide anvils in the 18/11 multi-anvils configuration. c-In_2O_3 was maintained for 6 h at HP-HT conditions (12 GPa and 1375 °C). Subsequently, the sample was quenched in temperature and decreased slowly in pressure. The recovered sample was composed of different micron sized crystals of rh-In_2O_3. These crystals were annealed to 300 °C during 3 h in a furnace to improve the crystallinity of the sample and ground to obtain fine rh-In_2O_3 powder. **Appendix 6.1** shows the "P-T phase diagram" starting from c-In_2O_3 and rh-In_2O_3 samples studied during this thesis work.

Room-temperature angle-dispersive powder XRD and RS experiments at HP were conducted in annealed rh-In_2O_3 samples up to 15.9 and 30.0 GPa, respectively, in a membrane-type DAC. In both experiments, a powder sample was loaded inside a 150 μm diameter hole drilled in an inconel gasket together with a mixture of MEW in a 16:3:1 proportion as a PTM. For pressure calibration in angle-dispersive powder XRD and RS measurements we introduced inside the pressure cavity Cu powder **[110**] and ruby **[109]**, respectively. Our measurements in rh-In_2O_3 allow direct comparison with previous experiments in isostructural compounds, e.g., rh-Al_2O_3, studied with different PTM.

On the one hand, angle-dispersive powder XRD measurements at different pressures were performed in the MSPD beamline **[118]** at ALBA synchrotron facility. This beamline is equipped with Kirkpatrick-Baez mirrors to focus the monochromatic beam and a Rayonix CCD detector with a sensitive area of 165 mm. We used a wavelength of 0.4246 Å and the

sample−detector distance during the experiment was set to 244.0347 mm (refined value). The 2-D diffraction images were integrated with FIT2D software **[120]**. Lattice parameters of XRD patterns were obtained with Rietveld refinements performed using POWDERCELL **[121]** and GSAS **[122]** program packages. On the other hand, RS measurements at ambient temperature and different pressures were excited using the 632.8 nm HeNe laser and collected in backscattering geometry with a Horiba Jobin Yvon LabRam HR UV spectrometer equipped with a thermoelectrically cooled multichannel CCD detector (resolution below 2 cm^{-1}). RS spectra have been analyzed by fitting Raman peaks with a Voigt profile by fixing the Gaussian line width to the experimental setup resolution in order to obtain the three free parameters of the Lorentzian profile.

6.4. Theoretical calculations

Total-energy *ab initio* calculations were performed for both rh-In_2O_3 and α-Al_2O_3 within the DFT **[124]** using the VASP **[147]**. In particular, we have used the PAW **[125]** scheme implemented in this package. The PAW method takes into account the full nodal character of the all-electron charge density distribution in the core region. The GGA was used for the description of the exchange-correlation energy with the PBEsol prescription **[130]**. A set of plane waves was employed and extended up to a kinetic energy cutoff of 520 eV due to the presence of oxygen using dense special k-point grids appropriate to sample the BZ. The cutoff energy and the k-point sampling employed ensure a high convergence of 1−2 meV per formula unit in the total energy as well as an accurate calculation of the forces on the atoms. At each selected volume, the structure was fully relaxed to their optimized configuration through the calculation of the forces on atoms and the stress tensor **[130]**. For each relaxed configuration, the forces on the atoms were smaller than 0.005 eV/Å, and the deviations of the stress tensor from a diagonal hydrostatic form were less than 0.1 GPa. We obtain a set of E, V, and P (pressure, like others energy derivatives, is obtained theoretically from the value of the calculated stress tensor) for each phase as well as the evolution of its structural properties with increasing pressure.

We have also performed lattice dynamics calculations of the phonon modes in rh-In_2O_3 at the center of the BZ (Γ point). Our theoretical results enable us to assign the Raman-active modes observed in rh- In_2O_3 (see **Figure 6.1 (b)**) because calculations provide information about the symmetry of the modes and polarization vectors, which is not readily accessible in the present experiment. Highly converged results on forces are required for the calculation of the

dynamical matrix. We used the direct force constant approach (or supercell method) **[131]**. The construction of the dynamical matrix at the Γ point of the BZ involves separate calculations of the forces in which a fixed displacement from the equilibrium configuration of the atoms within the cell is considered. The use of crystal symmetries aids by reducing the number of such independent displacements, and consequently the computational effort required to study the different structures considered in this work. Diagonalization of the dynamical matrix provides both the frequencies of the normal modes and their polarization vectors. This theoretical procedure was also used to explain satisfactorily the pressure dependence of the structural and vibrational properties in c-In_2O_3 up to 30 GPa with similar experimental conditions as those in this work **[161]**.

6.5. Results and discussion

6.5.1. Characterization of samples at ambient conditions.

Figure 6.1 shows angle-dispersive powder XRD pattern **(a)** and RS spectra **(b)** at ambient pressure of both as-grown and annealed samples of rh-In_2O_3. Typical CCD images of XRD are shown in **Figure 6.S1** in the Supplementary Material (**section 6.7.**).

The powder XRD pattern of the annealed sample has been indexed with DICVOL06 **[175]** obtaining lattice parameters a = 5.4854 Å and c = 14.5107 Å in an hexagonal crystal system with figures of merit M(17) = 27.2 and F(17) = 75.2. The observed systematic extinctions correspond with the *R-3c* space group of the corundum-type structure. Rietveld refinement of experimental angle-dispersive powder XRD pattern of the annealed sample at ambient conditions yields experimental lattice parameters and atomic positions which compare well to those from our *ab initio* theoretical calculations (see **Table 6.1**) and also with previous experiments and calculations.

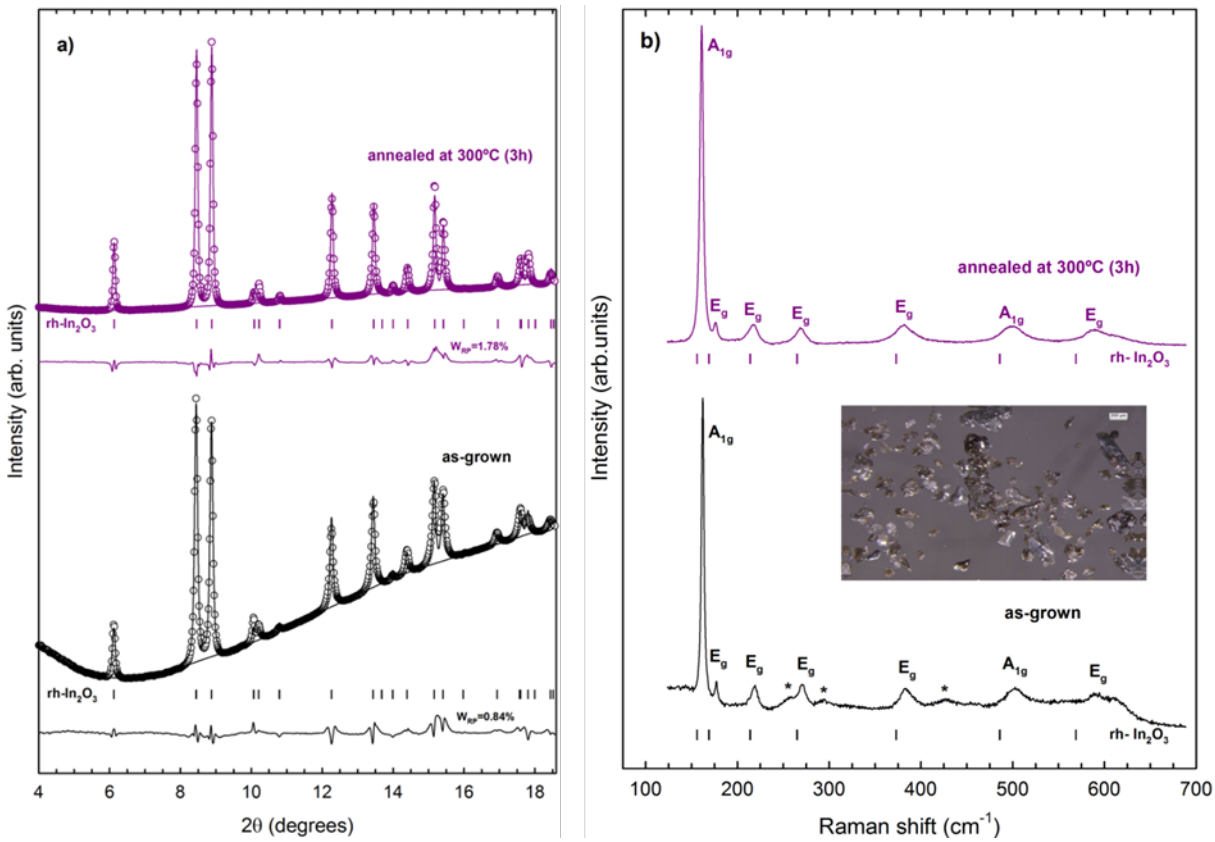

Figure 6.1: ***(a)*** *Angle-dispersive powder XRD pattern and* ***(b)*** *RS spectrum of rh-In_2O_3 at ambient pressure. In both cases, the bottom pattern or spectrum corresponds to the as-grown sample while the upper one corresponds to the annealed sample. The seven first-order Raman-active modes theoretically predicted for the corundum phase are marked with vertical ticks at the bottom. Three modes not corresponding to first-order modes of rh-In_2O_3 are observed in the as-grown sample (marked with asterisk).* ***Inset:*** *Picture of the as-grown rh-In_2O_3 microcrystals.*

a **(Å)**	***c*** **(Å)**	**Method**
5.483	14.493	[a]Experimental
5.487	14.510	[b]Experimental
5.490	14.520	[c]Experimental
5.481	14.498	[d]Experimental
5.519	14.554	[a]Theoretical
5.493	14.424	[e]Theoretical
5.479	14.415	[f]Theoretical

rh-In_2O_3		Experimental			Theoretical		
Atom	**Wyckoff site**	**x**	**y**	**z**	**x**	**y**	**z**
In	12c	0	0	0.144[a] 0.166[c]	0	0	0.1426[a] 0.1424[g] 0.1423[h]
O	18e	0.295[a] 0.305[c]	0	0.25	0.2958[a] 0.2961[g] 0.2954[h]	0	0.25

[a]Reference 63. [b]References 23 and 25. [c]Reference 24. [d]Reference 44. [e]Reference 172. [f]Reference 174. [g]Reference 21. [h]Reference 173.

Table 6.1: *Experimental (from Rietveld refinement) and theoretical values of the lattice parameters and atomic positions obtained for the rh-In_2O_3 at ambient conditions. Values of previous works are given for comparison. The same atomic setting is employed to facilitate the comparison.*

The corundum-type structure has a primitive unit cell with 2 formula units. Group theory predicts that this structure should have 30 vibrational modes with the irreducible representation **[171],**

$$\Gamma_{30} = 2A_{1g}(R) + 2A_{2u}(IR) + 5E_g(R) + 4E_u(IR) + 2A_{1u} + 3A_{2g} + A_{2u} + E_u \qquad \textbf{(6.1)}$$

where E modes are doubly degenerated. These vibrational modes can be divided into 3 acoustic modes (A_{2u} and E_u) and 27 optical modes, thus resulting in 7 Raman-active (R) modes, 6 infrared-active (IR) modes, and 5 silent (A_{1u} and A_{2g}) modes. In fact, **Figure 6.2 (b)** shows seven Raman-active modes in our samples. The Raman spectrum is dominated by the lowest frequency A_{1g} mode located at 161 cm^{-1} at ambient pressure. The number of Raman-active modes and the frequencies and intensities are in good agreement with previous studies reporting the synthesis of rh-In_2O_3 **[28, 38]**. Therefore, our RS measurements confirm the corundum-type structure of our samples. Three broad extra Raman-modes, marked with asterisks in **Figure 6.1 (b)**, are observed in as-grown samples and disappear after the annealing process. These extra modes, whose origin is unknown but which do not correspond to other known polymorphs of In_2O_3, could be second-order modes which are better observed in slightly defective samples with small grains and low-crystalline quality than in annealed samples with larger grains and better crystalline quality.

6.5.2. XRD measurements at high pressures.

Figure 6.2 (a) displays a selection of the experimental room-temperature angle-dispersive powder XRD patterns of rh-In_2O_3 at different pressures up to 15.9 GPa. Bragg reflections

located at ~11.7 and 13.5 degrees at 1.2 GPa correspond to (111) and (200) cubic (*Fm-3m*) Cu, respectively, and were used to determine the pressure inside the DAC. The rest of the Bragg reflections at 1.2 GPa can be attributed to rh-In_2O_3. Above 5 GPa, hexagonal (*P63/mmc*) Re Bragg reflections (see # marks) appear in the XRD pattern. Probably, a small flake of Re metallic layer, which protects the sample from possible contaminations during the synthesis process, has been unintentionally mixed with the powdered sample. Note that Rietveld refinement was performed using the complete XRD patterns in order to keep as much information as possible from our experimental data. In the experiment, the pressure was smoothly increased up to 15.9 GPa and then released down to 1 GPa (see XRD pattern of the recovered sample in **Figure 6.2 (a)**). Diffractograms up to 13.5 GPa can be indexed with rh-In_2O_3. At 14.5 GPa, the beginning of the phase transition from rh-In_2O_3 to o3-In_2O_3 is observed. Both structures coexist until the maximum pressure reached in the XRD experiment (see Rietveld refinements in **Figure 6.2 (b)**). **Tables 6.S1**, **6.S2**, and **6.S3** (in the Supplementary Material) summarize the experimental lattice parameters and atomic positions obtained from Rietveld refinements shown in **Figure 6.2 (b)** and their comparison with theoretical calculations at similar pressures. The results for both rh-In_2O_3 and o3-In_2O_3 are in good agreement with our previous results **[172]**. Consequently, the larger stability of the corundum-type phase previously reported by Gurlo *et al.* could be related to the nanocrystalline size of the samples synthesized by those authors, which were obtained by compressing nanocrystalline c-In_2O_3 **[40]**. Finally, we want to comment that rh-In_2O_3 is recovered on decreasing pressure, thus showing the reversibility of the rh-In_2O_3 to o3-In_2O_3 transition in good agreement with our previous work **[172]**.

We must note that Bragg reflections in our experiment show a slight broadening with increasing pressure above 10 GPa which could be due to a slight loss of quasi-hydrostatic conditions of the PTM **[176]**. In this regard, small non-hydrostatic stresses should not influence the structural stability of relatively uncompressible (B_0 > 150 GPa) compounds as sesquioxides **[177]**. We will show below that this hypothesis is well supported by the good agreement between experiments and theoretical calculations.

Figure 6.3 graphs the experimental and theoretical pressure dependence of the unit-cell volume per formula unit of rh-In_2O_3. Both experimental and theoretical data were fitted to a third-order Birch−Murnaghan EoS **[62, 178]** in the hydrostatic region of the PTM (below 11 GPa). A rather good agreement between the experimental and theoretical EoS is found. Taking into account the unit-cell volume per formula unit of rh-In_2O_3 at room pressure (V_0/Z

= 62.86 (3) Å^3), we have estimated the density (ρ_{rh} = 7.398 (4) g/cm^3) of rh-In_2O_3 at ambient pressure in good agreement with previous estimations **[24, 25]**. These values can be compared to the values reported in the literature for unit-cell volume per formula unit (V_0/Z = 64.28 Å^3) and density (ρ_c = 7.179 g/cm^3) of c-In_2O_3 at room pressure **[172]**.

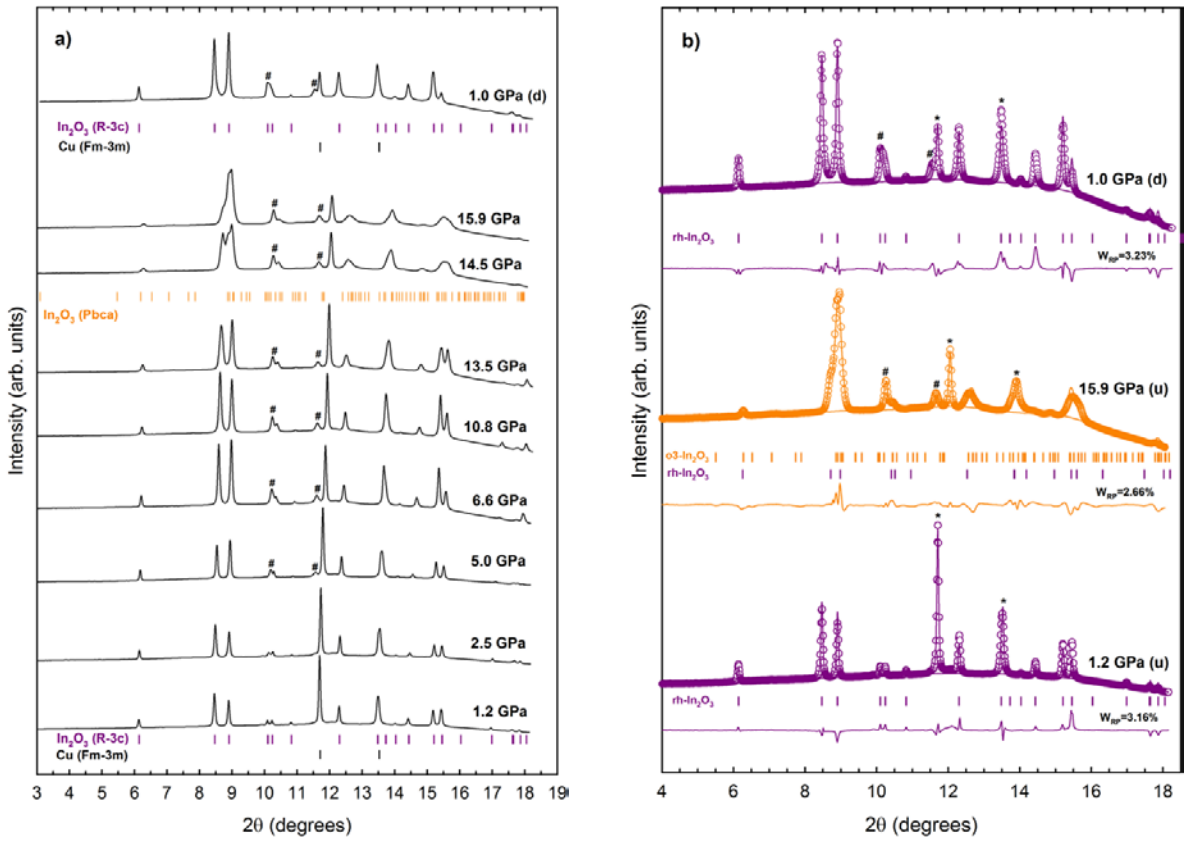

***Figure 6.2: (a)**. Selected XRD patterns of rh-In_2O_3 at several pressures up to 15.9 GPa. Diffractograms have been shifted vertically for clarity. Different Bragg reflections are assigned in the graph to their corresponding phase: rh-In_2O_3 (R-3c) (purple line), cubic (Fm-3m) Cu (black line), and o3-In_2O_3 (Pbca) (orange line). Some impurities of hexagonal ($P6_3/mmc$) Re are marked with (#). **(b)** Refinements of the experimental angle-dispersive XRD patterns were performed on upstroke (u) at 1.2 GPa with the rh-In_2O_3 structure, at 15.9 GPa with a mixture of rh-In_2O_3 and o3-In_2O_3 phases and on downstroke (d) at 1.0 GPa with the rh-In_2O_3 structure. Residuals of the Rietveld refinements are plotted below the experimental (circles) and fitted (lines) XRD profiles. Bragg reflections of Cu are assigned by (*) and some impurities of hexagonal ($P6_3/mmc$) Re are marked with (#)*

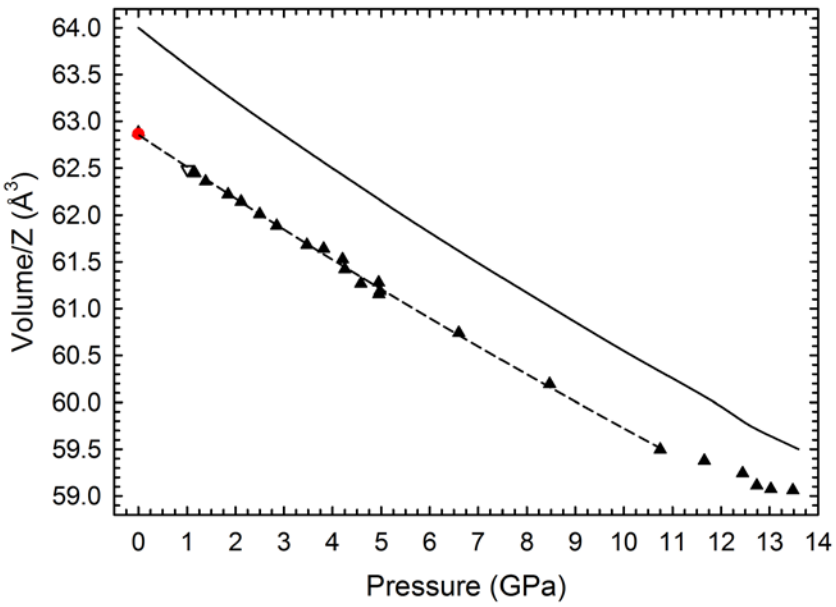

Figure 6.3: *Pressure dependence of the unit-cell volume per formula unit in rh-In_2O_3. Experimental data (triangles) during the upstroke (full) and downstroke (empty). The value at ambient pressure from Bekheet et al.* ***[44]*** *(red circle) is also shown for comparison. 3rd order Birch−Murnaghan EoS curves fitted to experimental data (dashed line) in the hydrostatic region of the PTM (below 11 GPa) and to theoretical data (solid line) are also shown.*

Our experimental bulk modulus at ambient pressure for rh-In_2O_3 (B_0 = 176 (7) GPa) matches in between our theoretical GGA-PBESol calculations (158 GPa) and previous calculations (176−184 GPa) using LDA **[21, 36, 173]**. Clearly, our experimental bulk modulus for rh-In_2O_3 is consistent with theoretical values and considerably smaller than previous experimental values (212−215 GPa) **[52, 53]**, which were obtained from XRD measurements performed only in the HP region.

Table 6.2 summarizes our experimental and theoretical results for the EoS of rh-In_2O_3 along with results from the literature for several sesquioxides in different phases. It is rather curious that the bulk modulus of rh-In_2O_3 is smaller than that of c-In_2O_3 despite the smaller unit-cell volume per formula unit of the rhombohedral corundum-type phase compared to the cubic phase. In fact, a unit-cell volume per formula unit (density) decrease (increase) of around 3.0% is found when the crystal structure goes from c-In_2O_3 to rh-In_2O_3. Both the smaller experimental unit-cell volume per formula unit and bulk modulus of rh-In_2O_3 compared to c-In_2O_3 are in good agreement with our *ab initio* calculations which show similar trends (see **Table 6.2**). In contrast, a much smaller bulk modulus has been found in rh-In_2O_3 (176 GPa) than in the corundum-type phases of Al_2O_3 and Ga_2O_3, whose bulk moduli are well above 220

GPa (see **Table 6.2**) **[36, 152, 179]**. This trend is in good agreement with the larger unit-cell volume per formula unit of the corundum-type phase in In_2O_3 than in Ga_2O_3 and Al_2O_3 and is also in good agreement with available theoretical calculations (especially with our own calculations in both In_2O_3 and Al_2O_3 using GGA-PBESol for the sake of comparison). Thus, the agreement of experimental and theoretical results supports the goodness of our calculations. It is also noteworthy that the bulk modulus of rh-In_2O_3 is much smaller than the bulk modulus of corundum-type Ti_2O_3 (> 206 GPa) **[180, 181]**, and Cr_2O_3 (222−231 GPa) **[182, 183]** taking fixed $B_0' = 4$. A comparison with corundum-type Fe_2O_3 and V_2O_3 is not possible since these two sesquioxides show controversial results with bulk moduli ranging from 150 to 260 GPa **[182, 184−188]**. Our theoretical estimations for both compounds are of the order or larger than 200 GPa and at present we have no idea for the possible deviation between experimental and calculated bulk moduli in these two compounds. In summary, our structural results confirm that rh-In_2O_3 is one of the sesquioxides with corundum-type structure with the smallest bulk modulus.

	Phase	V_0/Z (Å^3)	B_0 (GPa)	B_0'	Method	EoS type
Al_2O_3	R-3c	42.51	257 (6)	4	Exp. (XRD)[a]	BM2
	R-3c	42.8(4)	257 (1)	4	Theo. (GGA-PBEsol)[b]	BM2
	R-3c	42.41	240 (5)	3.97	Theo. (LDA)[c]	BM3
Ga_2O_3	R-3c	48.16 (4)	223 (2)	4	Exp. (XRD)[d]	BM2
	R-3c	47.24	243	4.0	Theo. (LDA)[d]	BM3
In_2O_3	R-3c	62.86 (3)	180 (7)	3.2 (1.2)	Exp. (XRD)[b]	BM3
	R-3c	62.87 (3)	176 (7)	4	Exp. (XRD)[b]	BM2
	R-3c		213 (8)	4.62	Exp. (XRD)[e]	BM3
	R-3c		215.2 (1.9)	4.74	Exp. (XRD)[f]	BM3
	R-3c	63.968 (12)	162.8 (2.0)	3.8 (3)	Theo. (GGA-PBEsol)[b]	BM3
	R-3c	63.993 (13)	161.3 (2.0)	4	Theo. (GGA-PBEsol)[b]	BM2
	R-3c	62.82	183.6	4.62	Theo. (LDA)[g]	BM3
	R-3c	63.25	182	3.0	Theo. (LDA)[d]	BM3
	R-3c	62.46	176	4.24	Theo. (LDA)[h]	BM3
	Ia-3	64.78	144 (8)	4	Exp. (XRD)[d]	BM2
	Ia-3	64.28 (13)	184 (10)	4	Exp. (XRD)[i]	BM2
	Ia-3	65.72 (2)	169.4(1.2)	4	Theo. (GGA-PBEsol)[i]	BM2

[a]Reference 62. [b]Reference 63. [c]Reference 189. [d]Reference 36. [e]Reference 52. [f]Reference 53. [g]Reference 21. [h]Reference 173. [i]Reference 172.

Table 6.2: *Comparison of theoretical and experimental unit-cell volume per formula unit, bulk modulus, and its pressure derivative for the corundum-type structure (R-3c) of Al_2O_3, Ga_2O_3, and In_2O_3 at room pressure. Values for cubic-type (Ia-3) In_2O_3 are also given for comparison.*

Figure 6.4 shows the experimental and theoretical pressure dependence of the *a* and *c* lattice parameters in rh-In_2O_3 in the hydrostatic region of the PTM. For comparison, we have included in **Figure 6.4** the lattice parameters obtained in the downstroke and those obtained at ambient pressure in crystals of rh-In_2O_3 by Bekheet et al **[44]**. Both *a* and *c* parameters (*x* = a, c) have been fitted to a modified Murnaghan's equation of state with free parameters x_0, B_0, and B_0'.

$$x = x_0 \left(1 + \frac{B_0'}{B_0} P\right)^{-\left(\frac{1}{3B_0'}\right)} \quad \textbf{(6.2)}$$

The results of these fits are shown in **Table 6.3**. The axial compressibilities of the *a*- and *c*-axis defined as:

$$\kappa_x = \frac{-1}{x}\frac{\partial x}{\partial P} \quad \textbf{(6.3)}$$

and can be obtained as:

$$\kappa_x = \frac{1}{3B_0} \quad \textbf{(6.4)}$$

with the B_0 values obtained from the fit of the lattice parameters to the equation **(6.2)**. It can be observed that *c* lattice parameter is more compressible than *a* lattice parameter. In fact, there is a much better agreement between the experimental and theoretical evolution of the *a* lattice parameter than of *c* lattice parameter with pressure, despite both experimental and theoretical data show similar trends. Furthermore, one can compare the relative compressibilities of the experimental lattice parameters of isostructural rh-In_2O_3 and rh-Al_2O_3 **[77]**. The experimental relative compressibility of *a* (*c*) lattice parameter defined by $\Delta a/a_0$ ($\Delta c/c_0$) is 1.57% (3.69%) for rh-In_2O_3 and 0.96% (1.34%) for rh-Al_2O_3 in the same pressure range (up to 15.9 GPa) **[109, 179, 182, 191−193]**. Consequently, we can conclude that the major contribution to the increase of sensitivity of the crystalline structure of rh-In_2O_3 to pressure compared to rh-Al_2O_3 comes from the larger compressibility along the *c* axis in rh-In_2O_3 than in rh-Al_2O_3.

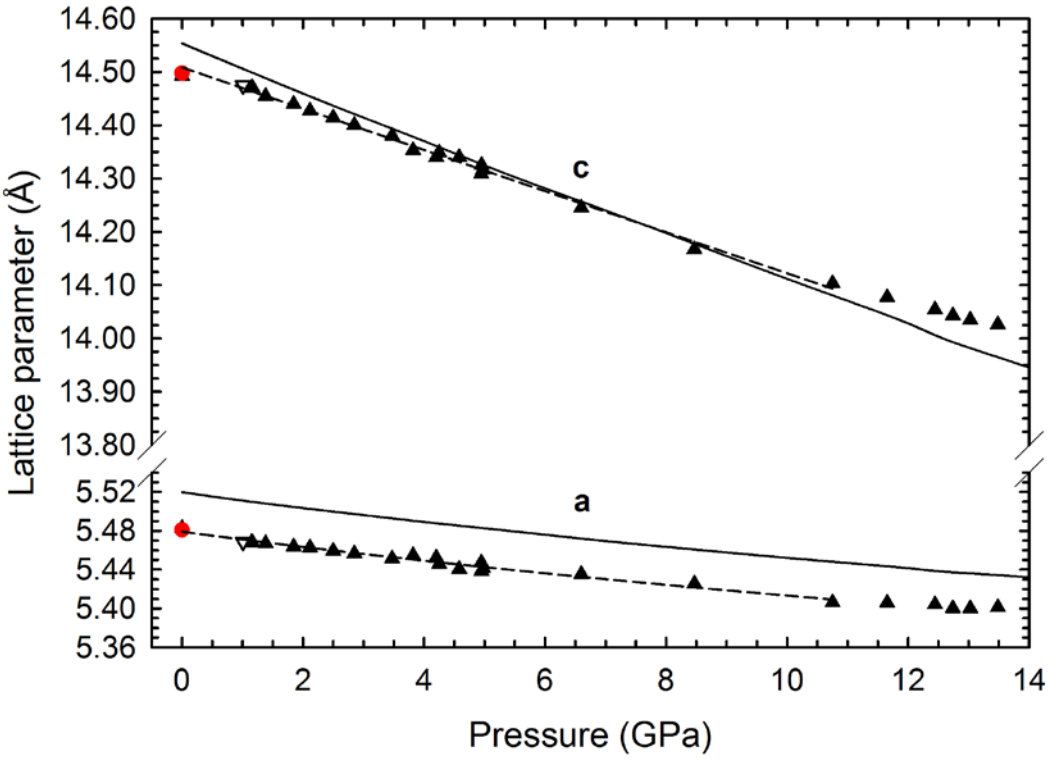

Figure 6.4: *Pressure dependence of the lattice parameters in rh-In_2O_3. Experimental data (triangles) during the upstroke (full) and downstroke (empty). The values at ambient pressure from Bekheet et al.* ***[44]*** *(red circle) are shown for comparison. Experimental data fit (dashed line) to the modified Murnaghan's equation in the hydrostatic region of the PTM and theoretical ab initio calculations (solid line) are also shown. Note that a different scale has been used for the vertical axes.*

a_0 (Å)	B_{0a} (GPa)	B_{0a}'	κ_a (TPa^{-1})	c_0 (Å)	B_{0c} (GPa)	B_{0c}'	κ_c (TPa^{-1})	Method
5.479 (2)	220 (30)	11.8	1.5 (2)	14.511 (5)	121 (7)	0.48	2.75 (16)	Exp. (XRD)
5.5200 (3)	216 (3)	11.8 (4)	1.54 (2)	14.552 (1)	106.0 (9)	0.48 (11)	3.14 (3)	Theo. (GGA-PBEsol)

Table 6.3: *Theoretical and experimental lattice parameters, bulk modulus, and pressure derivative of bulk modulus at ambient pressure in rh-In_2O_3 obtained from a fit to modified Murnaghan's equation. The axial compressibilities κ_a and κ_c for the a- and c-axis are also included.*

In order to understand the larger compressibility of rh-In_2O_3 compared to rh-Al_2O_3 we have studied the evolution under pressure of the theoretically calculated cation−anion distances in both compounds (see **Figure 6.5**).

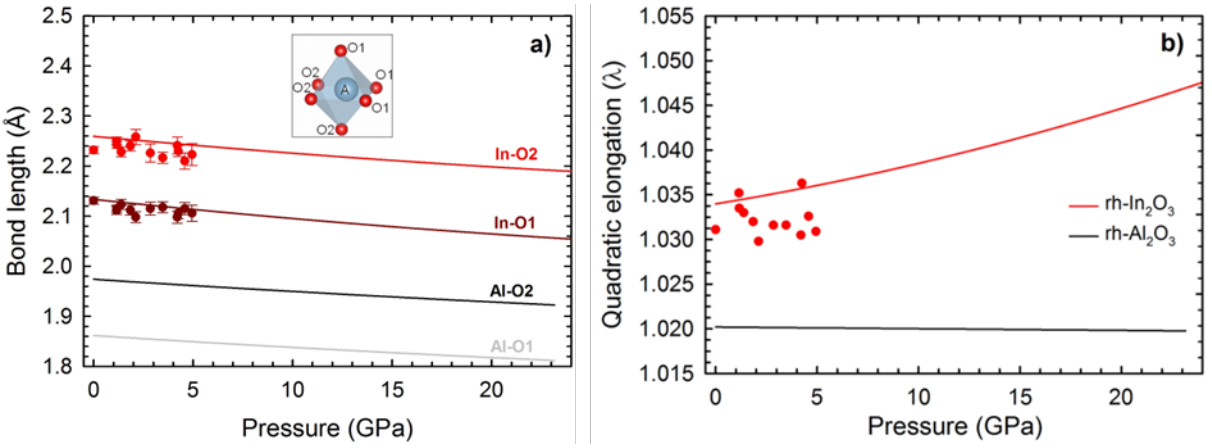

Figure 6.5: (a) *Pressure dependence of the experimental (circles) and theoretical (solid lines) cation-oxygen bond lengths of the AO_6 polyhedron (A = Al, In) in corundum-type A_2O_3 sesquioxides.* ***Inset:*** *Representation of the AO_6 polyhedron of the corundum phase in A_2O_3 sesquioxides, where the cation is not located in the center of the polyhedron.* ***(b)*** *Pressure dependence of the experimental (circles) and theoretical (solid lines) quadratic elongation of rh-Al_2O_3 and rh-In_2O_3.*

Unlike the cubic bixbyite-type structure of A_2O_3 sesquioxides, which has two non-equivalent *A* atoms surrounded by six O atoms, the corundum-type structure is characterized by only one type of *A* atoms (12c Wyckoff position). The *A* atom is surrounded by six O atoms (18e Wyckoff position) forming an octahedron composed of two connected trigonal pyramids (see inset of **Figure 6.5**). This structure is then structurally characterized by *a* and *c* lattice parameters and two internal parameters: the *z* internal parameter (off-center position in the octahedra) of the *A* atom and the *x* atomic coordinate of the O atom. In the most regular atom distribution of the corundum-type structure, *A* atoms are located at (0, 0, 1/6), while O atoms are located at (1/3, 0, 1/4). Therefore, our experimental and theoretical data at ambient pressure (see **Table 6.1**) indicate that rh-In_2O_3 has a slightly distorted corundum-type structure. **Figure 6.S2** shows the theoretical and experimental atomic positions (*x* of O and *z* of In) obtained from Rietveld refinements up to 5 GPa. Moreover, the pressure dependence (quadratic fit) of the theoretical atomic positions of O and In in rh-In_2O_3 is shown in **Table 6.S4**. The good agreement between experimental and theoretical data observed in **Figure 6.S2** gives confidence to use our calculated data at higher pressures in order to discuss the pressure dependence of cation−anion bond distances.

The octahedral volume of rh-In_2O_3 at ambient pressure (13.47 $Å^3$) is larger than that of rh-Al_2O_3 (9.14 $Å^3$). The larger volume for rh-In_2O_3 can be explained by the larger In ionic radius compared with that of Al. The main difference between both compounds is that octahedra are

slightly more distorted in rh-In_2O_3 than in rh-Al_2O_3, as evidenced by the slightly large difference in the bond distances between the two trigonal pyramids in both compounds: 2.1341 Å (In−O1) and 2.2599 Å (In−O2) for rh-In_2O_3 and 1.8617 Å (Al−O1) and 1.9741 Å (Al−O2) for rh-Al_2O_3. The theoretical values of the In−O distances in rh-In_2O_3 are in good agreement with our experimental values (2.1624 and 2.1836 Å) and experimental values previously reported (2.07 and 2.27 Å) **[24]**. **Figure 6.5 (a)** shows the experimental and theoretical pressure dependence of the *A*−O (*A* = Al, In) relative bond distances in rh-In_2O_3 and rh-Al_2O_3 and **Table 6.S5** (in the Supplementary Material) shows the linear fit of these theoretical data. As observed, the cation−anion bond lengths decrease with pressure at a higher rate in rh-In_2O_3 than in rh-Al_2O_3. This different behavior shows that rh-In_2O_3 is more compressible (smaller bulk modulus) than rh-Al_2O_3 in good agreement with our experimental volume data.

Another interesting issue of the calculations is the rather different decrease rate of the two cation−anion bond distances (In−O1 and In−O2) for the octahedron of rh-In_2O_3 compared to those of rh-Al_2O_3 (Al−O1 and Al−O2), which decrease at a similar rate. This result indicates a quite different deformation of the AO_6 polyhedron in both compounds. In order to understand better the deformation in the octahedron with increasing pressure **Figure 6.5 (b)** displays the pressure dependence of the quadratic elongation (λ) for rh-Al_2O_3 and rh-In_2O_3, which gives a reliable indication of the distortion in the octahedron **[194]**. This parameter has been calculated by the average of the distortion in the bond-lengths implied in the octahedron, as described by the equation **(6.5)**,

$$\langle \lambda \rangle = \frac{1}{n} \sum_{i=1}^{n} \left(\frac{l_i}{l_0} \right)^2 \qquad \textbf{(6.5)}$$

where l_i is the cation−anion bond length that forms the real polyhedron and l_0 is the theoretical bond length in the most regular polyhedron. **Table 6.S6** shows the linear and quadratic fit of the quadratic elongation for rh-Al_2O_3 and rh-In_2O_3, respectively. As observed, the mean quadratic elongation of the polyhedron of rh-In_2O_3 increases with pressure; i.e., the octahedron becomes more distorted as pressure increases. A similar behavior has been found in hematite (rh-Fe_2O_3) **[184**], whereas the opposite is observed in rh-Al_2O_3, whose polyhedron becomes more regular with increasing pressure. This trend could explain the high stability of rh-Al_2O_3 under pressure. In fact, theoretical and experimental studies show the phase transition from rh-Al_2O_3 to the Rh_2O_3−II-type (*Pbcn*) structure to occur above 96 GPa **[194]**.

In contrast, rh-In_2O_3 shows a much lower phase transition pressure (14 GPa) from rh-In_2O_3 to o3-In_2O_3.

6.5.3. RS Measurements at High Pressures.

Selected Raman spectra of rh-In_2O_3 at different pressures are reported on upstroke to 30.0 GPa (**Figure 6.6 (a)**) and downstroke to ambient pressure (**Figure 6.6 (b)**).

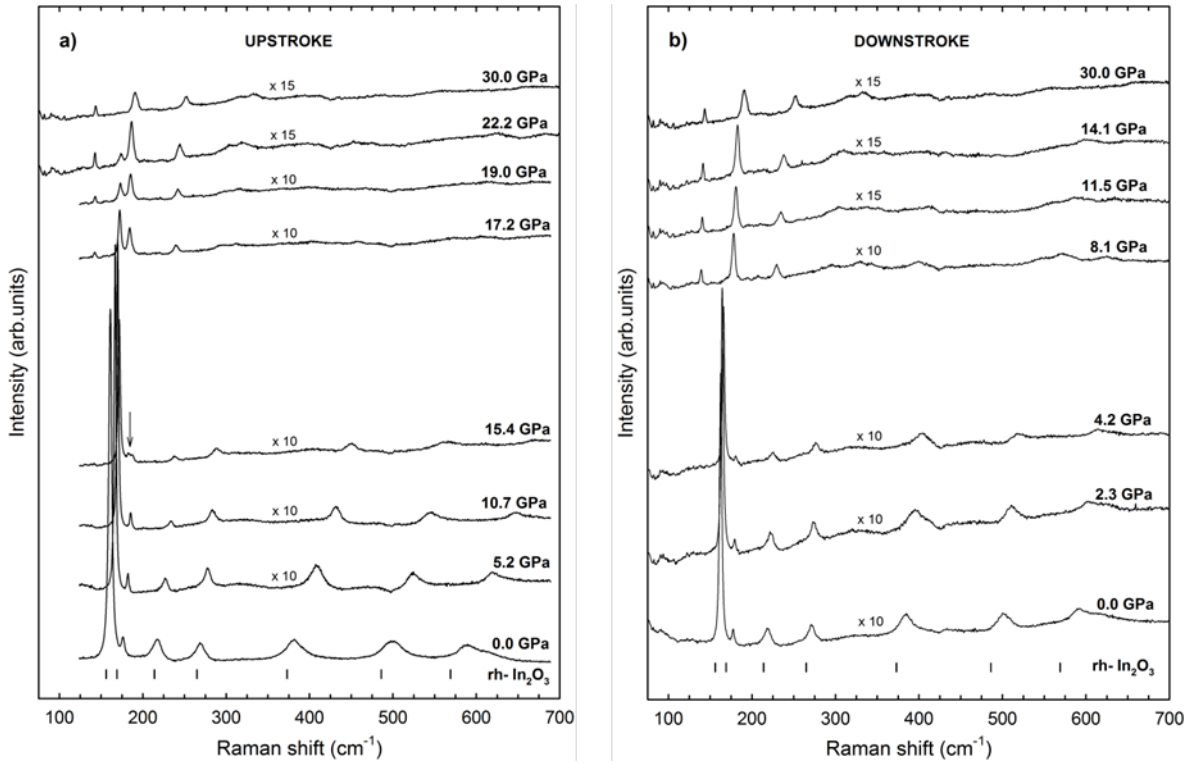

Figure 6.6: *Selected RS spectra of rh-In_2O_3 at different pressures on upstroke up to 30.0 GPa* ***(a)*** *and on downstroke down to ambient pressure* ***(b)****. Ticks at the bottom of the Raman spectrum represent the ab initio calculations of the rh-In_2O_3 Raman mode frequencies. RS spectra of o3-In_2O_3 are taken in a longer wavenumber range than those of rh-In_2O_3 in order to detect more first-order Raman-active modes in the former phase as predicted by ab initio calculations.*

From ambient pressure to 15.4 GPa, we can observe all seven Raman-active modes of rh-In_2O_3 predicted by group theory. Above this pressure, we observed a decrease in the intensity of the Raman modes related to rh-In_2O_3, being the lowest-frequency A_{1g} mode, the last one to disappear above 26 GPa. Meanwhile, new peaks related to another phase (identified as o3-In_2O_3) **[172]** appear, being the dominant peak observed around 183 cm^{-1} (see vertical arrow in **Figure 6.6 (a)**). Note that o3-In_2O_3 is also characterized by two additional Raman modes around 142 and 239 cm^{-1} at 15.4 GPa. This result is in good agreement with Raman results

observed for this phase in **Ref. 172**. Thus, our RS measurements indicate that on upstroke rh-In_2O_3 is stable up to 15 GPa and it coexists with a new phase (o3-In_2O_3) up to 26 GPa. In the downstroke process, the o3-In_2O_3 phase is stable down to 8 GPa. Below that pressure, the sample was transformed again into the metastable rh-In_2O_3 phase (see **Figure 6.6 (b)**). Curiously, no coexistence is found between both phases on downstroke.

Figure 6.7 shows the pressure dependence of the experimental and theoretical frequencies of the first-order Raman-active modes of rh-In_2O_3. Our frequencies at ambient pressure are in good agreement with previous reports **[28, 38]** and with our *ab initio* calculations.

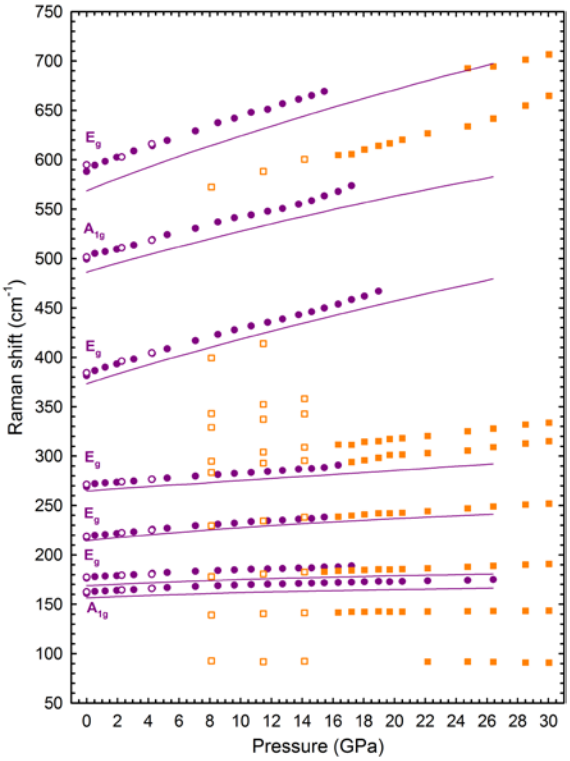

Figure 6.7: *Pressure dependence of the Raman-mode frequencies of rh-In_2O_3 (violet circles) and o3-In_2O_3 (orange squares). Full (empty) symbols correspond to the upstroke (downstroke) process. The symmetry and the theoretical pressure dependence of Raman-active mode frequencies of rh-In_2O_3 (solid lines) are also plotted.*

Moreover, thanks to our *ab initio* calculations we have assigned the symmetry (A_{1g} or E_g) of the different observed Raman modes. As measured, all Raman-active mode frequencies increase with pressure in a monotonous way up to the maximum pressure attained in the experiment and a good agreement is found between the pressure dependence of experimental and theoretical frequencies of the first-order Raman-active modes.

Table 6.4 summarizes the ambient pressure experimental and theoretical frequencies, pressure coefficients and Grüneisen parameters of the Raman-active modes of rh-In_2O_3 and rh-Al_2O_3. When comparing data of isostructural corundum-type In_2O_3 and Al_2O_3 in **Table 6.4** it can be observed that frequencies of the same modes are larger in Al_2O_3 than in In_2O_3 due to the smaller mass of Al than In. Moreover, the pressure coefficients of the two highest-frequency modes are much larger in rh-In_2O_3 than in rh-Al_2O_3, thus showing a larger sensitivity to pressure of Raman stretching modes in rh-In_2O_3 than in rh-Al_2O_3. This result is in good agreement with the larger variation of In−O distances than of Al−O distances with increasing pressure already discussed. In fact, Grüneisen parameters are rather similar for the two highest-frequency modes in rh-In_2O_3 and rh-Al_2O_3. Since the pressure coefficients of the stretching modes reflect the rate of change of decrease of interatomic cation−anion distances, the above result suggests that both compounds have similar sensitivity for stretching *A*−O forces. However, Grüneisen parameters are smaller for low-frequency modes in rh-In_2O_3 than in rh-Al_2O_3. Furthermore, both Grüneisen parameters for low- and high-frequency modes are similar in rh-Al_2O_3 and quite different (up to a factor 1.7) in rh-In_2O_3. These results indicate a different sensitivity in both compounds for bending *A*−O forces and that both stretching and bending forces are more similar in rh-Al_2O_3 than in rh-In_2O_3. All these results are in good agreement with the different distortion of the octahedral AO_6 units discussed in the previous section where an increase (decrease) of the regularity of octahedron in rh-Al_2O_3 (rh-In_2O_3) with increasing pressure has been observed. In summary, the different distortion of the octahedron of the corundum structure can be understood as a consequence of the different behavior of stretching and bending forces in this unit in both compounds.

Finally, we would like to stress that the higher sensitivity of rh-In_2O_3 to compression than its isostructural compounds Al_2O_3, Ga_2O_3, and Cr_2O_3 could be relevant for its use as pressure calibrant. The most usual method for pressure calibration in the laboratory relies on spectroscopic techniques. In particular, the pressure dependence of the photoluminescence lines R1 and R2 of ruby, assigned to internal transitions in the Cr^{3+} cation, follows a well-known tendency **[109, 115]**. However, the relatively small pressure coefficient of these lines leads to a considerable error in the determination of pressure in the low-pressure range. Therefore, the existence of compounds with structures more sensitive to pressure than ruby and with the possibility to host Cr^{3+} cations opens a new path in the search for more accurate pressure sensors. In this context, the possibility to obtain metastable rh-In_2O_3 at ambient conditions (reported by many authors in the last years) **[39, 44]**, the stability of the rh-In_2O_3

up to 14 GPa at ambient temperature, and the low value of the bulk modulus of rh-In_2O_3 here reported suggest that Cr^{3+}-doped rh-In_2O_3 could be a possible candidate to substitute ruby at least below 14 GPa. It is expected that the higher sensitivity of the host material (rh-In_2O_3) would produce an increase in the pressure coefficient of the luminescence lines of Cr^{3+} with respect to ruby and consequently, a more accurate determination of pressure. However, for that purpose metastable corundum-type Cr^{3+}-doped In_2O_3 must be prepared in an easy way as a single crystalline phase and its photoluminescence under pressure must be studied for different concentrations of Cr^{3+} doping. **Appendix 6.2** shows the first attempts of the synthesis of metastable corundum-type Cr^{3+}-doped In_2O_3.

	rh-In_2O_3								**rh-Al_2O_3**			
	***Ab initio* calculations**				**Experimental**				**Exp. [c]**	**Experimental [d]**		
Mode (Sym)	ω_0 (cm^{-1})	$\frac{\partial\omega}{\partial P}$ $\left(\frac{cm^{-1}}{GPa}\right)$	$\frac{\partial^2\omega}{\partial P^2}$ $\left(\frac{cm^{-1}}{GPa^2}\right)$	γ^a	ω_0 (cm^{-1})	$\frac{\partial\omega}{\partial P}$ $\left(\frac{cm^{-1}}{GPa}\right)$	$\frac{\partial^2\omega}{\partial P^2}$ $\left(\frac{cm^{-1}}{GPa^2}\right)$	γ^b	ω_0 (cm^{-1})	ω_0 (cm^{-1})	$\frac{\partial\omega}{\partial P}$ $\left(\frac{cm^{-1}}{GPa}\right)$	γ
A_{1g}	156 (1)	0.65 (3)	-0.012 (2)	0.66	162.3 (2)	0.85 (4)	-0.015 (1)	0.92	164	418.5	1.70	1.15
E_g	169 (1)	0.73 (3)	-0.010 (2)	0.68	177.1 (2)	1.01 (6)	-0.022 (3)	1.00		378.4	1.34	0.99
E_g	214 (1)	1.54 (3)	-0.023 (2)	1.14	218.1 (3)	1.85 (8)	-0.039 (5)	1.49	221.8	430.6	2.79	1.73
E_g	265 (1)	1.11 (6)	-0.005 (5)	0.66	270.7 (4)	1.33 (13)	-0.011 (7)	0.86	273	448.7[e]	1.66[e]	1.05[e]
									309			
E_g	373 (2)	4.91 (5)	-0.040 (4)	2.08	383.8 (6)	4.69 (16)	-0.022 (8)	2.15	385	576.4	2.76	1.28
A_{1g}	486 (2)	4.46 (6)	-0.033 (4)	1.45	501.9 (9)	3.92 (25)	0.005 (14)	1.37	504.5	645.2	3.48	1.49
E_g	569 (2)	6.14 (5)	-0.059 (4)	1.70	590.3 (6)	5.95 (18)	-0.058 (12)	1.77	596	750.6	4.22	1.52

[a]Obtained with theoretical B_0= 158 GPa. [b]Obtained with experimental B_0= 176 GPa. [c]Reference 28. [d]Reference 195. [e]Reference 196.

Table 6.4: *Ambient-pressure experimental frequencies, pressure coefficients, and Grüneisen parameters of the Raman active modes of rh-In_2O_3 and rh-Al_2O_3.*

6.6. Conclusions

We have synthesized rh-In_2O_3 at HP-HT in a MA press and performed an experimental and theoretical study of their structural and vibrational properties under pressure. Thanks to XRD and RS measurements and *ab initio* calculations, we have performed a detailed and exhaustive comparison of the evolution of rh-In_2O_3 and rh-Al_2O_3 structures under pressure. XRD measurements in rh-In_2O_3 under pressure have allowed us to obtain an accurate experimental EoS that is in good agreement with theoretical calculations. We have found a smaller bulk

modulus for rh-In_2O_3 than for isomorphic rh-Al_2O_3, rh-Ga_2O_3, and rh-Cr_2O_3. This result suggests the possibility to use Cr^{3+}-doped rh-In_2O_3 at ambient temperature as a more sensitive pressure sensor than ruby at least up to 14 GPa. The increase of the quadratic elongation parameter of rh-In_2O_3 with pressure suggests the presence of a mechanical instability of this structure at higher pressures. This result is in good agreement with the much lower stability (phase transition pressure) of rh-In_2O_3 than of rh-Al_2O_3. Our *ab initio* calculations have allowed us to assign the symmetry of the different observed first-order Raman-active modes of rh-In_2O_3. Besides, RS measurements confirm the phase transition to o3-In_2O_3 (*Pbca*-type) observed by angle-dispersive powder XRD above 14 GPa, as well as the behavior of the octahedral unit and the cation−anion distances with increasing pressure as described by our theoretical calculations.

6.7. Supplementary material

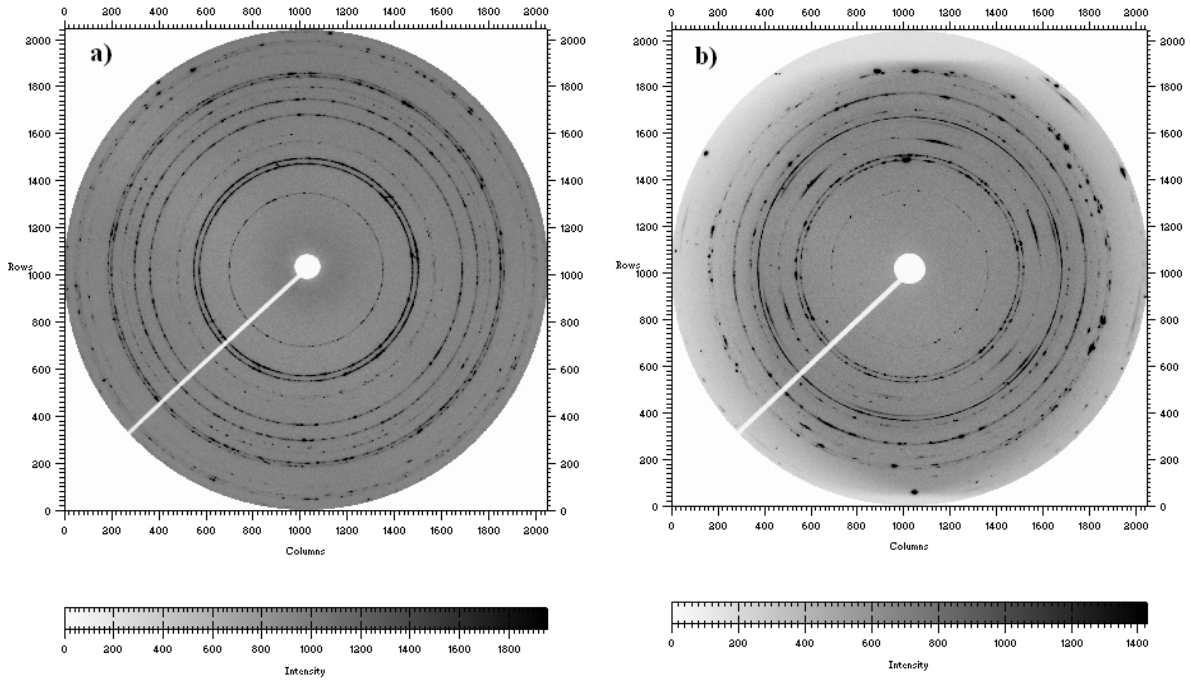

Figure 6.S1: *Typical CCD images of angle-dispersive powder XRD for the annealed sample (300 ºC) at ambient pressure (a) and 10.8 GPa (b) of rh-In_2O_3.*

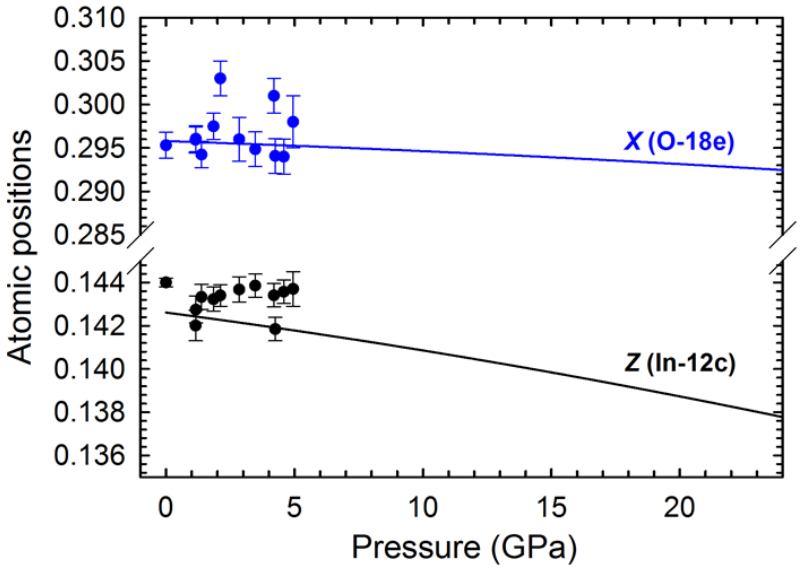

Figure 6.S2: *Experimental (circles) and theoretical (solid lines) pressure dependence of the (X, 0, 0.25) and (0, 0, Z) atomic positions of 18e (O) and 12c (In) Wyckoff positions, respectively in rh-In_2O_3. Experimental results have been obtained from Rietveld refinements of XRD data.*

rh-In_2O_3	**P (GPa)**	**a (Å)**	**c (Å)**	**Atom**	**Wyckoff site**	**x**	**y**	**z**
Exp.	1.2	5.4637 (3)	14.4399 (12)	In	12c	0	0	0.1427
				O	18e	0.2980	0	0.25
Theo.	1.1	5.5092	14.4950	In	12c	0	0	0.1424
				O	18e	0.2954	0	0.25

Table 6.S1: *Experimental and theoretical values of lattice parameters and atomic positions of rh-In_2O_3.*

rh-In_2O_3	**P (GPa)**	**a (Å)**	**c (Å)**	**Atom**	**Wyckoff site**	**x**	**y**	**z**
Exp.	15.9	5.421 (4)	13.906 (10)	In	12c	0	0	0.1495
				O	18e	0.2937	0	0.25
Theo.	16.3	5.4214	13.8484	In	12c	0	0	0.1395
				O	18e	0.2937	0	0.25

o3-In_2O_3	**P (GPa)**	**a (Å)**	**b (Å)**	**c (Å)**	**Atom**	**Wyckoff site**	**x**	**y**	**z**
Exp.	15.9	5.378 (3)	5.494 (3)	14.516 (8)	In1	8c	0.0003	0.7840	0.4310
					In2	8c	0.9675	0.7732	0.1789
					O1	8c	0.3591	0.8682	0.2012
					O2	8c	0.2062	0.5109	0.3757
					O3	8c	0.1455	0.6525	0.0531
Theo.	16.1	5.4105	5.5251	15.5220	In1	8c	0.0003	0.7840	0.4310
					In2	8c	0.9974	0.7305	0.1830
					O1	8c	0.3591	0.8682	0.2012
					O2	8c	0.2062	0.5109	0.3757
					O3	8c	0.1455	0.6525	0.0531

Table 6.S2: *Experimental and theoretical values of lattice parameters and atomic positions of rh-In_2O_3 and o3-In_2O_3.*

R-3c	P (GPa)	a (Å)	c (Å)	Atom	Wyckoff site	x	y	z
Exp.	1.0	5.4687 (3)	14.4751 (15)	In	12c	0	0	0.1436
				O	18e	0.2816	0	0.25
Theo.	1.1	5.5092	14.4950	In	12c	0	0	0.1424
				O	18e	0.2954	0	0.25

Table 6.S3: *Experimental (during downstroke) and theoretical values of the lattice parameters and atomic positions of rh-In_2O_3.*

Wyckoff site	x_0 or z_0	γ (10^{-4} GPa^{-1})	δ (10^{-6} GPa^{-2})
x (O – 18e)	0.29579 (3)	-0.99 (4)	-1.64 (13)
z (In – 12c)	0.14261 (2)	-1.56 (2)	-1.87 (5)

Table 6.S4: *Theoretical pressure dependence of the (x, 0, 0.25) and (0, 0, z) atomic positions for the 18e (O) and 12c (In) Wyckoff positions, from a quadratic fit to $x=x_0+\gamma P+\delta P^2$ and $z=z_0+\gamma P+\delta P^2$, respectively.*

Cation-oxygen bond	l_0 (Å)	dl/dP (Å/GPa)
Al – O1	1.8604 (4)	-0.00216 (3)
Al – O2	1.9728 (4)	-0.00223 (3)
In – O1	2.129 (1)	-0.00316 (6)
In – O2	2.2555 (9)	-0.00280 (5)

Table 6.S5: *Theoretical cation-oxygen bond lengths in the AO_6 polyhedron (A=Al, In) at ambient pressure and its pressure coefficient in corundum-type A_2O_3 sesquioxides from a linear fit to $l(P)=l_0+dl/dP \cdot P$).*

Compound	λ_0	α (10^{-5} GPa^{-1})	β (10^{-6} GPa^{-2})
rh-Al_2O_3	1.0202	-1.875 (2)	
rh-In_2O_3	1.03398 (5)	37.2 (7)	8.1 (3)

Table 6.S6: *Theoretical quadratic elongation (λ) and its pressure derivatives for rh-Al_2O_3 (after a linear fit to $\lambda=\lambda_0+\alpha P$) and rh-$In_2O_3$ (after a quadratic fit to $\lambda=\lambda_0+\alpha P+\beta P^2$).*

Appendix 6.1: "P-T phase diagram" starting from c-In_2O_3 and rh-In_2O_3 samples.

Commercial c-In_2O_3 (99.99% pure from Sigma-Aldrich Inc.) was employed as starting material for the HP-HT syntheses. **Figure A6.1.1**, **Figure A6.1.2** and **Figure A6.1.3** show the XRD pattern, the Raman spectrum and the microanalysis study of c-In_2O_3 at ambient conditions, respectively.

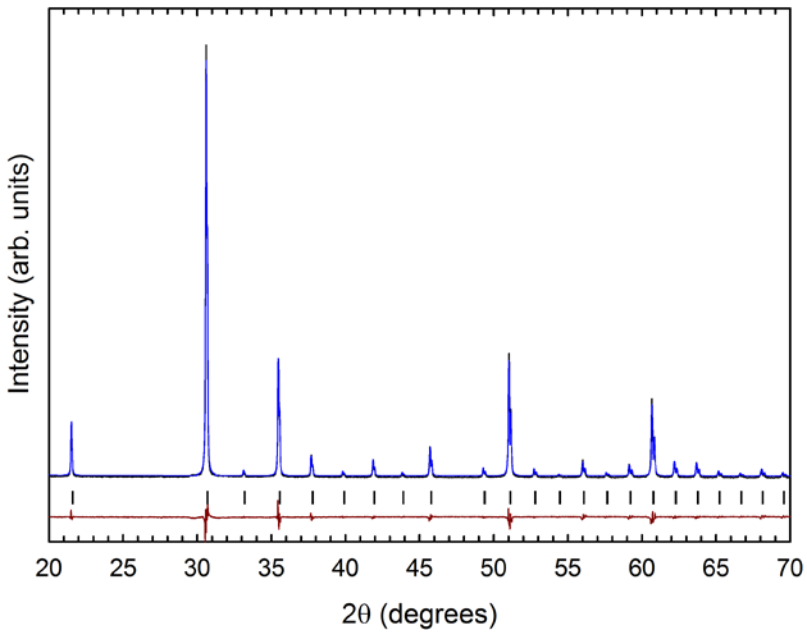

Figure A6.1.1: *Rietveld refinement of c-In_2O_3 at ambient conditions used for the HP-HT syntheses.*

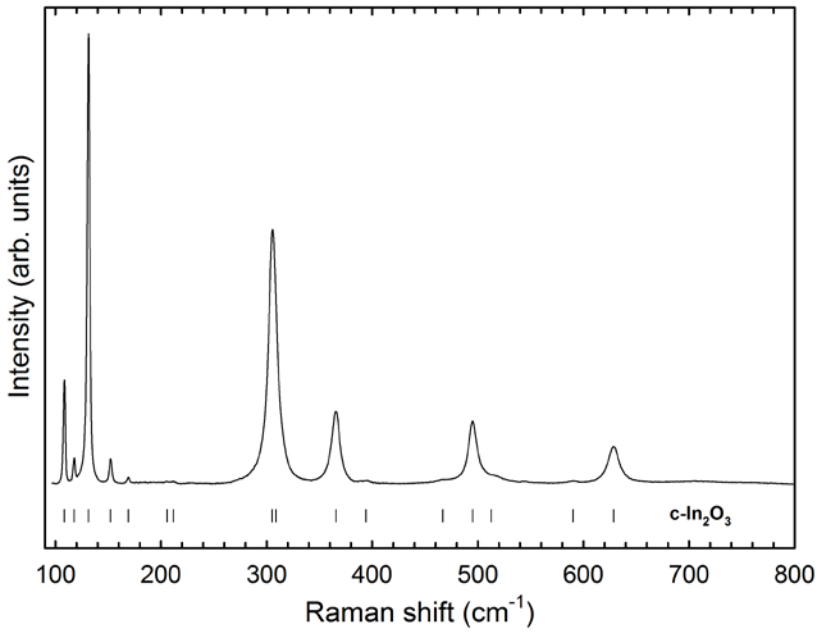

Figure A6.1.2: *Raman spectrum of c-In_2O_3 at ambient conditions used for the HP-HT syntheses.*

The atomic % of C, O and In obtained through the microanalysis were 4.2%, 61.3% and 34.5%, respectively.

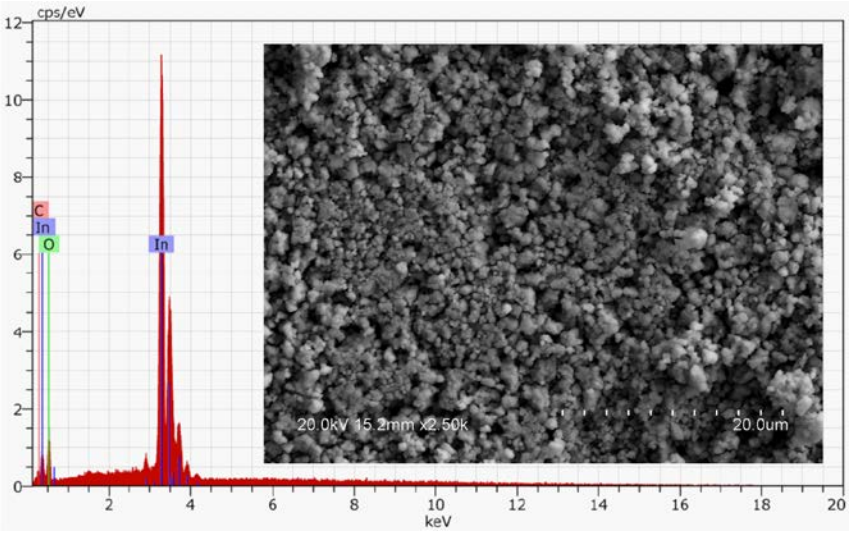

Figure A6.1.3: *Morphology and microanalysis of c-In_2O_3 employed for the HP-HT syntheses.*

The details of all HP-HT syntheses starting from c-In_2O_3 are shown from **Table A6.1.1** to **Table A6.1.5**. HP-HT syntheses were ordered chronologically. We comment all the synthesis problems that we found till get pure rh-In_2O_3 and what we proposed to solve it.

Set-up	Synthesis conditions					Results
	P_{Oil} (bar)	**P (GPa)**	**Power (W)**	**Temperature (ºC)**	**Time (h)**	
10 mm pyrophyllite gasket With Teflon ring Graphite heater BN capsule 2 thermocouples	875	7.2	320	770	2	Raman: c-In_2O_3 XRD: c-In_2O_3
	Due to the rupture of the Teflon ring, the thermocouples were not in the center of the sample. During the HP-HT synthesis, the thermocouples reading were 140 and 290 ºC.					
10 mm pyrophyllite gasket Without Teflon ring Graphite heater BN capsule	890	5.1	330	790	2	Raman: c-In_2O_3 XRD: c-In_2O_3
	A homogeneous c-In_2O_3 was recovered					
10 mm pyrophyllite gasket Without Teflon ring Graphite heater BN capsule	860	5.0	400	960	2	Raman: c-In_2O_3 XRD: c-In_2O_3
	A homogeneous c-In_2O_3 was recovered					
10 mm pyrophyllite gasket Without Teflon ring Graphite heater BN capsule	860	5.0	500	1190	2	XRD: c-In_2O_3 + rh-$InBO_3$
	Figure A6.1.4 shows the XRD pattern measured at the University of Valencia. A reaction between the c-In_2O_3 and the h-BN is produced. Corundum-type structure of $InBO_3$ (rh-$InBO_3$) begins to appear. Moreover, some Bragg reflections denoted with an asterisk (*) could not be explained with the most expected structures: o1-In_2O_3, o2-In_2O_3, o3-In_2O_3, rh-In_2O_3 and the orthorhombic ($Pmn2_1$) InOOH.					

10 mm pyrophyllite gasket With Teflon ring Graphite heater BN capsule	860	7.2	510	1220	8	XRD: c-In_2O_3 + rh-$InBO_3$
	For this HP-HT conditions, similar XRD pattern but with different Bragg reflections intensities as shown in **Figure A6.1.4** is obtained.					
10 mm pyrophyllite gasket Without Teflon ring Graphite heater BN capsule Thermocouple	870	5.0	360	860	11	XRD: c-In_2O_3
	A homogeneous c-In_2O_3 was recovered. The thermocouple reading was 1000 ºC					
10 mm pyrophyllite gasket Without Teflon ring Graphite heater BN capsule Thermocouple	860	5.0	380	910	24	XRD: c-In_2O_3 SEM (at. %): O: 62 % - In:38 %
	A homogeneous c-In_2O_3 was recovered. **Figure A6.1.5** shows the sample where we performed the microanalysis study. The thermocouple reading was 1100 ºC					
10 mm pyrophyllite gasket Without Teflon ring Graphite heater BN capsule 25 μm Pt foil Thermocouple	840	4.9	310	750	0	XRD: c-In_2O_3 SEM (at. %): O: 63 % - In:37 %
	Increasing the power to reach the desire HT conditions, the power felt down drastically. We performed a home-made Pt capsule. A homogeneous c-In_2O_3 was recovered. The recovered sample had the same morphology as the previous synthesis (similar as **Figure A6.1.5**)					

Table A6.1.1: *HP-HT syntheses starting from c-In_2O_3 employing the 10 mm CW anvils in the PE large volume press at the University of Valencia.*

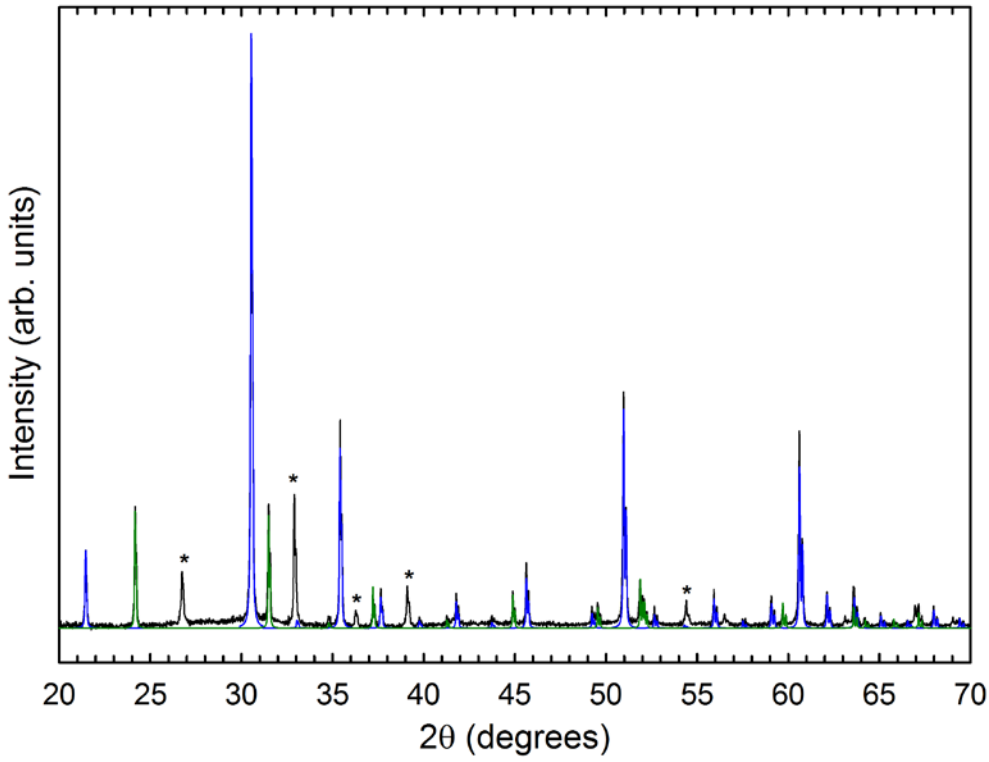

Figure A6.1.4: *Black line corresponds to XRD pattern measured at the University of Valencia. Blue and green lines are simulated XRD spectra using c-In_2O_3 and rh-$InBO_3$ structures, respectively. We could not explain the Bragg reflections denoted with asterisk (*)*

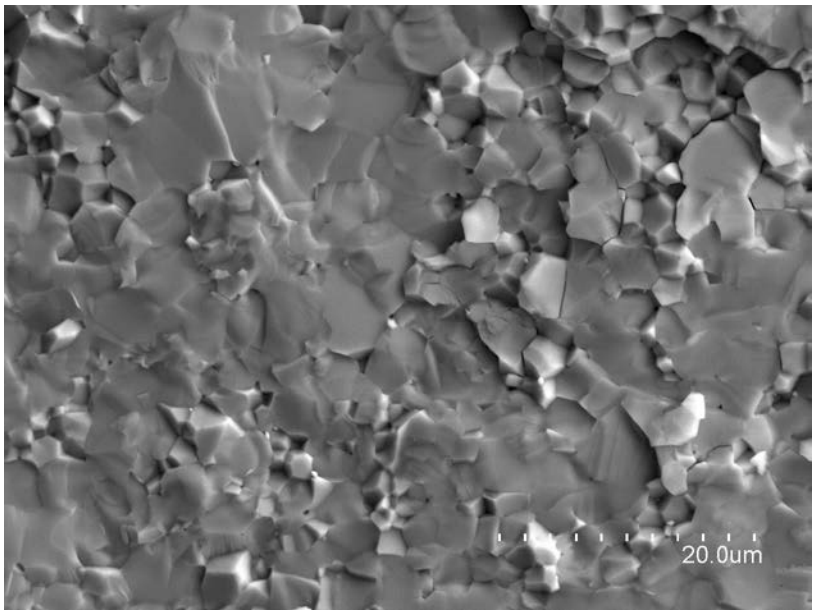

Figure A6.1.5: *Morphology of the recovered sample (c-In_2O_3) at the synthesis conditions of 5 GPa and 910 ºC.*

Set-up	Synthesis conditions			Results
	P (GPa)	**Temperature (ºC)**	**Time (h)**	
10 mm pyrophyllite gasket With Teflon ring Graphite heater BN capsule	6.6	1070	8	XRD: c-In_2O_3 + rh-$InBO_3$
	c-In_2O_3 was annealed to 700ºC during 4 h to remove all possible water from the sample. rh-$InBO_3$ starts to appear through the reaction between the sample (c-In_2O_3) and the h-BN capsule. In that HP-HT synthesis was when we discovered that reaction.			
10 mm pyrophyllite gasket With Teflon ring Graphite heater 25 μm Pt capsule	6.6	T > 1070	22	XRD: c-In_2O_3 + rh-In_2O_3
	The measurement of temperature was wrong because we did not employ the h-BN insulator capsule between the graphite and the Pt capsule. The current probably passed through Pt foil instead of graphite, and thus the temperature reached during the HP-HT synthesis would be higher than 1070 ºC. **Figure A6.1.6** shows the powder XRD pattern measured at IMPMC. Most of Bragg reflections could be explained with the rh-In_2O_3 and the c-In_2O_3 structure. Some Bragg reflections could not be explained with the o1-In_2O_3, o2-In_2O_3 and o3-In_2O_3. We though that this "extra Bragg reflections" are related with some reaction between the sample and the Pt capsule as we can see in the image of the inset of **Figure A6.1.6**.			
10 mm pyrophyllite gasket With Teflon ring Graphite heater BN capsule 25 μm Pt capsule	6.6	1070	2	XRD: c-In_2O_3
	A reaction between the sample and the Pt capsule took place because new Bragg reflections are observed that could not be explained with the most expected phases, i.e., o1-In_2O_3, o2-In_2O_3, o3-In_2O_3, rh-In_2O_3 or even the cubic (Fm-3m) Pt. **Figure A6.1.7** shows the XRD pattern obtained and the recovered crystals.			

Table A6.1.2: *HP-HT syntheses starting from c-In_2O_3 employing the 10 mm CW anvils in the PE large volume press at the IMPMC.*

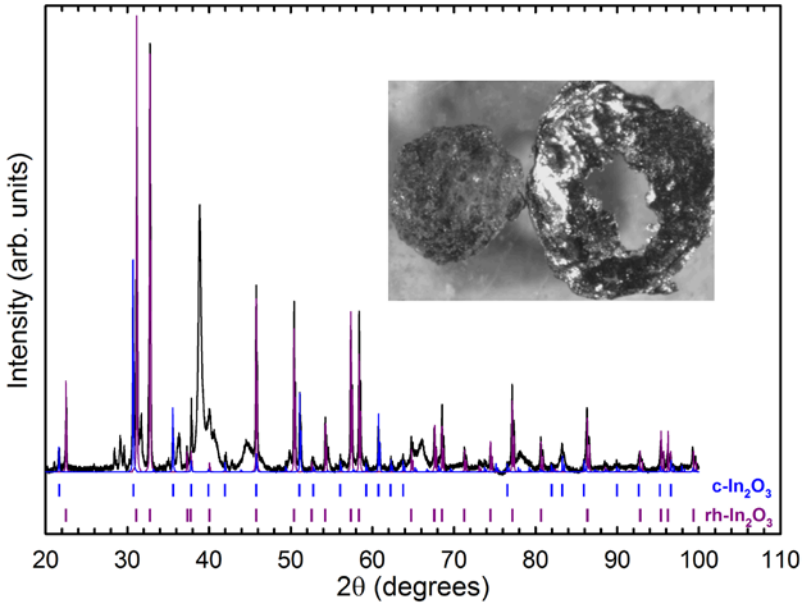

Figure A6.1.6: *Black line corresponds to XRD pattern measured at the IMPMC. Blue and violet lines are the simulated XRD patterns using c-In_2O_3 and rh-$In2O_3$ structures, respectively. Moreover, vertical marks have been added to show the most intense Bragg reflections of each phase. Inset: Shows the sample and the Pt capsule recovered.*

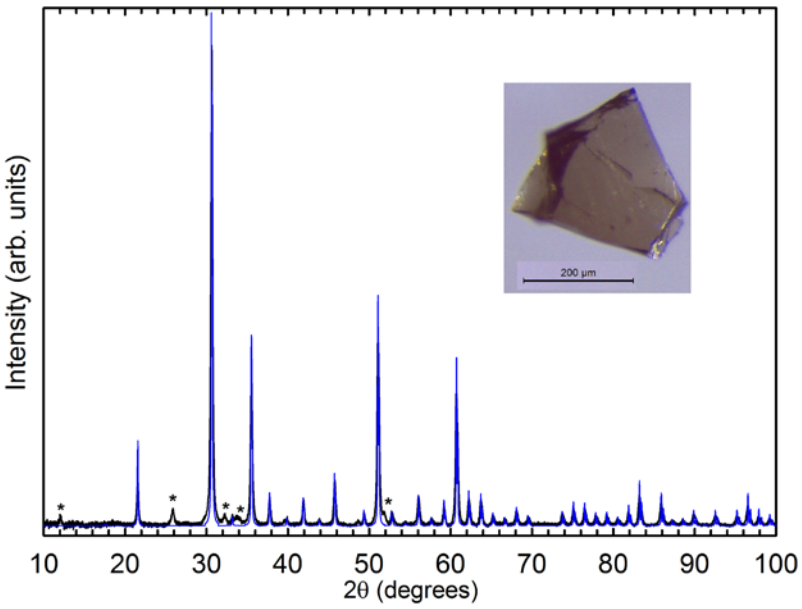

Figure A6.1.7: *Black line corresponds to XRD pattern measured at the IMPMC. Blue and violet lines correspond to simulated XRD patterns using c-In_2O_3 and rh-In_2O_3 structures. We could not explain the Bragg reflections denoted with an asterisk (*). Inset: Shows one of the synthesized crystals.*

In concordance with the new temperature calibration for the 10 mm set-up the temperature data published in **Table A6.1.1** have been corrected to the new values due to an overestimation of the temperature.

Set-up	Synthesis conditions					Results
	P_{Oil} (bar)	**P (GPa)**	**Power (W)**	**Temperature (ºC)**	**Time (h)**	
10 mm pyrophyllite gasket With Teflon ring Graphite heater BN capsule 25 μm Pt foil + 2 Pt disk (0.1 mm)	840	7.1	412	990	2	Raman: c-In_2O_3 + rh-In_2O_3 SEM (at. %): O: 64 % - In:36 %
	We performed a home-made Pt capsule with the combination of a Pt foil and two Pt disks. Strange voltage values were observed during the heating process in comparison with other HP-HT synthesis.					
10 mm pyrophyllite gasket With Teflon ring Graphite heater BN capsule 25 μm Pt foil + 2 Pt disk (0.1 mm)	850	7.2	415	1000	3	XRD: rh-In_2O_3 + c-In_2O_3 + InOOH SEM (at. %): O: 68 % - In:32 %
	Most of the sample was analyzed by XRD to get an idea of the majority phase recovered. The most intense Bragg reflections correspond the rh-In_2O_3 as we could observe in **Figure A6.1.8**. Formation of InOOH could be related with the reaction of the sample with some remaining water under HP-HT conditions.					
10 mm pyrophyllite gasket With Teflon ring Graphite heater BN capsule 25 μm Pt foil + 2 Pt disk (0.1 mm)	850	7.2	382	920	3	Raman: c-In_2O_3 SEM (at. %): O: 64 % - In:36 %
	To prevent InOOH formation c-In_2O_3 was compacted at ~8 kbar and then annealed to 200ºC during 1 hour before loading it into the Pt capsule. We have followed this procedure for all subsequent HP-HT synthesis.					
10 mm pyrophyllite gasket With Teflon ring Graphite heater BN capsule 12.5 μm Pt foil + 2 Pt disk (0.1 mm)	860	7.2	398	960	3	Raman: c-In_2O_3 + rh-In_2O_3
	We decided to employ a thinner Pt capsule (12.5 μm) compared with previous one (25 μm) for easier manipulation.					
10 mm pyrophyllite gasket With Teflon ring Graphite heater BN capsule 12.5 μm Pt foil + 2 Pt disk (0.1 mm)	860	7.2	446	1070	3	Raman: rh-In_2O_3 + c-In_2O_3 SEM (at. %): O: 65 % - In:35 %
	The recovered sample was a mixture of rh-In_2O_3 and the c-In_2O_3 structure. The recuperated Pt capsule was badly damaged (cracked) as shown in **Figure A6.1.9**.					
10 mm pyrophyllite gasket With Teflon ring Graphite heater BN capsule 25 μm Pt foil + 2 Pt disk (0.1 mm)	850	7.2	412	990	3	Raman: rh-In_2O_3 + c-In_2O_3
	A mixture of rh-In_2O_3 and c-In_2O_3 is observed.					
10 mm pyrophyllite gasket With Teflon ring Graphite heater BN capsule 25 μm Pt foil + 2 Pt disk (0.1 mm)	860	7.2	545	1300	3	Raman: rh-In_2O_3
	The Raman spectra presents some "extra Raman modes" (denoted with *) that could not be explained with the rh-In_2O_3 as shown in **Figure A6.1.10**. Moreover, Pt capsule looked like it had melted, but, according to D. Errandonea *et al*. **[197]**, at 7.2 GPa Pt should melt around 2100 ºC. Therefore, probably there was some chemical reaction between the sample and Pt capsule at those HP-HT conditions.					

10 mm pyrophyllite gasket Without Teflon ring Graphite heater BN capsule 25 μm Pt foil + 2 Pt disk (0.1 mm) Thermocouple	850	5.0	460	1100	3	Raman: c-In_2O_3
	The thermocouple was placed close to the Pt capsule in order to get an idea of the temperature reached in the HP-HT synthesis. The thermocouple reading during the HP-HT synthesis was 1150 ºC.					
10 mm pyrophyllite gasket With Teflon ring Graphite heater BN capsule 25 μm Pt foil + 2 Pt disk (0.1 mm)	840	7.1	500	1190	3	Raman: rh-In_2O_3 + c-In_2O_3
	A mixture of rh-In_2O_3 and c-In_2O_3 is observed in the recovered sample.					
10 mm pyrophyllite gasket With Teflon ring Graphite heater BN capsule 25 μm Pt foil + 2 Pt disk (0.1 mm)	840	7.1	530	1260	3	XRD: Not identified SEM (at. %): C: 49 % - O: 9 % - In:24 % - Pt: 18 %
	The power supplied to the furnace was unstable during the HP-HT synthesis. A reaction between the sample and the Pt could occur, as revealed in the microanalysis study of the recovered sample showed in **Figure A6.1.11**. However, we could not be able to identify the compound that was formed, from its XRD pattern.					
10 mm pyrophyllite gasket With Teflon ring Graphite heater BN capsule 25 μm Mo foil + 2 Mo disk (0.3 mm)	830	7.1	540	1290	3	XRD: Not identified Raman: No information
	We decided to change the metal capsule from Pt to Mo in order to prevent the reaction during the HP-HT synthesis. The power supplied to the furnace was unstable during the HP-HT synthesis. A reaction between the sample and the Mo capsule probably occurred. We could not be able to identify most of the Bragg reflections in the XRD pattern, as shown in **Figure A6.1.12**. Some Bragg reflections correspond to c-In_2O_3.					
10 mm pyrophyllite gasket With Teflon ring Graphite heater BN capsule 25 μm Mo foil + 2 Mo disk (0.3 mm)	600	6.1	460	1100	0.5	XRD: c-In_2O_3 Raman: c-In_2O_3
	We used HP-HT conditions published by Maged F. Bekheet *et al*. **[44]** for the synthesis of rh-In_2O_3. However, the sample recovered had the cubic structure, as revealed by XRD and RS measurements.					
10 mm pyrophyllite gasket With Teflon ring Graphite heater BN capsule 25 μm Pt foil + 2 Pt disk (0.1 mm)	600	6.1	504	1200	0.5	XRD: c-In_2O_3 Raman: c-In_2O_3
	A homogeneous c-In_2O_3 sample was recovered.					
10 mm pyrophyllite gasket With Teflon ring Graphite heater BN capsule 25 μm Pt foil + 2 Pt disk (0.1 mm)	600	6.1	460	1100	24	XRD: c-In_2O_3 Raman: c-In_2O_3
	We increased considerably the synthesis time to check possible kinetic effects for the cubic to corundum transformation. This HP-HT synthesis was really stable during the 24 hours. A more or less homogeneous sample is obtained (see **Figure A6.1.13**), but with cubic structure**.**					

Table A6.1.3: *HP-HT syntheses starting from c-In_2O_3 employing the 10 mm CW anvils in the PE large volume press at the University of Valencia.*

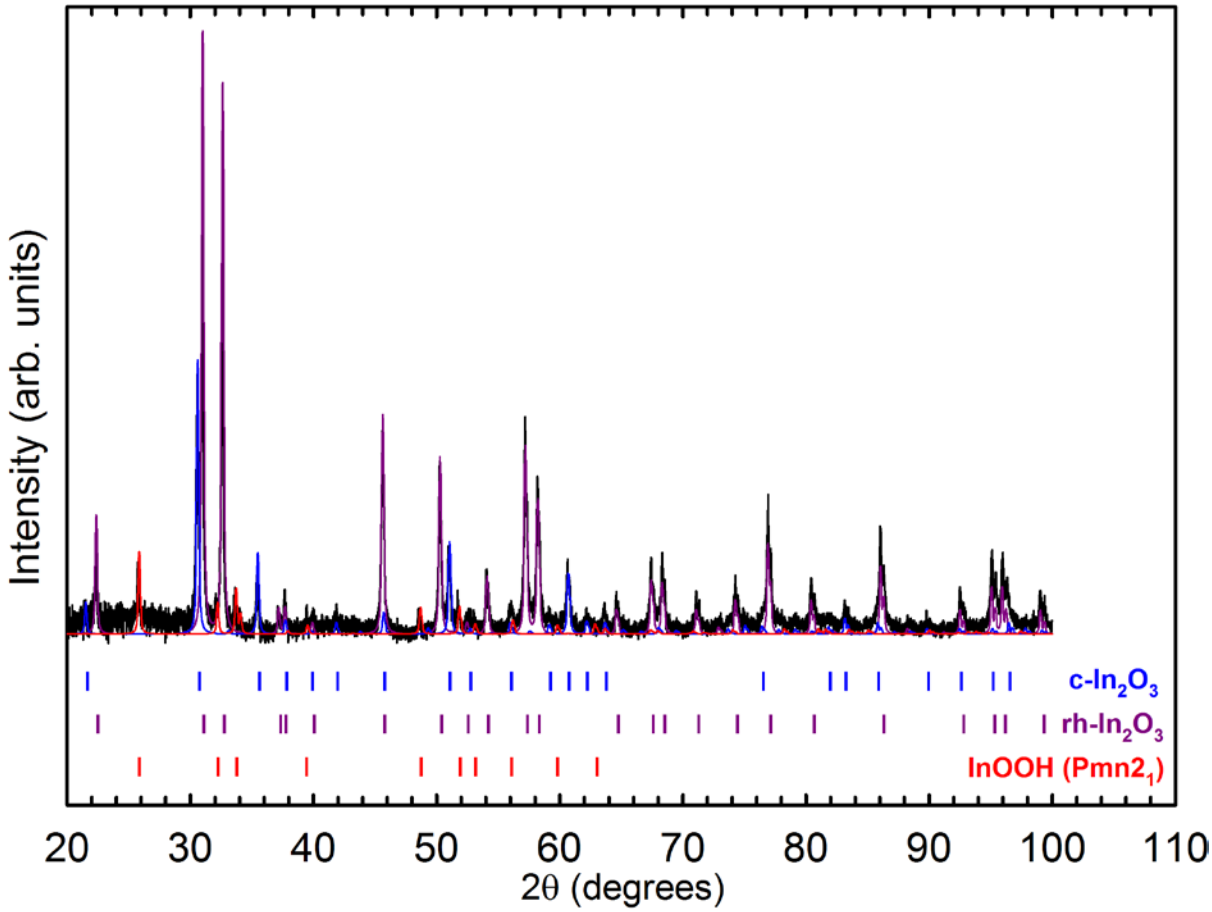

Figure A6.1.8: *Black line corresponds to the XRD pattern measured at the ICMol (University of Valencia). Violet, blue and red lines are simulated XRD patterns using rh-In_2O_3, c-In_2O_3 and orthorhombic ($Pmn2_1$) InOOH structures, respectively. Moreover, vertical marks have been added to show the most intense Bragg reflections of each phase.*

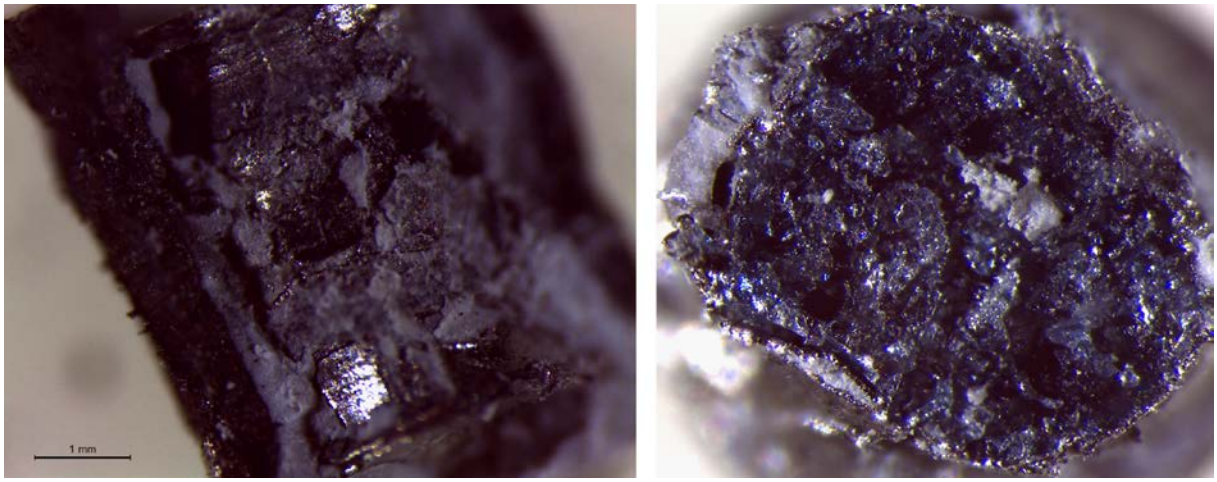

Figure A6.1.9: *Recovered cracked Pt capsule (left). Recovered crystals (right) from the HP-HT synthesis at 7.2 GPa and 1070 ºC.*

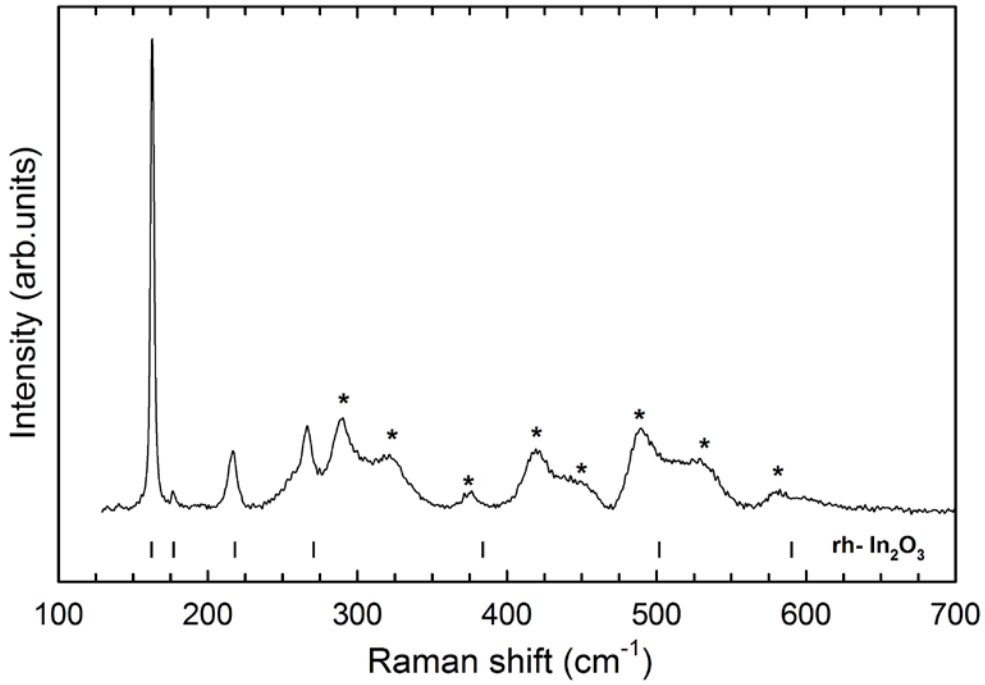

Figure A6.1.10: *Raman spectra of the recovered sample at the synthesis conditions of 7.2 GPa and 1300 ºC.*

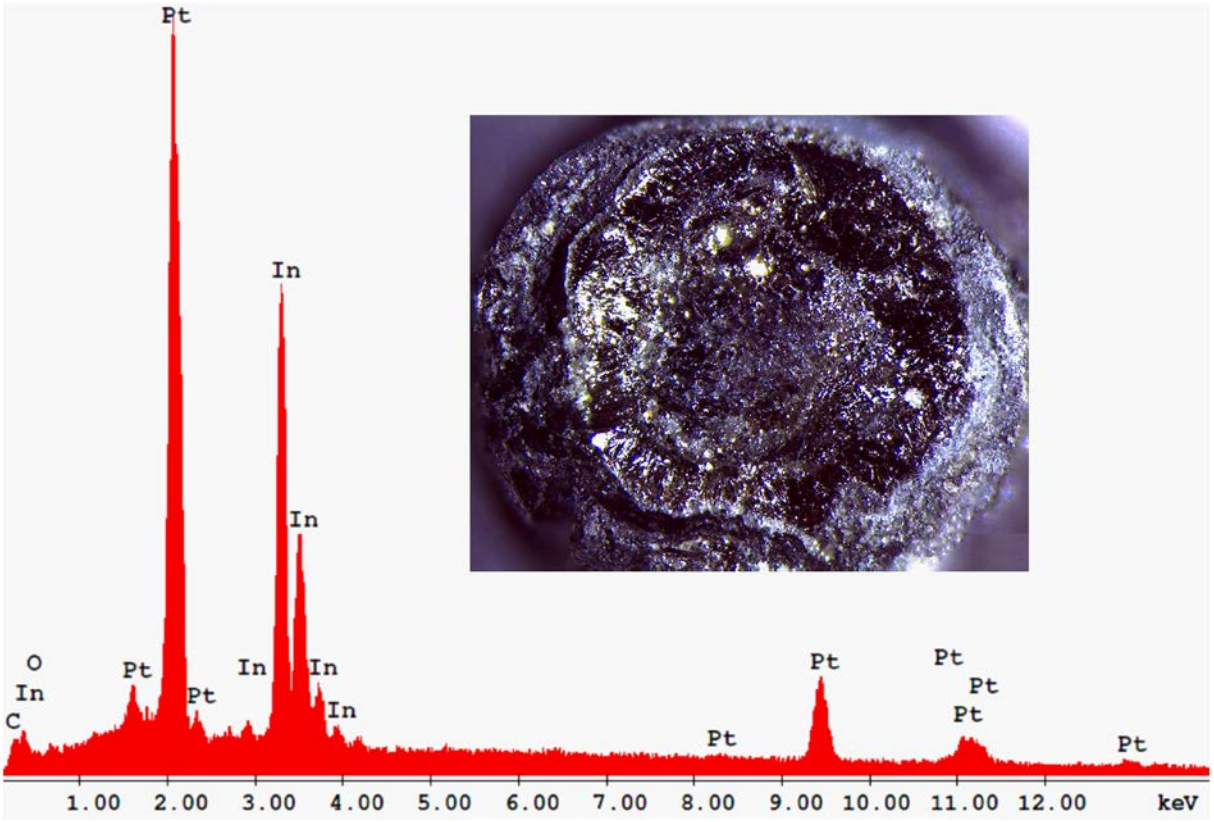

Figure A6.1.11: *Microanalysis of the recovered sample at the synthesis conditions of 7.1 GPa and 1260 ºC. The inset shows an image of the sample. We can see the metallic appearance of the whole sample, confirming the reaction with the Pt foil.*

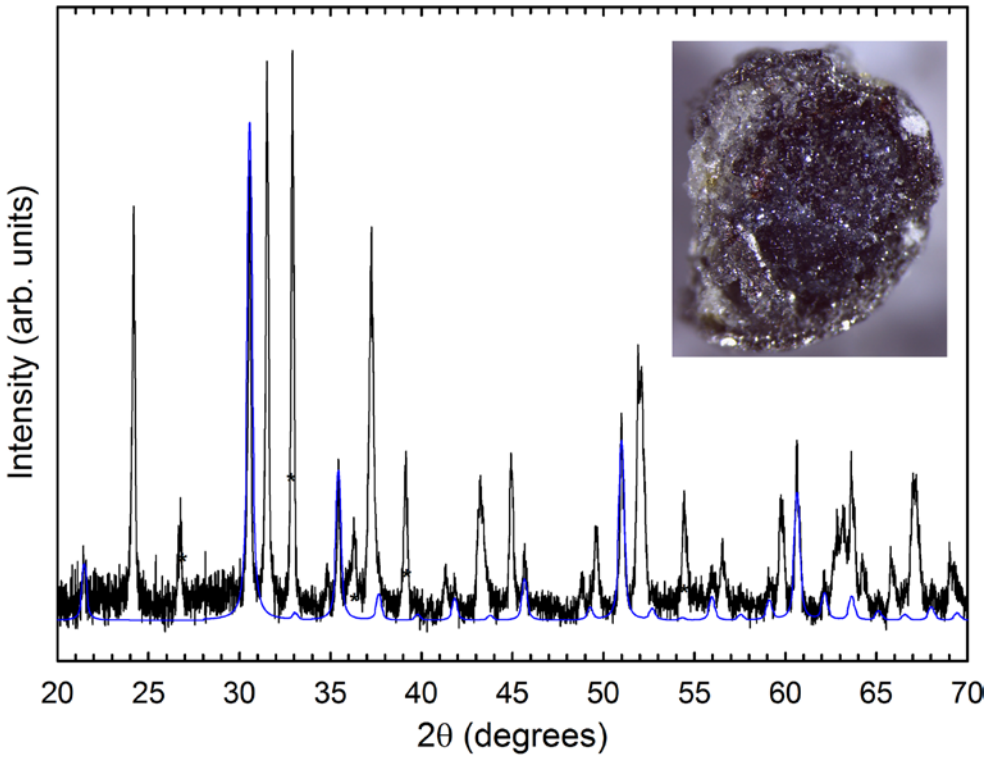

Figure A6.1.12: *Black line corresponds to the XRD pattern measured at the ICMol (University of Valencia). Blue line is the simulated XRD pattern with c-In_2O_3 structure. A picture of the recovered sample was also showed.*

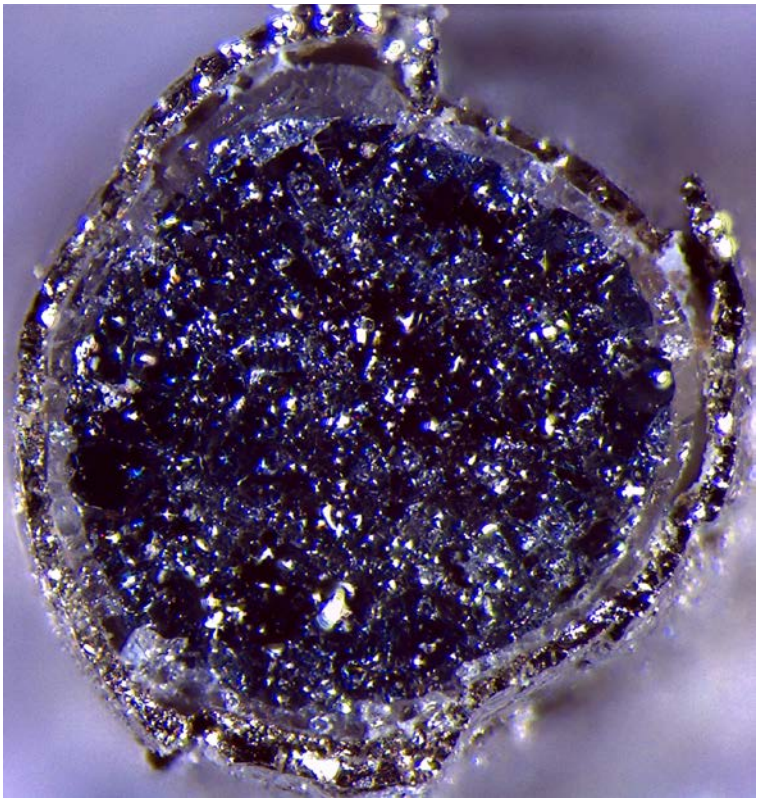

Figure A6.1.13: *Recovered c-In_2O_3 from the HP-HT synthesis (6.1 GPa and 1100 ºC).*

Set-up	Synthesis conditions			Results
	P (GPa)	Temperature (ºC)	Time (h)	
10/5 MgO:Cr $LaCrO_3$ furnace 25 μm Re capsule	20	1400	7	XRD: rh-In_2O_3 + InOOH Raman: rh-In_2O_3
	No reaction was observed between the Re capsule and the sample. Two different kind of crystals were recovered from this HP-HT synthesis (see **Figure A6.1.14**). On the one hand, the XRD pattern of the dark crystals (90%) corresponds to rh-In_2O_3 structure. However, the clear crystals (10%) could be explained as a mixture of the rh-In_2O_3 and the orthorhombic InOOH. On the other hand, the Raman spectra of both types of crystals could be explained with the rh-In_2O_3 and some extra Raman modes. InOOH appears because we forget to anneal the staring material (c-In_2O_3) to remove the humidity.			
18/11 MgO:Cr Graphite furnace 25 μm Re capsule	8	1325	4	XRD: rh-In_2O_3 Raman: rh-In_2O_3
	Clear crystals were recovered. The XRD pattern was completely explained with the rh-In_2O_3. However, in the Raman spectra appear some extra Raman modes that could not be explained with the rh-In_2O_3 (at least with the first order Raman-active modes).			
10/5 MgO:Cr $LaCrO_3$ furnace 25 μm Re capsule	20	2000	3.5	XRD: rh-In_2O_3 Raman: rh-In_2O_3 SEM (at. %): O: 69 % - In:31 %
	Dark crystals were recovered. In the Raman spectra appear some extra Raman modes that could not be explained with the first order Raman-active modes of rh-In_2O_3.			
18/11 MgO:Cr Graphite furnace 25 μm Re capsule	8	340	0.5	XRD: c-In_2O_3 Raman: c-In_2O_3
	The experiment failed. We had a bad electrical contact in the sample assembly in the heating process.			
18/11 MgO:Cr Graphite furnace 25 μm Re capsule	8	1500	5	XRD: Not identified Raman: No information
	Instable furnace behaviour. Probably the temperature (1500 ºC) was too high for the graphite furnace.			
18/11 MgO:Cr Graphite furnace 25 μm Re capsule	6	1325	6	XRD: c-In_2O_3 Raman: c-In_2O_3 + rh-In_2O_3 SEM (at. %): O: 72 % - In:28 %
	Most of the recovered sample was c-In_2O_3.			
18/11 MgO:Cr Graphite furnace 25 μm Re capsule	14	500	6	XRD: rh-In_2O_3 Raman: rh-In_2O_3 + c-In_2O_3 SEM (at. %): O: 72 % - In:28 %
	Only in the borders of the Re capsule, the three most intense Raman-active modes (A_g, T_g and A_g) of the c-In_2O_3 structure were observed in the measured Raman spectra.			
18/11 MgO:Cr Graphite furnace 25 μm Re capsule	12	1375	6	XRD: rh-In_2O_3 Raman: rh-In_2O_3
	The rh-In_2O_3 structure was obtained (see **Figure 6.1**). Crystals recovered in this synthesis experiment have been used to perform the HP study of the rh-In_2O_3 structure.			
18/11 MgO:Cr Graphite furnace 25 μm Re capsule	10	1325	4.5	XRD: rh-In_2O_3
	The recovered sample was rh-In_2O_3.			

Table A6.1.4: *HP-HT syntheses have been made employing a Sumitomo 1200 tons MA press at the Bayerisches Geoinstitut (BGI) in Bayreuth (Germany).*

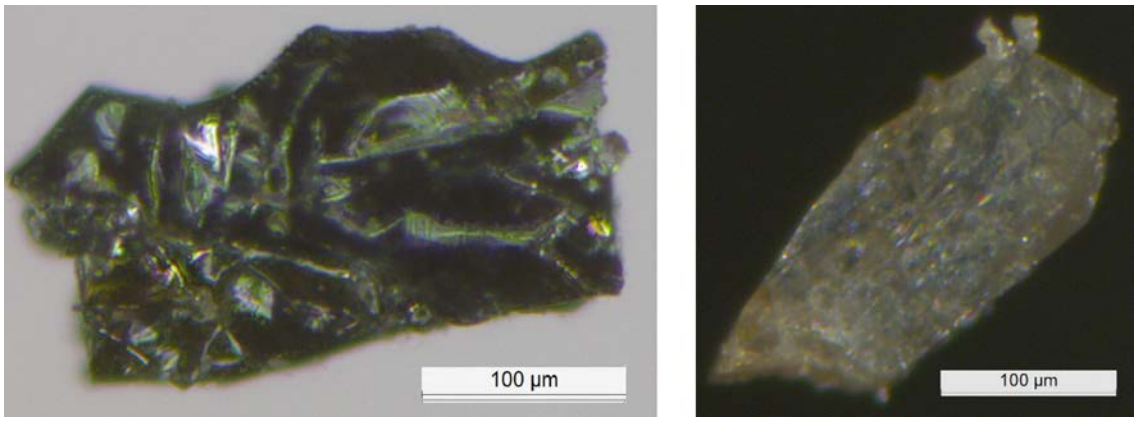

Figure A6.1.14: *Recovered sample from the HP-HT synthesis (20 GPa and 1400 ºC) employing the 25 µm Re capsule. Dark crystals (left) and clear crystal (right) were shown.*

Set-up	Synthesis conditions					Results
	P_{Oil} (bar)	**P (GPa)**	**Power (W)**	**Temperature (ºC)**	**Time (h)**	
5 mm WC anvils 5 mm pyrophyllite gasket With Teflon ring 12.5 µm Re capsule (furnace)	390	12.2	80	360	1.5	Raman: c-In_2O_3
	The recovered sample was completely c-In_2O_3.					
5 mm WC anvils 5 mm pyrophyllite gasket With Teflon ring 12.5 µm Re capsule (furnace)	400	12.3	95	450	1.5	XRD: rh-In_2O_3 Raman: rh-In_2O_3
	Figure A6.1.15 shows the Raman spectra of the recovered sample (rh-In_2O_3). So far, this is the best rh-In_2O_3 Raman spectra obtained. Most of the sample was rh-In_2O_3 (light yellow). Just in the border (top and bottom) of the Re capsule was found c-In_2O_3 (orange) as we can see in the **Figure A6.1.15**. This difference is probably due to vertical temperature gradients in the furnace.					
5 mm WC anvils 5 mm pyrophyllite gasket With Teflon ring 12.5 µm Re capsule (furnace)	390	12.2	95	450	6	XRD: rh-In_2O_3 Raman: rh-In_2O_3
	Test of the effect of the synthesis time. The recovered sample was rh-In_2O_3. Same results as previous HP-HT synthesis.					
7 mm WC anvils 7 mm pyrophyllite gasket With Teflon ring 12.5 µm Re capsule (furnace)	790	7.6	103	510	1.5	Raman: c-In_2O_3
	Pure c-In_2O_3 is recovered after the HP-HT synthesis.					
7 mm WC anvils 7 mm pyrophyllite gasket With Teflon ring 12.5 µm Re capsule (furnace)	810	7.7	110	560	1.5	Raman: c-In_2O_3
	Pure c-In_2O_3 is recovered after the HP-HT synthesis.					
7 mm WC anvils 7 mm pyrophyllite gasket With Teflon ring 12.5 µm Re capsule (furnace)	800	7.6	125	670	1.5	Raman: c-In_2O_3
	Pure c-In_2O_3 is recovered after the HP-HT synthesis.					

7 mm WC anvils 7 mm pyrophyllite gasket With Teflon ring 25 μm Re capsule (furnace)	720	7.3	300	960	0.25	Raman: c-In_2O_3 + rh-In_2O_3
	A furnace instability forced us to stop the synthesis after 15 minutes (quench). A mixture of c-In_2O_3 and rh-In_2O_3 structures has been obtained.					
7 mm WC anvils 7 mm pyrophyllite gasket With Teflon ring 25 μm Re capsule (furnace)	730	7.3	300	960	1	Raman: c-In_2O_3 + rh-In_2O_3
	The furnace instability observed in the previous experiment is reproduced after 1 hour.					
5 mm WC anvils 5 mm pyrophyllite gasket With Teflon ring 12.5 μm Re capsule (furnace)	390	12.2	110	560	0.75	Raman: rh-In_2O_3
	Pure rh-In_2O_3 Raman spectra were obtained (see **Figure A6.1.16**). **Figure A6.1.16** shows the cross section of the recovered sample. A thin layer of c-In_2O_3 is formed in both ends of the Re capsule.					

Table A6.1.5: *HP-HT syntheses starting from c-In_2O_3 employing the 5 and 7 mm CW anvils in the PE large volume press at the University of Valencia.*

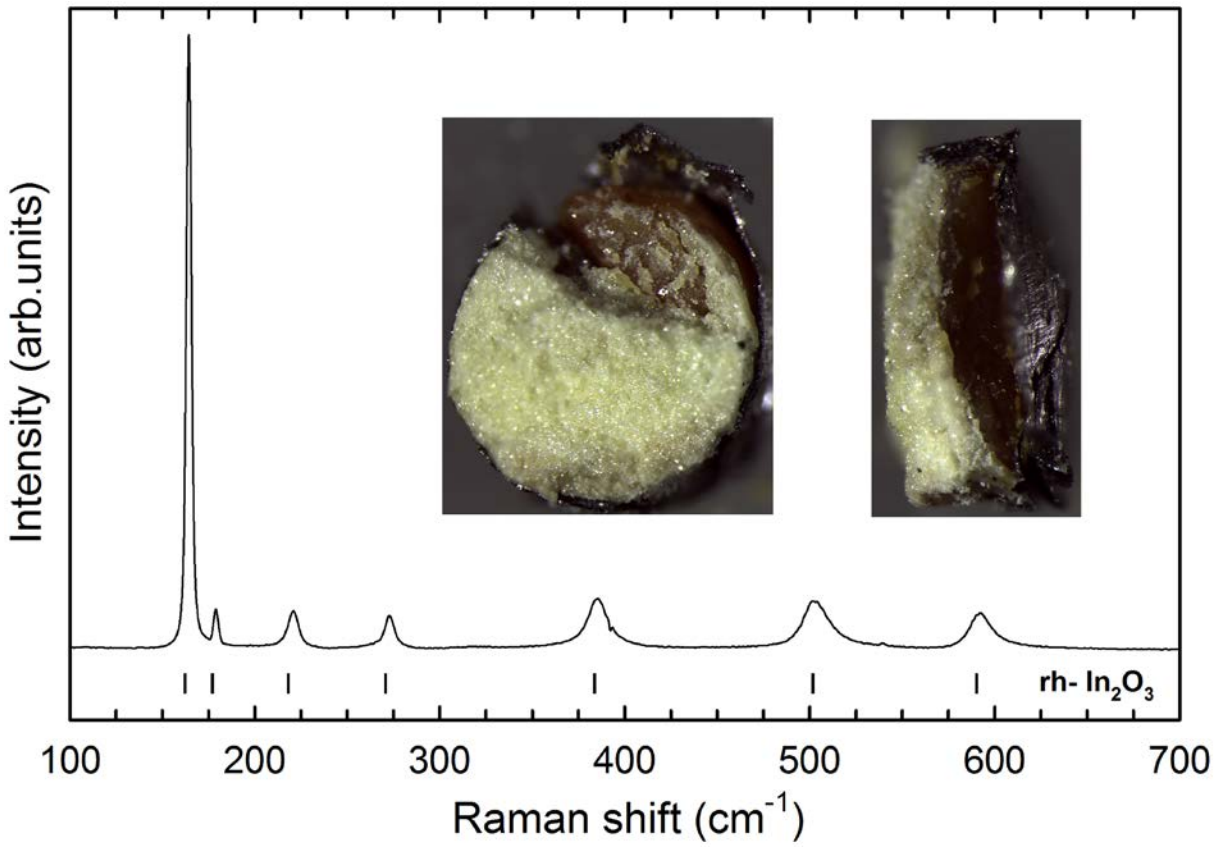

Figure A6.1.15: *Raman spectrum of the recovered sample in the midpoint of the furnace, corresponding to rh-In_2O_3 (light yellow on the inset). c-In_2O_3 (orange) is observed just at top and bottom of the Re furnace.*

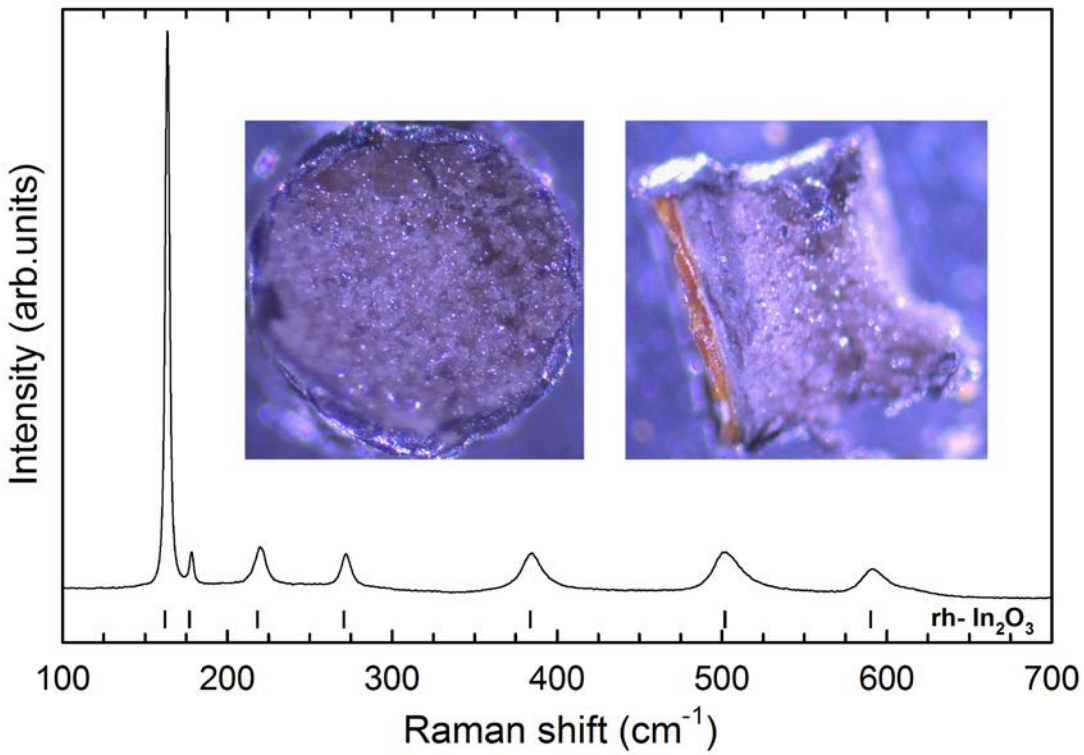

Figure A6.1.16: *Raman spectra of the recovered sample corresponding to rh-In_2O_3 (whitish crystals). c-In_2O_3 (orange) is observed just as a thin layer at the top and bottom of the Re capsule.*

Figure A6.1.17 resumes the "P-T phase diagram" obtained for all the HP-HT synthesis starting from c-In_2O_3. The data published by H. Saitoh *et al*. **[39]** are also given for comparison. I wanted to highlight with quotation marks because we have determined only the P-T conditions which allow to recover rh-In_2O_3 as a metastable phase at ambient conditions. A proper P-T phase diagram determination would require an in-situ study.

The best rh-In_2O_3 crystals (from a point of view of the quality of Raman spectra) were obtained in the region around 12 GPa and between 500 and 600 ºC.

Moreover, we have studied the thermal stability of rh-In_2O_3 at ambient pressure by heating a sample (synthesized at 20 GPa and 1400ºC during 7 h) and recording the corresponding Raman spectra. The results are shown in **Figure A6.1.18**. As we can see, rh-In_2O_3 transforms back to c-In_2O_3 at 600ºC.

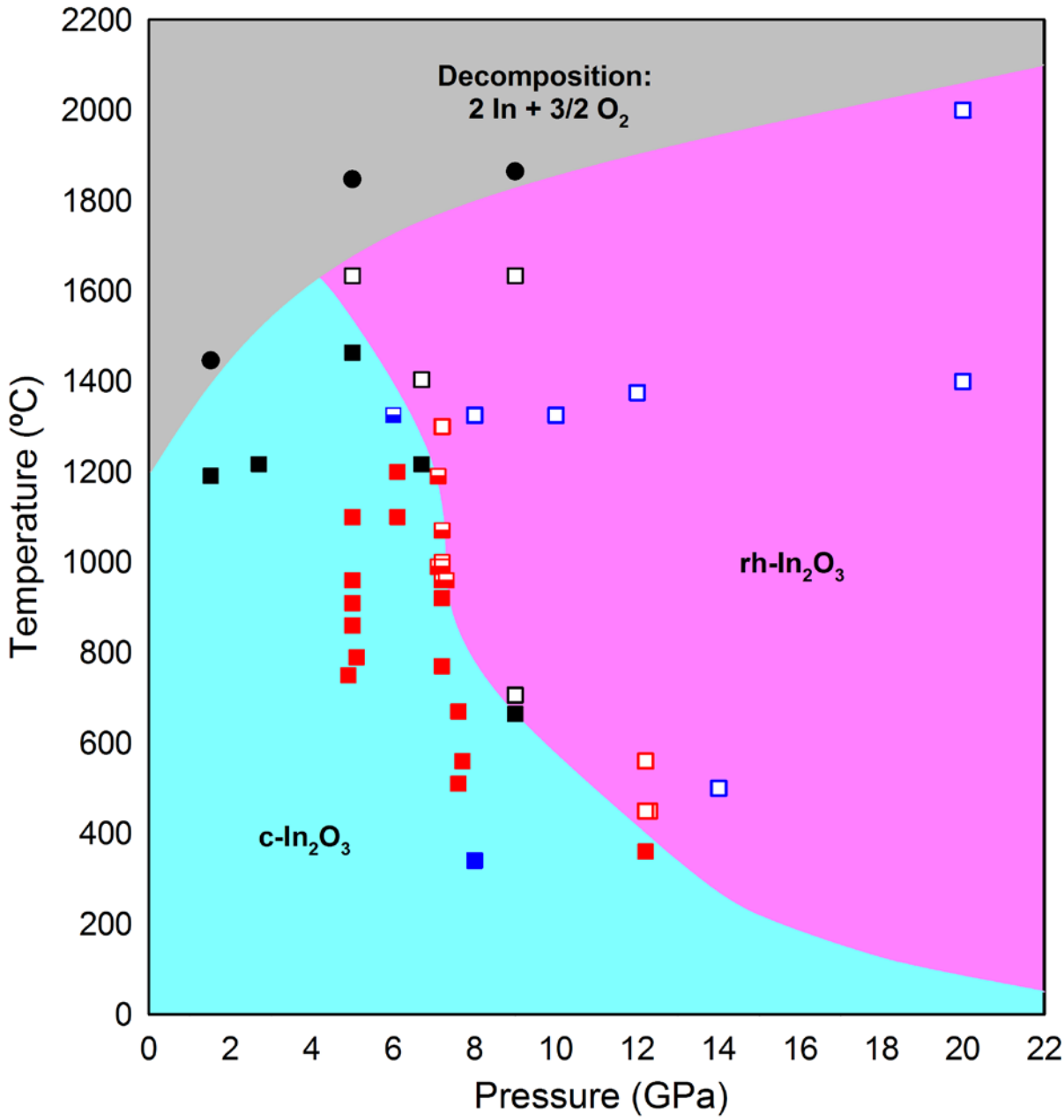

Figure A6.1.17: *"P-T phase diagram" obtained for all the HP-HT synthesis starting from c-In_2O_3. Cyan, pink and gray are the proposed areas for c-In_2O_3 (filled squares), rh-In_2O_3 (empty squares) and decomposition of In_2O_3 (filled circles), respectively. Red and blue symbols correspond to experimental data obtained at the University of Valencia and at the BGI, respectively. Black symbols are the data published by H. Saitoh et al.* ***[39]****.*

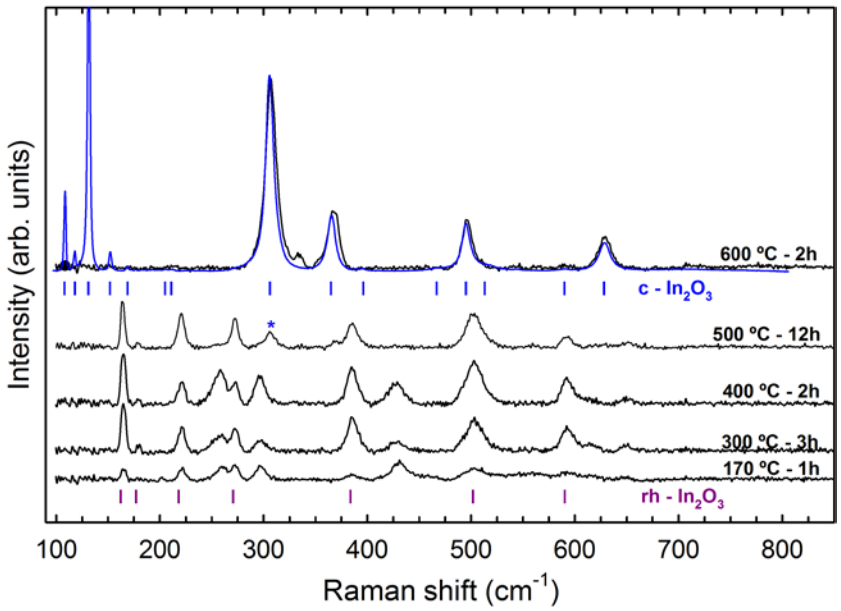

Figure A6.1.18: *Raman spectra as a function of temperature starting from rh-In_2O_3. Blue line corresponds to the experimental Raman spectrum of c-In_2O_3 at ambient conditions. Violet (blue) vertical marks correspond with the main Raman-active modes frequencies of the experimental rh-In_2O_3 (c-In_2O_3) phase.*

Table A6.1.6 resumes all the annealed performed.

Synthesis conditions		
Temperature (ºC)	**Time (h)**	**Results**
170	1	rh-In_2O_3
300	3	rh-In_2O_3
400	2	rh-In_2O_3
500	12	rh-In_2O_3 + c-In_2O_3
600	2	c-In_2O_3

Table A6.1.6: *Temperature phase diagram starting from rh-In_2O_3 at ambient pressure (1atm), employing a commercial heater at BGI.*

The rh-In_2O_3 Raman spectra remain stable till 400 ºC. At 500 ºC, the Raman modes that could not be explained with the first order Raman-active mode of the rh-In_2O_3 disappear. Moreover, the T_g and A_g Raman-active modes located at 300 cm^{-1} (denotes with a blue asterisk) corresponding to the c-In_2O_3 structure begin to appear. At 600 ºC the sample transform completely from rh-In_2O_3 to c-In_2O_3. Due to the edge filter employed, only Raman frequencies higher than 150 cm^{-1} could be observed. This was the main reason for not observing the most intense Raman-active mode (A_g) of the c-In_2O_3 structure, around135 cm^{-1}.

Therefore, we could conclude that the rh-In_2O_3 is stable at least till 500 ºC.

Appendix 6.2: Synthesis of metastable corundum-type Cr^{3+}-doped In_2O_3.

As we have mentioned several times, Cr^{3+}-doped In_2O_3 is a candidate material to be employed as a HP sensor. Moreover, this HP sensor should be more sensitive than Cr^{3+}-doped Al_2O_3 because the bulk modulus of rh-In_2O_3 (176 GPa) is lower than the rh-Al_2O_3 (257 GPa) and therefore rh-In_2O_3 will present a higher compressibility than rh-Al_2O_3.

In this appendix, we will discuss the first attempts to get corundum-type Cr^{3+}-doped In_2O_3. **Table A6.2.1** resumes all the HP-HT synthesis performed at BGI.

Set-up	Synthesis conditions			Results
	P (GPa)	Temperature (ºC)	Time (h)	
18/11 MgO:Cr Graphite furnace 25 μm Re capsule	8	1325	5	XRD: rh-In_2O_3 Raman: rh-In_2O_3 SEM (at. %): O: 73.7 % - In:26.0 % - Cr: 0.3 %
	We manually mixed 150mg of c-In_2O_3 per 1mg of Cr_2O_3 to obtained approximately $[In_{0.99}Cr_{0.01}]_2O_3$. So far, these HP-HT conditions were the optimal conditions to obtain rh-In_2O_3. **Figure A6.2.1** show the Raman spectrum obtained of the reddish recovered sample. Black asterisks (*) denote some Raman-active modes that could not be explained with the rh-In_2O_3. These "extra Raman active modes" disappear as we could observe in **Figure A6.1.18**.			
18/11 MgO:Cr Graphite furnace 25 μm Re capsule	8	1325	3	XRD: rh-In_2O_3 Raman: rh-In_2O_3 SEM (at. %): O: 71.7 % - In:27.0 % - Cr: 1.3 %
	We manually mixed 34.7mg of c-In_2O_3 per 1mg of Cr_2O_3 to obtained approximately $[In_{0.95}Cr_{0.05}]_2O_3$. Similar crystals as showed in **Figure A6.2.1** are recovered. **Figure A6.2.2** shows the crystals in which we performed the microanalysis study. **Figure A6.2.3** shows the Raman spectrum of the recovered sample. As we can see, the Raman spectra obtained present worse quality than the obtained in the previous synthesis (see **Figure A6.2.1**).			
18/11 MgO:Cr Graphite furnace 25 μm Re capsule	10	1325	6	XRD: rh-In_2O_3 Raman: rh-In_2O_3
	We manually mixed 71.25mg of c-In_2O_3 per 1mg of Cr_2O_3 to obtained approximately $[In_{0.975}Cr_{0.025}]_2O_3$. **Figure A6.2.4** and **Figure A6.2.5** show the XRD pattern and the Raman spectrum of a crystal of the recovered sample, respectively. A preferential orientation is observed in the XRD pattern measured.			

Table A6.2.1: *HP-HT syntheses have been made employing a Sumitomo 1200 tons MA press at BGI. The starting material was several concentration of Cr^{3+}-doped c-In_2O_3*

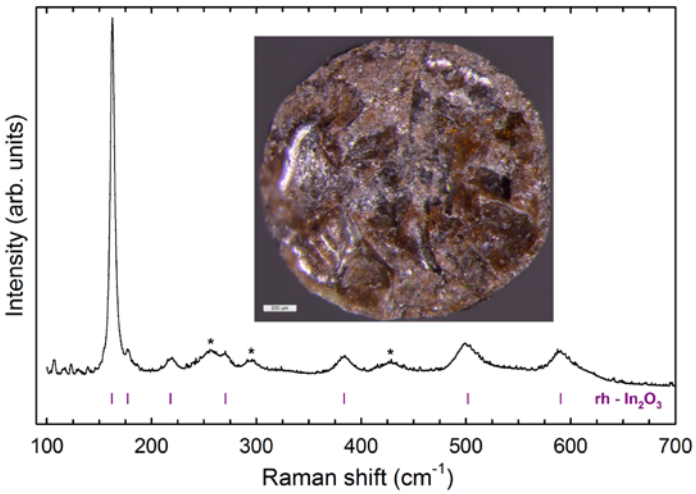

Figure A6.2.1: *Raman spectra of the reddish recovered rh-$(In_{0.99}Cr_{0.01})_2O_3$ sample. Violet vertical marks correspond with the experimental Raman-active modes frequencies of the rh-In_2O_3 phase.*

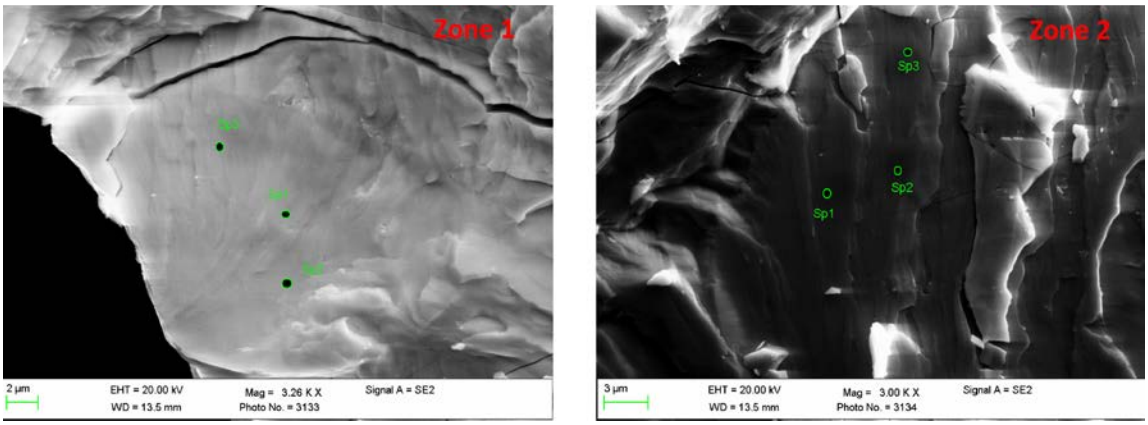

Figure A6.2.2: *Microanalysis study of the reddish recovered rh-$(In_{0.95}Cr_{0.05})_2O_3$ sample.*

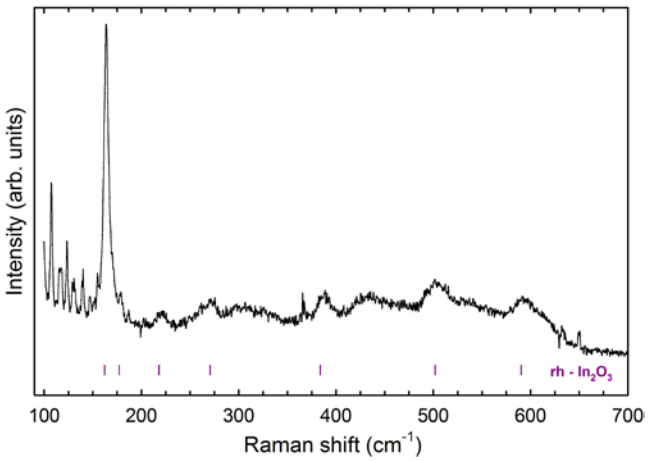

Figure A6.2.3: *Raman spectra of the recovered rh-$(In_{0.95}Cr_{0.05})_2O_3$ sample. Violet vertical marks correspond with the experimental Raman-active modes frequencies of the rh-In_2O_3 phase.*

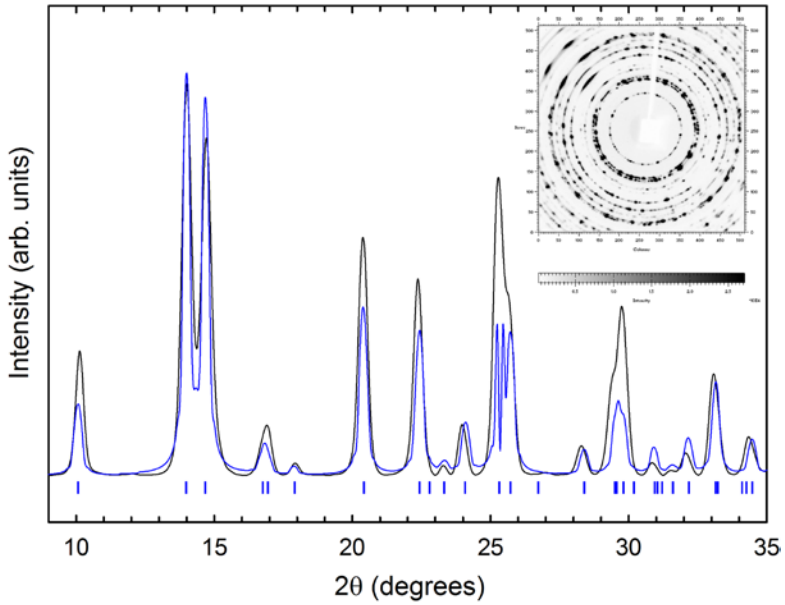

Figure A6.2.4: *CCD image and XRD pattern of a crystal of the recovered rh-$(In_{0.975}Cr_{0.025})_2O_3$ sample. Blue line corresponds with the simulated XRD pattern of rh-In_2O_3 at ambient conditions.*

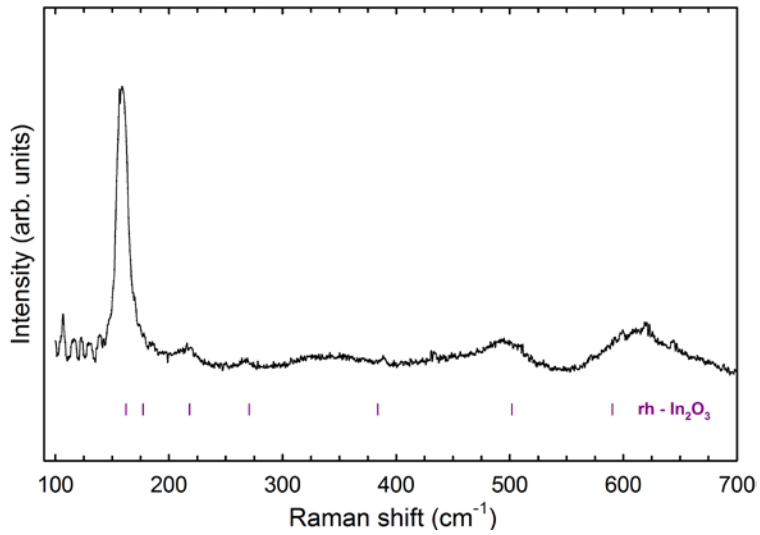

Figure A6.2.5: *Raman spectra of the recovered rh-$(In_{0.975}Cr_{0.025})_2O_3$ sample. Violet vertical marks correspond with the experimental Raman-active modes frequencies of the rh-In_2O_3 phase.*

In the HP-HT synthesized samples (with different Cr^{3+} concentration) we have not observed a luminescence signal. Probably, a manual mixing of c-In_2O_3 and Cr_2O_3 powders does not allow to achieve a homogeneous distribution of Cr in the starting sample. This could be the reason why Cr is finally not incorporated into the crystal lattice of rh-In_2O_3.

We have begun to collaborate with a chemistry group at the University of Valencia (Prof. Eduardo Martínez Tamayo) to get a better distribution of Cr in the starting c-In_2O_3 sample. Therefore, we hope that in the near future we will be able to make new attempts to synthesize Cr doped rh-In_2O_3.

Chapter 7

Structural and vibrational properties of corundum-type In_2O_3 nanocrystals under compression

7.1. Abstract

This work reports the structural and vibrational properties of nanocrystals of rh-In_2O_3 at high pressures by using angle-dispersive XRD and RS measurements up to 30 GPa. The EoS and the pressure dependence of the Raman-active modes of the corundum-type phase in nanocrystals are in good agreement with previous studies on bulk material and theoretical simulations on bulk rh-In_2O_3. Nanocrystalline rh-In_2O_3 showed stability under compression at least up to 20 GPa, unlike bulk rh-In_2O_3 which gradually transforms to the orthorhombic Rh_2O_3−III-type structure above 12–14 GPa. The different stability range found in nanocrystalline and bulk corundum-type In_2O_3 is discussed.

7.2. Introduction

Working with nanocrystals opens the door to enhanced properties of materials **[198, 199]**; and adds the possibility of obtaining metastable HP crystalline and amorphous phases at room conditions with different properties from the original material **[42, 200–202]**. It is well known that most nanocrystals undergo a pressure-induced phase transition at larger pressures than in the bulk and that many nanocrystals suffer a pressure-induced amorphization **[200]**; however,

many questions remain open regarding the behavior of nanocrystals at HP in comparison with bulk materials. In particular, the different thermodynamic stability of crystalline phases in nanocrystals as compared to bulk material **[200, 201]**, and whether the compressibility of nanocrystals is different to that of bulk material or if the different compressibility comes from a different degree of hydrostaticity affecting micro and nanocrystal powders.

Several works have been devoted to the study of In_2O_3 nanocrystals at HP, some have focused on nanocrystals of cubic bixbyite-type In_2O_3 **[53, 161, 203]**, and some have been devoted to study nanocrystals of rhombohedral corundum-type In_2O_3 **[40, 43, 161]**. In fact, a different stability range of the rhombohedral phase under compression has been observed depending on the sample size. Gurlo et al, who studied nanocrystals of rh-In_2O_3, suggested that this compound is stable at room temperature between room pressure and 30 GPa **[40]**; however, two recent studies reported that bulk rh-In_2O_3 undergoes a transformation above 12–14 GPa in good agreement with theoretical simulations **[63, 172]**. The apparent lack of phase transition in nanocrystals up to 30 GPa suggests the existence of large kinetic barriers to explain their extended structural stability.

In this work we report a HP study of the structural and vibrational properties of nanocrystals of rh- In_2O_3 by means of angle-dispersive powder XRD and RS measurements up to 30 GPa. Both the EoS and the pressure dependence of the Raman-active modes of the corundum phase in nanocrystals are reported, showing a nice agreement with previous studies on rh-In_2O_3 nanocrystals **[40]**. These results have been compared with experimental and theoretical structural and lattice dynamics results on bulk rh-In_2O_3 offering an explanation to the previously apparent contradicting results observed between bulk and nanocrystalline rh-In_2O_3.

7.3. Methods

7.3.1. Experimental details

Rh-In_2O_3 nanoparticles were synthesized by thermal dehydration of InOOH nanoparticles previously prepared from a solvothermal reaction between indium nitrate and tetramethylammonium hydroxide **[204]**. XRD measurements confirm that nanocrystalline powders are pure and crystallize in corundum-type structure with a hexagonal unit cell showing a lattice parameters $a = b = 5.485$ Å and $c = 14.530$ Å, which are in good agreement with reference JCPDS card 220336 ($a = b = 5.487$ Å and $c = 14.510$ Å). On the other hand, transmission electron microscopy confirmed both the crystalline structure and purity and

determined that nanocrystals have a rice-grain type morphology with an average length (width) of 20 (13) nm and a uniform distribution between 10 (6) and 30 (20) nm **[204]**. Room-temperature experiments in rh-In_2O_3 nanocrystals were conducted up to 30 GPa in a membrane-type DAC. In HP-XRD and HP-RS experiments, powder sample was loaded inside a 150 μm diameter hole drilled in an inconel gasket together with a mixture of MEW in a 16:3:1 proportion as a quasihydrostatic PTM as in a previous work **[63]**, in order to compare results for bulk and nanocrystalline rh-In_2O_3 under the same conditions. Additionally, a second XRD experiment with Ar as PTM was done in order to prove if nanopowders could be affected by non-hydrostatic effects using MEW and to compare with previous results described in the literature **[63]**. For pressure calibration in angle-dispersive powder XRD and RS measurements we introduced inside the pressure cavity Cu powder **[110]** and ruby **[109]**, respectively. In the XRD experiments we collected also two patterns, one in the region where the Cu peaks are strong and the other where there is no Cu signal. The first pattern was used to determine pressure and the second one to analyze the crystal structure of In_2O_3.

Angle-dispersive powder XRD measurements at different pressures were performed in the MSPD beamline **[118]** at ALBA synchrotron facility. This beamline is equipped with Kirkpatrick–Baez mirrors to focus the monochromatic beam and a SX165 CCD detector with a diameter of 165 mm. We used a wavelength of 0.4246 Å and the sample-detector distance during the experiment was set to 240 mm. The 2D diffraction images were integrated with FIT2D software **[120]**. Lattice parameters of XRD patterns were obtained with Rietveld refinements performed using POWDERCELL **[121]** and GSAS **[122]** program packages. On the other hand, RS measurements at room temperature and different pressures were excited using the 632.8 nm HeNe laser (with a power below 10mW) and collected in backscattering geometry with a Horiba Jobin Yvon LabRam HR UV spectrometer equipped with a thermoelectrically cooled multichannel CCD detector (resolution below 2 cm^{-1}).

7.3.2. Theoretical calculations

Total-energy *ab initio* calculations were performed for bulk rh-In_2O_3 within the DFT **[124]** using the VASP **[147]** as described in **[63]** for bulk rh-In_2O_3. In particular, we have used the PAW **[125]** scheme implemented in this package and the GGA was used for the description of the exchange-correlation energy with the PBEsol prescription **[130]**.

We have also performed lattice dynamics calculations of the phonon modes in bulk rh-In_2O_3 at the center of the Brillouin zone (Γ point) using the direct force constant approach (or

supercell method) **[131]** already described in **[63]**. Our theoretical results provide both the frequencies of the normal modes and their polarization vectors and enable us to assign the Raman-active modes observed in nanocrystalline rh-In_2O_3 as previously done for bulk rh-In_2O_3 **[63]**.

7.4. Results

7.4.1. XRD measurements

Figure 7.1 (a) shows a selection of the experimental angle-dispersive powder XRD patterns of nanocrystalline rh-In_2O_3 at room temperature at different pressures up to 20.5 GPa obtained in the first experiment (using MEW mixture as PTM). **Figure 7.1 (b)** shows similar results up to 29.8 GPa obtained in the second experiment (using argon (Ar) as PTM).

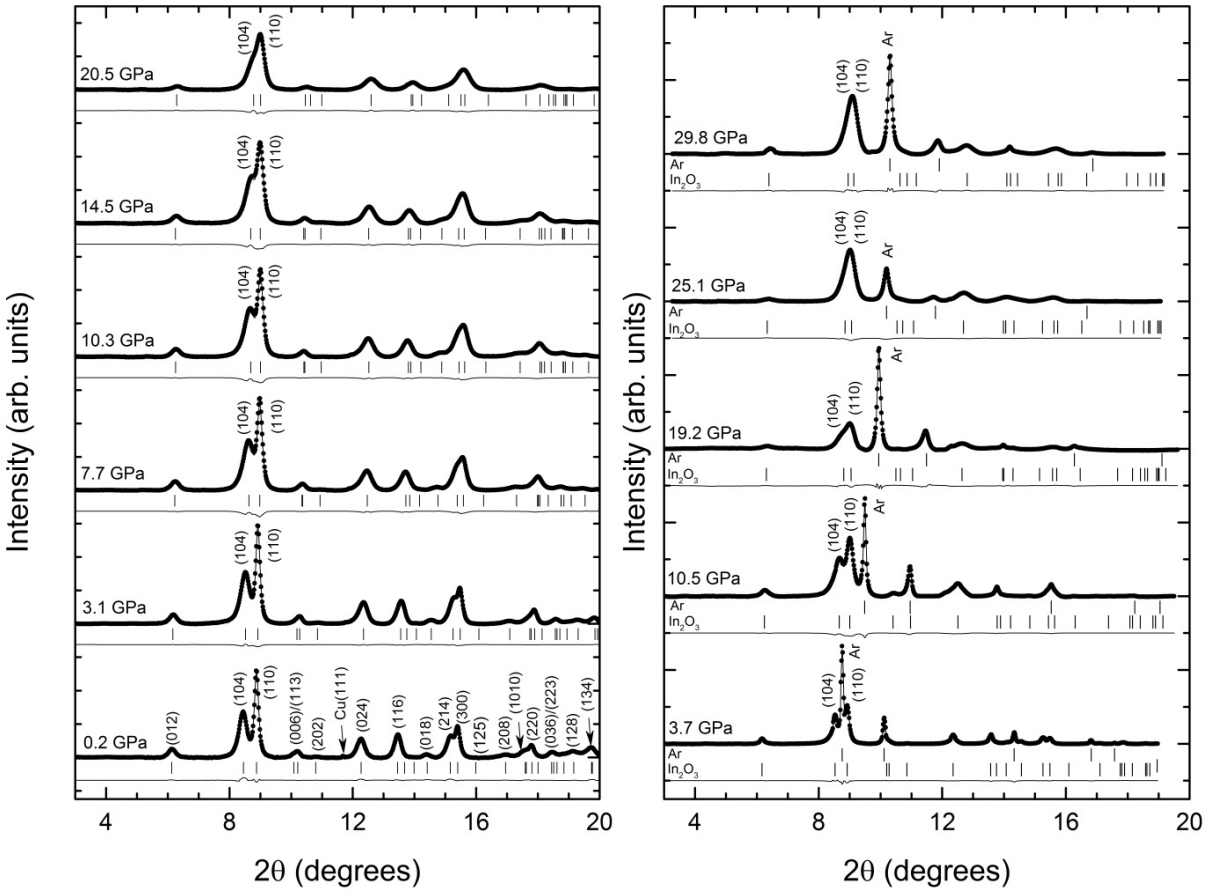

Figure 7.1: *Selected X-ray diffraction patterns of nanocrystalline rh-In_2O_3 at several pressures using MEW **(a)** and Ar **(b)** as PTM. Diffraction patterns have been shifted vertically for clarity. Different diffraction peaks are assigned in the graph to rh-In_2O_3 (R-3c), Ar and Cu phases. Refinements and residuals of the fit to these phases are also shown.*

All the XRD patterns can be indexed with the corundum-type structure. Under compression some of the peaks shift faster to higher angles than others due to the anisotropic compressibility of In_2O_3 which will be discussed in detail later. This phenomenon is illustrated in **Figures 7.1 (a)** and **(b)** by the (104) and (110) Bragg peaks which gradually merge under compression because the interplanar distance associated to the (104) peak decreases faster than that corresponding to the (110) reflection with increasing pressure. In the second experiment, in addition to the Bragg peaks of the sample, Bragg peaks of Ar are also detected. These peaks can be easily identified because, due to the large compressibility of Ar, they shift faster to higher angles under compression than the peaks corresponding to In_2O_3. The Ar peaks were used to confirm the pressure determined from Cu using the EoS of Ar **[205]**. The pressure determined from Ar agrees within 0.1 GPa with the pressure determined from Cu. The results of both XRD experiments indicate that the phase transition to the *Pbca*-type phase observed in bulk rh-In_2O_3 above 12–14 GPa **[63, 172]**, is not observed in nanocrystals even at 29.8 GPa.

We would like to comment here that beyond 20 GPa all the peaks assigned to corundum-type In_2O_3 can be also explained with the *Pbca*-type structure. However, this structure has a peak at low angles, the (002) peak expected to be located around 3.2°, which is not present in the corundum-type structure. In our experiments, we did not observe this peak, which supports the stability of the corundum-type structure up to 29.8 GPa. This result is in agreement with the larger stability of the corundum phase measured by Gurlo *et al.* in nanocrystalline rh-In_2O_3 samples with particle size between 50 and 100 nm **[40]**. XRD peaks in our first experiment show slight broadening with increasing pressure above 10 GPa which could be due to a slight loss of quasi-hydrostatic conditions of the PTM. The same broadening is observed in the second experiment but around 20 GPa. This is a consequence of the better quasi-hydrostatic conditions generated by Ar than by MEW above 10 GPa **[206]**. In this regard, it is expected that small non-hydrostatic stresses do not influence the structural stability of relatively uncompressible compounds, like sesquioxides **[177]**.

In this work, we have extracted the evolution of the structural parameters of nanocrystalline rh-In_2O_3 under compression by Rietveld refinement. In **Figure 7.1**, one can see the experimental diffraction pattern (black symbols), the Rietveld refinement performed (black line) and the residuals (gray lines) showing a good fit to the experimental data. **Figure 7.2** represents the experimental pressure dependence of the hexagonal unit-cell volume per formula unit, lattice parameters *a* and *c* and the *c*/*a* ratio in nanocrystalline rh-In_2O_3. The

experimental data of the unit-cell volume per formula unit up to 29.8 GPa can be fitted with a third-order Birch–Murnaghan EoS **[62, 178]**, which yields V_0/Z = 62.78 (7) Å^3, B_0 = 169(6) GPa and B_0' = 6.2(9). These values are in good agreement with theoretical data of bulk material fitted up to 30 GPa (V_0/Z = 63.88 Å^3, B_0 = 169 GPa and B_0' = 3.3) and with previous experimental (B_0 = 176–180 GPa) and theoretical estimations in bulk material **[63]**. Note that the value of the bulk modulus for rh-In_2O_3 nanocrystals is slightly smaller than that in bulk material (see **Table 7.1**). In relation to this, it must be noted that a decrease of the bulk modulus in nanocrystals with respect to bulk material has been observed in a number of oxides, like TiO_2 **[207, 208]**, ZrO_2 **[209, 210]**, SnO_2 **[211]**, MgO **[212]**, ZnO **[213]** and Al_2O_3 **[214]**.

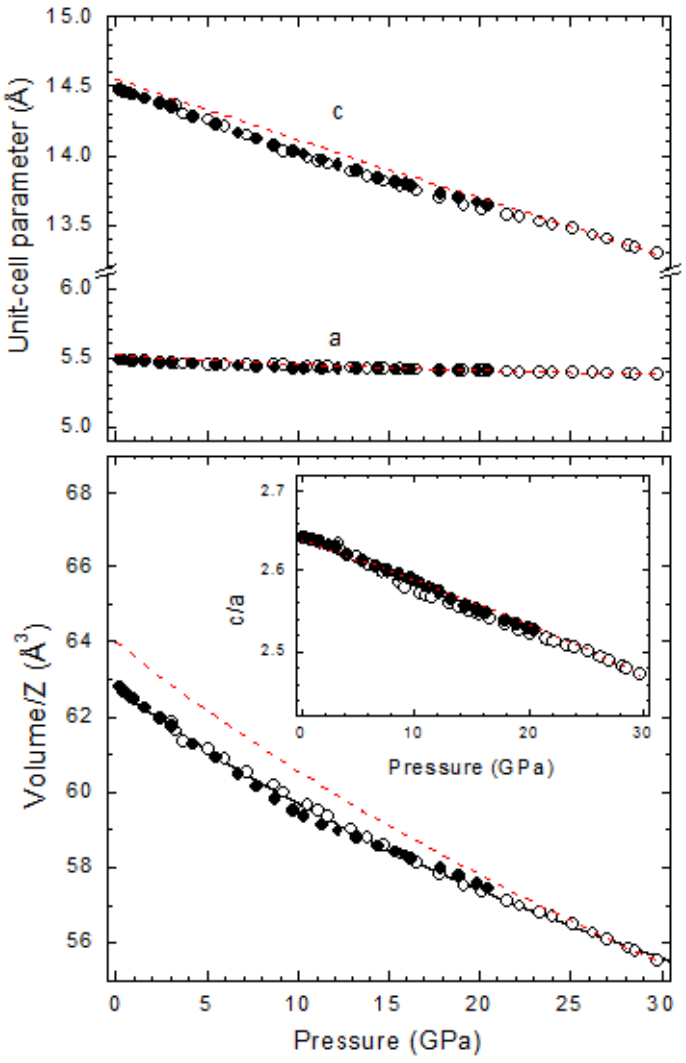

Figure 7.2: *Pressure dependence of the unit-cell parameters* ***(a)*** *and volume per formula unit* ***(b)*** *in nanocrystalline rh-In_2O_3 for our first experiment (closed symbols) and the second experiment (open symbols). The* ***inset*** *shows the pressure dependence of the c/a ratio in nanocrystalline rh-In_2O_3. Red dashed lines correspond to theoretical data of bulk rh-In_2O_3.*

	Phase	V_0/Z (Å^3)	B_0 (GPa)	B_0'	Method
nano	R-3c	62.78 (1)	169(6)	6.2 (9)	Exp. (XRD)[a]
	R-3c	61.49	305.5	2.9	Exp. (XRD)[b]
bulk	R-3c	62.86 (4)	180(7)	3.2 (1.2)	Exp. (XRD)[c]
	R-3c	63.88	167	3.3	Theo. (GGA-PBEsol)[d]

[a]Reference 215. [b]Reference 53. [c]Reference 63. [d]Data up to 30 GPa.

Table 7.1: *Comparison of theoretical and experimental unit-cell volume per formula unit, bulk modulus, and its pressure derivative for bulk and nanocrystalline rh-In_2O_3 at room pressure.*

A deviation of the compressibility of nanocrystals above certain pressure has been found in other works. In particular, nanocrystals of anatase TiO_2 pressurized with a 4:1 methanol-ethanol mixture were found to undergo deviations of the compressibility of the *a* axis and unit-cell volume per formula unit above 10–12 GPa which were attributed to the appearance of an intermediate local distortion (~ 2Å) with TiO_2-II structure **[216]**. On the other hand, a significantly lower bulk modulus (B_0 = 148 ± 5 GPa) compared to theoretical calculations (B_0 = 169.4 GPa) has been recently observed in c-In_2O_3 nanocrystals with a high defect density under compression with a 4:1 methanol-ethanol mixture as PTM **[203]**. In that work, authors claimed that the different bulk modulus of two nanocrystalline samples with similar sizes and morphologies were due to their different defect densities. Another possibility is that the change in compressibility observed above 8 GPa in In_2O_3 nanocrystals could be due to non-hydrostatic conditions as it was reasoned for nanocrystalline TiO_2 anatase **[207]**. Note that nanocrystalline powder is more prone to non-hydrostatic conditions than bulk powder because the surface areas of nanocrystalline grains tend to be more surrounded by other nanocrystalline grains than by the molecules of the PTM. On the other hand, the surface areas of microcrystalline grains tend to be more surrounded by the molecules of the PTM than by other grains. In any case, it was demonstrated for nanocrystalline TiO_2 anatase that the EoS obtained prior to observation of non-hydrostatic conditions is in good agreement with the EoS obtained under truly hydrostatic conditions along the whole range of the experiments **[207]**. Since measurements in nanocrystalline rh-In_2O_3 using MEW or Ar show similar results (see **Figure 7.2**), we are confident of the bulk modulus obtained for nanocrystals with an average grain size around 20 nm up to 30 GPa. It must be stressed that the bulk modulus we have obtained for rh-In_2O_3 nanocrystals in the present study is much smaller than that reported (305 GPa) in a previous work **[53]**. In fact, Qi et al **[53]**, also reports an overestimation of the bulk modulus in rh-In_2O_3 as was also confirmed in our previous work **[63]**. The main reason for the overestimation of the bulk modulus in **[53]** is the lack of structural data for the corundum-

type phase at low pressures and the inherent uncertainty caused by the extrapolation of the bulk modulus from data above 20 GPa.

On the other hand, our experiment shows that both *a* and *c* lattice parameters show a rather similar pressure dependence in both bulk material and nanocrystals, also observed in the *c/a* ratio (inset of **Figure 7.2 (b)**). The lattice parameters of rh-In_2O_3 nanocrystals show an almost linear variation with pressure. Both *a* and *c* parameters (*x* = *a*, *c*) have been fitted to a modified Murnaghan's equation with free parameters x_0, B_0 and B_0'.

$$x = x_0 \left(1 + \frac{B_0'}{B_0} P\right)^{-\left(\frac{1}{3B_0'}\right)} \quad \textbf{(7.1)}$$

The results of these fits are shown in **Table 7.2**. The axial compressibilities of the *a*- and *c*-axis defined as:

$$\kappa_x = \frac{-1}{x}\frac{\partial x}{\partial P} \quad \textbf{(7.2)}$$

and can be obtained as:

$$\kappa_x = \frac{1}{3B_0} \quad \textbf{(7.3)}$$

with the B_0 values obtained with the Murnaghan EoS fit for the lattice parameters. The experimental compressibility of the *a* (*c*) axis is 1.4 (3.0) 10^{-3} GPa^{-1}. This result indicates that the *c* axis is more than two times more compressible than the *a* axis as it occurs in bulk rh-In_2O_3 **[63]**. Consequently, we can conclude that the major contribution to the compressibility of nanocrystalline rh-In_2O_3 comes from the larger compressibility of the *c* axis than that of the *a* axis. These behaviors are in agreement with experiments and theoretical calculations already published for bulk rh-In_2O_3 **[63]** and theoretical calculations (see **Table 7.2**). Similarly, the *c*/*a* ratio in bulk and nanocrystalline rh-In_2O_3 shows the same tendency in good agreement with our theoretical calculations; however, this behavior is different to that reported in corundum-type Al_2O_3, V_2O_3, Cr_2O_3, and Fe_2O_3 **[182]**, as already discussed in our previous work regarding bulk rh-In_2O_3 **[63]**.

a_0 (Å)	B_{0a} (GPa)	B_a'	c_0 (Å)	B_{0c} (GPa)	B_c'	Method
5.4831 (8)	233 (16)	11.8	14.461 (8)	109 (3)	0.48	Our Exp. (XRD)
5.479 (2)	220 (30)	11.8	14.511 (5)	121 (7)	0.48	Exp. (XRD)
5.520 (1)	216 (3)	11.8 (4)	14.552 (1)	106.0 (9)	0.48 (11)	Theo. (GGA-PBEsol)

Table 7.2: *Experimental lattice parameters and their bulk modulus and pressure derivative of bulk modulus at room pressure in nanocrystalline rh-In_2O_3 as compared to experimental and theoretical parameters in bulk rh-In_2O_3.*

7.4.2. Raman scattering

The corundum structure of In_2O_3 has 7 Raman-active modes whose frequencies at ambient pressure have been already reported in bulk material and nanocrystals **[28, 38, 63, 217, 218]**. **Figure 7.3** shows selected Raman spectra of nanocrystalline rh-In_2O_3 at different pressures up to 29.3 GPa using MEW as PTM. As observed, the RS spectrum of nanocrystals is dominated by the A_{1g} mode with lowest frequency (near 163 cm^{-1} at room pressure).

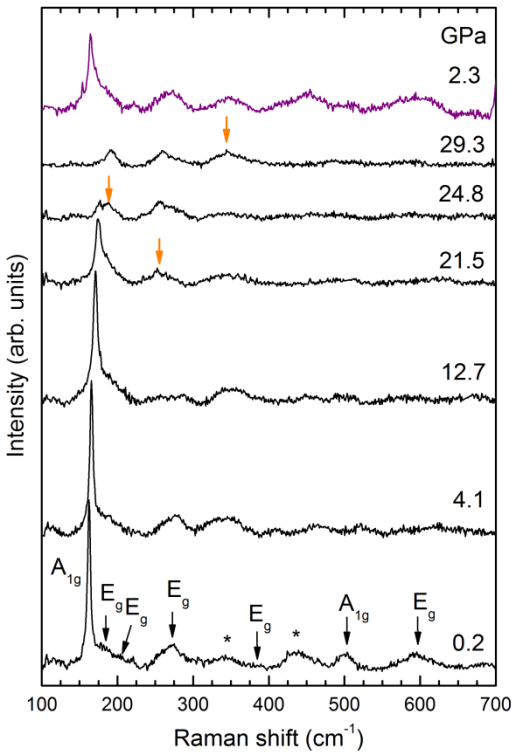

Figure 7.3: *Selected RS spectra of nanocrystalline rh-In_2O_3 at different pressures on upstroke up to 29.3 GPa. In the RS spectrum at 0.2 GPa, first-order Raman modes of rh-In2O3 are indicated by black arrows, while second-order Raman modes are denoted with asterisks. Above 20 GPa, orange arrows in the RS spectra indicate the new peaks assigned to the Pbca phase. The top violet RS spectrum at 2.3 GPa shows the reversibility of the sample to the corundum phase on downstroke.*

Table 7.3 summarizes the Raman-active modes of our nanocrystals at ambient conditions, which are also compared to those found in bulk material. All Raman frequencies in nanocrystals differ by less than 10 cm^{-1} from those of the bulk material. In order to analyse the influence of the morphology of the nanocrystals in their Raman frequencies, different nanocrystalline geometries can also be compared. Hierarchical nanocrystals orderly dendrite-like aggregates **[217]** and 3D rh-In_2O_3 nanoflowers **[218]** were characterized by XRD and Raman spectroscopy at room conditions. In the former geometry, the Raman spectrum showed peaks at 164, 222, 273, 385, 504, and 595 cm^{-1} whereas in the latter, the Raman modes appeared at 163, 219, 384, 501 and 590 cm^{-1}. Regarding the XRD patterns of these samples at room conditions, both studies reported a good correlation with lattice planes obtained from the JCPDS database. It can be concluded that the difference in Raman frequency between the different geometries of rh-In_2O_3 nanocrystals is less than 5 cm^{-1}, which reveals the low influence of the morphology in the vibrational properties.

	Bulk rh-In_2O_3								**Nano rh-In_2O_3**		
	***Ab initio* calculations**				**Experimental [b]**				**Experimental**		
Mode (Sym)	ω_0 (cm^{-1})	$\frac{\partial\omega}{\partial P}$ $\left(\frac{cm^{-1}}{GPa}\right)$	$\frac{\partial^2\omega}{\partial P^2}$ $\left(\frac{cm^{-1}}{GPa^2}\right)$	γ^a	ω_0 (cm^{-1})	$\frac{\partial\omega}{\partial P}$ $\left(\frac{cm^{-1}}{GPa}\right)$	$\frac{\partial^2\omega}{\partial P^2}$ $\left(\frac{cm^{-1}}{GPa^2}\right)$	γ	ω_0 (cm^{-1})	$\frac{\partial\omega}{\partial P}$ $\left(\frac{cm^{-1}}{GPa}\right)$	γ^c
A_{1g}	156 (1)	0.65 (3)	-0.012 (2)	0.66	162.3 (2)	0.85 (4)	-0.015 (1)	0.93	163.2 (2)	0.590 (14)	0.61
E_g	169 (1)	0.73 (3)	-0.010 (2)	0.68	177.1 (2)	1.01 (6)	-0.022 (3)	1.01	181.3 (5)	0.54 (4)	0.50
E_g	214 (1)	1.54 (3)	-0.023 (2)	1.14	218.1 (3)	1.85 (8)	-0.039 (5)	1.50	223.9 (5)	1.30 (3)	0.97
E_g	265 (1)	1.11 (6)	-0.005 (5)	0.66	270.7 (4)	1.33 (13)	-0.011 (7)	0.87	270.0 (1.0)	1.49 (11)	0.93
E_g	373 (2)	4.91 (5)	-0.040 (4)	2.08	383.8 (6)	4.69 (16)	-0.022 (8)	2.16	388.3 (9)	4.61 (6)	2.0
A_{1g}	486 (2)	4.46 (6)	-0.033 (4)	1.45	501.9 (9)	3.92 (25)	0.005 (14)	1.38	502.5 (6)	4.75 (5)	1.6
E_g	569 (2)	6.14 (5)	-0.059 (4)	1.70	590.3 (6)	5.95 (18)	-0.058 (12)	1.78	599.0 (1.0)	5.42 (11)	1.53

*[a]Theoretical B_0 = 158 GPa used for calculating the Grüneisen parameter. [b]From **[63]** (experimental B_0 = 177 GPa used for calculating the Grüneisen parameter). [c]Experimental B_0 = 169 GPa used for calculating the Grüneisen parameter.*

***Table 7.3:** Room-pressure frequencies, pressure coefficients and Grüneisen parameters of the Raman active modes of experimental and theoretical bulk and experimental nanocrystalline rh-In_2O_3.*

As regards the pressure dependence of the Raman-active modes, the A_{1g} mode of the corundum phase is observed up to 24.8 GPa; i.e., almost up to the same pressure as in bulk rh-

In_2O_3 (26 GPa) **[63]**. However, a slight change in the RS spectrum is observed above 21.5 GPa (more clear in the spectra at 24.8 and 29.3 GPa) with the appearance of new peaks which are coincident with the decrease of the intensity of the A_{1g} peak of the corundum phase. The new modes can be reasonably attributed to o3-In_2O_3 since the most intense mode of this phase has a slightly larger frequency (near 183 cm^{-1}) than the A_{1g} mode of the corundum phase **[63, 172]**. In this way, all RS modes of the sample at 29.3 GPa can be attributed to the orthorhombic *Pbca* phase. Finally, in the downstroke process, the rhombohedral phase was recovered below 8 GPa (see top RS spectrum in **Figure 7.3**); i.e., at a similar pressure as in bulk material **[63]**. This result indicates that the hysteresis in rh-In_2O_3 nanocrystals is larger than in bulk material.

It is noteworthy that a HP phase transition from the corundum type phase to the *Pbca* phase is observed above 20 GPa in RS measurements, but not in XRD measurements. The explanation for this discrepancy could come from different aspects. First, it is well known that RS measurements are more sensitive to local structural changes than XRD measurements and HP phase transitions are observed at lower pressures in RS measurements than in XRD measurements **[219]**. In our nanocrystals, this fact could lead to the observation of the HP transition beyond 25 GPa by XRD measurements. Second, the nanometric size of samples, leading to broader XRD peaks than those in bulk material, and the fact that many peaks of the rhombohedral *R-3c* and orthorhombic *Pbca* phases are coincident in the range between 20 and 30 GPa, provides additional difficulty to the observation of the HP phase transition even beyond 25 GPa since the small peak near 3.2° could be smeared out in nanocrystals. Third, it has been recently shown that HP transformations in nanocrystals can be affected by internal defects **[203]** or even surface effects **[220, 221]**, which could eventually depend on the PTM. This means that the HP phase transition measured in RS measurements using MEW could be retarded when using Ar, which will explain the lack of phase transition even up to 30 GPa in this work and on that of Gurlo *et al.* **[40]**. Supporting this assumption, we already observed a similar behavior on bulk c-In_2O_3 under compression **[172]**. The transition pressure from cubic-to-orthorhombic *Pbcn* phase appeared at 35 GPa using the most hydrostatic PTM (helium), whereas it was observed at slightly lower pressures (31 GPa) using MEW. Finally, it must be stressed that some transitions not observed by XRD at ambient temperature can be induced by local laser heating in small bandgap materials or in samples with dark defects which are precursors of the HP phase transition **[222]**. The lack of radiation damage by laser heating in rh-In_2O_3 nanocrystals is supposed by the large bandgap energy of this compound

(above 3.75 eV at ambient pressure) **[33]**. In fact, the energy bandgap of rh-In_2O_3 under compression remains in the UV region up to around 20 GPa. The **Appendix 7.1** shows the theoretical and experimental energy bandgap of several polymorphs of In_2O_3. The origin of this controversy could be unveiled by new single crystal XRD experiments well above 20 GPa in rh-In_2O_3 nanocrystals using a nanosize beam **[223]** and using argon, neon or helium as PTM.

Figure 7.4 shows the pressure dependence of the experimental and theoretical frequencies of the first-order Raman-active modes of rh-In_2O_3 nanocrystals. All Raman-active mode frequencies increase with pressure in a monotonous way up to the maximum pressure attained in the experiment in good agreement with previously reported experimental and theoretical Raman modes for bulk rh-In_2O_3 **[63]**.

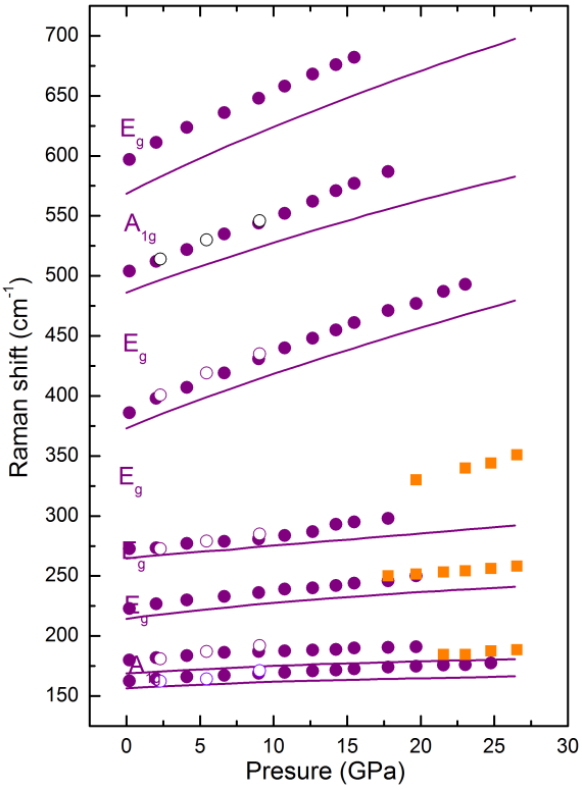

Figure 7.4: *Pressure dependence of the Raman-active mode frequencies in nanocrystalline rh-In_2O_3 (violet circles) and o3-In_2O_3 (orange squares). Full (empty) symbols correspond to the upstroke (downstroke) process. Solid lines correspond to ab initio simulated Raman-active modes of bulk rh-In_2O_3. The symmetry of the Raman-active modes of rh-In_2O_3 is indicated.*

Table 7.3 summarizes the zero-pressure experimental and theoretical frequencies, pressure coefficients and the Grüneisen parameters of the Raman active modes of rh-In_2O_3

nanocrystals. Above 20 GPa new peaks have been attributed to the *Pbca* phase due to the similarity to previously reported RS spectrum and pressure dependences of the observed peaks. It must also be considered that different rh-In_2O_3 nanocrystals with different morphologies other than rice-grain type have been grown in the last decade **[217, 218]**. A priori, we expect that all nanoparticles with similar size behave in a similar way **[208]**. In any case, future HP experiments using rh-In_2O_3 nanocrystals with different morphologies will help to understand the HP behavior of rh-In_2O_3 nanocrystals.

Finally, we would like to stress that the higher sensitivity of rh-In_2O_3 to compression than its isostructural compounds Al_2O_3, Ga_2O_3, and Cr_2O_3 could be relevant for pressure calibration. As commented in our previous work on bulk rh-In_2O_3 **[63]**, the most usual method for pressure calibration in the laboratory relies on spectroscopic techniques in ruby, whose sensitivity is related to the bulk modulus of this material. Therefore, the existence of compounds with a smaller bulk modulus than ruby and with the possibility to host Cr^{3+} cations opens a new path in the search for more accurate pressure sensors. In this context, the low value of the bulk modulus of rh-In_2O_3 and the stability of the rh-In_2O_3 nanocrystals at least up to 20 GPa (8 GPa more than bulk material at least) at room temperature **[63]** suggest that Cr^{3+}-doped rh-In_2O_3 nanocrystals could be a possible candidate to substitute ruby at least below 20 GPa. It is expected that the higher sensitivity of the host material (rh-In_2O_3) would produce an increase of the pressure coefficient of the luminescence lines of Cr^{3+} of about 30% with respect to ruby and consequently, a more accurate determination of pressure. However, for that purpose metastable corundum-type Cr^{3+}-doped In_2O_3 nanocrystals must be prepared in an easy way as a single crystalline phase and its photoluminescence under pressure need to be studied for different concentrations of Cr^{3+} doping.

7.5. Conclusions

We have presented the structural and vibrational behavior of rh-In_2O_3 nanocrystals up to 30 GPa and compared them to those of the bulk material and theoretical simulations. Angle-dispersive powder XRD measurements in rh-In_2O_3 nanocrystals have allowed us to obtain a more accurate experimental EoS for this compound in good agreement with theoretical calculations and experiments for bulk rh-In_2O_3. Also similar pressure coefficients for the Raman-active modes have been observed in nanocrystals, thus confirming the similar bulk modulus of our nanocrystals and bulk material.

Our RS measurements confirm that rh-In_2O_3 nanocrystals undergo a phase transition towards the *Pbca* phase at much higher pressures (above 20 GPa) than in bulk material. However, such a phase transition has not been confirmed with our powder XRD measurements even up to 30 GPa. The origin of this discrepancy has been circumscribed to three possible effects, proposing a new experiment to solve it. On the downstroke, the original corundum-type phase was observed in nanocrystals below 8 GPa, as it occurs in bulk material.

Finally, it must be stressed the difference in the structural stability established between nanocrystalline and bulk rh-In_2O_3 but keeping a similar compressibility, which extends the possible applications of this compound at larger pressure ranges. Those effects are important in forthcoming studies of the possibility to use Cr^{3+}-doped rh-In_2O_3 nanocrystals at room temperature as a more sensitive pressure sensor than ruby at least up to 20 GPa.

Appendix 7.1: Theoretical and experimental energy bandgap of several polymorph of In_2O_3.

Figure A7.1.1 shows the theoretical *ab initio* electronic band structure of different polymorphs of In_2O_3. It is observed that the four polymorphs studied present a direct bandgap at the Γ point. The values of the direct and indirect energy bandgap of the different polymorphs of In_2O_3 can be observed in **Table A7.1.1**.

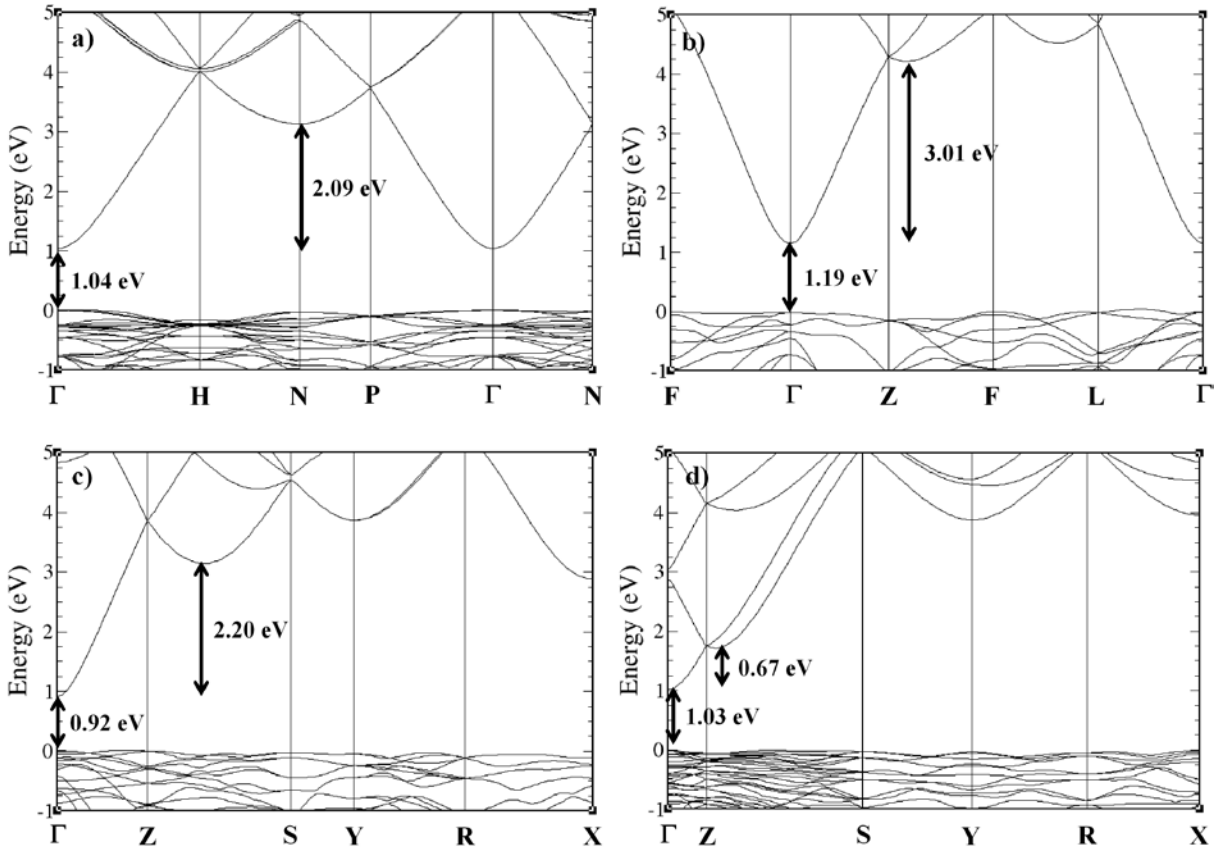

Figure A7.1.1: *Theoretical ab initio electronic band structure of (a) c-In_2O_3, (b) rh-In_2O_3, (c) o1-In_2O_3 and (d) o3-In_2O_3 at 1 atm.*

Polymorph	Direct energy bandgap (eV)	Indirect energy bandgap (eV)
c-In_2O_3	1.04	3.13
rh-In_2O_3	1.19	4.20
o1-In_2O_3	0.92	3.12
o3-In_2O_3	1.03	1.70

Table A7.1.1: *Direct and indirect band-gap of c-In_2O_3, rh-In_2O_3, o1-In_2O_3 and o3-In_2O_3 at 1 atm.*

Figures A7.1.2, **A7.1.3**, **A7.1.4**, **A7.1.5** and **A7.1.6** show the absorption measurements in the IR (red line) and VIS (black line) range.

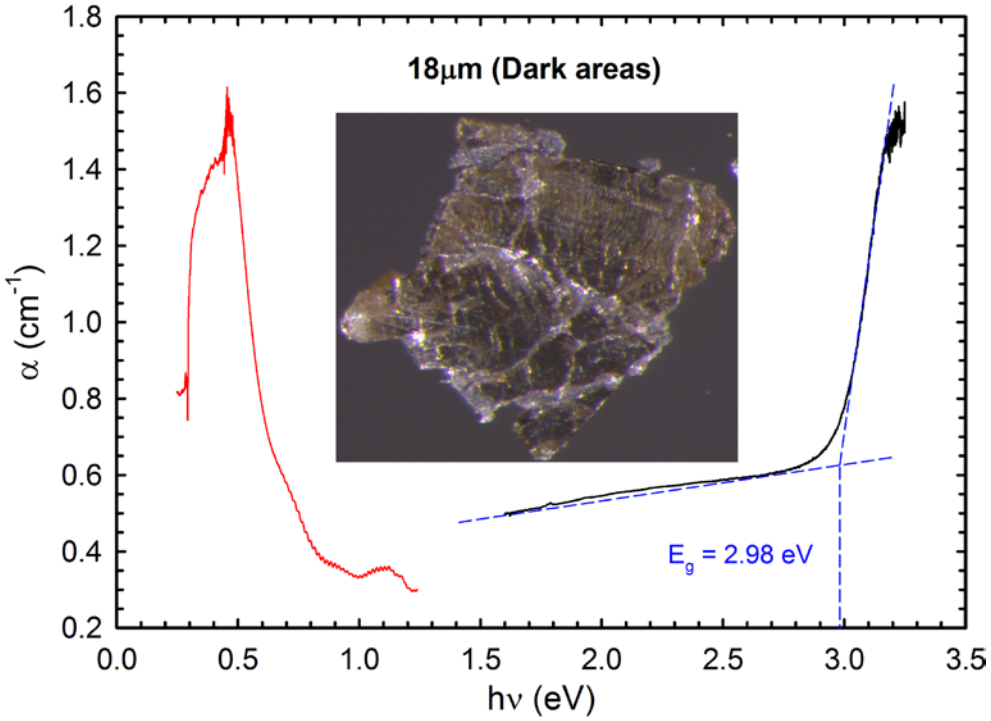

Figure A7.1.2: *Dark areas of the rh-In_2O_3 crystal synthetized from c-In_2O_3 at 20 GPa, 1400 ºC during 7 h. Red (black) lines are related with the IR (VIS) absorption measurements.*

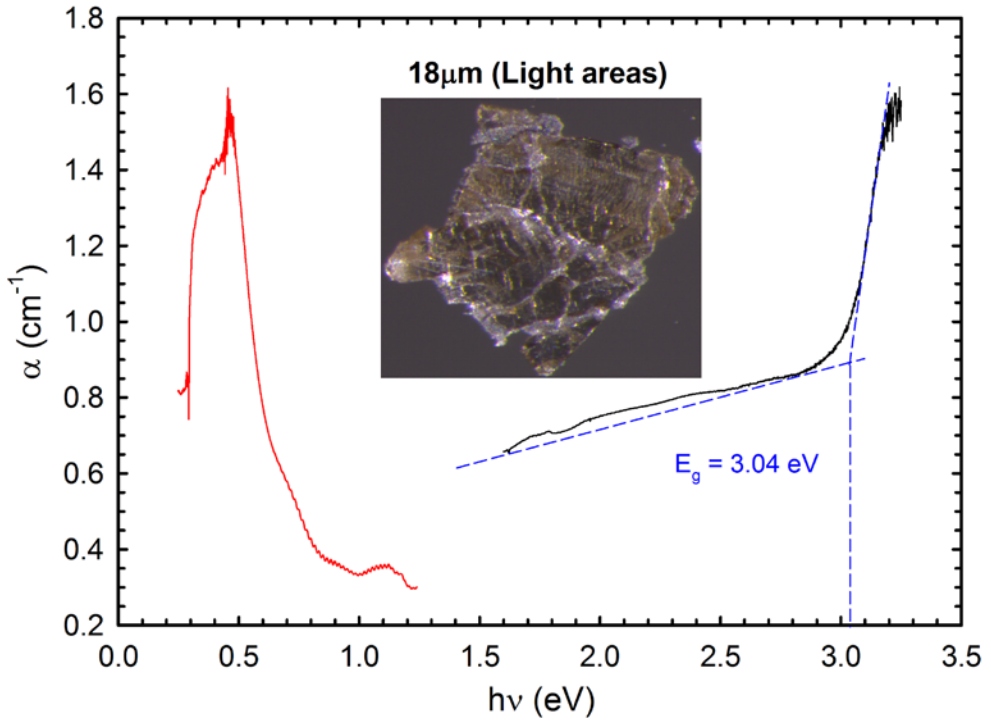

Figure A7.1.3: *Light areas of the rh-In_2O_3 crystal synthetized from c-In_2O_3 at 20 GPa, 1400 ºC during 7 h. Red (black) lines are related with the IR (VIS) absorption measurements.*

As we can observe in the absorption measurements (VIS range), the bandgap of rh-In_2O_3 is slightly higher (~ 0.06 eV) in the light areas than in the dark areas.

From the same synthesis (20 GPa, 1400 ºC during 7 h) we annealed some dark crystals (majority of the synthetized sample) to 350ºC during 3 h. **Figure A7.1.4** shows an increment of the energy bandgap of the annealed sample compared with the sample without heat treatment.

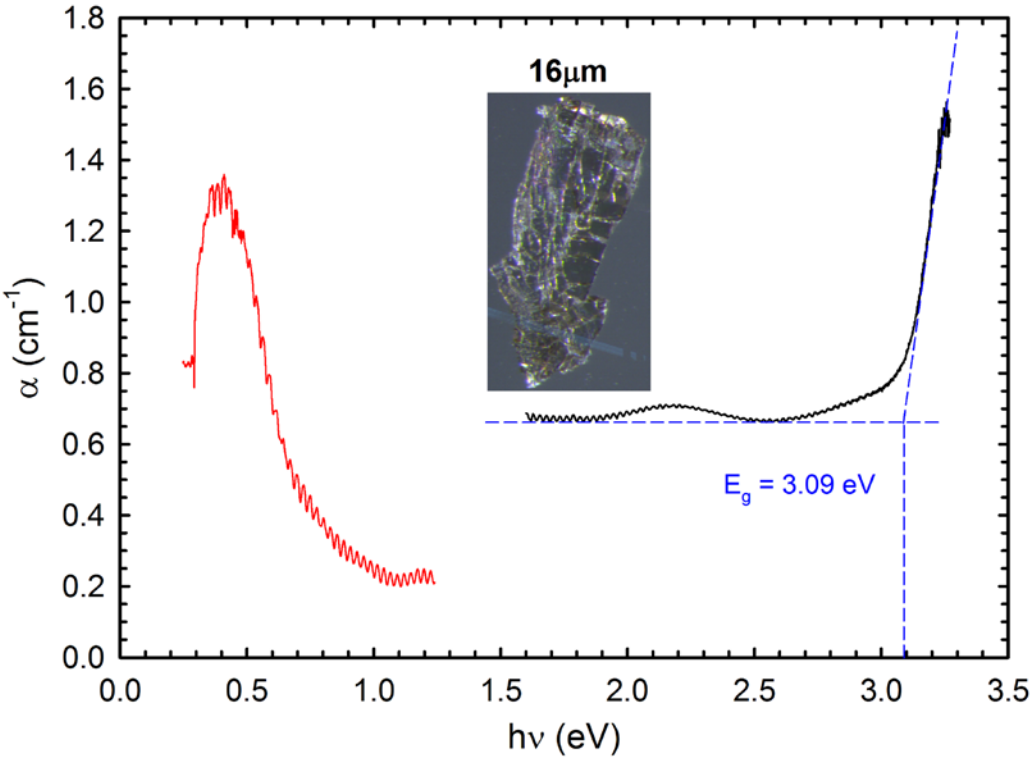

Figure A7.1.4: *rh-In_2O_3 dark crystal synthetized from c-In_2O_3 at 20 GPa, 1400 ºC during 7 h and annealed at 350 ºC during 3 h. Red (black) lines are related with the IR (VIS) absorption measurements.*

Increasing the temperature of the synthesis to 2000 ºC and keeping the pressure constant to 20 GPa, the energy bandgap increases till approximately the same value as the annealed sample as we can observe in **Figure A7.1.5**. Perhaps, the black stripes in the rh-In_2O_3 crystal showed in the **Figure A7.1.5** could be related to a higher proportion of Indium.

Figure A7.1.6 shows the energy bandgap with a closer synthesis conditions to the optimal conditions determined experimentally (12 GPa and 1375 ºC) through *ex-situ* experiments to obtain a pure rh-In_2O_3 phase.

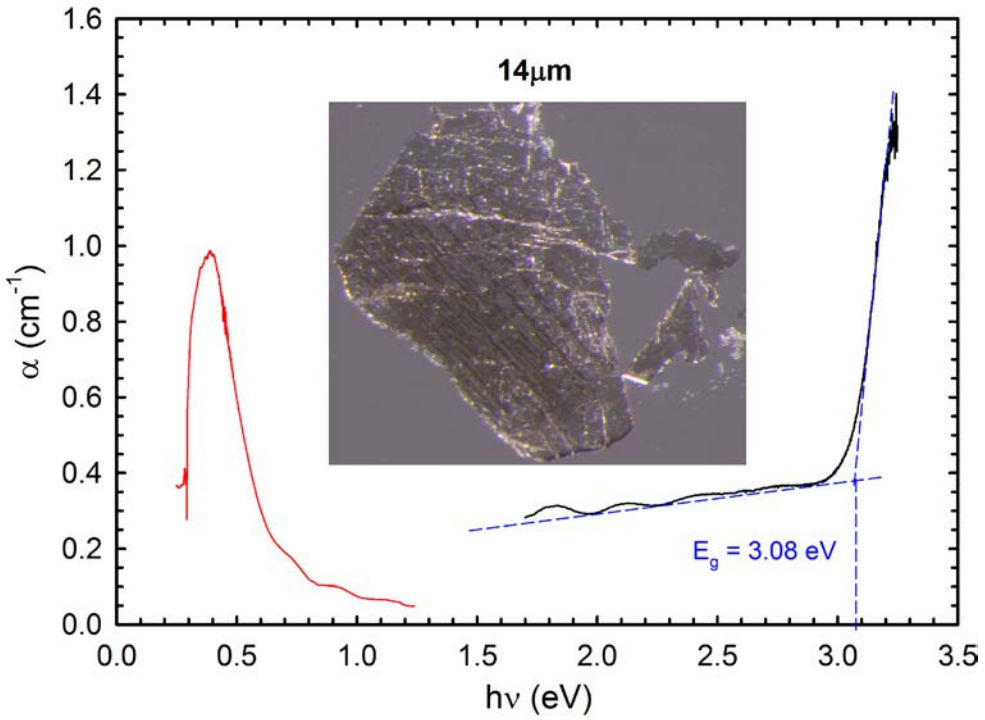

Figure A7.1.5: *rh-In_2O_3 dark crystal synthetized from c-In_2O_3 at 20 GPa, 2000 ºC during 3.5 h. Red (black) lines are related with the IR (VIS) absorption measurements.*

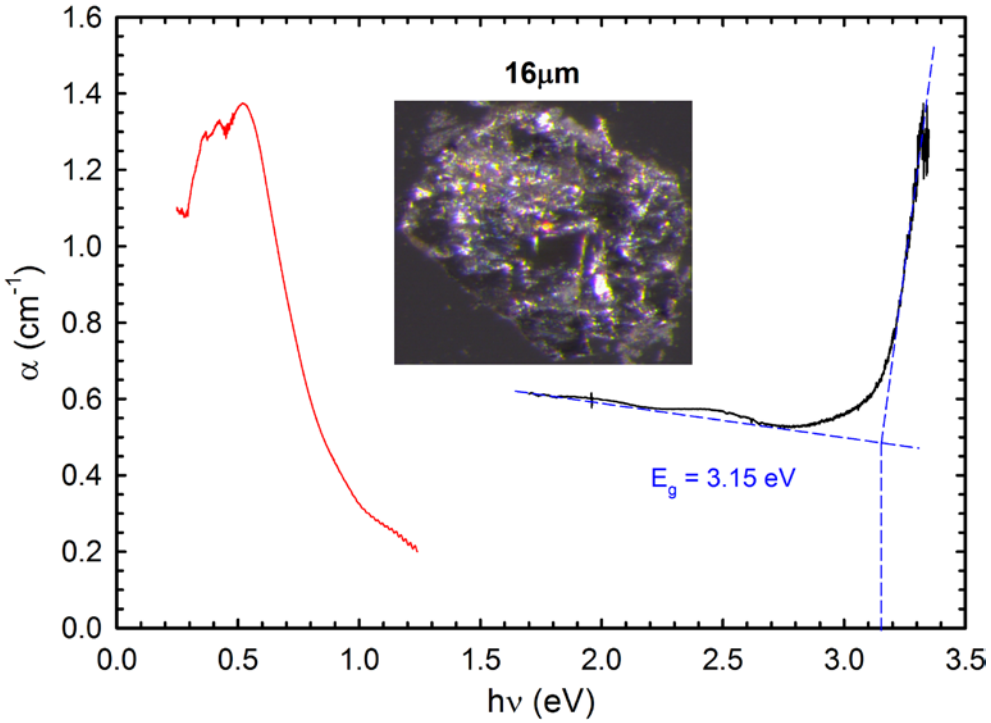

Figure A7.1.6: *rh-In_2O_3 crystal synthetized from c-In_2O_3 at 8 GPa, 1325 ºC during 4 h. Red (black) lines are related with the IR (VIS) absorption measurements.*

Table A7.1.2 resumes the experimental values of the energy bandgap obtained from absorption measurements for different rh-In_2O_3 synthetized crystals.

Synthesis conditions	Thickness (μm)	E_g (eV)
20GPa – 1400ºC – 7h (dark zones)	18	2.98
20GPa – 1400ºC – 7h (light zones)	18	3.04
20GPa – 1400ºC – 7h and annealed to 350ºC during 3 h	16	3.09
20GPa – 2000ºC – 3.5h	14	3.08
8GPa – 1325ºC – 4h	16	3.15

Table A7.1.2: *Experimental energy bandgap for different rh-In_2O_3 synthetized crystals.*

Clearly, it is observed a big underestimation of the theoretical bandgap compared with the experimental values. This is a common result since DFT-based *ab initio* calculations based on LDA or GGA tend to underestimate the experimental bandgap **[224]**.

Chapter 8

Conclusions

The conclusions after performing this thesis work could be summarized in the following ideas.

After carrying out a comparative vibrational study of bulk and nanocrystalline c-In_2O_3 under compression employing a 16:3:1 mixture of MEW as a PTM we conclude that the c-In_2O_3 structure is stable at least up to 30 GPa under quasi-hydrostatic conditions. Thanks to *ab initio* calculations, we have been able to assign the symmetry of 16 (8) observed Raman-active modes in bulk (nanocrystalline) c-In_2O_3, despite Raman-active mode frequencies are underestimated about a 5% by theoretical *ab initio* calculations.

We have reported the discovery of a new polymorph of In_2O_3 at high pressures. The new polymorph (o3-In_2O_3) crystallizes in the orthorhombic Rh_2O_3−III structure with *Pbca* space group (N. 61). To determine that polymorph, we performed a structural and vibrational study under pressure up to 50 GPa of bulk c-In_2O_3 helped with theoretical *ab initio* calculations. **Scheme 5.1** shows the sequence of pressure-induced phase transitions in In_2O_3 up to 50 GPa. Two experiments, using helium (XRD study) or a 16:3:1 mixture of MEW (Raman study) as a PTM, show that c-In_2O_3 transforms into o1-In_2O_3 around 35 GPa in the upstroke process under quasi-hydrostatic conditions. In the downstroke process, the sample transforms from o1-In_2O_3 to o3-In_2O_3 between 40 and 20 GPa (depending on the PTM employed in the experiment), and then to the rh-In_2O_3, the recovered structure at ambient conditions, below 8 GPa. A subsequent recompression of rh-In_2O_3 shows a phase transition to o3-In_2O_3. Therefore, o3-In_2O_3 is clearly the post-corundum phase; i.e., the high-pressure phase between

the *R-3c* and the *Pbcn* phases. The difference in the transition pressures observed experimentally and predicted in the theoretical calculations could be attributed to the presence of high kinetic barriers for pressure-induced transformations in this compound. Moreover, we could obtain experimentally the equations of state of c-In_2O_3, o1-In_2O_3 and o3-In_2O_3 phases, whose V_0 and B_0 parameters obtained with a second-order Birch-Murnaghan EoS (B_0' = 4) compare reasonably well with those obtained by theoretical *ab initio* calculations.

In order to try to recover o3-In_2O_3 as a metastable phase at room conditions starting from bulk c-In_2O_3, we performed different HP-RS experiments under non-hydrostatic conditions using silicone oil as a PTM and also without PTM up to 27.2 and 39.6 GPa, respectively. The conclusions of these experiments were: First, in the upstroke process, c-In_2O_3 transforms into o1-In_2O_3 through an intermediate o3-In_2O_3 phase. This contrast with our results when MEW (16:3:1) or helium was used as a PTM. In such cases, c-In_2O_3 transforms directly into o1-In_2O_3. Second, although o3-In_2O_3 coexists with rh-In_2O_3 down to 0.7 GPa in the downstroke process when a non-hydrostatic PTM is used, we could not recover o3-In_2O_3 as a metastable phase at ambient conditions. In this context, we think that new experiments, e.g. performing a new pressure cycle up to 50 GPa in the worst hydrostatic conditions, i.e., without PTM could lead in the downstroke process to have pure o3-In_2O_3 close to 4 GPa. At that pressure, two quench strategies could be undertaken. The first one is to quench the sample in pressure and the second one is to quench the sample in temperature introducing the DAC into a tank of liquid nitrogen and after that decrease the pressure to ambient pressure in order to get pure o3-In_2O_3.

We were able to synthesize rh-In_2O_3 using large volume presses (Sumitomo 1200 tons multi-anvil press and 200 tons PE press) to generate HP-HT conditions. After many synthesis attempts, we could recover the corundum-type In_2O_3 structure as metastable phase at ambient conditions. The major drawback to overcome was the chemical reaction of the starting c-In_2O_3 sample with the surrounding material at HT. In the early HP-HT synthesis attempts, c-In_2O_3 reacted with the h-BN capsule, forming corundum-type structure of $InBO_3$ (rh-$InBO_3$). To avoid that, we decided to introduce the starting c-In_2O_3 sample into a metallic capsule. We tried platinum and molybdenum as materials for the sample capsule, but in both cases some chemical reaction was observed. Finally, the use of rhenium prevented the occurrence of chemical reaction, and we could synthesize pure rh-In_2O_3 samples.

Figure A6.1.17 summarizes the P-T conditions that allowed us to recover rh-In_2O_3 as a metastable phase at ambient conditions. The best rh-In_2O_3 crystals (from a point of view of the quality of Raman spectra) were obtained in the region around 12 GPa and between 500 and 600 ºC as we could observe in **Figure A6.1.15** and **Figure A6.1.16**. The thermal stability of several crystals of rh-In_2O_3 was studied by RS measurements. We could conclude that rh-In_2O_3 is stable at least up to 500 ºC at ambient pressure.

In order to analyze the HP stability of rh-In_2O_3, we used the sample synthesized at 12 GPa and 1375 ºC (the best rh-In_2O_3 sample obtained till that moment) and subsequently annealed at 300 ºC during 3 h to improve its crystal quality. XRD measurements under pressure allowed us to obtain an accurate experimental equation of state of the corundum-type phase of In_2O_3 that was in good agreement with theoretical calculations. We have found a smaller bulk modulus for rh-In_2O_3 than for isomorphic rh-Al_2O_3, rh-Ga_2O_3 and rh-Cr_2O_3. This result suggests the possibility to use Cr^{3+}-doped rh-In_2O_3 at ambient temperature as a more sensitive pressure sensor than ruby, at least up to 14 GPa. The increase of the quadratic elongation parameter of rh-In_2O_3 with pressure suggests the presence of a mechanical instability of this structure at higher pressures. This result is in good agreement with the much lower stability (phase transition pressure) of rh-In_2O_3 than of rh-Al_2O_3. Besides, RS measurements confirm the phase transition to o3-In_2O_3 (*Pbca*-type) observed by angle-dispersive powder XRD above 14 GPa, as well as the behavior of the octahedral unit and the cation−anion distances with increasing pressure as described by our theoretical calculations.

We performed several attempts to synthesize Cr^{3+}-doped rh-In_2O_3 at HP-HT conditions, but we have not observed a luminescence signal in any of the recovered samples. Probably, a manual mixing of c-In_2O_3 and rh-Cr_2O_3 powders does not allow us to achieve a homogeneous distribution of Cr in the starting sample. This could be the reason why Cr is finally not incorporated into the crystal lattice of rh-In_2O_3. We have begun a collaboration with a chemistry group at the University of Valencia (Prof. Eduardo Martínez Tamayo) to get a better distribution of Cr in the starting c-In_2O_3 sample. Therefore, we hope that in the near future we will be able to make new attempts to synthesize different Cr^{3+}-doped rh-In_2O_3.

Finally, we have also studied the structural and vibrational behavior of rh-In_2O_3 nanocrystals up to 30 GPa. The results have been compared to those of the bulk material and theoretical simulations. Angle-dispersive powder XRD measurements in rh-In_2O_3 nanocrystals have allowed us to obtain a more accurate experimental EoS for this compound in good agreement

with the experiments performed in bulk rh-In_2O_3 and with theoretical calculations. The pressure coefficients for the Raman-active phonon frequencies measured in nanocrystals, confirm the similar bulk modulus of our nanocrystals and bulk material. Moreover, RS measurements show that rh-In_2O_3 nanocrystals undergo a phase transition towards the *Pbca* phase at much higher pressures (above 20 GPa) than in bulk material. However, such a phase transition has not been observed in powder XRD measurements even up to 30 GPa. The origin of this discrepancy might be related to three possible effects: First, RS measurements are more sensitive to local structural changes than XRD measurements. Second, the nanometric size of samples, leading to broader XRD peaks than those in bulk material, and the fact that many peaks of the rhombohedral *R-3c* and orthorhombic *Pbca* phases are coincident in the range between 20 and 30 GPa. Third, it has been recently shown that HP transformations in nanocrystals can be affected by internal defects or even surface effects.

On the downstroke, the original corundum-type phase was observed in nanocrystals below 8 GPa, as it occurs in bulk material. Finally, it must be stressed that the difference in the structural stability established between nanocrystalline and bulk rh-In_2O_3, despite having a similar compressibility, could allow us to extend the possible applications of this compound at larger pressure ranges. Those effects are important in forthcoming studies of the possibility to use Cr^{3+}-doped rh-In_2O_3 nanocrystals at room temperature as a more sensitive pressure sensor than ruby at least up to 20 GPa.

Bibliography

[1] C.G. Granqvist, *Appl. Phys. A: Solids Surf.* **57**, 19 (1993).

[2] H. Mizoguchi and P.M. Woodward, *Chem. Mater.* **16**, 5233 (2004).

[3] A.J. Breeze, Z. Schlesinger, S.A. Carter and P.J. Brock, *Phys. Rev. B* **64**, 125205 (2001).

[4] R.B.H. Tahar, T. Ban, Y. Ohya and Y. Takahashi, *J. Appl. Phys.* **83**, 2631 (1998).

[5] T.C. Kaspar, T. Droubay and J.E. Jaffe, *Appl. Phys. Lett.* **99**, 263504 (2001).

[6] X. Xirouchaki, G. Kiriakidis, T.F. Pedersen and H. Fritzsche, *J. Appl. Phys.* **79**, 9349 (1996).

[7] C.W. Tang and S.A. Vanslyke, *Appl. Phys. Lett.* **51**, 913 (1987).

[8] J.H. Burroughes, D.D.C. Bradley, A.R. Brown, R.N. Marks, K. Mackay, R.H. Friend, P.L. Burns and A.B. Holmes, *Nature* **347**, 539 (1990).

[9] L.M. Tang, L.L. Wang, D. Wang, J.Z. Liu and K.Q. Chen, *J. Appl. Phys.* **107**, 083704 (2010).

[10] B.C.H. Steele and S.J. Golden, *Appl. Phys. Lett.* **59**, 2357 (1991).

[11] B.H. Lee, I.G. Kim, S.W. Cho and S.H. Lee, *Thin Solid Films* **302**, 25 (1997).

[12] S.F. Hsu, C.C. Lee, S.W. Hwang and C.H. Chen, *Appl. Phys. Lett.* **86**, 253508 (2005).

[13] F. Favier, E.C. Walter, M.P. Zach, T. Benter and R.M. Penner, *Science* **293**, 2227 (2001).

[14] T. Takada, K. Suzuki and M. Nakane, *Sens. Actuators B* **13**, 404 (1993).

[15] M.Z. Atashbar, B. Gong, H.T. Sun, W. Wlodarski and R. Lamb, *Thin Solid Films* **354**, 222 (1999).

[16] M. Himmerlich, Ch.Y. Wang, V. Cimalla, O. Ambacher, S. Krischok, *J. Appl. Phys.* **111**, 093704 (2012).

[17] X.Y. Lai, D. Wang, N. Han, J. Du, J. Li, C.J. Xing, Y.F. Chen and X.T. Li, *Chem. Mater.* **22**, 3033 (2010).

[18] I.A. Rauf, *Films. Mater. Lett.* **18**, 123 (1993).

[19] G.B. Palmer, K.R. Poeppelmeier, T.O. Mason, *Chem. Mater.* **9**, 3121 (1997).

[20] C.A. Hoel, J.M.G. Amores, E. Moran, M.A. Alario-Franco, J.F. Gaillard, K.R. Poeppelmeier, *J. Am. Chem. Soc.* **132**, 16479 (2010).

[21] S. Zh Karazhanov, P. Ravindran, P. Vajeeston, A. Ulyashin, T.G. Finstad and H. Fjellvag, *Phys. Rev. B* **76**, 075129 (2007).

[22] M. Marezio, *Acta Crystallogr.* **20**, 723 (1966).

[23] R.D. Shannon, *Solid State Commun.* **4**, 629 (1966).

[24] A.N. Christen and N.C. Broch, *Acta Chem. Scand.* **21**, 1046 (1967).

[25] C.T. Prewitt, R.D. Shannon, D.B. Rogers and A.W. Sleight, *Inorg. Chem.* **8**, 1985 (1969).

[26] T. Atou, K. Kusaba, K. Fukuoka, M. Kikuchi and Y. Syono, *J. Solid State Chem.* **89**, 378 (1990).

[27] A. Gurlo, N. Barsan, U. Weimar, M. Ivanovskaya, A. Taurino, and P, Siciliano, *Chem. Mater.* **15**, 4377 (2003).

[28] D.B. Yu, S.H. Yu, S.Y. Zhang, J. Zuo, D.B. Wang and Y.T. Qian, *Adv. Funct. Mater.* **13**, 497 (2003).

[29] W.S. Seo, H.H. Jo, K. Lee and J.T. Park, *Adv. Mater.* **15**, 795 (2003).

[30] M. Epifani, P. Siciliano, A. Gurlo, N. Barsan and U. Weimar, *J. Am. Chem. Soc.* **126**, 4078 (2004).

[31] D.B. Yu, D.B. Wang, and Y.T. Qian, *J. Solid State Chem.* **177**, 1230 (2004).

[32] M. Sorescu, L. Diamandescu, D. Tarabasanu-Mihaila, and V.S. Teodorescu, *J. Mater. Sci.* **39**, 675 (2004).

[33] C.H. Lee, M. Kim, T. Kim, A. Kim, J. Paek, J.W. Lee, S.Y Choi, K. Kim, J.B. Park and K. Lee, *J. Am. Chem. Soc.* **128**, 9326 (2006).

[34] C.L. Chen, D.R. Chen, X.L. Jiao and C.Q. Wang, *Chem. Commun.* **44**, 4632 (2006).

[35] J.Q. Xu, Y.P. Chen, Q.Y. Pan, Q. Xiang, Z.X. Chen and X.W Dong, *Nanotechnology* **18**, 115615 (2007).

[36] H. Yusa, T. Tsuchiya, N. Sata and Y. Ohishi, *Phys. Rev. B: Condens. Matter Mater. Phys.* **77**, 064107 (2008).

[37] H. Yusa, T. Tsuchiya, J. Tsuchiya, N. Sata and Y. Ohishi, *Phys. Rev. B: Condens. Matter Mater. Phys.* **78**, 092107 (2008).

[38] C.Y. Wang, Y. Dai, J. Pezoldt, B. Lu, T. Kups, V. Cimalla and O. Ambacher, *Cryst. Growth Des.* **8**, 1257 (2008).

[39] H. Saitoh, W. Utsumi and K. Aoki, *J. Cryst. Growth* **310**, 2295 (2008).

[40] A. Gurlo, D. Dzivenko, P. Kroll and R. Riedel, *Phys. Status Solidi RRL* **2**, 269 (2008).

[41] A. Gurlo, P. Kroll and R. Riedel, *Chem. - Eur. J.* **14**, 3306 (2008).

[42] A. Gurlo, *Angew. Chem., Int. Ed.* **49**, 5610 (2010).

[43] M.F. Bekheet, M.R. Schwarz, S. Lauterbach, H.J. Kleebe, P. Kroll, R. Riedel and A. Gurlo, *Angew. Chem., Int. Ed.* **52**, 6531 (2013).

[44] M.F. Bekheet, M.R. Schwarz, S. Lauterbach, H.J. Kleebe, P. Kroll, A. Stewart, U. Kolb, R. Riedel and A. Gurlo, *High Pressure Res.* **33**, 697 (2013).

[45] K. Umemoto and R.M. Wentzcovitz, *Phys. Chem. Miner.* **38**, 387 (2011).

[46] H.R. Hoekstra, *Inorg. Chem.* **5**, 754 (1966).

[47] Y.F. Hao, G.W. Meng, C.H. Ye and L.D. Zhang, *Crystal Growth & Design* **5**, 1617 (2005).

[48] Z. Zhuang, Q. Peng, J. Liu, X. Wang and Y. Li, *Inorg. Chem.* **46**, 5179 (2007).

[49] Y. Fan, Z. Li, L. Wang and J. Zhan, *Nanotechnology* **20**, 285501 (2009).

[50] L.-Y. Chen, Z.-X. Wang and Z.-D. Zhang, *New J. Chem.* **33**, 1109 (2009).

[51] A. Gurlo, M. Ivanovskaya, N. Barsan and U. Weimar, *Inorg. Chem. Commun.* **6**, 569 (2003).

[52] D. Liu, W.W. Lei, B. Zou, S.D. Yu, J. Hao, K. Wang, B.B. Liu, Q.L. Cui and G.T. Zou, *J. Appl. Phys.* **104**, 083506 (2008).

[53] J. Qi, J.F. Liu, Y. He, W. Chen and C. Wang, *J. Appl. Phys.* **109**, 063520 (2011).

[54] A. Walsh and D.O. Scanlon, *Phys. Rev. B* **88**, 16120 (2013).

[55] S.G. Chen, Y.F. Huang, H.N. Xiao, H.W. Liao, C.G. Long, C.Ye and Q. Xia, *Mater. Lett.* **61**, 1937 (2007).

[56] A. Singhal, S.N. Achary, J. Manjanna, O.D. Jayakumar, R.M. Kadam and A.K. Tyagi, *J. Phys. Chem. C* **113**, 3600 (2009).

[57] Y. Zhang, J. Li, Q. Li, L. Zhu, X. Liu, X. Zhong, J. Meng and X. Cao, *Scr. Mater.* **56**, 409 (2007).

[58] O.M. Berengue, A.D. Rodrigues, C.J. Dalmaschio, A.J.C. Lanfredi, E.R. Leite and A.J. Chiquito, *J. Phys. D: Appl. Phys.* **43**, 045401 (2010).

[59] J.C. Chervin, B. Canny, J.M. Besson, and Ph. Pruzan, *Rev. Sci. Inst.* **66**, 2595 (1995).

[60] R. Boehler, *Rev. Sci. Inst.* **77**, 115103 (2006).

[61] http://almax-industries.com/Plate_Dac.html

[62] F.D. Murnaghan, *Proc. Natl. Acad. Sci. U. S. A.* **30**, 244 (1944).

[63] B. García-Domene, J.A. Sans, F.J. Manjón, Sergey V. Ovsyannikov, L.S. Dubrovinsky, D. Martinez-Garcia, O. Gomis, D. Errandonea, H. Moutaabbid, Y. Le Godec, H. M. Ortiz, A. Muñoz, P. Rodríguez-Hernández and C. Popescu, *J. Phys. Chem. C* **119**, 29076 (2015).

[64] M. Laue, *Aufsätze und Vorträge* (in Russian), L. S. Freiman (ed.), Nauka, Moscow 211 (1969).

[65] "Fundamentals of Powder Diffraction and Structural Characterization of Materials", V.K. Pecharsky and P.Y. Zavalij, *Springer* (2009).

[66] "Theories and Techniques of Crystal Structure Determination", U. Shmueli, *Oxford University Press* (2007).

[67] "Crystal structure determination", W. Massa, *Springer* (2000).

[68] "Structure determination from powder diffraction, in Structure determination from powder diffraction data", A.K. Cheetham, ed. by W.I.F. David, K. Shankland, L.B. McCusker and Ch. Baerlocher, *Oxford University Press* (2002).

[69] "International tables for crystallography, Vol. A: Space group symmetry", Th. Hahn, *Springer* (2005).

[70] R.J. Angel, *Rev. Mineral. Geochem.* **41**, 35 (2001).

[71] A. Smekal, *Naturwissenschaften* **11**, 873 (1923).

[72] C.V. Raman. *Indian J. Phys.* **2**, 387 (1928).

[73] R. Singh, *Phys. Perspect.* **4,** 399 (2002).

[74] "Pressure Raman effects in Covalent and Molecular Solids, in Light Scattering in Solids IV", B.A. Weinstein and R. Zallen, ed. by M. Cardona and G. Güntherodt, *Springer* **54**, 463 (1984).

[75] "Vibrational Spectroscopy at High External Pressures", J.R. Ferraro, *Academic Press, Orlando* (1984).

[76] A.F. Goncharov, *Int. J. Spectr.* **2012**, 617528 (2012).

[77] "Vibrational Spectroscopy, in An Introduction to High Pressure Science and Technology", J. Rodríguez and F.J. Manjón, ed. by J.M. Recio and J.M. Menéndez, *CRC Press*, 275 (2015).

[78] "Infrared and Raman spectra of inorganic and coordination compounds, Part A: Theory and applications in inorganic chemistry", K. Nakamoto, *Wiley* (2009).

[79] W. Holzer, W.F. Murphy and H.J. Bernstein, *J. Chem. Phys.* **52**, 399 (1970).

[80] C.F. Shaw III, *J. Chem. Educ.* **58**, 343 (1981).

[81] "Introductory Raman Spectroscopy", J.R. Ferraro, K. Nakamoto and C.W. Brown, *2nd ed., Academic Press, San Diego, C* (2003).

[82] S.A. Asher, *Anal. Chem.* **65**, 59A (1993).

[83] "Laboratory Raman Spectroscopy", D.P. Strommen and K. Nakamoto, *Wiley* (1984).

[84] "Optical Processes in Semiconductors", J.I. Pankove, *Dover Publications* (1971).

[85] A. Einstein, *Verhandlungen der Deutschen Physikalischen Gesellschaft* **18**, 318 (1916).

[86] A. Einstein, *Physikalische Zeitschrift* **18**, 121 (1917).

[87] J.M. Besson and R.J. Nelmes, *Phys. B* **213**, 31 (1995).

[88] J.S. Loveday, R.J. Nelmes, W.G. Marshall, R.M. Wilson, J.M. Besson, S. Klotz, G. Hamel and S. Hull, *High Pressure Res.* **14**, 7 (1995).

[89] S. Klotz, J.M. Besson, G. Hamel, R.J. Nelmes, J.S. Loveday and W.G. Marshall, *High Pressure Res.* **14**, 249 (1996).

[90] Y. Le Godec, M.T. Dove, S.A.T. Redfern, M.G. Tucker, W.G. Marshall, G. Syfosse and S. Klotz, *High Pressure Res.* **23**, 281 (2003).

[91] G. Morard, M. Mezouar, N. Rey, R. Poloni, A. Merlen, S. Le Floch, P. Toulemonde, S. Pascarelli, A. San-Miguel, C. Sanloup and G. Fiquet, *High Pressure Res.* **27**, 223 (2007).

[92] J.P. Perrillat, *Mineral. Mag.* **72**, 683 (2008).

[93] A.D. Rosa, J. Pohlenz, C. de Grouchy, B. Cochain, Y. Kono, S. Pasternak, O. Mathon, T. Irifune and M. Wilke, *High Pressure Res.* **36**, 332 (2016).

[94] "In-situ and Kinetic Studies Using Neutrons, In-Situ Materials Characterization: Across Spatial and Temporal Scales", G. Eckold and H. Schober, *Springer* **193**, 147 (2014).

[95] R. Debord, D. Leguillon, G. Syfosse and M. Fischer, *High Pressure Res.* **23**, 451 (2003).

[96] M. Gauthier, D. Lheureux, F. Decremps, M. Fischer, J. Itie, G. Syfosse and A. Polian, *Rev. Sci. Instrum.* **74**, 3712 (2003).

[97] Manual of the VX3 PE press located at the University of Valencia.

[98] M. McMahon, R. Nelmes, H. Liu and S. Belmonte, *Phys. Rev. Lett.* **77**, 1781 (1996).

[99] H. Ai-Min, G. Chun-Xiao, L. Ming, H. Chun-Yuan, H. Xiao-Wei, Z. Dong-Mei, Y. Cui-Ling, G. Rui and Z. Guang-Tian, *Chin. Phys.* **16**, 2087 (2007).

[100] H. Ting-Jing, C. Xiao-Yan, L. Xue-Fei, W. Jing-Shu, L. Xiu-Mei, W. Ling-Sheng, Y. Jing-Hai and G. Chun-Xiao, *Chin. Phys. B* **24**, 116401 (2015).

[101] Akifumi Onodera, *Phys. Chem. Jpn.* **39**, 2 (1969).

[102] D. Martínez-García, Ch. Ferrer-Roca, Y. Le Godec, P. Munsch, J.P. Itié, V. Muñoz-Sanjosé, *High Pressure Res.* **22**, 403 (2002).

[103] G.D. Pitt and M.K.R. Vyas, *J.Phys.C: Solid State Phys.* **6**, 274 (1973).

[104] "Les systèmes Fe-FeS et Fe-S-Si à haute pression et haute température. Implications pour les noyaux des corps planétaires", G. Morard, *PhD. Thesis* (2006).

[105] N. Kawai and S. Endo, *Rev. Sci. Instrum.* **4**, 425 (1970).

[106] http://home.hiroshima-u.ac.jp/kawazoe/html/Kawazoe04-Method-EN.html

[107] D. Frost, B. Poe, R. Tronnes, C. Liebske, A. Duba, and D. Rubie, *Phys. Earth Planet. Inter.* **143**, 507 (2004).

[108] http://www.bgi.uni-bayreuth.de/index.php?page=2&lng=en&view=6&id=2

[109] K. Syassen, *High Pressure Res.* **28**, 75 (2008).

[110] A. Dewaele, P. Loubeyre and M. Mezouar, *Phys. Rev. B* **70**, 094112 (2004).

[111] "High pressures experimental methods", M.I. Eremets, *Oxford University Press* (1996).

[112] R. Forman, S. Block, J. Barnett and G. Piermarini, *Science* **176**, 284 (1972).

[113] J. Yen and M. Nicol, *J. Appl. Phys.* **72**, 5535 (1992).

[114] W. Holzapfel, *J. Appl. Phys.* **93**, 1813 (2003).

[115] H.K. Mao, J. Xu and P.M. Bell, *J. Geophys. Res.* **91**, 4673 (1986).

[116] L. de Broglie, *Found. Phys.* **1**, 5 (1970).

[117] "Scanning microscopy for nanotechnology, techniques and applications", W. Zhou, Z.L. Wang, *Springer* (2006).

[118] F. Fauth, I. Peral, C. Popescu and M.Knapp, *Powder Diffr.* **28**, S360 (2013).

[119] https://www.cells.es/en/beamlines/bl04-mspd

[120] A.P. Hammersley, S.O. Svensson, M. Hanfland, A.N. Fitch and D. Häusermann, *High Pressure Res.* **14**, 235 (1996).

[121] W. Kraus and G. Nolze, *J. Appl. Crystallogr.* **29**, 301 (1996).

[122] B.H. Toby, *J. Appl. Crystallogr.* **34**, 210 (2001).

[123] A. Mujica, A. Muñoz and R. Needs, *Rev. Mod. Phys.* **75**, 863 (2003).

[124] P. Hohenberg and W. Kohn, *Phys. Rev. B* **136**, 864 (1964).

[125] P.E. Blöchl, *Phys. Rev. B* **50**, 17953 (1994).

[126] G. Kresse and J. Furthmüller, *Phys. Rev. B* **54**, 11169 (1996).

[127] G. Kresse and D. Joubert, *Phys. Rev. B* **59**, 1758 (1999).

[128] W. Kohn, L.J. Sham, *Phys. Rev.* **140**, 1133 (1965).

[129] J.P. Perdew, K. Burke and M. Ernzerhof, *Phys. Rev. Lett.* **77**, 3865 (1996).

[130] J.P. Perdew, A. Ruzsinszky, G.I. Csonka, O.A. Vydrov, G.E. Scuseria, L.A. Constantin, X. Zhou and K. Burke, *Phys. Rev. Lett.* **100**, 136406 (2008).

[131] K. Parlinski (2008). Phonon Software: http://wolf.ifj.edu.pl/phonon/

[132] P.D.C. King, T.D. Veal, F. Fuchs, Ch.Y. Wang, D.J. Payne, A. Bourlange, H. Zhang, G. R. Bell, V. Cimalla, O. Ambacher, R.G. Egdell, F. Bechstedt and C.F. McConville, *Phys. Rev. B* **79**, 205211 (2009).

[133] I. Hotovy, J. Pezoldt, M. Kadlecikova, T. Kups, L. Spiess, J. Breza, E. Sakalauskas, R. Goldhahn and V. Rehacek, *Thin Solid Films* **518**, 4508 (2010).

[134] P. Erhart, A. Klein, R.G. Egdell and K. Albe, *Phys. Rev. B* **75**, 153205 (2007).

[135] Z.F. Pu, M.H. Cao, Y. Jing, K.L. Huang and C.W. Hu, *Nanotechnology* **17**, 799 (2006).

[136] A.P. Alivisatos, *Science* **271**, 933 (1996).

[137] M.A. El-Sayed, *Acc. Chem. Res.* **34**, 257 (2001).

[138] W.B. White and V.G. Keramida, *Spectrochim. Acta, Part A* **28**, 501 (1972).

[139] H. Sobotta, H. Neumann, G. Kuhn and V. Riede, *Cryst. Res. Technol.* **25**, 61 (1990).

[140] N.V. Porotnikov and O.I. Kondratov, *Zh. Neorg. Khim.* **38**, 653 (1993).

[141] C. Vigreux, L. Binet, D. Gourier and B. Piriou, *J. Solid State Chem.* **157**, 94 (2001).

[142] G. Korotcenkov, V. Brinzari, M. Ivanov, A. Cerneavschi, J. Rodriguez, A. Cirera, A. Cornet and J. Morante, *Thin Solid Films* **479**, 38 (2005).

[143] C. Matei Ghimbeu, J. Schoonman and M. Lumbreras, *Ceram. Int.* **34**, 95 (2008).

[144] Ch.Y. Wang, V. Cimalla, H. Romanus, Th. Kups, G. Ecke, Th. Stauden, M. Ali, V. Lebedev, J. Pezoldt and O. Ambacher, *Appl. Phys. Lett.* **89**, 011904 (2006).

[145] X. Tao, L. Sun, Z. Li and Y. Zhao, *Nanoscale Res. Lett.* **5**, 383 (2010).

[146] G. Kresse and J. Furthmuller, *Comput. Mater. Sci.* **6**, 15 (1996).

[147] G. Kresse and J. Hafner, *Phys. Rev. B* **47**, 558 (1993).

[148] G. Kresse and J. Hafner, *Phys. Rev. B* **49**, 14251 (1994).

[149] K. Parlinski, Z.Q. Li and Y. Kawazoe, *Phys. Rev. Lett.* **78**, 4063 (1997).

[150] Akhilesh K. Arora, M. Rajalakshmi, T.R. Ravindran and V. Sivasubramanian, *J. Raman Spectrosc.* **38**, 604 (2007).

[151] F.J. Manjon, J. Lopez-Solano, S. Ray, O. Gomis, D. Santamaria-Perez, M. Mollar, V. Panchal, D. Errandonea, P. Rodriguez-Hernandez and A. Munoz, *Phys. Rev. B* **82**, 035212 (2010).

[152] D. Machon, P. F. McMillan, B. Xu and J. Dong, *Phys. Rev. B* **73**, 094125 (2006).

[153] Q. Guo, Y. Zhao, C. Jiang, W.L. Mao and Z. Wang, *Solid State Commun.* **145**, 250 (2008).

[154] C. Meyer, J.P. Sanchez, J. Thomasson and J.P. Itie, *Phys. Rev. B* **51**, 12187 (1995).

[155] A. Gurlo, *Nanoscale* **3**, 154 (2011).

[156] J.L. Lan, Y.H. Lin, Y. Liu, S.L. Xu, and C.W. Nan, *J. Am. Ceram. Soc.* **95**, 2465 (2012).

[157] J.R. Sootsman, D.Y. Chung and M.G. Kanatzidis, *Angew. Chem., Int. Ed.* **121**, 8768 (2009); *Angew. Chem., Int. Ed.* **48**, 8616 (2009).

[158] K. Ellmer, *Nat. Photonics* **6**, 809 (2012).

[159] M. Murakami, K. Hirose, K. Kawamura, N. Sata and Y. Ohishi, *Science* **304**, 855 (2004).

[160] R. Caracas and R.E. Cohen, *Phys. Rev. B* **76**, 184101 (2007).

[161] B. García-Domene, H.M. Ortiz, O. Gomis, J.A. Sans, F.J. Manjón, A. Munoz, P. Rodríguez-Hernández, S.N. Achary, D. Errandonea, D. Martínez-García, A.H. Romero, A. Singhal and A.K. Tyagi, *J. Appl. Phys.* **112**, 123511 (2012).

[162] J.W.M. Biesterbos, J. Hornstra and J. Less, *J. Common Met.* **30**, 121 (1973).

[163] B. Xu, H. Stokes and J.J. Dong, *J. Phys.: Condens. Matter* **22**, 315403 (2010).

[164] L.A. Martínez-Cruz, A. Ramos-Gallardo and A. Vegas, *J. Solid State Chem.* **110**, 397 (1994).

[165] A. Vegas and M. Jansen, *Acta Cryst. B* **58**, 38 (2002).

[166] D. Santamaría-Pérez and R. Chuliá-Jordán, *High Press. Res.* **32**, 81 (2012).

[167] A. Vegas, *Crystallogr. Rev.* **7**, 189 (2000).

[168] S. Geller, *Acta Crystallogr., Sect. B* **27**, 821 (1971).

[169] S.V. Ovsyannikov, A.M. Abakumov, A.A. Tsirlin, W. Schnelle, R. Egoavil, J. Verbeeck, G. Van Tendeloo, K.V. Glazyrin, M. Hanfland and L. Dubrovinsky, *Angew. Chem., Int. Ed.* **52**, 1494 (2013).

[170] C. Ma, O. Tschauner, J.R. Beckett, G.R. Rossman and W.J. Liu, *Am. Mineral.* **97**, 1219 (2012).

[171] K. Robinson, G.V. Gibbs and P.H. Ribbe, *Science* **172**, 567 (1971).

[172] B. García-Domene, J.A. Sans, O. Gomis, F.J. Manjón, H.M. Ortiz, D. Errandonea, D. Santamaría-Pérez, D. Martínez-García, R. Vilaplana, A.L.J. Pereira, A. Morales-García, P. Rodríguez-Hernández, A. Muñoz, C. Popescu and A. Segura, *J. Phys. Chem. C* **118**, 20545 (2014).

[173] F. Fuchs and F. Bechstedt, *Phys. Rev. B: Condens. Matter Mater. Phys.* **77**, 155107 (2008).

[174] T.P. Beales, .H.L. Goodman and K.A. Scarrott, *Solid State Commun.* **73**, 1 (1990).

[175] A. Boultif and D. Louer, *J. Appl. Crystallogr.* **37**, 724 (2004).

[176] S. Klotz, J.-C. Chervin, P. Munsch and G. Le Marchand, *J. Phys. D: Appl. Phys.* **42**, 075413 (2009).

[177] D. Errandonea, J. Ruiz-Fuertes, J.A. Sans, D. Santamaría-Perez, O. Gomis, A. Gomez and F. Sapina, *Phys. Rev. B: Condens. Matter Mater. Phys.* **85**, 144103 (2012).

[178] F. Birch, *Phys. Rev*. **71**, 809 (1947).

[179] L.W. Finger and R.M, Hazen, *J. Appl. Phys.* **49**, 5823 (1978).

[180] D. Nishio-Hamame, M. Katagiri, K. Niwa, A. Sano-Furukawa, T. Okada and T. Yagi, *High Pressure Res.* **29**, 379 (2009).

[181] S.V. Ovsyannikov, X. Wu, A.E. Karkin, V.V. Shchennikov and G.M. Manthilake, *Phys. Rev. B: Condens. Matter Mater. Phys.* **86**, 024106 (2012).

[182] Y. Sato and S. Akimoto, *J. Appl. Phys.* **50**, 5285 (1979).

[183] P. Dera, B. Lavina, Y. Meng and V.B. Prakapenka, *J. Solid State Chem.* **184**, 3040 (2011).

[184] G.K. Rozenberg, L.S. Dubrovinsky, M.P. Pasternak, O. Naaman, T. Le Bihan and R. Ahuja, *Phys. Rev. B: Condens. Matter Mater. Phys.* **65**, 064112 (2002).

[185] S.V. Ovsyannikov, D.M. Trots, A.V. Kurnosov, W. Morgenroth, H.P. Liermann and L. Dubrovinsky, *J. Phys.: Condens. Matter* **25**, 385401 (2013).

[186] Q. Zhang, X. Wu and S. Qin, *Chin. Phys. Lett.* **29**, 106101(2012).

[187] D.B. McWhan and J.P. Remeika, *Phys. Rev. B* **2**, 3734 (1970).

[188] L.W. Finger and R.M. Hazen, *J. Appl. Phys.* **51**, 5362 (1980).

[189] J. Tsuchiya, T. Tsuchiya and R.M. Wentzcovitch, *Phys. Rev. B: Condens. Matter Mater. Phys.* **72**, 020103 (2005).

[190] H.V. Hart and H.G. Drickamer, *J. Chem. Phys.* **43**, 2265 (1965).

[191] P. Richet, J.A. Xu and H.K. Mao, *Phys. Chem. Miner.* **16**, 207 (1988).

[192] H. Damour, D. Schiferl, W. Denner, H. Schulz and W.B. Holzapfel, *J. Appl. Phys.* **49**, 4411 (1978).

[193] A.P. Jephcoat, R.J. Hemley and H.K. Mao, *Physica B+C* **150**, 115 (1988).

[194] F.C. Marton and R.E. Cohen, *Am. Mineral.* **79**, 789 (1994).

[195] J.A. Xu, E. Huang, J.F. Lin and L.Y. Xu, *Am. Mineral.* **80**, 1157 (1995).

[196] G.H. Watson, W.B. Daniels and C.S. Wang, *J. Appl. Phys.* **52**, 956 (1981).

[197] D. Errandonea, *Phys. Rev. B*, **87**, 054108 (2013).

[198] R. Cherian, C. Gerard, P. Mahadevan, T.C. Nguyen and R. Maezono, *Phys. Rev. B* **82**, 235321 (2010).

[199] D. Guo, G.X. Xie and J.B. Luo, *J. Phys. D: appl. Phys.* **47**, 013001 (2014).

[200] L. Piot, S. Le Floch, T. Cornier, S. Daniele and D. Machon, *J. Phys. Chem. C* **117**, 11133 (2013).

[201] D. Machon, L. Piot, D. Hapiuk, B. Masenelli, F. Demoisson, R. Piolet, M. Ariane, S. Mishra, S. Daniele, M. Hosni, N. Jouini, S. Farhat and P. Meelinon, *Nano Lett.* **14**, 269 (2014).

[202] D. Machon and P. Melinon, *Phys. Chem. Chem. Phys.* **17**, 903 (2015).

[203] S.X. Tang, Y. Li, J. Zhang, H.Y. Zhu, Y.X. Dong, P.W. Zhu and Q.L. Cui, *RSC Adv.* **5**, 85105 (2015).

[204] A. Singhal, D. Jain, M.R. Pai, S. Agouram, D. Errandonea, and A.K. Tyagi, *RSC Adv.* **6**, 108393 (2016).

[205] D. Errandonea, R. Boehler, S. Japel, M. Mezouar and L.R. Benedetti, *Phys. Rev. B* **73**, 092106 (2006).

[206] D. Errandonea, Y. Meng, M. Somayazulu and D. Hausermann, *Physica B* **355**, 116 (2005).

[207] Y. Al-Khatatbeh, K.K.M. Lee and B. Kiefer, *J. Phys. Chem. C* **116**, 21635 (2012).

[208] C. Popescu, J.A. Sans, D. Errandonea, A. Segura and R. Villanueva, *Inorg. Chem.* **53**, 11598 (2014).

[209] P. Bouvier, E. Djurado, G. Lucazeau and T. Le Bihan, *Phys. Rev. B* **62**, 8731 (2000).

[210] O. Ohtaka, H. Fukui, K. Funakoshi, W. Utsumi, T. Irifune and T. Kikegawa, *High Press. Res.* **22**, 221 (2002).

[211] Y. He, J.F. Liu, W. Chen, Y. Wang, H. Wang, Y.W. Zeng, G.Q. Zhang, L.N. Wang, J. Liu, T.D. Hu, H. Hahn, H. Gleiter and J.Z. Jiang, *Phys. Rev. B* **72**, 212102 (2005).

[212] H. Marquardt, A. Gleason, K. Marquardt, S. Speziale, L. Miyagi, G. Neusser, H.R. Wenk and R. Jeanloz, *Phys. Rev. B* **84**, 064131 (2011).

[213] J.Z. Jiang, J.S. Olsen, L. Gerward, D. Frost, D. Rubie and J. Peyronneau, *Europhys. Lett.* **50**, 48 (2000).

[214] B. Chen, D. Penwell, L.R. Benedetti, R. Jeanloz and M.B. Kruger, *Phys. Rev. B* **66**, 144101 (2002).

[215] J.A Sans, R. Vilaplana, D. Errandonea, V.P. Cuenca-Gotor, B. García-Domene, C. Popescu, F.J. Manjón, A. Singhal, S.N. Achary, D. Martínez-García, J. Pellicer-Porres, P. Rodríguez-Hernández and A. Muñoz, *Nanotechnology* **28**, 205701 (2017).

[216] V. Swamy, A.Y. Kuznetsov, L.S. Dubrovinsky, A. Kurnosov and V.B. Prakapenka, *Phys. Rev. Lett.* **103**, 075505 (2009).

[217] M.M. Wu, C. Wang, Y. Zhao, L.S. Xiao, C. Zhang, X.Q. Yu, B.F. Luo, B. Hu, W.Q. Fan and W.D. Shi, *CrystEngComm.* **17**, 2336 (2015).

[218] H. Jiang, L.C. Zhao, L.G. Gai, L. Ma, Y. Ma and M. Li, *CrystEngComm.* **15**, 7003 (2013).

[219] J.M. Besson, J.P. Itie, A. Polian, G. Weill, J.L. Mansot and J. Gonzalez, *Phys. Rev. B* **44**, 4214 (1991).

[220] G. Liu, L. Kong, J. Yan, Z. Liu, H. Zhang, P. Lei, T. Xu, H.K. Mao and B. Chen, *Nanoscale* **8**, 11803 (2016).

[221] D. Machon, M. Daniel, P. Bouvier, S. Daniele, S. Le Floch, P. Melinon and V. Pischedda, *J. Phys. Chem. C* **115**, 22286 (2011).

[222] R. Vilaplana, O. Gomis, F.J. Manjon, H.M. Ortiz, E. Perez-Gonzalez, J. Lopez-Solano, P. Rodriguez-Hernandez, A. Munoz, D. Errandonea, V.V. Ursaki and I.M. Tiginyanu, *J. Phys. Chem. C* **117**, 15773 (2013).

[223] W.G. Yang, X.J. Huang, R. Harder, J.N. Clark, I.K. Robinson and H.K. Mao, *Nat. Commun.* **4**, 1680 (2013).

[224] J.P. Perdew, *Int. J. Quantum Chem., Quantum Chem. Symp.* **19**, 497 (1986)